Three-Dimensional Nonlinear Dynamics and Vibration Reduction of Gear Pairs and Planetary Gears

Dissertation

Presented in Partial Fulfillment of the Requirements for the Degree Doctor of Philosophy in the Graduate School of The Ohio State University

By

Tugan Eritenel, B.S., M.S.

Graduate Program in Mechanical Engineering

The Ohio State University

2011

Dissertation Committee:

Prof. Robert G. Parker, Advisor

Prof. Henry R. Busby

Prof. Gary L. Kinzel

Dr. Sandeep M. Vijayakar

Abstract

This work aims to provide insight into the three-dimensional vibration of gears by investigating the mechanisms of excitation and nonlinearity coming from the gear tooth mesh. The focus is on gear pairs and planetary gears.

The forces and moments generated at the gear tooth mesh cause three-dimensional relative displacements of contacting gear tooth, which disengage portions of gear tooth surface (partial contact loss) nominally designed to be in contact. While complete tooth disengagement (total contact loss) is the most commonly recognized nonlinearity in gears, partial contact loss is also a source of nonlinearity. A three-dimensional lumped-parameter gear mesh model produces the net force and moment at the gear mesh due to an arbitrary load distribution on the gear tooth surface using a translational and twist spring. Thus, the three-dimensional lumped-parameter model, named the equivalent stiffness model, concisely captures the nonlinear behavior. Both translational and twist stiffnesses depend strongly on spatial displacements at the gear mesh, and so are highly nonlinear and time-dependent. The twist moment periodically fluctuates over a mesh cycle, causing twist vibrations.

With gear pairs, there is a twist vibration mode, where the twist stiffness is active, and a mesh deflection mode, where the translational stiffness is active. The dynamic response is nonlinear due to partial and total contact loss. The dynamic

displacements distorts the instantaneous dynamic contact loads compared with the static design contact loads.

To quantitatively assess nonlinear vibrations of gear pairs, a method is developed to give a closed-form analytical expression of the frequency-amplitude curve. Partial contact loss is captured with quadratic and cubic nonlinear terms. The vibration excitation comes from the time-dependent fluctuations due to periodic tooth engagement. The closed-form solution, found using the method of multiple scales, enables immediate calculation of nonlinear dynamic response, stability of the response, and the frequency range of total contact loss.

With planetary gears, modes of vibration are crucial in understanding and reducing vibration. For equally-spaced planetary gears, all vibration modes belong to three types: 1) Rotational-axial modes (named for the displacements of the central members), 2) Translational-tilting modes (named for the displacements of the central members), and 3) Planet modes (only planets are active). This classification is mathematically derived. It depends only on planet spacing, and thus persists for axial asymmetry, e.g., use of helical gears, overhung shafts, different bearings at shaft ends.

Planet spacing and gear tooth counts in planetary gears, when selected based on a set of rules, eliminate some force and moment fluctuation harmonics. It is shown that these fluctuations stem from the relative phase between planet gear meshes. The set of rules that eliminate force and moment fluctuations are derived. The derivation relies solely on the circumferential symmetry, so it is equally valid for static and dynamic conditions, elastic or rigid components, and for axially asymmetric systems.

Acknowledgments

I am grateful to Prof. Robert G. Parker for the opportunity to pursue this PhD degree and the academic guidance. He has exposed me to the academic world through numerous conferences and to the engineering world through industrial projects. His invaluable suggestions during manuscript preparations has helped me improve my academic writing skills. I am thankful to Dr. Sandeep Vijayakar for providing exceptional finite element analysis capability that is used extensively in this work. I wish to express my thanks to him, Prof. Henry Busby, and Prof. Gary Kinzel for serving on my PhD committee. I thank the graduate students of the Dynamics and Vibrations Laboratory for the fruitful discussions and suggestions on many research problems I had faced. I could not have done this work without the support my family provided.

Vita

June 2001	B.S., Mechanical Engineering, Middle East Technical University, Ankara, Turkey
June 2003	M.S., Mechanical Engineering, The Ohio State University, Columbus, Ohio, USA
January 2002–September 2005	Graduate Research Assistant, The Ohio State University
September 2005–June 2006	Graduate Fellow, The Ohio State University
June 2006–present	Graduate Research Assistant, The Ohio State University

Publications

Research Publications

T. Eritenel and R. G. Parker. Vibration Suppression Rules for 3-D Helical Planetary Gears Using Mesh Phasing, *In preparation*, 2011.

T. Eritenel and R. G. Parker. Three-Dimensional Nonlinear Vibration of Gear Pairs, *In preparation*, 2011.

T. Eritenel and R. G. Parker. An Investigation of Nonlinearity in Gear Pairs Using a Lumped-Parameter Model, *In preparation*, 2011.

T. Eritenel and R. G. Parker. Nonlinear Vibration of Gears with Tooth Surface Modifications and Sphere/Half-Space Contact, *In preparation*, 2011.

T. Eritenel and R. G. Parker. Analysis of Nonlinear Rotational Vibrations of Gears With Tooth Surface Modifications Arising from Partial and Total Contact Loss, *7th European Nonlinear Dynamics Conference*, (Submitted), Rome, Italy 2011.

T. Eritenel and R. G. Parker. Modal Properties of Three-Dimensional Helical Planetary Gears, *Journal of Sound and Vibration*, Vol. 325, Issue. 1-2, pp. 397-420, 2009.

T. Eritenel and R. G. Parker. Dynamic Behavior of Gear Systems in Rotorcraft Applications, *3rd International Basic Research Conference on Rotorcraft Technology*, Nanjing, China, 2009.

T. Eritenel and R. G. Parker. Structured Vibration Modes and Natural Frequencies of Helical Planetary Gears, *13th Asia Pacific Vibration Conference*, University of Canterbury, Christchurch, New Zealand, 2009.

T. Eritenel and R. G. Parker. Computational Nonlinear Vibration Analysis of Gear Pairs Using a Three-Dimensional Model, In *ASME Design Engineering Technical Conferences, PTG*, no. DETC2009-87485, San Diego, CA, 2009.

T. Eritenel and R. G. Parker. Vibration Modes of Helical Planetary Gears, In *ASME Design Engineering Technical Conferences, PTG*, no. DETC2009-87494, San Diego, CA, 2009.

T. Eritenel and R. G. Parker. A Static and Dynamic Model for Three-Dimensional Multi-Mesh Gear Systems, In *ASME Design Engineering Technical Conferences, PTG*, no. DETC2005-85673, Long Beach, CA, 2005.

T. Eritenel, D. R. Houser, S. Vijayakar, J. M. Casella Effect of Tooth Deflection and Corner Contact on Backside Separation (Backlash) of Gear Pairs, In *ASME Design Engineering Technical Conferences, PTG*, no. DETC2003-48014, Chicago, IL, 2003.

Fields of Study

Major Field: Mechanical Engineering

Table of Contents

List of Tables

List of Figures

Figure **Page**

Chapter 1: Introduction

1.1 Background and Motivation

Power transmission in vehicles, helicopters, wind turbines, machine tools, etc., use gear trains in a wide variety of configurations including gear pairs, split-torque, and epicyclic (planetary) arrangements. Gears generate vibrations that decrease durability, reliability, and fatigue life. Gear noise, a result of vibration excited by the meshing gear teeth, has adverse effects on the environment, perceived quality, and comfort. Vibration reduction, therefore, has been of tremendous practical importance. This requires a fundamental understanding of gear dynamics. The existing body of knowledge is mostly derived from two-dimensional (2-D) vibration analysis. Thrust forces and tilting/twisting moments in practical systems have been documented as generating three-dimensional (3-D) vibrations, but much remains to be understood in the underlying mechanisms of vibration excitation, sources of nonlinearity, and the consequent nonlinear dynamic response.

1.2 Literature Review

Significant previous research effort has gone into identifying the sources of vibration excitation in geared systems and how to reduce them. Considering gear pairs,

since Harris [30] and Gregory et al. [26] first identified transmission error as the primary quantifier of vibration excitation, transmission error has been treated as the source of vibration [48, 70, 81, 82, 86]. Transmission error is a byproduct of gear mesh elastic deformation and tooth surface modifications. As transmission error is reduced via tooth surface modifications [81,104,116] or the use of helical gears, other excitation sources at the gear mesh begin to dominate and drive the response, thus undermining transmission error as a design metric of vibration reduction [37]. These excitations are moment due to the periodic shifting (shuttling) of the contact loads in the facewidth direction on the gear tooth surface, moment from the axial thrust [37, 96], and friction forces [66, 117, 120, 123]. Fluctuating mesh moments and axial thrust generate tilting/twisting and axial motions, as experiments show [9, 53, 78]. Twisting and axial motion are coupled with rotation and translation [13, 35, 39, 41, 53]. This is an issue in gear pairs [13, 24] as well as planetary gears [2, 93].

Although the nonlinear dynamic behavior of 2-D spur gears is well established in theory [11, 41, 49, 50, 54, 81, 86, 101] and by experiments [11, 45, 46, 48, 54, 105], experimental investigations [53, 112–114] are inconclusive regarding 3-D nonlinear vibration of helical gears. Relative twisting of the gears and axial motion introduces partial contact loss nonlinearity [6, 10, 34, 35, 81, 121, 122]. The contact pattern fluctuates under dynamic conditions [6, 121], and Velex and Ajmi [119] note the presence of nonlinear response in a helical gear set. These phenomena, nonlinear dynamics and 3-D motions, must be intertwined. The 3-D excitation mechanisms and the path to nonlinear response remain to be investigated.

The dynamic response of planetary gears involves multiple planet gears that mesh with the sun and the ring gears. Consequently, they are more complicated and

there is less research on vibration of planetary gears than there is on gear pairs. Symmetry in planetary gears gives rise to distinctive properties in the vibration modes [15, 20, 40, 58, 60, 87, 97, 98, 133], which provides a starting point in understanding the dynamics. Considering equally spaced planets, Lin and Parker [58] report three types of vibration modes: 1) Rotational modes, where the central members (the sun, ring and carrier) rotate but do not translate; 2) Translational modes, where the central members translate but do not rotate; and 3) Planet modes, where only the planets move and each planet's motion is a scalar multiple of the first planet. Similar classifications are shown when ring gear deformations are included [133], with diametrically-opposed planets [60, 87], and with compound planetary gears [52].

The properties of vibration modes of planetary gears can be employed to reduce vibration [4, 40, 58, 59, 61, 97, 98]. Analytical expressions of the sensitivity of natural modes to design parameters [59, 61] enable the tuning of the natural frequencies to circumvent resonant behavior. Lin and Parker [59] use modal properties to derive closed-form sensitivity expressions for design parameters. Guo and Parker [28] use the classification of vibration modes given in [52] to obtain closed form sensitivity expressions for compound planetary gears. Another approach, as experiments demonstrate [33, 107], is to eliminate vibrations by planet mesh phasing using planet spacing and tooth counts [62, 97, 98]. Despite the high level of understanding of planetary gear vibration and success in vibration suppression, the inherent assumptions of 2-D dynamic models in these studies limit their applicability. The aforementioned vibration reduction methods, identification of modal properties, sensitivity expressions, and mesh phasing are not addressed in the studies on 3-D planetary gear vibration [2, 40, 88].

1.3 Objectives

This work aims to explore the 3-D vibrations of gear pairs and planetary gears because 2-D models may be too restrictive considering real-world applications. Spatial 3-D vibrations may be important. A distinction must be made, however, between getting accurate dynamic response and enhancing the understanding of gear dynamics. Use of sophisticated large-scale computational models involving a finite element approach [1,2,93,124,127] can give accurate 3-D dynamic response. Insofar as sophisticated large-scale computational models can deal with gears and parts with a high degree of physical detail, they are limited to parametric studies.

This work is thus concerned with exploring the underlying mechanisms of excitation, nonlinearity, and methods of vibration reduction. To that end, the analytical models are simplified to enable mathematical generalizations while retaining crucial features to include 3-D motions and partial contact loss nonlinearity.

1.4 Scope of Investigation

The two most common types of gear configurations are investigated: gear pairs and planetary gears. The gear mesh forces and moments from the load distribution can be identically represented by a 3-D lumped-parameter model. The load distribution is approximated by a discretization scheme that gives the numerical values for the lumped-parameter model. The discretization method and the nonlinear characteristics of the gear mesh, given in Chapter 2, provide a basis for the subsequent nonlinear dynamic analysis in Chapters 3 and 4. It is shown in Chapter 5 that planetary gears, using lumped-parameter model and the circumferential symmetry, the

vibration modes fall into three distinct categories. In Chapter 6 formulae that eliminate force and moment fluctuations in planetary gears are found. The scope of each chapter is detailed in what follows.

Chapter 2 mathematically proves that a 3-D lumped-parameter model, named the equivalent stiffness model consisting of a translational and a twist spring, can reproduce the forces and moments that develop from an arbitrary load distribution on the gear tooth surface. A discretization of the distributed loads on the contact lines provides a numerical approximation. Elasticity of each discretized segment is represented by a network of springs. The contact condition of each segment is tracked so that the discretization considers partial contact loss.

In Chapter 3, nonlinear dynamic analysis is performed. The discretization of contact lines provide the dynamic gear tooth mesh forces and moments. The equivalent stiffness model is used to interpret the calculated dynamic response. The nonlinearity arises from partial and total contact loss, so the 3-D motions are intertwined with the nonlinearity of the gear mesh. The primary resonance of the twist vibration mode is excited by twist moments and the parametric resonance is excited by the fluctuating twist stiffness.

Chapter 4 derives closed-form analytical expressions of nonlinear vibration response of gear pairs, and so provides a design guideline, calculable with minimal effort, to reduce vibration. The analysis method embeds partial contact loss nonlinearity into quadratic and cubic nonlinear terms, thus can consider any source as input. Sphere/half-space contact vibrations are also analyzed for validation. A perturbation method (method of multiple scales) is used to solve the equation of motion.

The quadratic and cubic nonlinear terms yield nonlinear response. The parametric time-dependent terms excite the vibrations.

Chapter 5 characterizes the modal properties of helical planetary gears in 3-D. The mathematical proof of the modal properties and the conditions under which these properties hold generalize the findings on 2-D spur planetary gear models in the literature. The gear mesh is represented by the equivalent stiffness model of chapter 2. Computational observation of vibration modes uncovers three types of modes that are grouped depending on the motion of the central members (the sun gear, ring gear, and carrier): 1) Rotational-axial modes, where central members only rotate and move axially, and the planets' motions are identical; 2) Translational-tilting modes, where central members only translate and tilt – these modes are degenerate with natural frequency multiplicity of two; and 3) Planet modes, where the central members do not move. It is mathematically proven that this is an exhaustive categorization of the vibration mode types; no other vibration mode type is possible. This categorization persists for asymmetric configurations in the gear plane, such as gears overhung from shafts, and bearings with different stiffnesses at arbitrary shaft locations.

Chapter 6 finds a set of rules to eliminate the net force and moment fluctuations at certain harmonics on the central members (sun, ring carrier) of planetary gears. The analysis method relies solely on circumferential symmetry, and thus it is independent of modeling assumptions. It, therefore, equally applies to elastic or rigid members and under static or dynamic operating conditions. For equally-spaced planets, force/moment fluctuations from the gear mesh fall into three categories: 1) In-phase, 2) Sequential-phase, and 3) Counter-phase. On central members, in-phase designs

eliminate radial force and tilting moment fluctuations, sequential-phase designs eliminate axial thrust and torque fluctuations, and counter-phase designs eliminate all force and moment fluctuations. These three phasing conditions yield distinctive dynamic forces and moments on each planet. For diametrically opposed planets, there are two conditions: 1) In-phase, which eliminates radial force and tilting moment fluctuations on central members, and 2) Out-of-phase, which eliminates axial thrust and torque fluctuations.

Chapter 2: An Investigation of Nonlinearity in Gear Pairs Using a Lumped-Parameter Model

2.1 Introduction

The load on mating gear teeth is distributed along the lines of contact. This load distribution is generally not uniform but depends on tooth surface modifications, elastic deformations, and misalignments [18, 64, 76, 109–111]. For practical values of these quantities, the non-uniformity causes partial contact loss, where portions of contact lines theoretically in contact are out of contact. This leads to nonlinearity.

The distribution of load generates axial thrust and tilting/twisting moments, especially in helical gears, in addition to the useful mesh force [14, 37, 39, 76, 77]. These forces and moments can adversely affect the noise and vibration of gears because they induce misalignment and fluctuate over a mesh period [13, 37, 77]. The load distribution and the associated tilting/twisting moments depend on tooth surface modifications, misalignments, and displacements under load. Although calculation of load distribution that includes partial contact loss using contact mechanics or finite element analysis yields the nonlinear forces and moments at the gear mesh [18, 27, 51, 54, 57, 64, 104, 108–111, 121, 124, 126, 127, 131, 132], simpler lumped-parameter representations provide insight into the mechanisms that generate those

forces and moments. As discussed herein, lumped-parameter models can elucidate the nonlinearity of the gear mesh and explain how tilting/twisting moments that impact gear vibration are generated.

Considering the existing literature on lumped-parameter gear mesh models, a lumped translational stiffness at the gear mesh typically is used to represent the total mesh force. Fluctuation of this stiffness is important for noise generation because it excites vibration [26, 30, 39, 86]. The net moment from tooth meshing can similarly cause noise and vibration [9, 31, 37, 77], but an analogous stiffness that captures this moment and its fluctuation been investigated much less. Rigaud et al. [92] find a 2×2 stiffness matrix that couples translational and twisting motion of the gears. Nishino [77] uses a translational and a torsional stiffness to account for the forces and moments from the load distribution, but the stiffness expressions are approximate.

This work aims to identify a lumped-parameter model that accounts for the net force and moment transmission at the gear mesh. The lumped stiffnesses must be a consequence of force and moment balance and must be independent of the analysis method that gives the load distribution on the gear teeth. Considering that the net force and moment from the load distribution and the lumped-parameter model must be equal, the lumped-parameter model is named the equivalent stiffness model. The equivalent stiffness model must include the effects of tooth surface modifications, misalignments, and elastic deflections. The dependence of the lumped-parameter stiffnesses on elastic deflections causes nonlinearity that is important in dynamic analysis. Furthermore, we explore force/moment behavior of the gear mesh using the equivalent stiffness model.

To obtain numerical values of the equivalent stiffnesses, the load distribution is approximated by a discretization scheme using results from the literature [18,57,121]. The discretization divides the nominal contact lines into segments on which the contact is tracked. This captures partial contact loss and the resulting nonlinear behavior arising from tooth surface modifications, misalignments, and elastic deflections. Comparisons with finite element analysis verify the discretization scheme.

2.2 Modeling

2.2.1 Gear Mesh Analytical Model

The net force and moment at the gear mesh comes from the distribution of contact loads on the gear teeth. The dimensions of the gear teeth are large compared with those of the contact area, so the load distribution on the gear teeth may be considered as one-dimensional loading over a narrow strip or line-loading [38]. These lines of loads are named contact lines. Load distribution on a contact line is shown in Figure 2.1(a). The variable v keeps track of the position of contact along nominal contact lines by assigning a unique v for each contact point. The nominal contact lines depend on time t according to the specified pinion rotation speed Ω_p. When the elastic displacements and tooth modifications are small, the position of contact lines is found from the nominal kinematics from gear rotation.

The mesh deflection vector at a contact point on a contact line specified by v is the difference between the position vectors of the contact points on the pinion and gear. The projection of the mesh deflection vector along the tooth surface normal

gives the compressive deflection at υ as

$$\begin{aligned}\delta(\upsilon) = &[x_g - x_p + h(\upsilon) + \beta_p r_p + \beta_g r_g]\cos\psi \\ &+ [z_g - z_p - \phi_p r_p - \phi_g r_g - h(\upsilon)\theta_p]\sin\psi - A_p(\upsilon)\theta_p - A_g(\upsilon)\theta_g\end{aligned} \tag{2.1}$$

$$\begin{aligned}A_p(\upsilon) &= [c(\upsilon) - e_p]\cos\psi + b(\upsilon)\sin\psi \\ A_g(\upsilon) &= -[c(\upsilon) - e_g]\cos\psi + [B - b(\upsilon)]\sin\psi\end{aligned} \tag{2.2}$$

where $B = (r_p + r_g)\tan\Phi$. Figure 2.1 describes the relevant geometry. The fixed basis is defined as $\{\mathbf{E}_1, \mathbf{E}_2, \mathbf{E}_3\}$ oriented such that $\mathbf{E}_1$ is parallel to the line of action of the gear mesh. The translational (x_p, y_p, z_p) and angular $(\phi_p,\ \theta_p,\ \beta_p)$ coordinates of the pinion body are assigned to translations along and rotations about $\mathbf{E}_1$, $\mathbf{E}_2$, and $\mathbf{E}_3$, respectively. The translational and angular coordinates of the gear body follow similarly with subscript g. The base radii are r_p and r_g, Φ is the transverse operating pressure angle, and ψ is the base helix angle. Micron-level deviations of the tooth surface from an involute, such as from gear tooth surface modifications and manufacturing errors, are denoted by $h(\upsilon)$. For material removal $h(\upsilon) > 0$. The radial and axial positions of contact are, respectively, $b(\upsilon)$ measured from the pinion mass center along $\mathbf{E}_1$ and $c(\upsilon)$ measured along $\mathbf{E}_3$. We refer to rotation about $\mathbf{E}_1$ as tilting $(\phi_p,\ \phi_g)$ and rotation about $\mathbf{E}_2$ as twisting $(\theta_p,\ \theta_g)$. The quantities A_p and A_g are named moment arms because they turn out to generate twisting moments, as will be shown in the next paragraph.

The distributed mesh force normal to the tooth surface along all lines of contact is

$$\mathbf{f}(\upsilon) = \left(f(\upsilon)\cos\psi, 0, f(\upsilon)\sin\psi\right)^T, \quad \text{with} \quad f(\upsilon) = k(\upsilon)\,\delta(\upsilon) \tag{2.3}$$

The contact stiffness is $k(\upsilon)$. The value of $k(\upsilon)$ implicitly depends on tooth surface modifications, elastic deflections, and misalignments.The contact stiffness $k(\upsilon)$ must

be in compression ($\delta(\upsilon) \geq 0$) to generate force. This criterion for contact [18] is stated as $k(\upsilon) = 0$ for $\delta(\upsilon) < 0$. The condition of equilibrium states that the forces and moments be balanced. At a given point on the contact line, the distributed mesh force generates the following moments about the pinion and gear mass centers

$$\begin{aligned}
\mathbf{m}_p(\upsilon) &= \begin{pmatrix} -b(\upsilon) \\ r_p \\ c(\upsilon) - e_p \end{pmatrix} \times \begin{pmatrix} f(\upsilon)\cos\psi \\ 0 \\ f(\upsilon)\sin\psi \end{pmatrix} = f(\upsilon) \begin{pmatrix} r_p \sin\psi \\ A_p(\upsilon) \\ -r_p\cos\psi \end{pmatrix} \\
\mathbf{m}_g(\upsilon) &= \begin{pmatrix} B - b(\upsilon) \\ -r_g \\ c(\upsilon) - e_g \end{pmatrix} \times \begin{pmatrix} -f(\upsilon)\cos\psi \\ 0 \\ -f(\upsilon)\sin\psi \end{pmatrix} = f(\upsilon) \begin{pmatrix} r_g \sin\psi \\ A_g(\upsilon) \\ -r_g\cos\psi \end{pmatrix}
\end{aligned} \tag{2.4}$$

The total mesh force and moments about mass centers are

$$\mathbf{F} = (F\cos\psi, 0, F\sin\psi)^T, \quad \text{with} \quad F = \int_S f(\upsilon)\,\mathrm{d}\upsilon \tag{2.5}$$

$$\mathbf{M}_p = \begin{pmatrix} r_p F\sin\psi \\ \displaystyle\int_S f(\upsilon)A_p(\upsilon)\,\mathrm{d}\upsilon \\ -r_p F\cos\psi \end{pmatrix}, \; \mathbf{M}_g = \begin{pmatrix} r_g F\sin\psi \\ \displaystyle\int_S f(\upsilon)A_g(\upsilon)\,\mathrm{d}\upsilon \\ -r_g F\cos\psi \end{pmatrix} \tag{2.6}$$

The $\mathbf{E}_1$ components of the moments, $r_p F\sin\psi$ and $r_g F\sin\psi$, are tilting moments due to the axial thrust $F\sin\psi$. The $\mathbf{E}_2$ components are twisting moments and arise from the moment arms $A_p(\upsilon)$ and $A_g(\upsilon)$ defined in Eq. (2.2). The $\mathbf{E}_3$ components are the useful transmitted torque.

Use of Eqs. (2.1) through (2.6) give the force and moment balance about the pinion and gear mass centers cast in matrix form as

$$\mathbf{K}\mathbf{q} = \mathbf{f}_{\text{ext}}, \tag{2.7}$$

$$\mathbf{q} = \Big(\underbrace{\phi_p, \theta_p, \beta_p, x_p, y_p, z_p}_{\text{pinion}}, \underbrace{\phi_g, \theta_g, \beta_g, x_g, y_g, z_g}_{\text{gear}} \Big). \tag{2.8}$$

$$\mathbf{K} = \left[\begin{array}{cccccc|cccccc}
r_p^2 s^2 \int k\,\mathrm{d}\upsilon & r_p s \int kA_p\,\mathrm{d}\upsilon & -r_p^2 sc \int k\,\mathrm{d}\upsilon & r_p sc \int k\,\mathrm{d}\upsilon & 0 & r_p s^2 \int k\,\mathrm{d}\upsilon & r_p r_g s^2 \int k\,\mathrm{d}\upsilon & r_p s \int kA_g\,\mathrm{d}\upsilon & -r_p r_g sc \int k\,\mathrm{d}\upsilon & -r_p sc \int k\,\mathrm{d}\upsilon & 0 & -r_p s^2 \int k\,\mathrm{d}\upsilon \\
 & \int kA_p^2\,\mathrm{d}\upsilon & -r_p c \int kA_p\,\mathrm{d}\upsilon & c \int kA_p\,\mathrm{d}\upsilon & 0 & s \int kA_p\,\mathrm{d}\upsilon & r_g s \int kA_p\,\mathrm{d}\upsilon & \int kA_p A_g\,\mathrm{d}\upsilon & -r_g c \int kA_p\,\mathrm{d}\upsilon & -c \int kA_p\,\mathrm{d}\upsilon & 0 & -s \int kA_p\,\mathrm{d}\upsilon \\
 & & r_p^2 c^2 \int k\,\mathrm{d}\upsilon & -r_p c \int k\,\mathrm{d}\upsilon & 0 & -r_p sc \int k\,\mathrm{d}\upsilon & -r_p r_g c \int k\,\mathrm{d}\upsilon & -r_p c \int kA_g\,\mathrm{d}\upsilon & r_p r_g c^2 \int k\,\mathrm{d}\upsilon & r_p c^2 \int k\,\mathrm{d}\upsilon & 0 & r_p sc \int k\,\mathrm{d}\upsilon \\
 & \text{Symmetric} & & c^2 \int k\,\mathrm{d}\upsilon & 0 & sc \int k\,\mathrm{d}\upsilon & r_g sc \int k\,\mathrm{d}\upsilon & c \int kA_g\,\mathrm{d}\upsilon & -r_g c^2 \int k\,\mathrm{d}\upsilon & -c^2 \int k\,\mathrm{d}\upsilon & 0 & -sc \int k\,\mathrm{d}\upsilon \\
 & & & & 0 & 0 & 0 & 0 & 0 & 0 & 0 & 0 \\
 & & & & & s^2 \int k\,\mathrm{d}\upsilon & r_g s^2 \int k\,\mathrm{d}\upsilon & s \int kA_g\,\mathrm{d}\upsilon & -r_g sc \int k\,\mathrm{d}\upsilon & -sc \int k\,\mathrm{d}\upsilon & 0 & -s^2 \int k\,\mathrm{d}\upsilon \\
\hline
 & & & & & & r_g^2 s^2 \int k\,\mathrm{d}\upsilon & r_g s \int kA_g\,\mathrm{d}\upsilon & -r_g^2 sc \int k\,\mathrm{d}\upsilon & -r_g sc \int k\,\mathrm{d}\upsilon & 0 & -r_g s^2 \int k\,\mathrm{d}\upsilon \\
 & & & & & & & \int kA_g^2\,\mathrm{d}\upsilon & -r_g c \int kA_g\,\mathrm{d}\upsilon & -c \int kA_g\,\mathrm{d}\upsilon & 0 & -s \int kA_g\,\mathrm{d}\upsilon \\
 & & & & & & & & r_g^2 c^2 \int k\,\mathrm{d}\upsilon & r_g c^2 \int k\,\mathrm{d}\upsilon & 0 & r_g sc \int k\,\mathrm{d}\upsilon \\
 & & & & & & & \text{Symmetric} & & c^2 \int k\,\mathrm{d}\upsilon & 0 & sc \int k\,\mathrm{d}\upsilon \\
 & & & & & & & & & & 0 & 0 \\
 & & & & & & & & & & & s^2 \int k\,\mathrm{d}\upsilon
\end{array}\right] \tag{2.9}$$

$$\mathbf{f}_{\text{ext}} = \left(\begin{array}{c}
-r_p \cos\psi \int kh\,\mathrm{d}\upsilon \\
-\int kh\left[(c-e_p)\cos\psi + (h+b)\sin\psi\right]\,\mathrm{d}\upsilon \\
T_p - r_p \cos^2\psi \int kh\,\mathrm{d}\upsilon \\
-\cos^2\psi \int kh\,\mathrm{d}\upsilon \\
0 \\
-\cos\psi \sin\psi \int kh\,\mathrm{d}\upsilon \\
\hline
-r_g \cos\psi \int kh\,\mathrm{d}\upsilon \\
-\int kh\left[(e_g-c)\cos\psi + (B-b)\sin\psi\right]\,\mathrm{d}\upsilon \\
T_g + r_g \cos^2\psi \int kh\,\mathrm{d}\upsilon \\
\cos^2\psi \int kh\,\mathrm{d}\upsilon \\
0 \\
\cos\psi \sin\psi \int kh\,\mathrm{d}\upsilon
\end{array}\right) \tag{2.10}$$

where $s = \sin\psi$ and $c = \cos\psi$ only in Eq. (2.9). The upper-left matrix elements relate to the pinion degrees-of-freedom, the lower-right matrix elements relate to the gear degrees-of-freedom, and the upper-right matrix elements couple the pinion and the gear degrees-of-freedom. The vector $\mathbf{f}_{\text{ext}}$ includes external loading; the torques on the pinion T_p and gear T_g and tooth surface modifications $h(\upsilon)$ appear here.

All that is needed to find all numerical values in the mesh stiffness matrix $\mathbf{K}$ is a calculation of the stiffness distribution $k(\upsilon)$ and its coordinates $b(\upsilon)$ and $c(\upsilon)$. This calculation requires a computational contact algorithm or an approximate analytical method for contact. The stiffness distribution $k(\upsilon)$ accommodates any flexibility along the line of action including Hertz contact and elastic gear body deformations. Friction forcesare neglected but could be incorporated. It must be noted that Eq. 2.7 is merely a representation of force and moment balance specific for a state of displacement $\mathbf{q}$ of the system. A stiffness matrix $\mathbf{K}$ found at a given pinion and gear torque T_p, T_g, and time t may not be valid at other torques and time because $k(\upsilon)$, $b(\upsilon)$, and $c(\upsilon)$ depend on $\mathbf{q}$ and t.

2.2.2 Gear Body and Bearing Model

The gears are mounted on rigid shafts on two bearings, but these boundary conditions may be altered depending on the application. Figure 2.2 shows the gears on bearings. The axial positions of the bearings measured along $\mathbf{E}_3$ are L_p^A and L_p^B. The bearing translational and angular displacement vectors are

$$\begin{aligned}\mathbf{d}_p^A &= \left[\theta_p\left(L_p^A - e_p\right) + x_p\right]\mathbf{E}_1 + \left[\phi_p\left(e_p - L_p^A\right) + y_p\right]\mathbf{E}_2 + z_p\mathbf{E}_3,\\ \mathbf{d}_p^B &= \left[\theta_p\left(L_p^B - e_p\right) + x_p\right]\mathbf{E}_1 + \left[\phi_p\left(e_p - L_p^B\right) + y_p\right]\mathbf{E}_2 + z_p\mathbf{E}_3.\end{aligned} \tag{2.11}$$

$$\mathbf{\Gamma}_p^A = \phi_p\mathbf{E}_1 + \theta_p\mathbf{E}_2 + \beta_p\mathbf{E}_3. \tag{2.12}$$

The angular bearing deflection at point B is identical to Eq. (2.12) for rigid shafts. The bearings are isotropic in the $\mathbf{E}_1 - \mathbf{E}_2$ plane giving the stiffness matrix for translation as $\mathbf{B}_p^A = \text{diag}\left[k_p^A, k_p^A, k_p^{Az}\right]$, where the equality of stiffness in the two translation directions is evident. The bearing stiffness matrix for rotation is $\boldsymbol{\chi}_p^A = \text{diag}\left[\kappa_p^A, \kappa_p^A, \kappa_p^{Az}\right]$. Similar definitions follow for the remaining bearings.

The governing equations with the bearings follow from force and moment balances as

$$(\mathbf{K}+\mathbf{B})\mathbf{q}=\mathbf{f}_{\text{ext}} \tag{2.13}$$

$$\begin{aligned}
&\mathbf{B}_{1,1}=\mathbf{B}_{2,2}=\kappa_p^A+\kappa_p^B+k_p^A\left(L_p^A-e_p\right)^2+k_p^B\left(L_p^B-e_p\right)^2,\\
&\mathbf{B}_{1,5}=-\mathbf{B}_{2,4}=k_p^A(e_p-L_p^A)+k_p^B(e_p-L_p^B),\quad \mathbf{B}_{3,3}=\kappa_p^{Az}+\kappa_p^{Bz},\\
&\mathbf{B}_{4,4}=\mathbf{B}_{5,5}=k_p^A+k_p^B,\quad \mathbf{B}_{6,6}=\kappa_p^{Az}+\kappa_p^{Bz},\\
&\mathbf{B}_{7,7}=\mathbf{B}_{8,8}=\kappa_g^A+\kappa_g^B+k_g^A\left(L_g^A-e_g\right)^2+k_g^B\left(L_g^B-e_g\right)^2,\\
&\mathbf{B}_{7,11}=-\mathbf{B}_{8,10}=k_g^A(e_g-L_g^A)+k_g^B(e_g-L_g^B),\quad \mathbf{B}_{9,9}=\kappa_g^{Az}+\kappa_g^{Bz},\\
&\mathbf{B}_{10,10}=\mathbf{B}_{11,11}=k_g^A+k_g^B,\quad \mathbf{B}_{12,12}=k_g^{Az}+k_g^{Bz}
\end{aligned} \tag{2.14}$$

2.2.3 Equivalent Stiffnesses Model

We show that it is possible to reduce net effect of the distribution of contact forces on the contact lines to two discrete stiffnesses: a translational one acting at a certain point called the center of stiffness and a twist stiffness. This reduction, described in Figure 2.3, is called the equivalent stiffness model. The four parameters that the equivalent stiffness model requires are: translational mesh stiffness k_m, spread-twist stiffness k_t, and the center of stiffness coordinates $(\bar{b},\bar{c})$ that locate the translational mesh stiffness on the contact plane.

The total force and moments with respect to centers of mass are

$$\bar{\mathbf{F}}=(F\cos\psi,0,F\sin\psi)^T,\quad F=k_m\bar{\delta} \tag{2.15}$$

$$\bar{\mathbf{M}}_p=\begin{pmatrix} r_pF\sin\psi\\ k_t\gamma+F\bar{A}_p\\ -r_pF\cos\psi\end{pmatrix},\bar{\mathbf{M}}_g=\begin{pmatrix} r_gF\sin\psi\\ -k_t\gamma+F\bar{A}_g\\ -r_gF\cos\psi\end{pmatrix} \tag{2.16}$$

$$\begin{aligned}\bar{A}_p &= (\bar{c} - e_p)\cos\psi + \bar{b}\sin\psi \\ \bar{A}_g &= -(\bar{c} - e_g)\cos\psi + \left(B - \bar{b}\right)\sin\psi\end{aligned} \tag{2.17}$$

where $\bar{\delta}$ is mesh deflection at the center of stiffness found by substitution of $b(\upsilon) = \bar{b}$ and $c(\upsilon) = \bar{c}$ into Eq. (2.1). In the equivalent stiffness model, the spread-twist stiffness k_t produces a moment $k_t\gamma$, where $\gamma = \theta_p - \theta_g$ is the relative angular twist about $\mathbf{E}_2$. Force and moment balances give the equivalent stiffness model matrix $\bar{\mathbf{K}}$ as

$$\bar{\mathbf{K}} = \left[\begin{array}{cccccc} k_m r_p^2 s^2 & k_m r_p \bar{A}_p s & -k_m r_p^2 sc & k_m r_p sc & 0 & k_m r_p s^2 \\ & k_m \bar{A}_p^2 + k_t & -k_m r_p \bar{A}_p c & k_m \bar{A}_p c & 0 & k_m \bar{A}_p s \\ & & k_m r_p^2 c^2 & -k_m r_p c & 0 & -k_m r_p sc \\ & & & k_m c^2 & 0 & k_m sc \\ & & \text{Symmetric} & & 0 & 0 \\ & & & & & k_m s^2 \end{array}\right]$$

$$\left[\begin{array}{cccccc} k_m r_p r_g s^2 & k_m r_p \bar{A}_g s & -k_m r_p r_g sc & -k_m r_p sc & 0 & -k_m r_p s^2 \\ k_m r_g \bar{A}_p s & k_m \bar{A}_p \bar{A}_g - k_t & -k_m r_g \bar{A}_p c & -k_m \bar{A}_p c & 0 & -k_m \bar{A}_p s \\ -k_m r_p r_g c & -k_m r_p \bar{A}_g c & k_m r_p r_g c^2 & k_m r_p c^2 & 0 & k_m r_p sc \\ k_m r_g sc & k_m \bar{A}_g c & -k_m r_g c^2 & -k_m c^2 & 0 & -k_m sc \\ 0 & 0 & 0 & 0 & 0 & 0 \\ k_m r_g s^2 & k_m \bar{A}_g s & -k_m r_g sc & -k_m sc & 0 & -k_m s^2 \end{array}\right] \tag{2.18}$$

$$\left[\begin{array}{cccccc} k_m r_g^2 s^2 & k_m r_g \bar{A}_g s & -k_m r_g^2 sc & -k_m r_g sc & 0 & -k_m r_g s^2 \\ & k_m \bar{A}_g^2 + k_t & -k_m r_g \bar{A}_g c & -k_m \bar{A}_g c & 0 & -k_m \bar{A}_g s \\ & & k_m r_g^2 c^2 & k_m r_g c^2 & 0 & k_m r_g sc \\ & & & k_m c^2 & 0 & k_m sc \\ & & \text{Symmetric} & & 0 & 0 \\ & & & & & k_m s^2 \end{array}\right]$$

where $s = \sin\psi$ and $c = \cos\psi$ only in Eq. (2.18).

The stiffness matrix obtained from the equivalent stiffness model must be identical to that obtained from the load distribution. This is expressed as $\mathbf{K} = \bar{\mathbf{K}}$, where $\bar{\mathbf{K}}$ is the equivalent stiffness matrix. To find the equivalent translational mesh stiffness k_m, consider the matrix element $\mathbf{K}_{3,3}$ from Eq. (2.9). Equating this to $\bar{\mathbf{K}}_{3,3}$ from Eq. (2.18) gives

$$k_m = \int_S k(\upsilon)\,\mathrm{d}\upsilon. \tag{2.19}$$

Similarly, the requirement $\bar{\mathbf{K}}_{1,2} = \mathbf{K}_{1,2}$ with

$$\mathbf{K}_{1,2} = r_p \sin\psi \int_S k(\upsilon) A_p(\upsilon)\, \mathrm{d}\upsilon, \quad \bar{\mathbf{K}}_{1,2} = r_p \sin\psi k_m \bar{A}_p \tag{2.20}$$

yields the center of stiffness location

$$\bar{b} = \frac{\displaystyle\int_S k(\upsilon) b(\upsilon)\, \mathrm{d}\upsilon}{k_m}, \; \bar{c} = \frac{\displaystyle\int_S k(\upsilon) c(\upsilon)\, \mathrm{d}\upsilon}{k_m} \tag{2.21}$$

Finally, to find the twist stiffness k_t, $\bar{\mathbf{K}}_{2,2} = \mathbf{K}_{2,2}$ yields

$$k_t = \int_S k(\upsilon) A_p^2(\upsilon)\, \mathrm{d}\upsilon - k_m \bar{A}_p^2. \tag{2.22}$$

Similar calculations that require $\mathbf{K} = \bar{\mathbf{K}}$ for all remaining elements yield the same values of k_m, k_t, $\bar{b}$, and $\bar{c}$.

This proves that, at any instant t, the net effect of the load distribution can be contained in k_m, k_t, $\bar{b}$, and $\bar{c}$. These quantities depend on the instantaneous contact conditions implicit in $k(\upsilon)$, $b(\upsilon)$, and $c(\upsilon)$. They vary with gear deflections and as the gears rotate with a specified gear rotation speed. Thus, the equivalent stiffness model is nonlinear and time-dependent. The foregoing development establishes that the equivalent stiffness model identically reproduces the stiffness matrix arising from an arbitrary load distribution.

2.2.4 Physical Interpretation of the Equivalent Stiffness Model

Although the equivalent stiffness model with k_m, k_t, $\bar{b}$, and $\bar{c}$ represents the load distribution, a few more parameters provide further insight into the nonlinearity of the gear mesh. These additional parameters are the moment arms of the mesh force on the pinion and gear ($\bar{A}_p$ and $\bar{A}_g$), off-mid-plane twist stiffnesses on the pinion and gear (k_{po} and k_{go}), total twist stiffnesses on the pinion and gear (k_{pt} and k_{gt}), and the

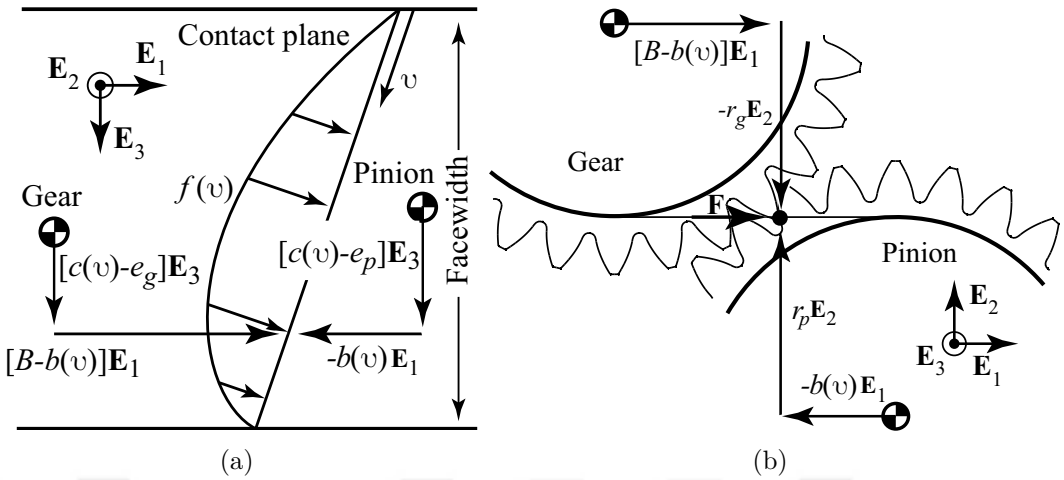

Figure 2.1: Distributed load and the position vectors from the pinion and gear mass centers. (a) Front view, (b) Side view.

coupling-twist stiffness (k_{ct}). The physical interpretation of the equivalent stiffness model and these additional parameters are discussed below.

Translational mesh stiffness k_m

This is the mesh stiffness given by Eq. (2.19) that resists any compression normal to the tooth surface. It generates the mesh force **F** normal to the tooth surface by Eq. (2.15). The line of action component is $F\cos\psi$, and the axial thrust component is $F\sin\psi$.

Center of stiffness $(\bar{b}, \bar{c})$

The axial component $\bar{c}$ of the center of stiffness, given in Eq. (2.21), accounts for the back and forth motion of the mesh force center identified as the shuttling of force [31,37]. The location of the center of stiffness fluctuates with nominal rotation because of two reasons: 1) In helical gears the axial span of contact lines along the facewidth

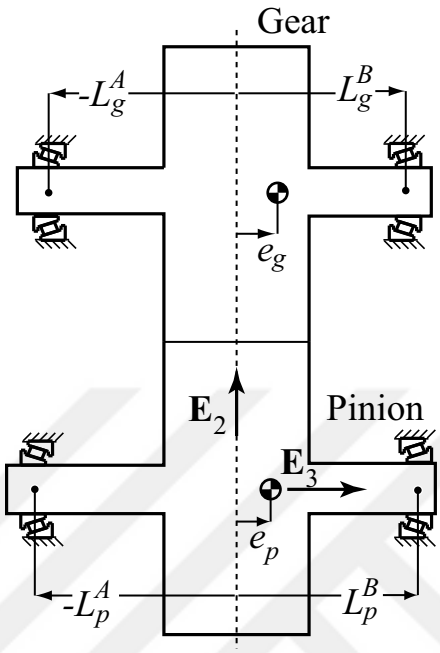

Figure 2.2: Bearing positions with respect to the reference dashed line placed at the center of the active facewidth.

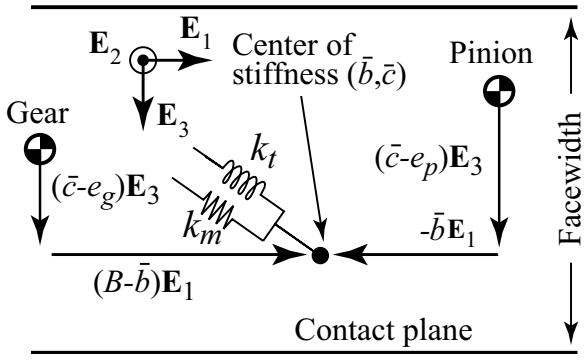

Figure 2.3: The equivalent model and the center of stiffness $(\bar{b}, \bar{c})$ where the total mesh force $\mathbf{F}$ acts and the translational stiffness k_m is attached.

continuously change, 2) If lead modifications vary with roll angle, that yields changes in load distribution with time because the initial separations are functions of time $h(\upsilon) = h(t)$. The radial component $\bar{b}$ of the center of stiffness locates the position of the mesh force along the line of action. Its nominal value of $\bar{b}_{\text{nom}} = r_p \tan\phi$ is geometrically defined and dominates the rotation-dependent fluctuations for typical pressure angles (ϕ).

Moment arms $\bar{A}_p$ and $\bar{A}_g$

These quantities are the moment arms of the mesh force that cause twisting moments about $\mathbf{E}_2$. They are given in Eq. (2.17) and include the moment arm due to: a) an offset $(\bar{c} - e_p)\cos\psi$ along the facewidth, and b) the radial offset $\bar{b}\sin\psi$ due to helix angle.

Total pinion and gear twist stiffnesses k_{pt} and k_{gt}

The total twist stiffnesses are the sum of the spread-twist stiffness and the off-mid-plane twist stiffness. This can be seen by dissecting $\mathbf{E}_2$ components of the mesh moment from Eq. (2.6) as

$$\begin{aligned}\mathbf{M}_p{\cdot}\mathbf{E}_2 &= \int_S f(\upsilon)A_p(\upsilon)\,\mathrm{d}\upsilon = \int_S k(\upsilon)\delta(\upsilon)\left\{[c(\upsilon) - e_p]\cos\psi + b(\upsilon)\sin\psi\right\}\,\mathrm{d}\upsilon \\ &= \left[\int_S k(\upsilon)A_p^2(\upsilon)\,\mathrm{d}\upsilon - k_m\bar{A}_p^2\right]\gamma + F\bar{A}_p = k_t\gamma + F\bar{A}_p\end{aligned} \tag{2.23}$$

where the second equality is obtained following the substitution of Eq. (2.1), the third following the substitution of Eqs. (2.2), (2.15), (2.17), (2.19), and the fourth following the substitution of Eq. (2.22). The analogous procedure for the gear gives $\mathbf{M}_g{\cdot}\mathbf{E}_2 = -k_t\gamma + F\bar{A}_g$. The total pinion and gear twist stiffnesses are

$$
\begin{aligned}
k_{pt} =& \mathbf{K}_{2,2} = \bar{\mathbf{K}}_{2,2} = \int_S k(\upsilon) A_p^2(\upsilon)\, \mathrm{d}\upsilon = k_{po} + k_t \\
k_{gt} =& \mathbf{K}_{8,8} = \bar{\mathbf{K}}_{8,8} = \int_S k(\upsilon) A_g^2(\upsilon)\, \mathrm{d}\upsilon = k_{go} + k_t
\end{aligned}
\tag{2.24}
$$

Spread-twist stiffness k_t

This stiffness gives the moment, $k_t\gamma$, which results from the spread of contact along the facewidth direction. This spreading of contact resists gear twist even if the center of stiffness at which the net force acts is aligned axially with the center of mass: $\mathbf{M}_p{\cdot}\mathbf{E}_2 = k_t\gamma$ for $\bar{A}_p = 0$.

The off-mid-plane twist stiffnesses k_{po} and k_{go}

With known k_t from Eq. (2.22), the off-mid-plane twist stiffnesses are found from Eq. (2.24) as

$$
k_{po} = k_m \bar{A}_p^2, \quad k_{go} = k_m \bar{A}_g^2 \tag{2.25}
$$

The off-mid-plane twist stiffnesses capture the twist stiffness arising from a moment about $\mathbf{E}_2$ generated by the mesh force being offset. This is seen in Eq. (2.23) as moments $F\bar{A}_p$ and $F\bar{A}_g$. They arise from two factors: the offset along the facewidth direction $\mathbf{E}_3$, i.e., $F(\bar{c} - e_p)\cos\psi$, and the offset along the radial direction $\mathbf{E}_1$, i.e., $F\bar{b}\sin\psi$. The off-mid-plane stiffnesses vanish for spur pinion-gear pairs ($\psi = 0$) that are symmetric about the mid-plane ($\bar{c} = e_p$). They are always present in helical gears where $\sin\psi \neq 0$ or when the center of stiffness fluctuates periodically in the facewidth direction as the gears rotate.

Coupling-twist stiffness k_{ct}

This stiffness couples pinion and gear twist by generating a twisting moment on the gear due to a twist in the pinion. It is given by

$$k_{ct} = \bar{\mathbf{K}}_{2,8} = k_m \bar{A}_p \bar{A}_g - k_t \tag{2.26}$$

Again, there are two factors involved: the off-mid-plane component $k_m \bar{A}_p \bar{A}_g$ and the spread-of-contact component k_t.

Discussion of the Equivalent Stiffness Model

The equivalent stiffness model allows separate calculation (possibly using commercial finite element or advanced gear tooth contact models) of the force-displacement curve of the translational spring k_m and moment-rotation curve of the twist stiffnesses k_{pt}, k_{gt}, k_{po}, k_{go}, and k_t. This feature identifies the nonlinearity of translation and twisting individually. The equivalent stiffness model also paves the way for simpler dynamic analysis via numerical integration and mathematical analysis. As an example, one could calculate the strain energy stored in the equivalent stiffnesses to identify the vibration modes where these stiffnesses are active. When these stiffnesses are viewed as periodically fluctuating parameters over a mesh cycle, the fluctuating twist stiffness excites twisting modes just as the fluctuating mesh stiffness k_m excites the mesh deflection modes [26, 30, 92].

2.2.5 Approximation of Load Distribution With a Discretization Scheme

The distribution of contact is discretized following the approach from [18, 121]. Each nominal contact line is divided into n segments with equal length. Within the

ith segment, $f(\upsilon) \approx f_i$, $k(\upsilon) \approx k_i$, $b(\upsilon) \approx b_i$, $c(\upsilon) \approx c_i$, and $\delta(\upsilon) \approx \delta_i$. Each contact stiffness k_i is at the center of its segment. As the contact lines progress with gear rotation, the length $l(t)$ of segments in that contact line changes. Each contact line has a specified number of segments. This discretization is based on the nominal lines of contact with no gear deflections, so it is valid only for small elastic deflections.

To find an expression for the contact stiffnesses k_i, the tooth deflection is divided into two components: local (ϵ_i) and bulk (δ_b). Discussion of this categorization can be found in [6,18,57,79]. The local deflection represents the Hertz contact deflections. The associated local stiffness is $k_c l(t)$, where the constant k_c is the local stiffness per unit contact length. The bulk deflection component represents all deflections except local deflection, including gear blank deflection, tooth bending, and shear. Because the Hertz contact deflections are localized and occur far from the bulk deflections, the bulk deflection is assumed to be the same for all contact segments. The bulk stiffness k_b is assumed constant. The bulk stiffness is in series with the local stiffnesses, so the total deflection at the ith contact point is

$$\delta_i = \epsilon_i + \delta_b \tag{2.27}$$

The mesh force must simultaneously equal the sum of all forces carried by the local stiffnesses and the force carried by the bulk stiffness due to the series connection. Thus,

$$F = \sum_{i=1}^{n} f_i = k_c l(t) \sum_{i=1}^{n} \epsilon_i H(\epsilon_i) = k_b \delta_b, \tag{2.28}$$

$$H(\epsilon_i) = \begin{cases} 1 & \epsilon_i \geq 0 \\ 0 & \epsilon_i < 0 \end{cases} \tag{2.29}$$

where $H(\epsilon_i)$ is the Heaviside function that represents the contact or no contact condition at each contact stiffness. Use of Eqs. (2.27) and (2.28) reduce the network of

local and bulk stiffnesses into n contact springs (k_i, $i = 1, 2, \ldots, n$) in parallel across the contact line. The stiffness of the ith contact spring is

$$k_i = \frac{k_b k_c l(t) H(\epsilon_i)}{k_b + k_c l(t) \sum_{i=1}^{n} H(\epsilon_i)}. \tag{2.30}$$

Even though the local stiffness per unit contact length k_c and the bulk stiffness k_b are constants, the stiffness of each contact segment k_i changes with partial contact loss and contact line length. This is a mathematical result of the spring network, and it is more realistic than assuming a constant stiffness for each contact segment [121, 128]. To explain physically, a segment can only be as stiff as the softest component. For example, consider a gear with wide facewidth but a thin rim (a T shaped profile). Each stiffness k_i is higher if only a few segments are in contact than having a lot of segments in contact because having a lot of segments in contact dilutes k_i as the total stiffness $\sum_{i=1}^{n} k_i$ is limited by the stiffness of the compliant thin rim.

The local stiffness per unit length k_c and the bulk stiffness k_b are parameters of the gear pair determined by the contact mechanics and elasticity of the gears. These constants can be approximated analytically [18] or semi-analytically [121] by assigning certain types of stiffnesses, such as Hertz contact, tooth bending, and shear, to k_c and k_b. In this work k_c and k_b are solved for from the deflections obtained from an external finite element tool; k_c and k_b are numerical values that best fit the deflection obtained from the analysis tool. Tooth bending flexibility only truly belongs to bulk stiffness when one pair of teeth is in contact. If multiple pairs of teeth are in contact, then a third layer of spring network for tooth bending that fluctuates with number of tooth pairs in contact must provide better accuracy. The two stiffnesses, local and bulk, may not be good approximations if they are found analytically that contains

the tooth bending elasticity in the bulk stiffness, but the local and bulk stiffnesses, being values that best fit finite element analysis data, automatically share the tooth bending elasticity giving the upcoming results that compare reasonably well.

The following stipulations simplify the procedure for finding k_c and k_b: 1) The tooth surface is perfectly involute, that is, $h_i = 0$ for all i; 2) All degrees of freedom are constrained to be zero except the pinion rotation β_p; and 3) A specified moment about $\mathbf{E}_3$ is applied to the pinion. With these stipulations, the deflections at all contact points are identical and equal to the static transmission error, $STE = \delta_1 = \delta_2 = \ldots = \delta_n$. Consequently, all points are in contact by Eq. (2.29); $H(\epsilon_1) = H(\epsilon_2) = \ldots = H(\epsilon_n) = 1$, so $k_1 = k_2 = \ldots = k_n$ by Eq. (2.30). Use of Eq. (2.27), and Eq. (2.30) gives

$$STE = F\left[\frac{1}{k_b} + \frac{1}{k_c L(t)}\right], \tag{2.31}$$

where $L(t) = nl(t)$ is the total contact line length at an instant t. The two unknowns (k_c, k_b) are solved using the data from the results of the external analysis tool. Although any two instances can be used, to increase accuracy, two data points are found from the averages of four points where transmission error is the highest $\{STE_{\text{high}}, L_{\text{high}}\}$ within a mesh period and the four points where transmission error is the lowest $\{STE_{\text{low}}, L_{\text{low}}\}$.

2.3 Analysis

2.3.1 Solution Procedure

In this work, the moment about $\mathbf{E}_3$ is specified and the bearings (springs) give the remaining boundary conditions. There are situations, however, when the boundary

conditions specify non-zero deflections of one or more of the twelve degrees-of-freedom (as opposed to the case of specified torques and forces).

The nonlinear equations of motion in Eq. (2.13) are solved by iteration as follows. For given $\mathbf{K}(\mathbf{q}^*, t) + \mathbf{B}$ and $\mathbf{f}_{\text{ext}}(\mathbf{q}^*, t)$ calculated from the previous guess $\mathbf{q}^*$, the solution $\mathbf{q}$ is found by Gauss elimination. This solution is used as the initial guess in the next iteration. Iteration stops when the error in $\mathbf{q}$ is less than a specified tolerance. A limit of 30 iterations is used when some highly misaligned or modified gears yield a small but nonzero error. The starting initial guess is $\mathbf{q}^* = \mathbf{0}$, which corresponds to the undeflected position of the gears with $H(\epsilon_i) = 1$. The deflection $\mathbf{q}^*$ alone does not define the contact conditions $H(\epsilon_i)$ that are required to find $\mathbf{K}(\mathbf{q}^*, t)$, and $\mathbf{f}_{\text{ext}}(\mathbf{q}^*, t)$. The needed quantities are the local deflections (ϵ_i). They are found from Eq. (2.27) where the constant known mesh force F gives the bulk deflection $\delta_b = F/k_b$. With known ϵ_i, Eq. (2.29) gives the contact conditions $H(\epsilon_i)$, which gives k_i by Eq. (2.30). Subsequently, $\mathbf{K}(\mathbf{q}^*, t)$ and $\mathbf{f}_{\text{ext}}(\mathbf{q}^*, t)$ are found.

2.3.2 Comparison With Finite Element Model

This section compares the static deflections from the analytical model with those from a finite element model to build confidence in the formulation. The finite element model is based on the study by Vijayakar [124], and it is commercially available as computer software [125]. This finite element model is specialized for analyzing near-field contact between elastic bodies while using conventional finite elements for the far-field elastic deformation of the bodies. It has been used in many gear studies [5, 65–67, 85, 86, 99, 100, 103] and considers partial contact loss. The analytical model

uses the constants (k_c, k_b) from the finite element model using the method described with Eq. (2.31).

Two example gear pairs are analyzed. To keep the focus on the gear mesh model, the bearing deflections are set to zero by constraining all degrees of freedom except the pinion rotation (β_p) in the analytical and the finite element model. The first example is the helical gear pair defined in Table 2.1. Young's modulus is 206 GPa and Poisson's ratio is 0.3. The pinion torque is 200 N-m, which is below the maximum torque for infinite life based on the Fairfield gear design software. Table 2.2 gives the tooth surface modifications on the gear, chosen to improve misalignment tolerance and to eliminate corner contact [17, 63, 64].

Table 2.1: Example gear parameters.

Parameter	Pinion	Gear
Number of teeth	27	35
Base helix angle, ψ [deg]	28.08	
Center distance [mm]	88.9	
Transverse module [mm]	3	
Transverse operating pressure angle, Φ [deg]	24.6	
Transverse tooth thickness [mm]	5.2253	4.764
Facewidth [mm]	20.0	20.0
Tip diameter [mm]	84.0	104.8
Root diameter [mm]	70.612	91.5416
Bearing A axial position, L^A [mm]	-10	10
Bearing B axial position, L^B [mm]	-10	10
Center of mass position , e [mm]	0	0
Translational bearing stiffness, k^A, k^B [N/m]	100×10^6	100×10^6
Axial bearing stiffness, k^{Az}, k^{Bz} [N/m]	10×10^6	10×10^6
Twist bearing stiffness, κ^A, κ^B [Nm]	0	0
Mass (for Chapters 3 and 4), m [kg]	3	3
Tilting inertia, J^x [kg-m^2]	0.008	0.008
Rotational inertia, J^z [kg-m^2]	0.016	0.016

Table 2.2: Tooth surface modification on the gear in Table 2.1.

Parameter	Magnitude	Begins	Ends
Quadratic tip crown	10 μm	26 deg	Gear tip
Quadratic root crown	10 μm	26 deg	17 deg
Circular lead crown	10 μm	-10 mm	10 mm

The second example is the unity ratio spur gear pair from [47]. The pitch diameter is 150 mm, and the facewidth is 20 mm. Three variations of this spur gear pair as presented in [47] are analyzed. In all three variations, the tip relief amplitude is 10 μm and the lead crown is 5 μm on both the pinion and gear. The parameter that varies is the roll angle where tip relief starts.

Figure 2.4(a) compares the static transmission error of the helical gear pair from the finite element model with the analytical model. Figures 2.4(b), 2.4(c), and 2.4(d) show the static transmission error of the spur gear pair with tip relief on both gears starting at 20.9 deg (170 N-m torque), 22.2 deg (340 N-m torque), and 23.6 deg (340 N-m torque), respectively. The analytical model compares well with the benchmark finite element model in all cases.

Figure 2.5 compares contact patterns from the analytical model and the finite element model of the spur gear pair from [47]. The finite element model calculates the contact pressure, the force divided by the contact area averaged over a mesh period. Because the analytical model approximates the contact area, which is actually a thin elliptical region, by a line, the discretization scheme uses the contact force divided by the contact line length instead of the true pressure to find the contact pattern. Tip relief starts at 20.9 deg on both gears. The applied torque is 85 N-m in Figures 2.5(a)

and 2.5(b), 170 N-m in Figures 2.5(c) and 2.5(d), and 340 N-m in Figures 2.5(e) and 2.5(f). The contact from both models spans a larger area of the gear tooth surface with increasing torque. At all three torques there is partial contact loss because parts of the tooth surface are out of contact as the mesh deflection is not large enough to compensate for the separation from tooth surface modifications.

The analytical model can treat misaligned gears (that is, gears with a specified relative twist angle). The contact pressure from the finite element model at an instant when the misalignment (relative twist angle) $\gamma = 0.01$ deg is shown in Figure 2.6(a). Figures 2.6(c) and 2.6(b) compare contact patterns from the analytical and finite element models at 0.01 deg misalignment. Contact patterns from both models indicate severe partial contact loss. The analytical model effectively captures partial contact loss.

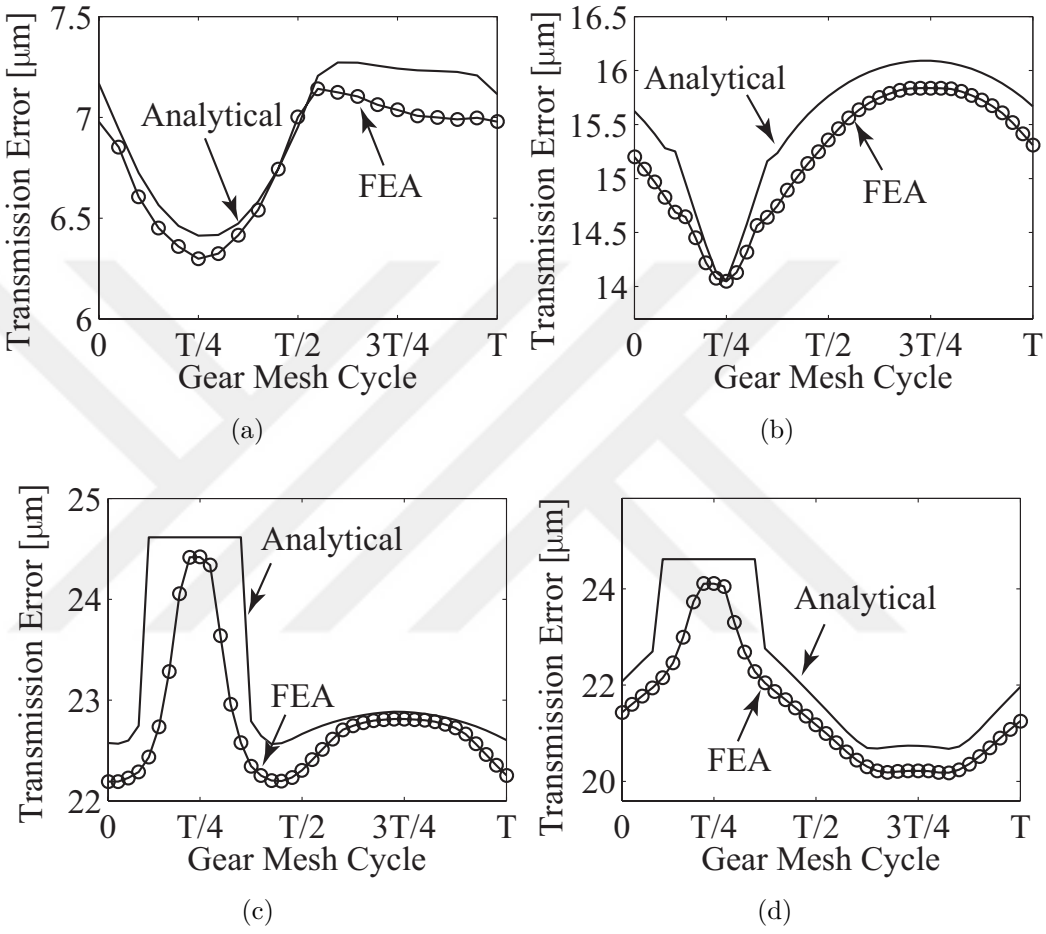

Figure 2.4: Static transmission error from the analytical (solid line) and finite element (circles) model. (a) Helical gear pair described in Tables 2.1 and 2.2. (b) Spur gear pair in experiments. Tip relief starting at $\alpha = 20.9$ deg. The applied torque is 170 N-m. (c) Spur gear pair in experiments. Tip relief starting at $\alpha = 22.2$ deg. The applied torque is 340 N-m. (d) Spur gear pair in experiments. Tip relief starting at $\alpha = 23.6$ deg. The applied torque is 340 N-m.

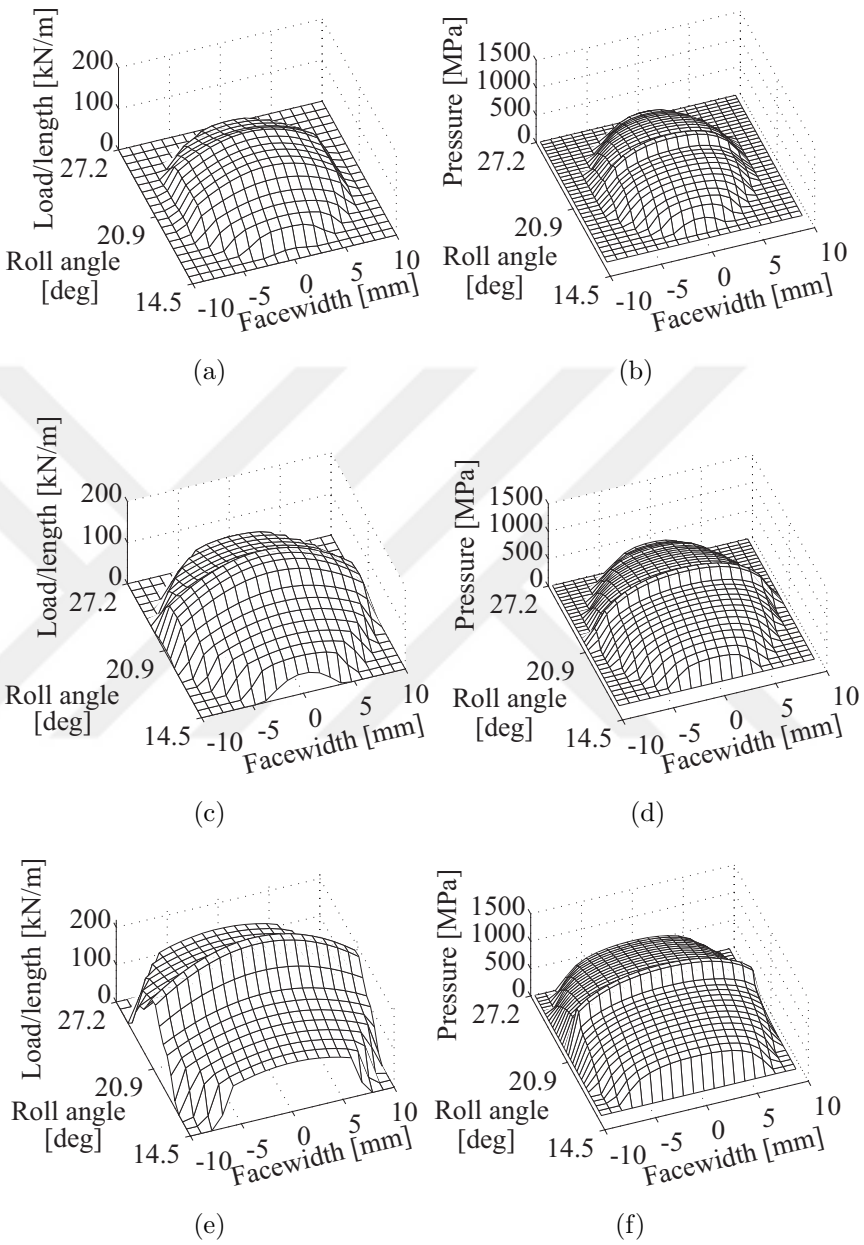

Figure 2.5: Contact patterns from the analytical model (a), (c), (e), and the finite element model (b), (d), (f), of the spur gear pair in experiments. Tip relief starts at $\alpha = 20.9$ deg. The applied torque is: (a,b) 85 N-m. (c,d) 170 N-m. (e,f) 340 N-m.

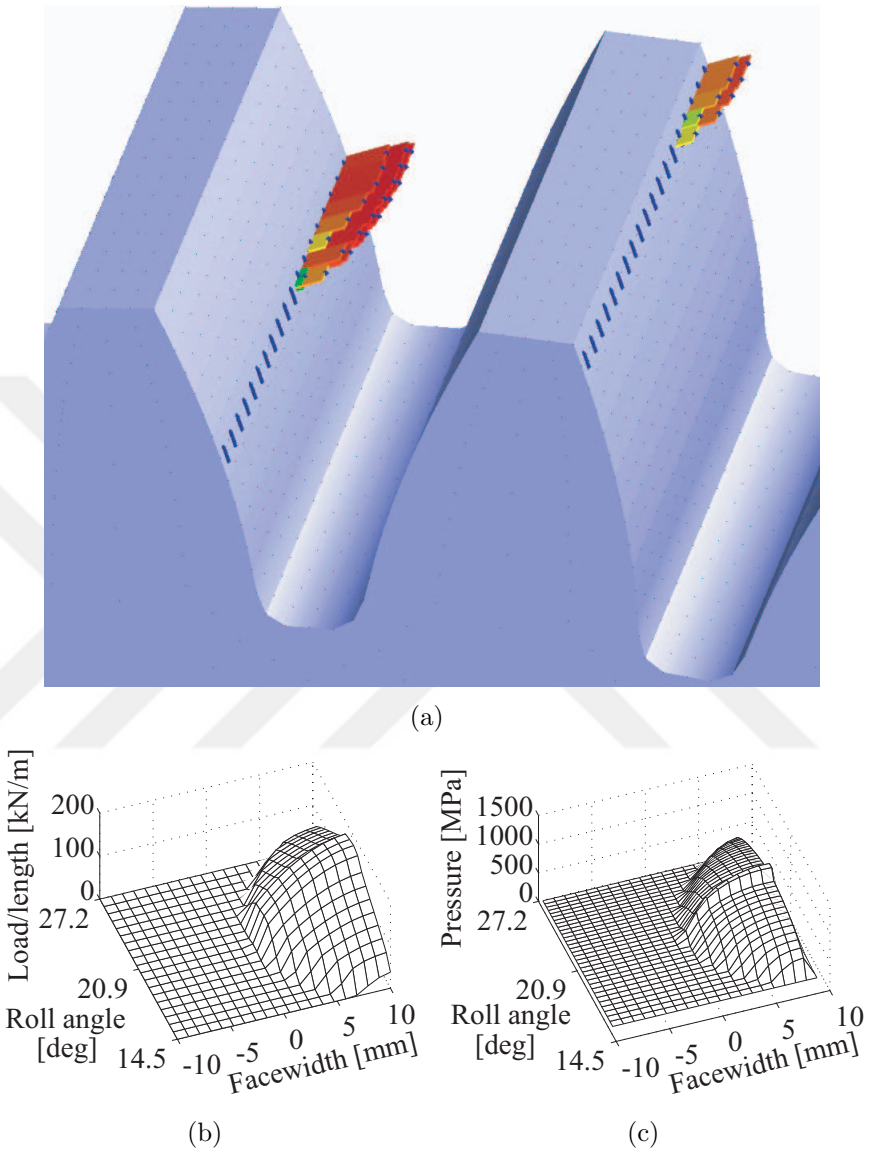

Figure 2.6: Contact analysis of the spur gear pair in experiments. Relative twist is $\gamma = 0.01$ deg. Tip relief starts at $\alpha = 20.9$ deg. The applied torque is 85 N-m. (a) Contact forces from the finite element model. Dots indicate theoretical contact lines, bars indicate contact pressure. (b) Contact pattern averaged over a mesh cycle from the finite element model (c) Contact pattern averaged over a mesh cycle from the analytical model.

2.3.3 Gear Mesh Nonlinearity

The equivalent model concisely contains the sources of nonlinearity from the gear mesh in the deflection-dependent changes of the translational stiffness k_m, spread-twist stiffness k_t, and center of stiffness $(\bar{b}, \bar{c})$. The nonlinear behaviors of these quantities are explored by examining the displacement and stiffness curves obtained by applying torque and twisting moments on the gear pairs. At each data point the average values of the translational stiffness k_m, the total twist stiffnesses k_{pt}, k_{gt}, off-mid-plane twists stiffnesses k_{po}, k_{go}, the spread-twist stiffness k_t, the center of stiffness $(\bar{b}, \bar{c})$, and the moment arms $\bar{A}_p$ and $\bar{A}_g$ over a mesh period are calculated.

Dependence on Mesh Deflection

To expose the effect of mesh deflection on the nonlinearity of the gear mesh, the mesh deflection of the modified helical gear pair described in Tables 2.1 and 2.2 is gradually increased from 1 μm to 20 μm by increasing the driving and absorbing torques on the pinion and gear about $\mathbf{E}_3$. All degrees-of-freedom except pinion and gear rotation are constrained to isolate the translational mesh deflection. The translational stiffness k_m and the spread-twist stiffness k_t are plotted in Figures 2.7(a) and 2.7(b). Figures 2.8(a), 2.8(b), and 2.8(c) show the contact pattern when the mesh deflection is 1 μm, 6 μm, and 10 μm, respectively.

The loaded surface area increases with increasing mesh deflection, thereby increasing the translational and spread-twist stiffnesses. This is a result of partial contact loss, and it makes the translational stiffness k_m and the spread-twist stiffness k_t nonlinear. The center of stiffness (not plotted) is always at the center of the facewidth

because the modifications are symmetric along the facewidth; increasing mesh deflection does not cause an axial shift in the load distribution.

Dependence on Twist (misalignment)

To expose the effect of twist on the nonlinearity of the gear mesh, the relative twist angle $\gamma = \theta_p - \theta_g$ is gradually varied by applying a moment on the pinion about $\mathbf{E}_2$. The shafts supported on bearings provide the boundary conditions.

With unmodified helical gears as described in Table 2.1, the translational and spread-twist stiffnesses, shown in Figures 2.9(a) and 2.9(b), are constant until $|\gamma| = 0.005$ deg, after which there is a sharp drop initiated by the separation of the edges of the teeth. This separation of the edges is reflected in the center of stiffness in Figure 2.9(c) with a sudden move of the center of stiffness toward the highly loaded side. Figures 2.10(a) and 2.10(b) show the contact pattern at two relative twisting angles: $\gamma = 0$ and $\gamma = 0.04$ deg.

When $|\gamma| < 0.005$ deg, which is just before the separation of the edges, the translational and spread-twist stiffnesses are linear and are at their maximum values because there is no partial contact loss for $|\gamma| < 0.005$. Twisting localizes the contact at the edges of the facewidth thereby reducing both the spread-twist stiffness and the translational stiffness.

For helical gears with modifications described in Tables 2.1 and 2.2, Figures 2.11(a), 2.11(b), and 2.11(c) show the translational stiffness k_m, spread-twist stiffness k_t, and the center of stiffness axial component $\bar{c}$. Figures 2.12(a) and 2.12(b) show the contact pattern at $\gamma = 0$ and $\gamma = 0.1$ deg. For $|\gamma| < 0.03$ deg, the stiffnesses change little from their highest values, but the center of stiffness varies. When $|\gamma| > 0.03$ deg, translational and spread-twist stiffnesses decrease because of partial

contact loss as the rounded contact pattern becomes distorted and more localized at the edges of the tooth face. The center of stiffness, plotted in Figure 2.11(c), moves toward the more heavily loaded area. Localization, however, is less pronounced in modified gears compared with the prior unmodified gears; larger twist angles are needed to alter the contact pattern. This is because the contact pattern is already localized as a result of tooth surface modifications.

The total pinion and gear twist stiffnesses, the spread-twist stiffness, and the coupling-twist stiffness are shown in Figures 2.13(a), 2.14(a), 2.15(a), and 2.16(a) for the unmodified spur, modified spur, unmodified helical, and modified helical gears, respectively. With the same order, Figures 2.13(b), 2.14(b), 2.15(b), and 2.16(b) show the moment arms A_p and A_g for the pinion and gear.

There is a crucial difference in the shape of the total twist stiffness between spur and helical gears: the total pinion and gear twist stiffnesses are symmetric about the relative twist angle $\gamma = 0$ in spur gears but asymmetric in helical gears. This is because in spur gears the length of the moment arm $|\bar{A}_p| = |\bar{c} - e_p|$ only depends on the amplitude of γ but not its sign. For helical gears, however, this symmetry does not exist due to the constant value of $\bar{b}\sin\psi$ arising from the helix angle. Consequently, $\bar{A}_p$, $\bar{A}_g$, and the twist stiffnesses become asymmetric about $\gamma = 0$.

The coupling-twist stiffness k_{ct} is nearly symmetric about $\gamma = 0$ for both spur and helical gears. This is because $\bar{A}_p$ is very close to the mirror image of $\bar{A}_g$ about $\gamma = 0$. If the pinion and gear base radii were equal, $r_p = r_g$, then $\bar{A}_p$ would exactly be the mirror image of $\bar{A}_g$ about $\gamma = 0$, so $\bar{A}_p\bar{A}_g$ and thus k_{ct} would be symmetric.

Dependence on Facewidth

The common spread-twist stiffness, the pinion off-mid-plane twist stiffness, and the pinion total twist stiffness of the pair described in Tables 2.1 and 2.2 is plotted versus facewidth in Figure 2.17. Gear stiffness is not plotted for clarity. Three cases are considered as follows: (I) the helix angle is zero, and there are no tooth surface modifications; (II) the helix angle is 30 deg, and there are no tooth surface modifications; and, (III) the helix angle is 30 deg, and tooth surface modifications in Table 2.2 are added.

The spread-twist stiffness in Figure 2.17(a) increases with increasing facewidth because the more the stiffness is distributed axially away from the center of the facewidth, the more resistant the gear mesh is to twisting. This is the opposite of localization. The dependence is strong for unmodified gears (I) and (II), but weak for modified gears (III) because modifications localize the load distribution that reduce the spread-twist stiffness. Comparing cases (I) and (II), the slight decrease in the translational mesh stiffness with helix angle reduces the spread-twist stiffness a little.

The pinion off-mid-plane twist stiffnesses in Figure 2.17(b) of cases (II) and (III) are almost constant with facewidth because a change in facewidth does not move the center of stiffness relative to the mass center, so the moment arm $\bar{A}_p$ is almost constant. Spur gears of case (I) have zero off-mid-plane twist stiffness because the mesh force does not create a moment ($\bar{A}_p = 0$). Gear off-mid-plane twist stiffnesses (not plotted) exhibit the same behavior. The off-mid-plane stiffnesses dominate total twist stiffness for narrow facewidth gears, but the spread-twist stiffness dominates the total twist stiffness for wide facewidth gears.

The unmodified helical gears of case (II) have the highest pinion total twist stiffness as seen in Figure 2.17(c). The helical gears of cases (II) and (III) start with a non-zero total twist stiffness due to the off-mid-plane component, whereas all the twist resistance in the spur gears of case (I) come from the spread-twist stiffness. For modified gears of (III) the rate of contribution from spread-twist it lower than that of the unmodified cases of (I) and (II) because modifications had reduced the spread-twist stiffness.

Dependence on Modifications

To expose the effect of tooth surface modifications, the translational stiffness k_m, spread-twist stiffness k_t, and off-mid-plane twist stiffness k_{po} versus mesh deflection $\bar{\delta}$ are plotted in Figures 2.18(a), 2.18(b), and 2.18(c) with various modifications of 0, 2, 5, 10, and 20 μm. Figure 2.18(d) shows spread-twist stiffness k_t versus twist angle γ with the same modifications. The helical gear pair used is described in Table 2.1 with surface modifications in Table 2.2, where the amplitudes of profile and lead modifications change as indicated.

The translational stiffness k_m and spread-twist stiffness k_t are independent of mesh deflection for unmodified gears unless contact is completely lost as seen in Figures 2.18(a) and 2.18(b). For the modified gears, however, the translational mesh stiffness continuously approaches the maximum value as the mesh deflection increases. The approach is slower with increasing tooth surface modification amplitude because more mesh deflection is needed to bring a larger portion of the tooth surface into contact. Partial contact loss is responsible for this smoothing of the translational mesh stiffness curve. In general, the larger the contact area, the higher the translational and spread-twist stiffness.

The nonlinear curve of the spread-twist stiffness is somewhat different than the translational stiffness because the translational stiffness only depend on the size of the contact area but the spread-twist stiffness is sensitive to localization of contact as well as the size of the contact area. The pinion-off-mid-plane twist stiffness in Figure 2.18(c) is almost a constant multiple of the translational stiffness, so their nonlinear curves are very similar.

Inspecting the spread-twist stiffness versus relative twist angle γ in Figure 2.18(d), the modified gears retain more of their existing (when aligned) spread-twist stiffness at higher twist angles than unmodified gears. Tooth surface modifications localize the contact pattern and make the tooth more rounded, thus reducing the spread-twist stiffness and the total twist stiffness.

Unmodified gears have a range where the spread-twist and translational stiffness is absolutely flat despite relative twist. In this region, twist angle does not cause partial contact loss. For gear motions that do not exceed the range where stiffness is flat, the system is linear. This linear region is distinct in unmodified spur and helical gears as seen in the twist stiffnesses and moment arms in Figures 2.13(a) and 2.15(a). The transition to nonlinear region, where partial contact loss dominates, is clear. With modified gears, although a similar region exists in Figures 2.14(a) and 2.16(a), it is not perfectly linear and the transition to the nonlinear region is smooth and not sudden.

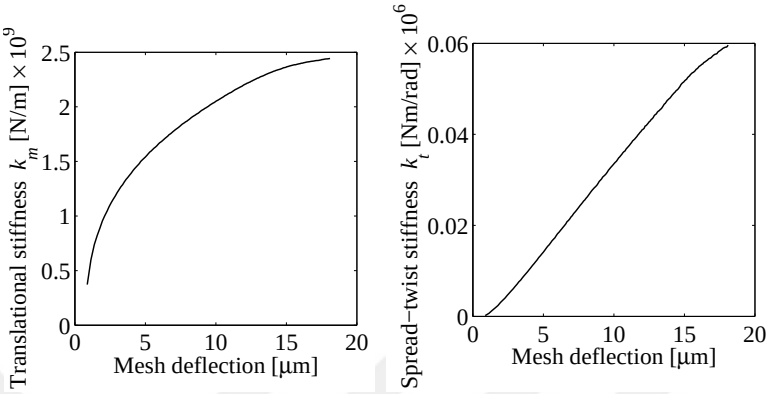

(a) (b)

Figure 2.7: (a) Translational mesh stiffness k_m variation versus mesh deflection for the modified helical gear pair in Tables 2.1 and 2.2. (b) Spread-twist stiffness k_t variation versus mesh deflection. Quantities are averaged over a mesh period.

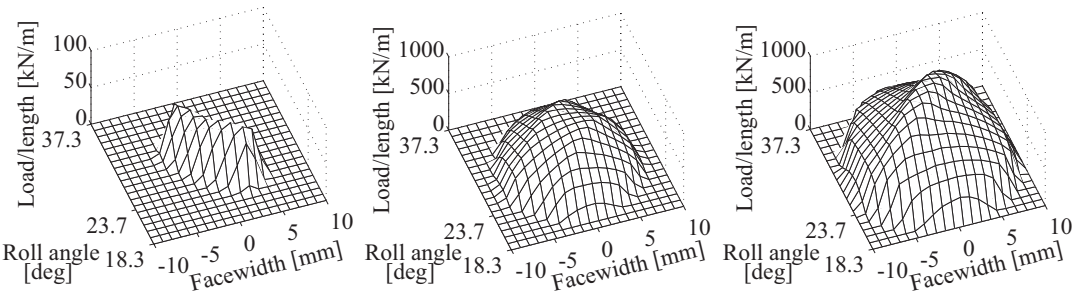

(a) 1 μm (b) 6 μm (c) 10 μm

Figure 2.8: Contact pattern of the modified helical gear pair in Tables 2.1 and 2.2. (a) Mesh deflection is 1 μm. (b) Mesh deflection is 6 μm. (c) Mesh deflection is 10 μm.

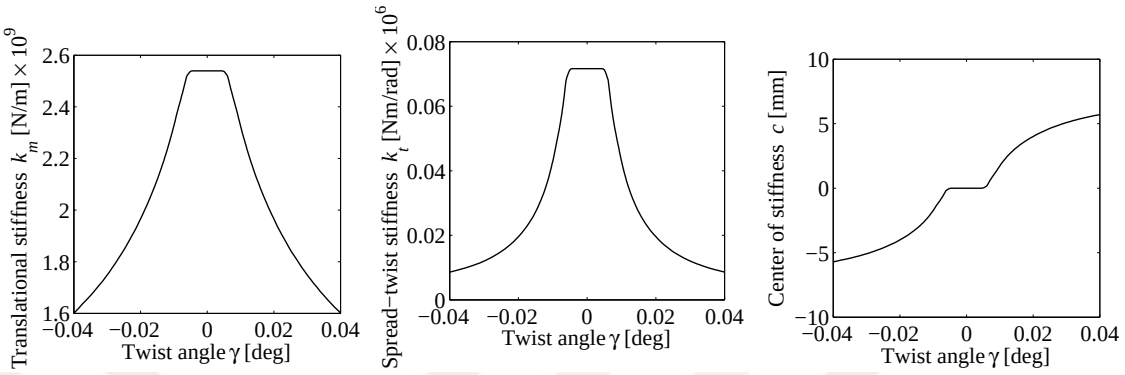

(a) (b) (c)

Figure 2.9: (a) Translational mesh stiffness k_m variation versus twist angle γ for the unmodified helical gear pair in Table 2.1. (b) Spread-twist stiffness k_t variation versus twist angle γ. (c) Variation of the center of stiffness $\bar{c}$ versus twist angle γ. Quantities are averaged over a mesh period.

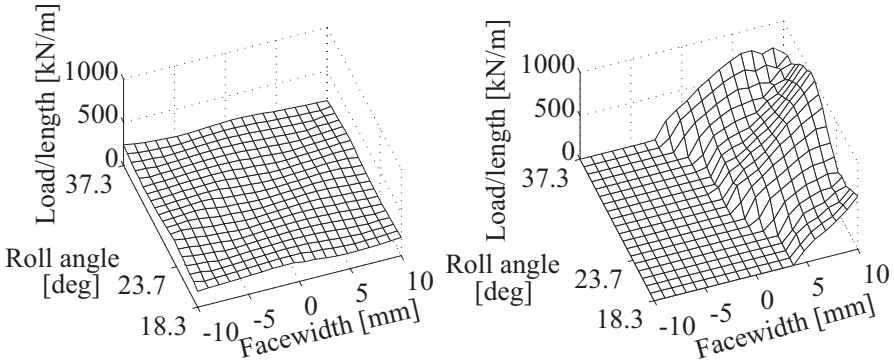

(a) 0 deg (b) 0.04 deg

Figure 2.10: Contact pattern of the unmodified helical gear pair in Table 2.1. (a) Gears are aligned, $\gamma = 0$ deg. (b) At $\gamma = 0.04$ deg.

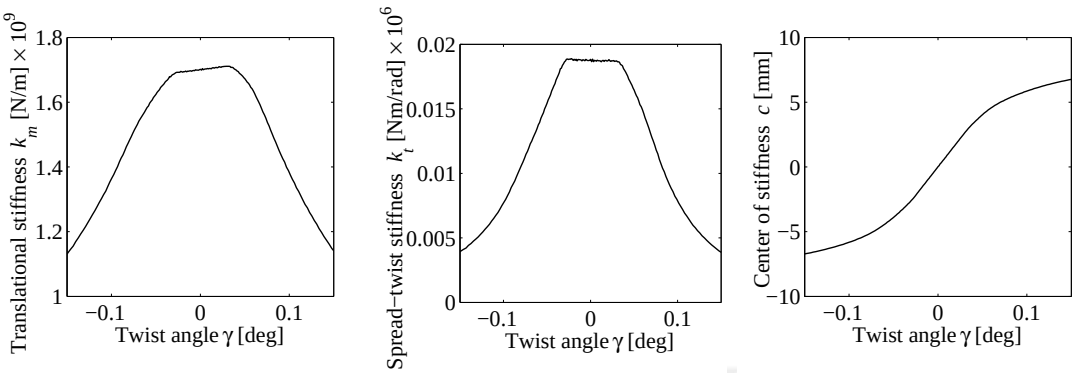

(a) (b) (c)

Figure 2.11: (a) Translational mesh stiffness k_m variation versus twist angle γ for the modified helical gear pair in Tables 2.1 and 2.2. (b) Spread-twist stiffness k_t variation versus mesh twist angle γ. (c) Variation of the center of stiffness $\bar{c}$ versus twist angle γ. Quantities are averaged over a mesh period.

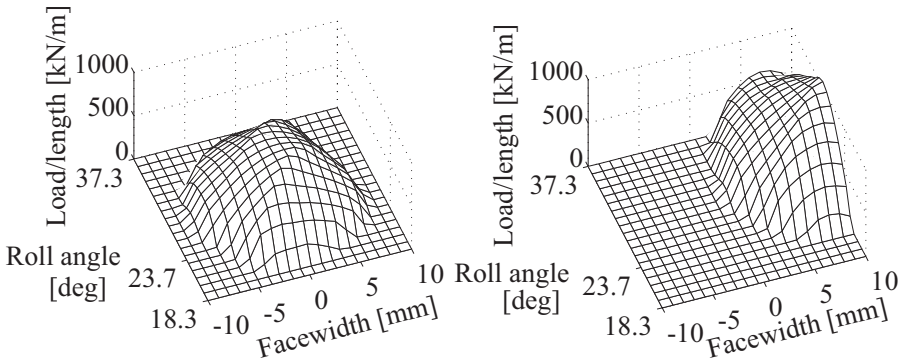

(a) 0 deg (b) 0.1deg

Figure 2.12: Contact pattern of the modified helical gear pair in Tables 2.1 and 2.2. (a) Gears are aligned, $\gamma = 0$ deg. (b) At $\gamma = 0.1$ deg.

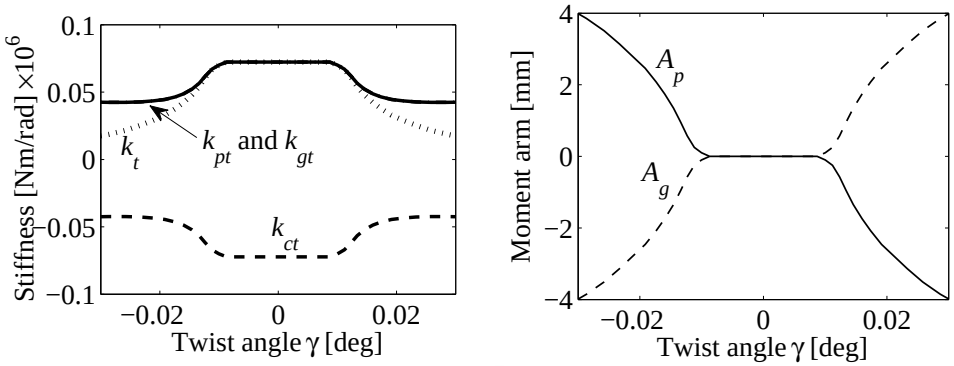

(a) (b)

Figure 2.13: (a) Total pinion twist stiffness k_{pt}, total gear twist stiffness k_{gt}, spread-twist stiffness k_t, and coupling-twist stiffness k_{ct}. (b) Moment arms for the pinion A_p and gear A_g from the unmodified spur gear with respect to twist angle.

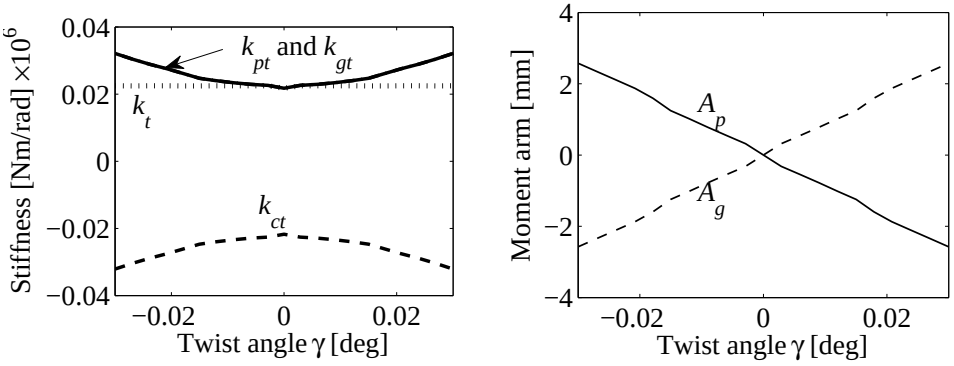

(a) (b)

Figure 2.14: (a) Total pinion twist stiffness k_{pt}, total gear twist stiffness k_{gt}, spread-twist stiffness k_t, and coupling-twist stiffness k_{ct}. (b) Moment arms for the pinion A_p and gear A_g from the modified spur gear with respect to twist angle.

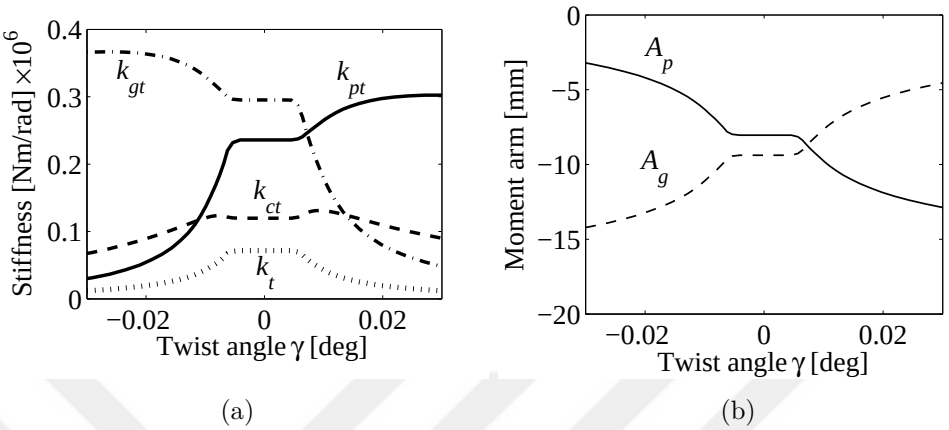

(a) (b)

Figure 2.15: (a) Total pinion twist stiffness k_{pt}, total gear twist stiffness k_{gt}, spread-twist stiffness k_t, and coupling-twist stiffness k_{ct}. (b) Moment arms for the pinion A_p and gear A_g from the unmodified helical gear with respect to twist angle.

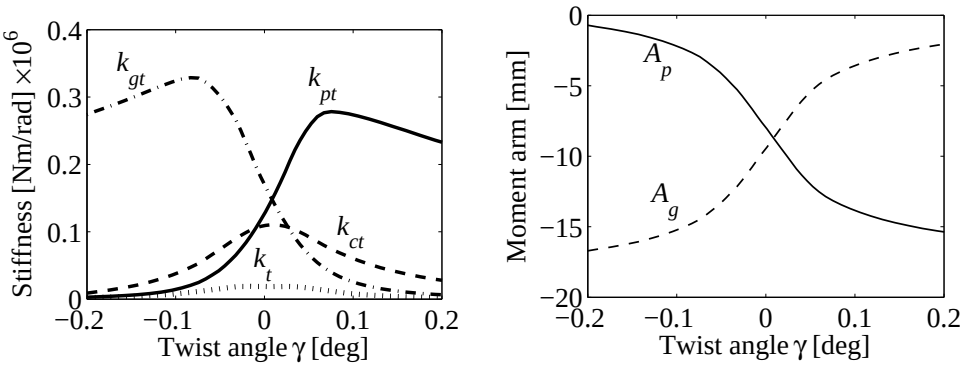

(a) (b)

Figure 2.16: (a) Total pinion twist stiffness k_{pt}, total gear twist stiffness k_{gt}, spread-twist stiffness k_t, and coupling-twist stiffness k_{ct}. (b) Moment arms for the pinion A_p and gear A_g from the modified helical gear with respect to twist angle.

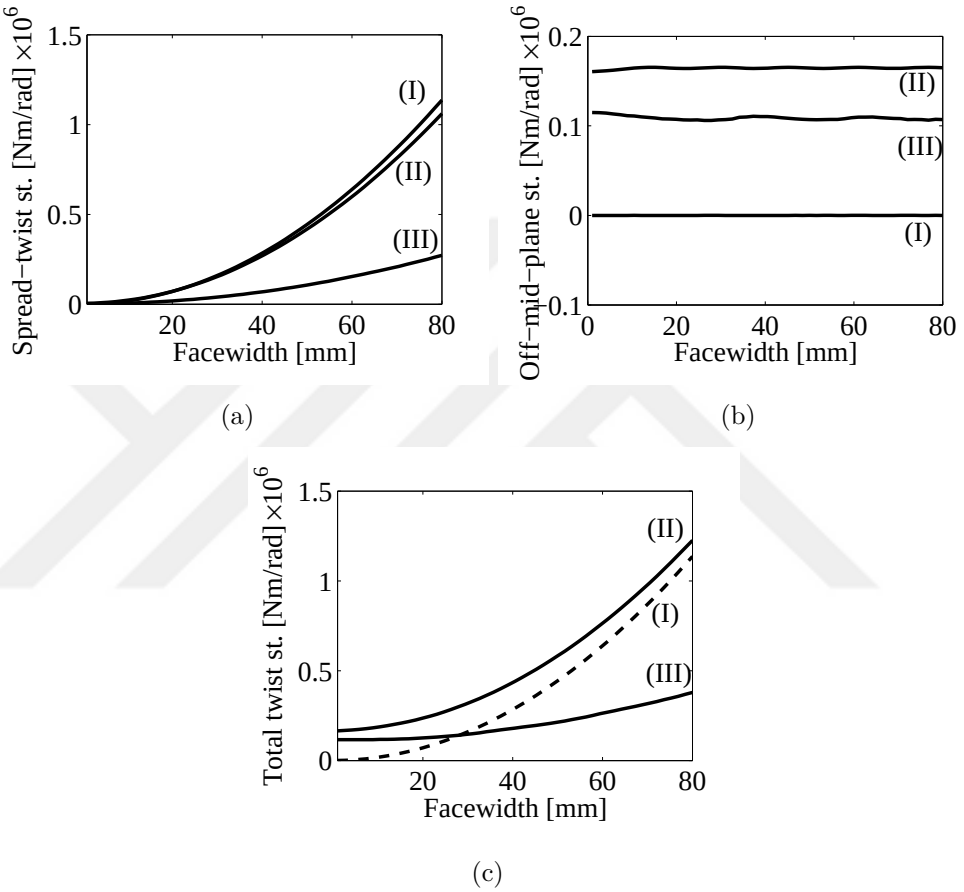

Figure 2.17: Spread-twist, pinion off-mid-plane twist, and pinion total pinion twist stiffness variation with facewidth. Gear parameters are in Table 2.1. (I) Helix angle is zero and teeth are unmodified. (II) Helix angle is 30 deg and gear teeth are unmodified. (III) Helix angle is 30 deg and gear teeth are modified according to Table 2.2.

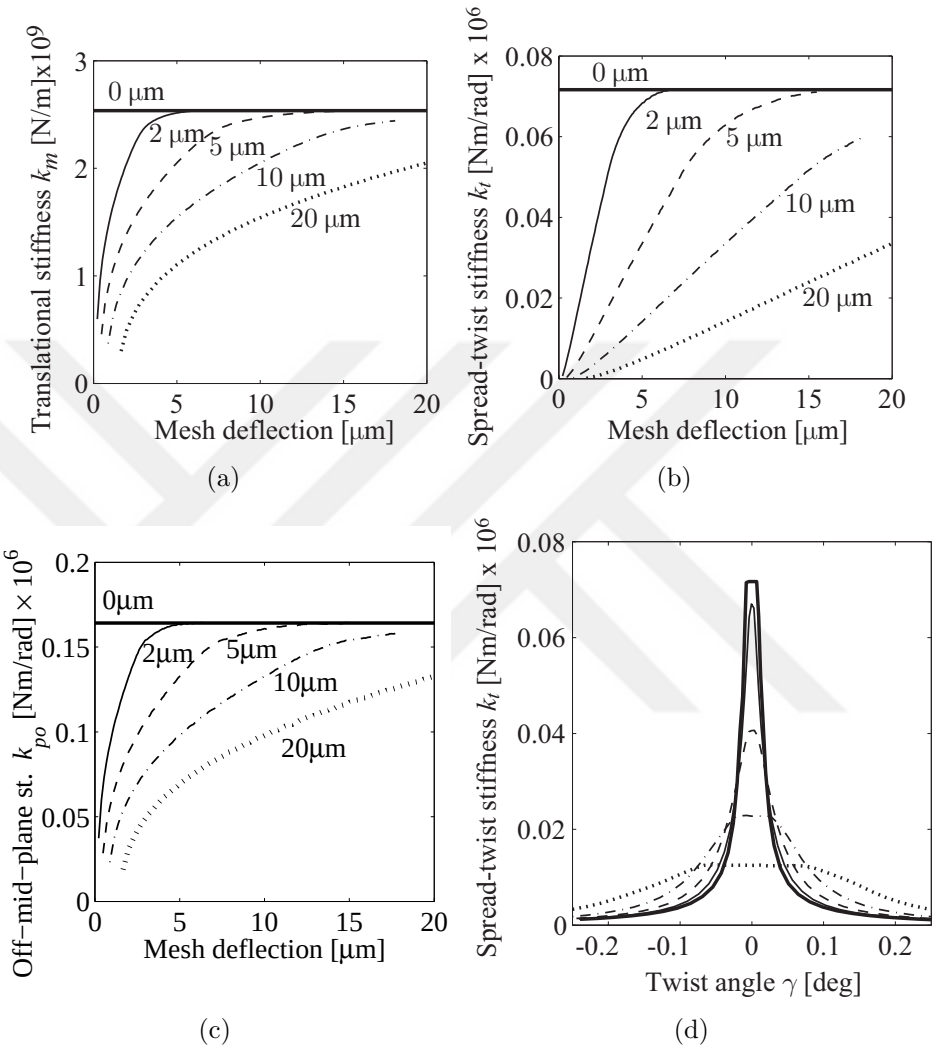

Figure 2.18: Translational and spread-twist stiffnesses of the helical gear pair described in Tables 2.1 and 2.2 for various levels of tooth surface modifications. Tooth surface modifications are: thick solid line 0 μm, solid line 2 μm, dashed line 5 μm, dash-dot line 10 μm, and dotted line 20 μm. (a) Translational mesh stiffness versus mesh deflection. (b) Spread-twist stiffness versus mesh deflection. (c) Pinion off-mid-plane twist stiffness versus mesh deflection. (d) Spread-twist stiffness versus twist angle.

2.3.4 Fluctuating Twist Moments and Stiffnesses as Sources of Dynamic Excitation

The twist moments and stiffnesses periodically fluctuate, so can excite vibration and noise. When a reduction in transmission error does not reduce noise, secondary excitation sources such as tilting/twisting moments may be causing vibrations. To investigate the nature of the time-dependent fluctuation, the total twist moments on the pinion and gear ($\mathbf{M}_p \cdot \mathbf{E}_2$, $\mathbf{M}_g \cdot \mathbf{E}_2$) and the spread-twist moment ($k_t\gamma$) common to pinion and gear are plotted in Figures 2.19 and 2.20 for unmodified spur gears and modified helical gears in two mesh periods. The values are obtained at three specified twist values of $|\gamma| = 0.04$, $\gamma = 0$ deg in unmodified gears and $|\gamma| = 0.14$, $\gamma = 0$ deg in modified gears.

Aligned ($\gamma = 0$ deg) spur gears generate no twist moments because $\bar{A}_p = \bar{A}_g = 0$. Aligned helical gears generate fluctuating twist moments with a mean value because $\bar{A}_p \neq \bar{A}_g \neq 0$ (or because the off-mid-plane twist stiffness). Moments on the pinion and gear are different. The twist moments in aligned helical gears are significant, being near 25% of the transmitted useful torque.

When misaligned ($\gamma = 0.04$ deg), spur gears, however, do produce fluctuating twist moments with a mean value. These moments are equal and opposite because they come from the spread-twist stiffness by $k_t\gamma$. In helical gears, misalignment ($\gamma = 0.14$ deg) yields a subtler effect: pinion twist moment increases but gear twist moment decreases compared with the aligned case (and vice-versa for a misalignment in the other direction $\gamma = -0.14$ deg). This is because the twist moments from the spread-twist and off-mid-plane stiffness add for the pinion but subtract for the gear.

The total twist stiffnesses of the pinion and gear and the common spread-twist and coupling-twist stiffnesses are plotted in Figures 2.21 and 2.22 for unmodified spur gears and modified helical gears with the same specified twist angles indicated above. The periodic fluctuation of twist stiffnesses in a mesh period are summarized using RMS (root-mean-square) calculation in Figure 2.23.

All types of twist stiffnesses in both spur and helical gears fluctuate with a mean value. The stiffness fluctuation, although exists, must not be important in aligned spur gears because aligned spur gears do not generate twist moments to excite twist vibrations. Misalignment has two competing effects on RMS twist stiffnesses: a) it tends to decrease RMS spread-twist stiffness in both spur and helical gears, b) in spur gears it increases RMS off-mid-plane stiffnesses but in helical gears it either decreases or increases the RMS off-mid-plane stiffnesses depending on the sign of the misalignment. Overall, aligned gears seem to have the least fluctuation when equal importance is attached to both total pinion and gear twist stiffnesses. A positive misalignment in the helical gears analyzed however can reduce, for example, the RMS gear twist stiffness, if that is specifically desired.

All twist moments and stiffnesses fluctuate periodically with gear rotation unless the gears are aligned and the helix angle is zero. The RMS fluctuation amplitudes strongly depends on the specified misalignment. Considering gear noise, the fluctuating twist moments can excite vibrations, and the stiffness fluctuation causes parametric excitation. This view can lead to a vibration reduction by reducing twist moment fluctuations. The strong dependence of RMS amplitudes on twist angle adds another nonlinear dimension; as the gears vibrate the dynamic changes in twist angle could alter the excitation strength.

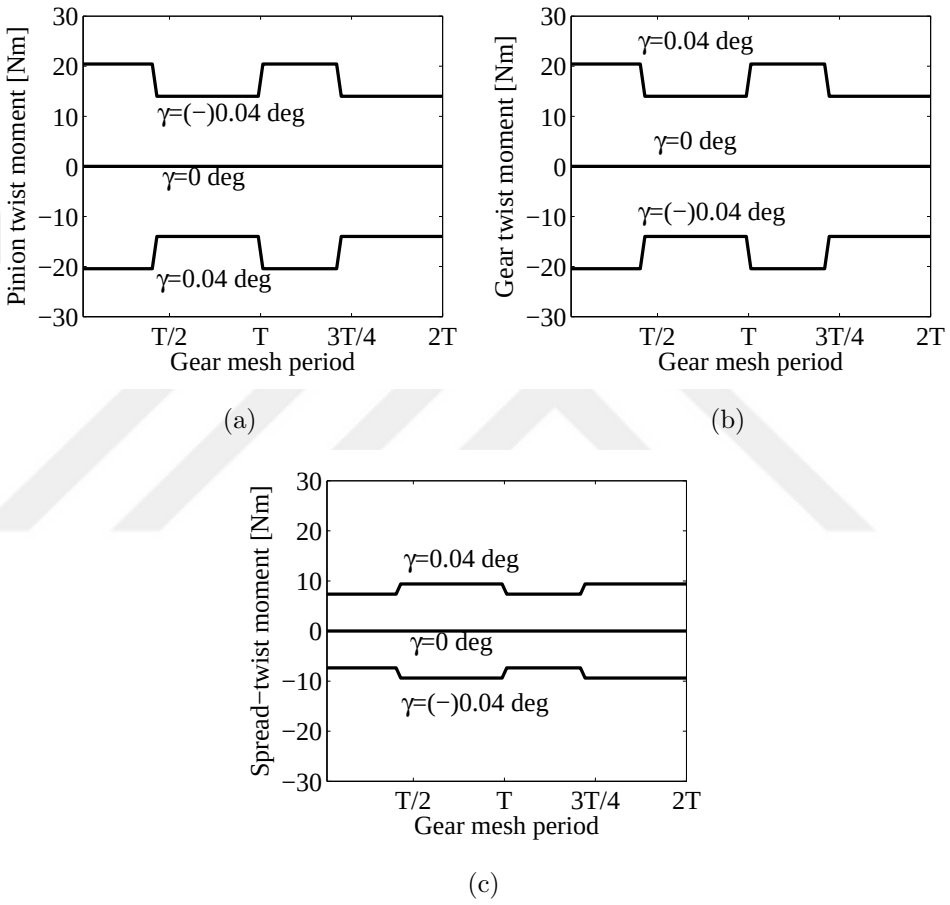

Figure 2.19: Twist moments in two mesh periods of the unmodified spur gear pair. (a) Total pinion twist moment, (b) total gear twist moment, (c) spread-twist moment.

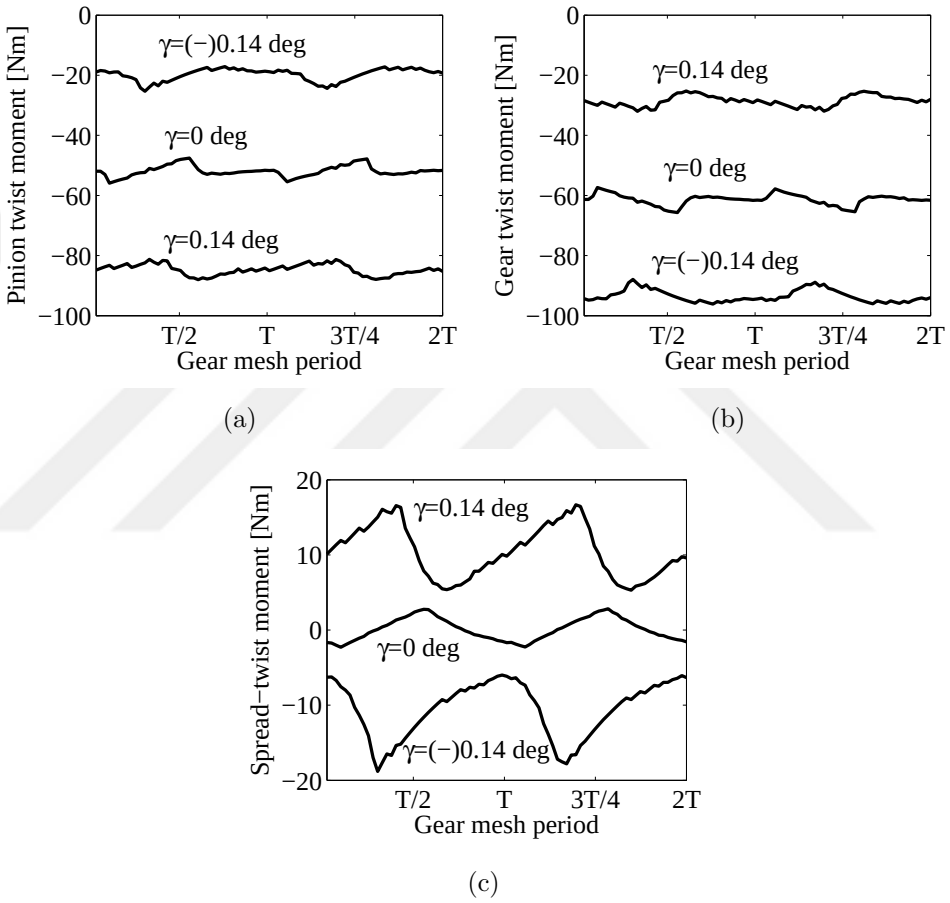

Figure 2.20: Twist moments in two mesh periods of the modified helical gear pair. (a) Total pinion twist moment, (b) total gear twist moment, (c) spread-twist moment.

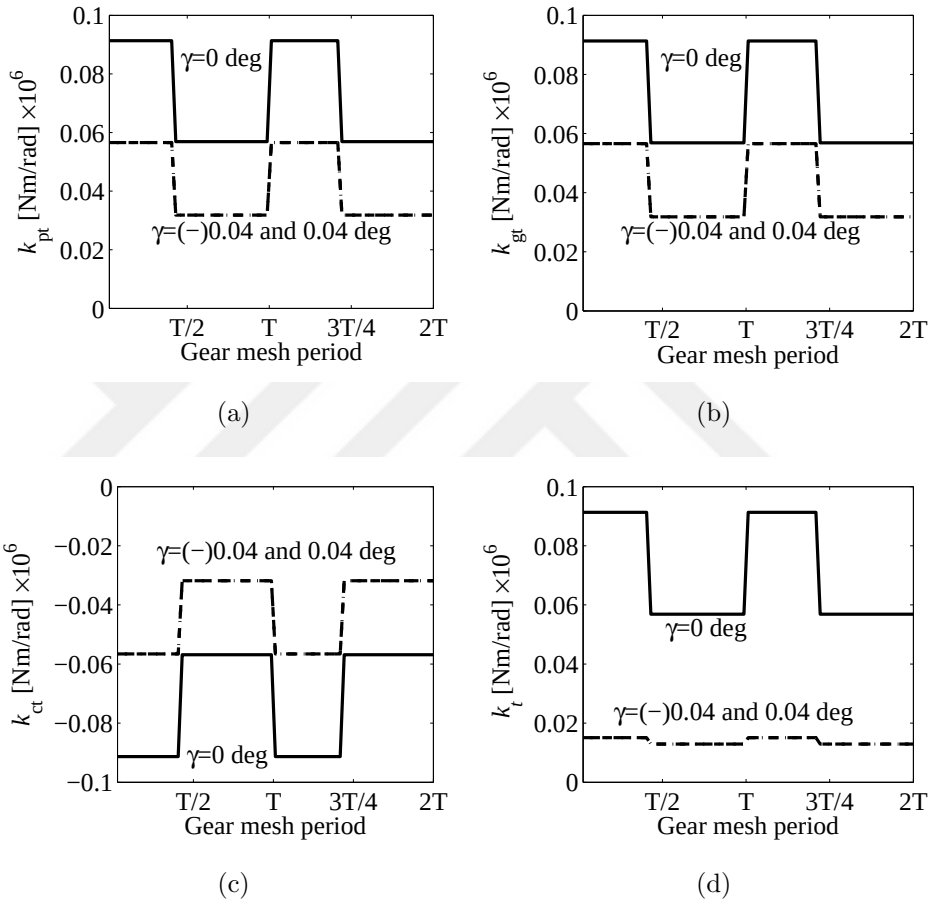

Figure 2.21: Twist stiffnesses in two mesh periods of the unmodified spur gear pair. (a) Total pinion twist stiffness k_{pt}, (b) total gear twist stiffness k_{gt}, (c) coupling-twist stiffness k_{ct}, (d) spread-twist stiffness k_t.

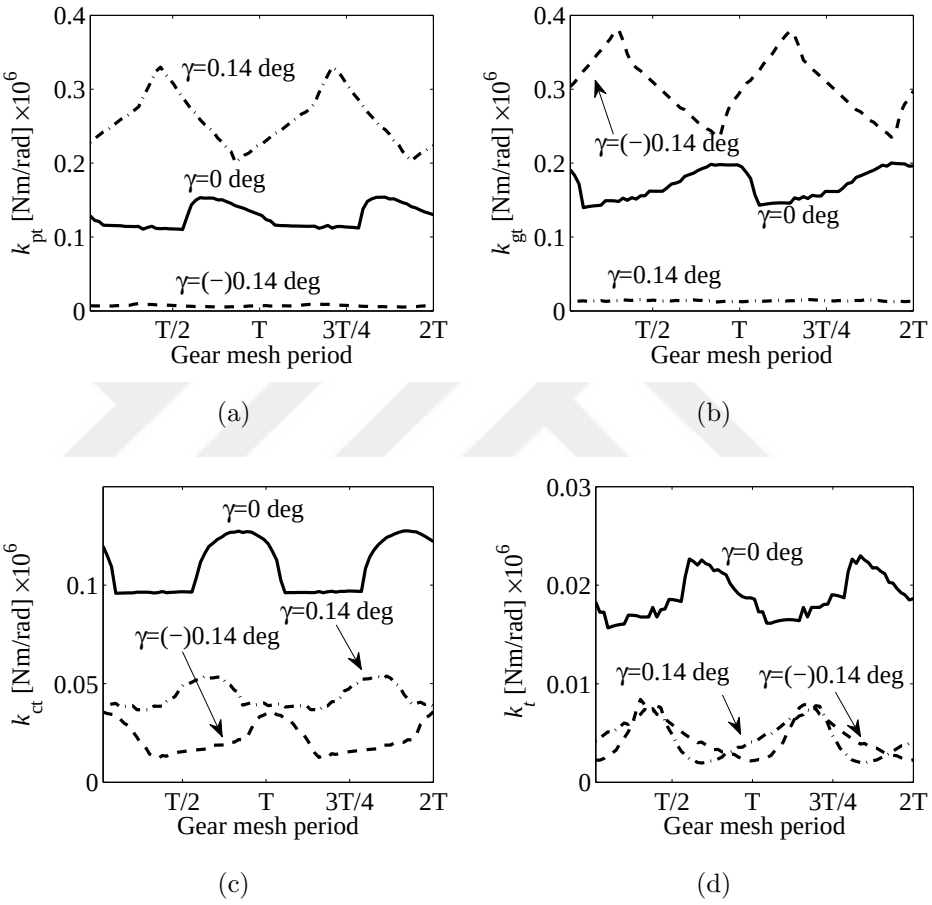

Figure 2.22: Twist stiffnesses in two mesh periods of the modified helical gear pair. (a) Total pinion twist stiffness k_{pt}, (b) total gear twist stiffness k_{gt}, (c) coupling-twist stiffness k_{ct}, (d) spread-twist stiffness k_t.

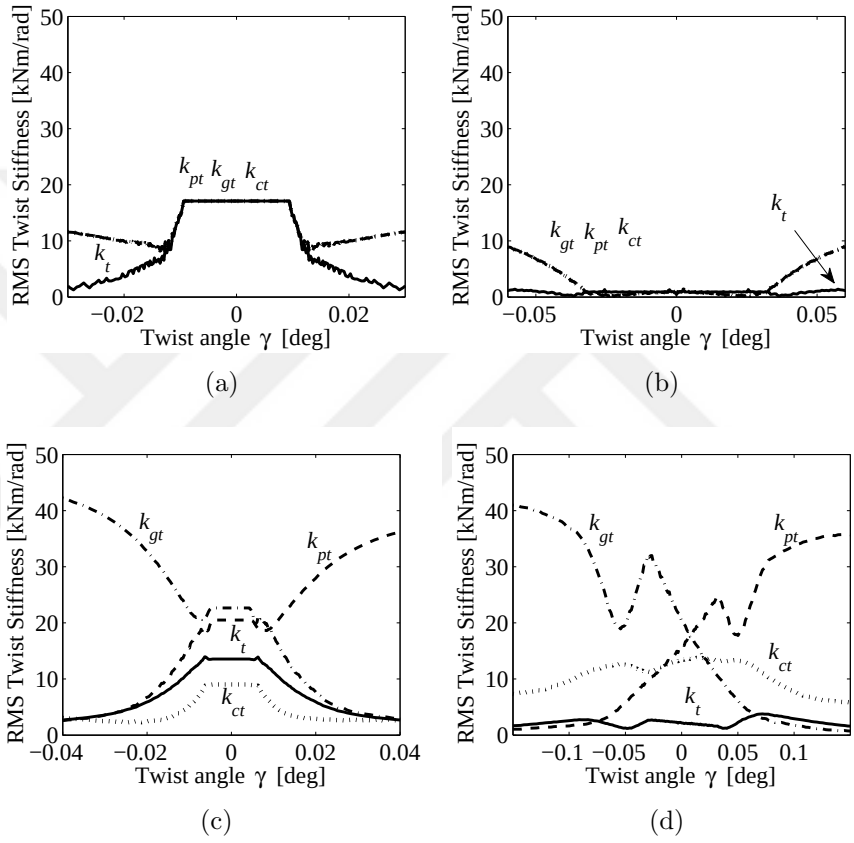

Figure 2.23: RMS twist stiffnesses over a mesh period. (a) Unmodified spur gears, (b) modified spur gears, (c) unmodified helical gears, (d) modified helical gears. Solid line: spread-twist stiffness, dashed line: total pinion twist stiffness k_{pt}, dotted line: coupling twist stiffness k_{ct}, dash-dot line: total gear twist stiffness k_{gt}.

2.4 Conclusions

A lumped-parameter that consists of a translational mesh stiffness acting at the center of stiffness and a spread-twist stiffness is mathematically shown to be identical to an arbitrary load distribution on the gear teeth. This reduction is named the equivalent stiffness model.

The distribution of the mesh force across the facewidth generates a twisting moment that has not been included in prior models that use a single translational spring to represent tooth compliance. The spread-twist stiffness captures this twisting moment. The total twist stiffness on a gear is the sum of the off-mid-plane twist stiffness, which results from the mesh force being offset from the mid-plane, and the spread-twist stiffness.

Portions of contact lines can disengage from gear deflection, misalignment, and tooth surface modification. This phenomenon is called partial contact loss. The equivalent model concisely captures the nonlinearity resulting from partial contact loss.

The nonlinear behavior of the translational and twist stiffnesses are numerically investigated. A discretization of the load distribution supplies the numerical values for the equivalent stiffness model. The translational stiffness correlates with the size of the contact area. When the contact area shrinks from modifications, mesh deflection, or twist, the translational stiffness decreases. The spread-twist stiffness correlates with the localization of contact. When the contact area is more localized from twist, tooth surface modifications, or mesh deflection, the spread-twist stiffness decreases. The off-mid-plane twist stiffness vanishes in centered spur gears but dominates the total twist stiffness in helical gears with narrow facewidth. The spread-twist

stiffness increases rapidly with larger facewidth. Both off-mid-plane and spread-twist stiffnesses are highly nonlinear.

The twist moments fluctuate periodically with a mean value with nominal gear rotation in helical gears. The total twist stiffnesses fluctuate with nominal gear rotation as well. These fluctuations have the potential to excite twist vibration. If vibrations are indeed excited by these twist moments, a reduction of the fluctuations may reduce gear noise. If the translational and spread-twist stiffnesses and the center of stiffness are explicitly known from computational analysis as functions of mesh deflection, mesh twist and nominal gear rotation, that may allow simplified three-dimensional nonlinear dynamic and static analyses.

Chapter 3: Twisting Vibration and Partial Contact Loss in Gear Pairs

3.1 Introduction

Research on spur gear pair dynamics [26, 30] identify static transmission error as the primary quantifier of vibration excitation. Since then, static transmission error has been used as an input to two-dimensional spur gear dynamic models [26,30,81,82], and it has proven to be an easily measurable and calculable design guideline to reduce gear vibration [81, 102, 130]. Helical gears have a lower fluctuation in static transmission error when compared with spur gears, so vibration excitation due to transmission error fluctuation is lower in helical gears. This reduction in static transmission error, however, does not always coincide with a reduction in vibration [36] because helical gears introduce additional excitations as a result of the non-zero helix angle [80] including a twisting moment, axial thrust, and an axial moment [13, 14, 23, 34, 35, 37, 77, 129]. Not only these moments excite dynamics, they also alter the load distribution on the gear teeth to create a three-dimensional nonlinear vibration problem.

The core of the problem is that the three-dimensional vibrations lead to loss of contact at portions of a gear tooth surface that otherwise would have been in contact.

This is called partial contact loss. The dynamic contact pattern is distorted as a result of partial contact loss [6,21]. Tooth surface modifications and specified misalignments also cause partial contact loss. To that end, Velex et al. [122] and Raclot and Velex [90] computationally show that misaligned gears exhibit partial contact loss under static conditions. There is, however, a crucial difference between [90, 122] and this work; partial contact loss in [90, 122] is due to a specified misalignment, but in this work partial contact loss occurs as a result of dynamic displacements even though the gears are perfectly aligned in assembly.

This work intends to scrutinize the nonlinear dynamic response as a result of partial contact loss due to three-dimensional dynamic displacements. Dynamic response is obtained using numerical integration. The modeling follows Chapter 2, where a discretization of the gear contact lines using network of springs tracks instantaneous dynamic contact conditions. The lumped-parameter model developed in Chapter 2, the equivalent stiffness representation, identically reproduces the net mesh forces and moments from any given load distribution on the contact lines. It uses a translational mesh stiffness acting at the center of stiffness and a twist stiffness. Response is interpreted using the instantaneous dynamic values from the equivalent stiffness representation.

3.2 Modeling

3.2.1 Gear Pair Dynamic Model

The gear pair model is constructed following [23]. The model consists of two gears mounted on shafts. Each gear body is combined with its supporting shaft into a single

rigid body. These gear-shaft bodies are each mounted on up two bearings placed at arbitrary axial locations. Figure 3.1 shows the gear model and the bases.

A fixed, right-handed, orthonormal basis $\{\mathbf{E}\} = \{\mathbf{E}_1, \mathbf{E}_2, \mathbf{E}_3\}$ is oriented such that $\mathbf{E}_1$ is parallel to the line of action of the gear mesh. The origin is on the rotation axis of the pinion body, midway in the active facewidth. Positive axial quantities are measured along $\mathbf{E}_3$ from the dashed line in Figure 3.1.The translational (x_p, y_p, z_p) and angular (ϕ_p, θ_p, β_p) coordinates of the pinion body are assigned to translations along and rotations about $\mathbf{E}_1$, $\mathbf{E}_2$, and $\mathbf{E}_3$, respectively. We refer to a rotation about $\mathbf{E}_1$ as tilting and a rotation about $\mathbf{E}_2$ as twisting. The translational and angular coordinates of the gear body follow similarly with subscript g. Body-fixed bases $\{\mathbf{e}^p\} = \{\mathbf{e}_1^p, \mathbf{e}_2^p, \mathbf{e}_3^p\}$ and $\{\mathbf{e}^g\} = \{\mathbf{e}_1^g, \mathbf{e}_2^g, \mathbf{e}_3^g\}$ for the pinion and gear are adopted.

The pinion translational and angular velocity vectors are

$$\begin{aligned}
\dot{\mathbf{r}}_p &= \dot{x}_p\mathbf{E}_1 + \dot{y}_p\mathbf{E}_2 + \dot{z}_p\mathbf{E}_3, \\
\boldsymbol{\omega}_p &= \left[\dot{\phi}_p - \theta_p\left(\dot{\beta}_p + \Omega_p\right)\right]\mathbf{e}_1^p + \left[\dot{\theta}_p + \phi_p\left(\dot{\beta}_p + \Omega_p\right)\right]\mathbf{e}_2^p + \left[\dot{\beta}_p + \Omega_p - \phi_p\dot{\theta}_p\right]\mathbf{e}_3^p,
\end{aligned} \tag{3.1}$$

where Ω_p is the specified constant angular rotational speed of the pinion. The velocity vectors for the gear are identical except with components for the gear.

The axial positions of the pinion bearings are measured along $\mathbf{E}_3$ by L_p^A and L_p^B. The pinion bearing deflection vectors are the relative deflections at the bearings with respect to ground, giving

$$\begin{aligned}
\mathbf{d}_p^A &= \left[\theta_p\left(L_p^A - e_p\right) + x_p\right]\mathbf{E}_1 + \left[\phi_p\left(e_p - L_p^A\right) + y_p\right]\mathbf{E}_2 + z_p\mathbf{E}_3, \\
\mathbf{d}_p^B &= \left[\theta_p\left(L_p^B - e_p\right) + x_p\right]\mathbf{E}_1 + \left[\phi_p\left(e_p - L_p^B\right) + y_p\right]\mathbf{E}_2 + z_p\mathbf{E}_3.
\end{aligned} \tag{3.2}$$

The bearing deflections for the gear follow similarly. The bearings resist tilting and twisting as well. The angular deflection of all pinion bearings are identical for rigid shafts, giving

$$\boldsymbol{\Gamma}_p^A = \boldsymbol{\Gamma}_p^B = \phi_p\mathbf{E}_1 + \theta_p\mathbf{E}_2 + \beta_p\mathbf{E}_3. \tag{3.3}$$

The bearings are isotropic in the $\mathbf{E}_1 - \mathbf{E}_2$ plane, so the bearing stiffness matrix for translation is $\mathbf{B}_p^A = \text{diag}\left[k_p^A, k_p^A, k_p^{Az}\right]$, where the equality of stiffness in the two translation directions is evident. The bearing stiffness matrix for rotation is $\boldsymbol{\chi}_p^A = \text{diag}\left[\kappa_p^A, \kappa_p^A, \kappa_p^{Az}\right]$. Similar definitions follow for other bearings.

Distributed gear contact loads are approximated by a discretization scheme described in Chapter 2 Section 2.2.5. The nominal contact lines for no mesh deflection are discretized into n segments with stiffness k_i, $i = 1, \ldots, n$. Displacements cause a difference between the position vectors of the contact points on the pinion and gear. That difference is the mesh deflection vector. The projection of the mesh deflection vector on the tooth surface normal gives the relative compressive deflection of the contact stiffness k_i as

$$\begin{aligned}\delta_i = &\left\{ \left[e_p - c_i\right]\theta_p + \left[c_i - e_g\right]\theta_g - x_p + x_g + h_i + \beta_p r_p + \beta_g r_g \right\} \cos\psi \\ &- \left\{ \left[b_i + h_i\right]\theta_p + \left[(r_p + r_g)\tan\Phi - b_i\right]\theta_g + z_p - z_g + \phi_p r_p + \phi_g r_g \right\} \sin\psi,\end{aligned} \tag{3.4}$$

where r_p and r_g are the base radii, Φ is the transverse operating pressure angle, and ψ is the base helix angle. The axial position of a contact point, measured from the origin along $\mathbf{E}_3$, is c_i, and the radial position of a contact point, measured from the origin along $\mathbf{E}_1$, is b_i. The positions of contact (b_i, c_i) are determined from known gear rotation speed. Micron-level deviations of the tooth surface from an involute, such as from gear tooth surface modifications and manufacturing errors, are denoted by h_i. Figure 3.1 depicts these quantities.

The contact stiffnesses k_i depend implicitly on time t due to specified nominal gear rotation and displacements $\mathbf{q}$. The formula for k_i is given by Eq. (2.30)

The kinetic and potential energies are

$$\begin{aligned} T &= \frac{1}{2}\sum_{k=p,g}\left(\boldsymbol{\omega}_k^T\mathbf{J}_k\boldsymbol{\omega}_k + \dot{\mathbf{r}}_k^T m_k\dot{\mathbf{r}}_k\right), \\ V &= \frac{1}{2}\sum_{k=p,g}\sum_{j=A,B}\left(\mathbf{d}_h^{j\,T}\mathbf{B}_h^j\mathbf{d}_h^j + \boldsymbol{\Gamma}_h^{j\,T}\boldsymbol{\chi}_h^j\boldsymbol{\Gamma}_h^j\right) + \frac{1}{2}\sum_{i=1}^{n}k_i\delta_i^2, \end{aligned} \tag{3.5}$$

The inertia tensor of the axisymmetric pinion body is $\mathbf{J}_p = \text{diag}\left[J_p^x, J_p^x, J_p^z\right]$ with similar definition for the axisymmetric gear body.

Lagrange's equations of motion for unconstrained generalized coordinates follow after substitution of equations Eqs. (3.1) through (3.4) into the energy expressions Eq. (3.5). In matrix form they are

$$\mathbf{M}\ddot{\mathbf{q}} + \mathbf{D}\dot{\mathbf{q}} + \Omega_p\mathbf{G}\dot{\mathbf{q}} + \left[\mathbf{K} + \mathbf{B} - \Omega_p^2\mathbf{C}\right]\mathbf{q} = \mathbf{f}_{\text{ext}} \tag{3.6}$$

The vector $\mathbf{q}$ comprises generalized coordinates

$$\mathbf{q} = \Big(\underbrace{\phi_p, \theta_p, \beta_p, x_p, y_p, z_p}_{\text{pinion}}, \underbrace{\phi_g, \theta_g, \beta_g, x_g, y_g, z_g}_{\text{gear}}\Big) \tag{3.7}$$

The vector $\mathbf{f}_{\text{ext}}$ includes external loading; the driving and absorbing torques and tooth surface modifications appear here. The matrix $\mathbf{K}$ is the three-dimensional mesh stiffness matrix. The matrix $\mathbf{B}$ is the bearing stiffness matrix. The elements of $\mathbf{K}$, $\mathbf{B}$ and $\mathbf{f}_{\text{ext}}$ are given in Eqs. (2.9), (2.14), and (2.10) with integration $\int(\ldots)\,\mathrm{d}\upsilon$ replaced by summation $\sum_{i=1}^{N}(\ldots)$. The terms that arise from the constant rotation speed are contained in the gyroscopic matrix $\mathbf{G}$ and the centripetal acceleration matrix $\mathbf{C}$. The inertia matrix $\mathbf{M}$, gyroscopic matrix $\mathbf{G}$, and centripetal acceleration matrix $\mathbf{C}$ are given by

$$\mathbf{M} = \text{diag}(J_p^x, J_p^x, J_p^z, m_p, m_p, m_p, J_g^x, J_g^x, J_g^z, m_g, m_g, m_g) \tag{3.8}$$

$$\begin{aligned} \mathbf{G}_{1,2} &= J_p^z - 2J_p^x, \quad \mathbf{G}_{2,1} = -J_p^z + 2J_p^x, \\ \mathbf{G}_{7,8} &= R(J_p^z - 2J_p^x), \quad \mathbf{G}_{8,7} = -R(J_p^z - 2J_p^x), \end{aligned} \tag{3.9}$$

$$\mathbf{C}_{1,1} = J_p^x, \quad \mathbf{C}_{2,2} = J_p^x, \quad \mathbf{C}_{7,7} = R^2 J_g^x, \quad \mathbf{C}_{8,8} = R^2 J_g^x. \tag{3.10}$$

where $R = \Omega_g/\Omega_p$, and all unspecified elements are zero.

3.2.2 Equivalent Stiffness Representation

The equivalent stiffness representation, detailed in Chapter 2 Section 2.2.3, identically reproduces the net effect of load distribution obtained from the discretization of contact line with the network of stiffnesses. There are four parameters in the equivalent stiffness representation: translational mesh stiffness k_m, the center of stiffness $(\bar{b}, \bar{c})$ at which the translational mesh stiffness acts, and the spread-twist stiffness k_t. These quantities are given by

$$k_m = \sum_{i=1}^{n} k_i, \; k_t = \sum_{i=1}^{n} \left(k_i A_{p,i}^2\right) - k_m \bar{A}_p^2. \tag{3.11}$$

$$\bar{b} = \frac{1}{k_m} \sum_{i=1}^{n} k_i b_i, \; \bar{c} = \frac{1}{k_m} \sum_{i=1}^{n} k_i c_i \tag{3.12}$$

where $A_{p,i}$ and $A_{g,i}$ are the moment arms given by

$$A_{p,i} = \left[(c_i - e_p)\cos\psi + b_i \sin\psi\right], \tag{3.13}$$

$$A_{g,i} = \left[-(c_i - e_g)\cos\psi + (B - b_i)\sin\psi\right] \tag{3.14}$$

The quantities with the overbar are obtained using $b_i = \bar{b}$, and $c_i = \bar{c}$. In Chapter 2, Figure 2.3 shows the equivalent stiffnesses, the center of stiffness, and the moment arms.

The total twist stiffness of the pinion and gear are composed of the spread-twist stiffness k_t, which is due to the spread of contact along the gear teeth, and an off-mid-plane component due to the mesh stiffness being offset by the moment arms $\bar{A}_p$

or $\bar{A}_g$. The total twist stiffnesses are

$$\begin{aligned} k_{pt} =& \mathbf{K}_{2,2} = \sum_{i=1}^{n} k_i A_{p,i}^2 = k_m \bar{A}_p^2 + k_t \\ k_{gt} =& \mathbf{K}_{8,8} = \sum_{i=1}^{n} k_i A_{g,i}^2 = k_m \bar{A}_g^2 + k_t \end{aligned} \tag{3.15}$$

Coupling twist stiffness k_{ct} couples pinion and gear twist by generating a twist in the gear due to a twist in the pinion, given by

$$k_{ct} = \mathbf{K}_{2,8} = \sum_{i=1}^{n} k_i A_{p,i} A_{g,i} = k_m \bar{A}_p \bar{A}_g - k_t \tag{3.16}$$

The total mesh force and moment due to spread of contact are

$$F = k_m \bar{\delta}, \quad M_s = k_t \gamma \tag{3.17}$$

where $\bar{\delta}$ is the equivalent mesh deflection and $\gamma = \theta_p - \theta_g$ is the relative twist angle between the pinion and the gear.

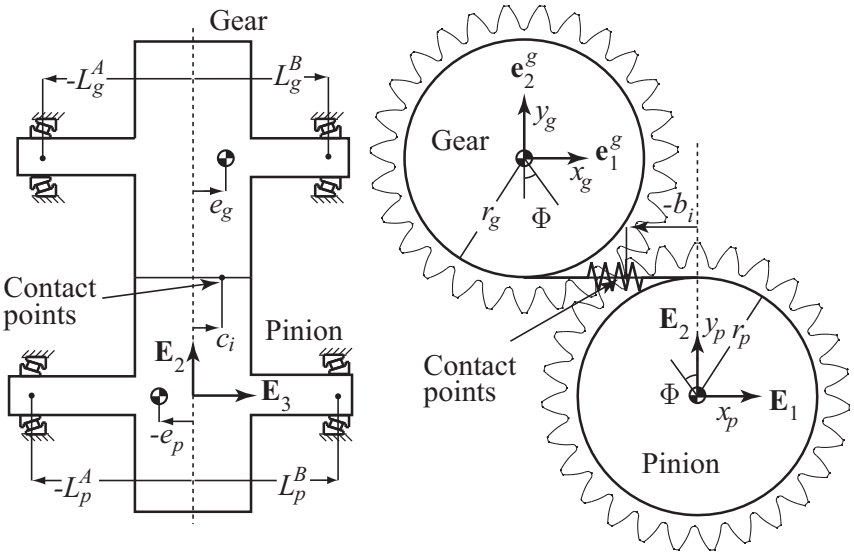

Figure 3.1: Gear pair model. The dashed line is at the center of the active facewidth.

3.3 Dynamic Analysis

3.3.1 Method

The nonlinear dynamic response is obtained using numerical integration of the equations of motion Eq. (3.6). The high-speed effects are neglected; $\Omega_p = 0$. Numerical integration at each excitation frequency is performed until the transient response is settled and the steady state response is reached. In order to minimize transient response, and so the computation time required, the initial guess for the numerical integration is set to the static solution $\mathbf{q} = \mathbf{q}_s$ at $t = 0$. The static solution is found from

$$(\mathbf{K} + \mathbf{B})\,\mathbf{q}_s = \mathbf{f}_{\text{ext}} \tag{3.18}$$

obtained by substitution of $\ddot{\mathbf{q}} = \dot{\mathbf{q}} = \mathbf{0}$, $\Omega_p = 0$ into Eq. (3.6).

Under dynamic conditions, the translational stiffness k_m, the spread-twist stiffness k_t, and the axial center of stiffness $\bar{c}$ along facewidth are found instantaneously as $\mathbf{q}$ is calculated at each time step from Eqs. (3.11) and (3.12). These instantaneous dynamic quantities are indicated by prefixing the word "dynamic" to stiffnesses and center of stiffness in the upcoming discussions. The dynamic quantities are different from quasi-static quantities and are crucial output metrics that help explore the nonlinear vibrations.

The numerical integration requires $\mathbf{K}$ and $\mathbf{f}_{\text{ext}}$. These, however, are not known *a priori* as they depend on the changing contact conditions H_i of the contact springs k_i. The iteration procedure described in [23] is adopted to solve $\mathbf{K}$ and $\mathbf{f}_{\text{ext}}$ for a given dynamic displacement vector $\mathbf{q}$ at an instant t.

3.3.2 Linearization

The time-average of the mesh stiffness matrix $\mathbf{K}$ at the operating torque over a mesh period gives the mean stiffness matrix $\mathbf{K}_m$. The excitation from the gear mesh is approximated as a periodic external force [81, 118], given by $(\mathbf{K}_m + \mathbf{B})\,\mathbf{q}_s(t)$. The external force vector with its harmonic content is found from the static deflection vector $\mathbf{q}_s(t)$, which is solved from Eq. (3.18) at several points over a mesh period. Linear time-invariant equations of motion are

$$\mathbf{M}\ddot{\mathbf{q}} + \mathbf{D}\dot{\mathbf{q}} + (\mathbf{K}_m + \mathbf{B})\,\mathbf{q} = (\mathbf{K}_m + \mathbf{B})\,\mathbf{q}_s(t), \tag{3.19}$$

which are solved in frequency domain using the first five harmonics of $\mathbf{q}_s(t)$. Damping matrix $\mathbf{D}$ is calculated using modal damping. Damping is difficult to estimate in gear dynamics [11]. It is taken to be less than 10%, but it varies among different gear pairs.

3.3.3 Spur Gear Pair With Modifications: Comparison with Experiments

In this subsection, some modified spur gears from [47] are analyzed with the purpose to find out whether partial contact loss occurs in experiments.

The static transmission errors generating $\mathbf{q}_s(t)$ are plotted in Figures 2.4(b), 2.4(c), and 2.4(d). Finite element analysis results are included to confirm the solution from the analytical model. The agreement between the analytical and finite element analysis verifies the discretization of load distribution. Dynamic response is plotted in Figure 3.2, which shows experimentally measured, linear, and nonlinear root mean square (RMS) of the transmission error with gear rotation speed. The mean is removed when calculating the RMS of quantities. The error bars, ± 1 μm, mark the

repeatability of the measurements, which was reported in a closely related paper by the same authors [46]. The agreement between the experimental measurements and numerical integration in Figure 3.2 verifies the analytical model under dynamic conditions.

Inspecting Figure 3.2, the nonlinear and experimental solutions gradually deviate from the linear solution. There is not a kink point as in [5, 44, 67, 72, 86] in the amplitude versus frequency curve that marks the onset of contact loss. This distinct behavior at the onset of contact loss will be observed in the upcoming analysis in Figure 3.16. Total contact loss starts at mesh frequencies $\Omega = 1.09$, $\Omega = 0.97$, $\Omega = 0.96$, $\Omega = 0.98$, but the nonlinear solution deviates from the linear solution *before* total contact loss starts.

Figure 3.3 compares the static and dynamic translational mesh stiffnesses (k_m) of the gear pairs in Figure 3.2 at selected gear rotation speeds. The dynamic stiffness values are from numerical integration. These selected speeds are adjacent to the speeds where total contact loss starts. In each case, total contact loss starts at the next lower speed. The static and dynamic translational mesh stiffnesses k_m are different. As the dynamic response amplitude increases, portions of gear teeth lose contact (partial contact loss). Hence the deviation of dynamic mesh stiffness from static mesh stiffness. Away from resonance (not shown), the static and dynamic mesh stiffnesses are almost identical for all four gear pairs.

The dynamic contact patterns at three speeds at torques of 85 N-m and 170 N-m are plotted in Figure 3.4. Figures 3.4(a) and 3.4(b) show contact patterns away from resonance, Figures 3.4(c) and 3.4(d) just before total contact loss, and Figures 3.4(e) and 3.4(f) at the frequency of peak response.

The contact patterns away from resonance (Figure 3.4(a) and 3.4(b)) are similar to static contact patterns in Figures 2.5(a) and 2.5(c), but the dynamic contact patterns just before total contact loss (Figures 3.4(c) and 3.4(f)) are much different than the static contact patterns. This distortion is the result of partial contact loss. The dynamic contact patterns at peak response frequency (Figures 3.4(e) and 3.4(f)) are also much different than static contact patterns, but this time because of total contact loss.

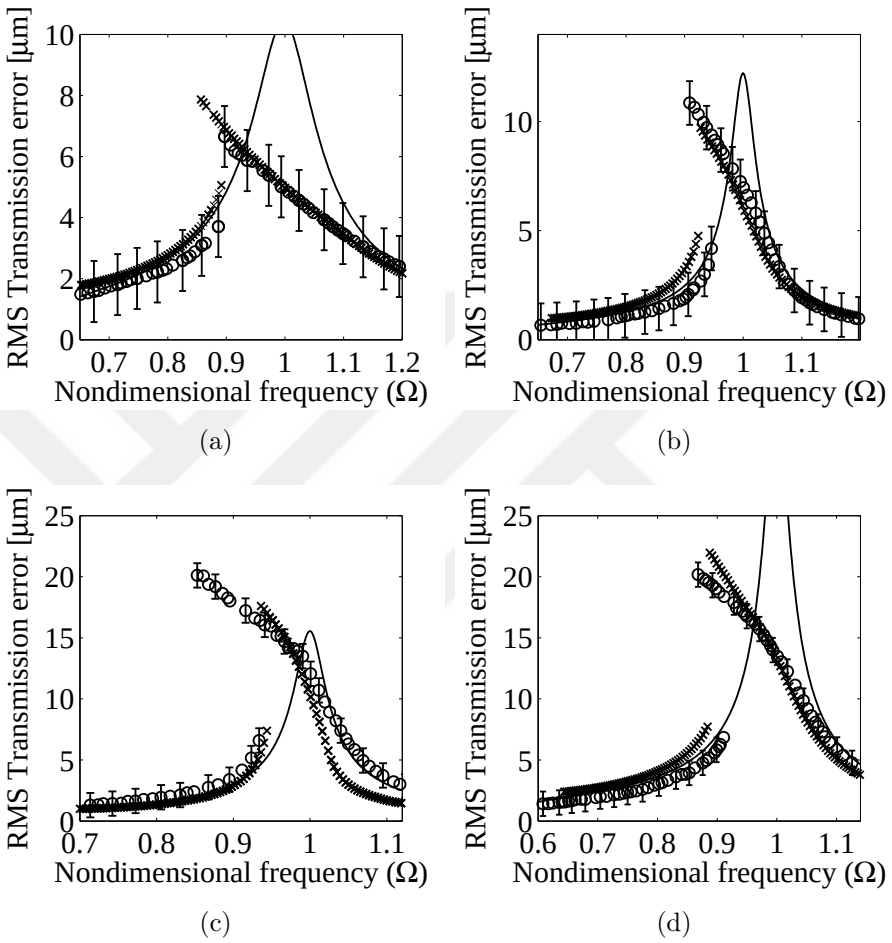

Figure 3.2: RMS (mean removed) of the transmission error from numerical integration (cross), linear solution (solid line), and experimental measurement from Figure 13 of [47] (circles with error bars). All gears have 10 μm of tip relief and 5 μm of circular lead crown. (a) Tip relief on both gears starts at $\alpha = 20.9$ deg; the torque is 85 N-m. (b) Tip relief on both gears starts at $\alpha = 20.9$ deg; the torque is 170 N-m. (c) Tip relief on both gears starts at $\alpha = 22.2$ deg; the torque is 340 N-m. (d) Tip relief on both gears starts at $\alpha = 23.6$ deg; the torque is 340 N-m.

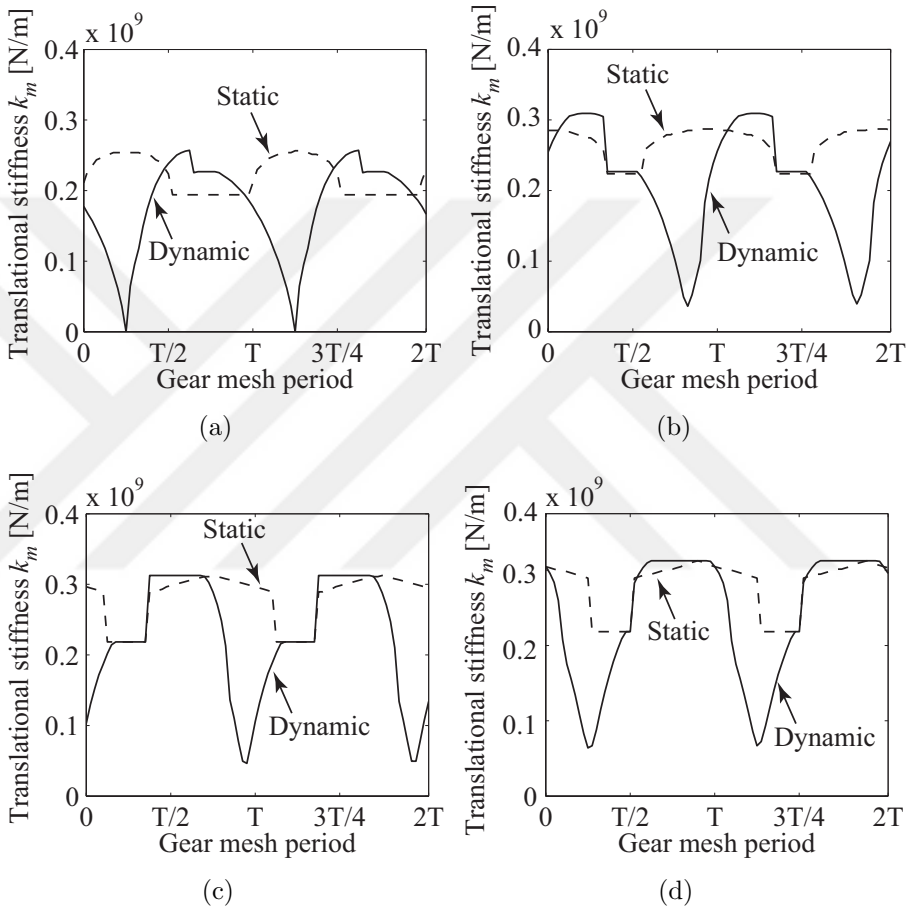

Figure 3.3: Static (dashed line) and dynamic (solid line) translational mesh stiffness at selected speeds. (a) $\Omega = 1.09$. (b) $\Omega = 0.97$. (c) $\Omega = 0.96$. (d) $\Omega = 0.98$. Subfigure indices in this figure and Figure 3.2 correspond to the same gear pairs.

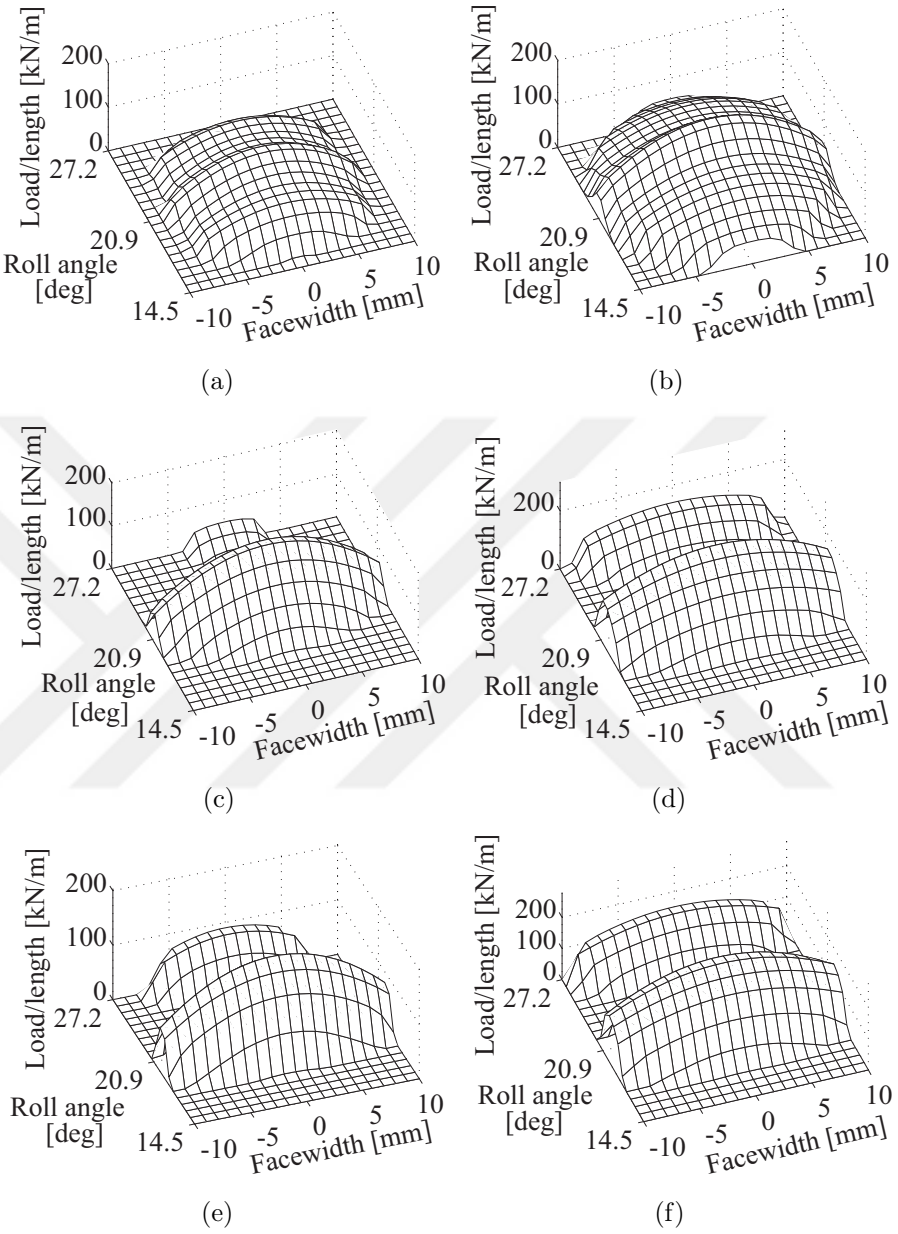

Figure 3.4: Dynamic contact patterns of the gear pair in Figures 3.2(a) and 3.2(b) at selected speeds. (a) Away from resonance, $\Omega = 0.61$; applied torque 85 N-m. (b) Away from resonance, $\Omega = 0.67$; applied torque 170 N-m. (c) Before total contact loss, $\Omega = 1.09$; applied torque 85 N-m. (d) Before total contact loss, $\Omega = 0.97$; applied torque 170 N-m. (e) At peak response frequency, $\Omega = 0.87$; applied torque 85 N-m. (f) At peak response frequency, $\Omega = 0.93$; applied torque 170 N-m.

3.3.4 Helical Gear Pair With Modifications

In this subsection, the modified helical gear pair described in Tables 2.1 and 2.2 is analyzed. The static transmission error generating $\mathbf{q}_s(t)$ is plotted and compared with finite element analysis in Figure 2.4(a). Figure 2.12(a) shows the static contact pattern.

Figure 3.5 shows the natural frequencies and modal strain energy distributions of each mode. In the horizontal axes, x_A denotes the energy stored in the pinion bearing at A in the x direction (along $\mathbf{E}_1$). The pinion bearing at B and the gear bearings follow similarly. The last two columns denote the gear mesh strain energy stored in the equivalent translational k_m and spread-twist stiffnesses k_t. The signs of the strain energy in the bearings reflect the direction of motion. The assignment of direction of motion in strain energy differentiates between translation and twisting of the gear-shaft bodies. The strain energies in the gear mesh are always positive. Some natural frequencies are repeated because the mass and the inertia of the pinion and gear are equal.

The 7th and the 12th vibration modes are interesting to explore because the 7th mode involves relative mesh twist, and the 12th mode involves mesh deflection. These are the only modes that cause a compression in the mesh twist and translational stiffnesses. One expects nonlinear dynamic response if these vibration modes are excited.

Twist Mode Peak at 490 Hz

The relative twisting peak at 490 Hz in Figure 3.9 is the resonance of the mesh twist mode (mode 7). The inset plots show dynamic contact patterns. The response is

nonlinear as confirmed by the differing linear and nonlinear curves. Figure 3.6 shows the static and dynamic mesh force F, static and dynamic translational and spread-twist mesh stiffnesses, static and dynamic center of stiffness, and dynamic contact pattern at 490 Hz. The dynamic mesh force in Figure 3.6(a) is always positive, and the dynamic fluctuation is mild. There is no total contact loss. The teeth remain engaged at all times. One would not expect the difference between linear and nonlinear response and static and dynamic contact patterns given that the dynamic mesh force is almost constant.

To explain, the high dynamic fluctuation of the the center of stiffness indicates significant relative twisting of the gears. Twisting distorts the dynamic contact pattern significantly compared with the static contact pattern in Figure 2.12(a). While the total mesh force changes only slightly and there is no total contact loss, its distribution on the tooth surface is markedly changed by twisting. This dynamically changes which contact segments are in contact. This kind of twist vibration mode has been neglected in prior studies, that must be restricted to narrow facewidth gears. The relatively low natural frequency make it a potentially troublesome resonance in practical applications.

The nonlinear resonant frequency of 490 Hz observed from Figure 3.9 is higher than the natural frequency of 425 Hz. Consider the dynamic natural frequency obtained using the stiffness matrix averaged over a few mesh cycles under stead-state dynamic conditions. The dynamic natural frequency of the twist mode (mode 7), shown in Figure 3.7(a), correlates with the increase in the response frequency. As a contrast, the mesh deflection mode dynamic natural frequency, plotted in Figure 3.7(b), correlates

with the decrease in the response frequency of the mesh deflection mode in Figure 3.13.

To explain the increase in the dynamic natural frequency of the twist mode, the twist is almost purely pinion and gear twisting; only the twist degrees-of-freedom θ_p and θ_g are active. Consequently, the simplest system that can reproduce the natural frequency of the twist mode must include θ_p and θ_g. The mass and stiffness matrices of this reduced system are

$$\mathbf{M}_t = \begin{bmatrix} \mathbf{M}_{2,2} & 0 \\ & \mathbf{M}_{8,8} \end{bmatrix}, \quad \mathbf{K}_t = \begin{bmatrix} k_{pt} + \mathbf{B}_{2,2} & k_{ct} \\ & k_{gt} + \mathbf{B}_{8,8} \end{bmatrix}. \tag{3.20}$$

The time histories of the total pinion twist stiffnesses k_{pt}, total gear twist stiffnesses k_{gt}, and coupling twist stiffnesses k_{ct} are shown in Figure 3.8. The mean value of the coupling twist stiffness during vibrations drops significantly while mean values of the total pinion and gear twist stiffnesses stay about the same. The drop in k_{ct} is due to the nonlinear dependence of the moment arms $\bar{A}_p$ and $\bar{A}_g$ on relative twist γ. This drop in k_{ct} drives the dynamic natural frequency higher.

The foregoing discussions of the twist mode is crucial because they highlight: 1) Twist mode, with its previously unidentified subharmonic resonance, is excited. 2) The interaction between the nonlinear gear mesh and the three-dimensional gear body displacements yield peculiar dynamic response.

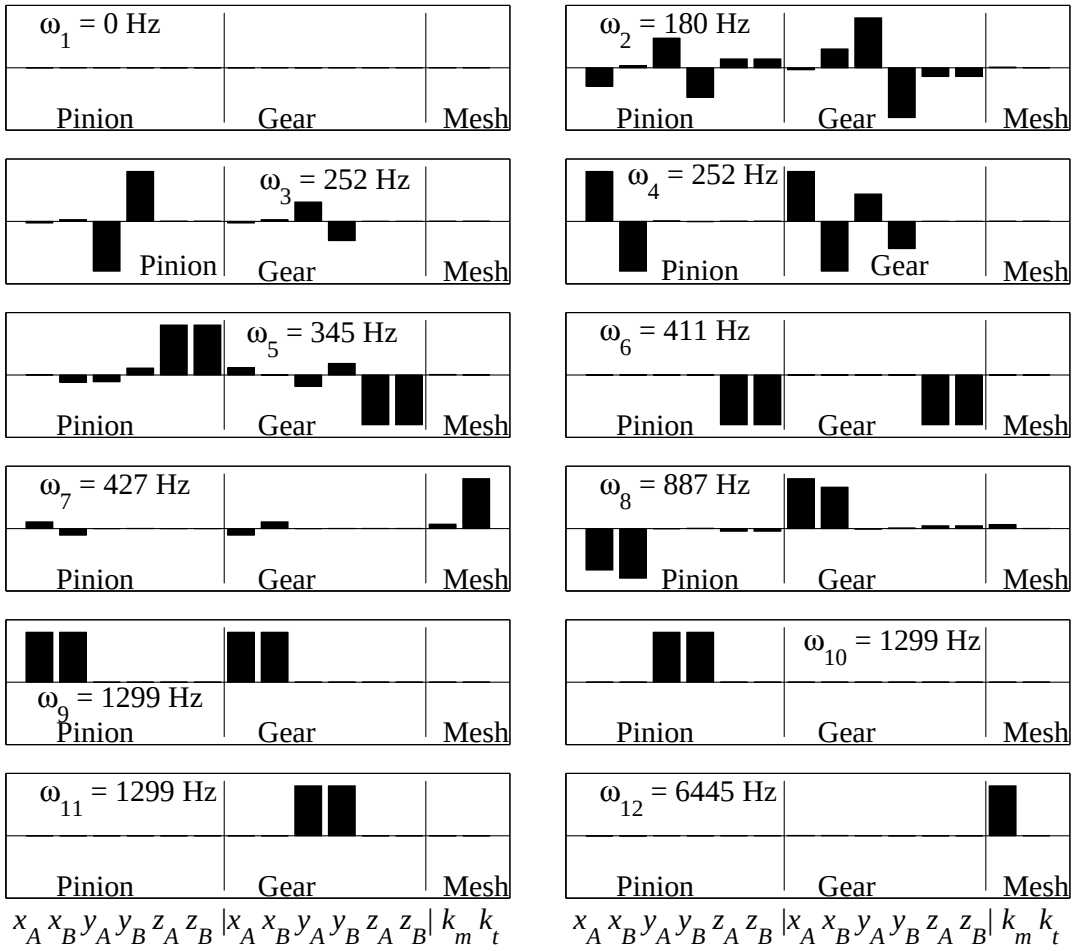

Figure 3.5: Strain energy in bearings and gear mesh of the modified helical gear pair in Tables 2.1 and 2.2. x_A through z_B mark the strain energy in bearing degrees of freedom. k_m marks the strain energy in the translational stiffness, and k_t marks the strain energy in the spread-twist stiffness. The positive/negative values distinguish the direction of motion. Mesh strain energies are always positive.

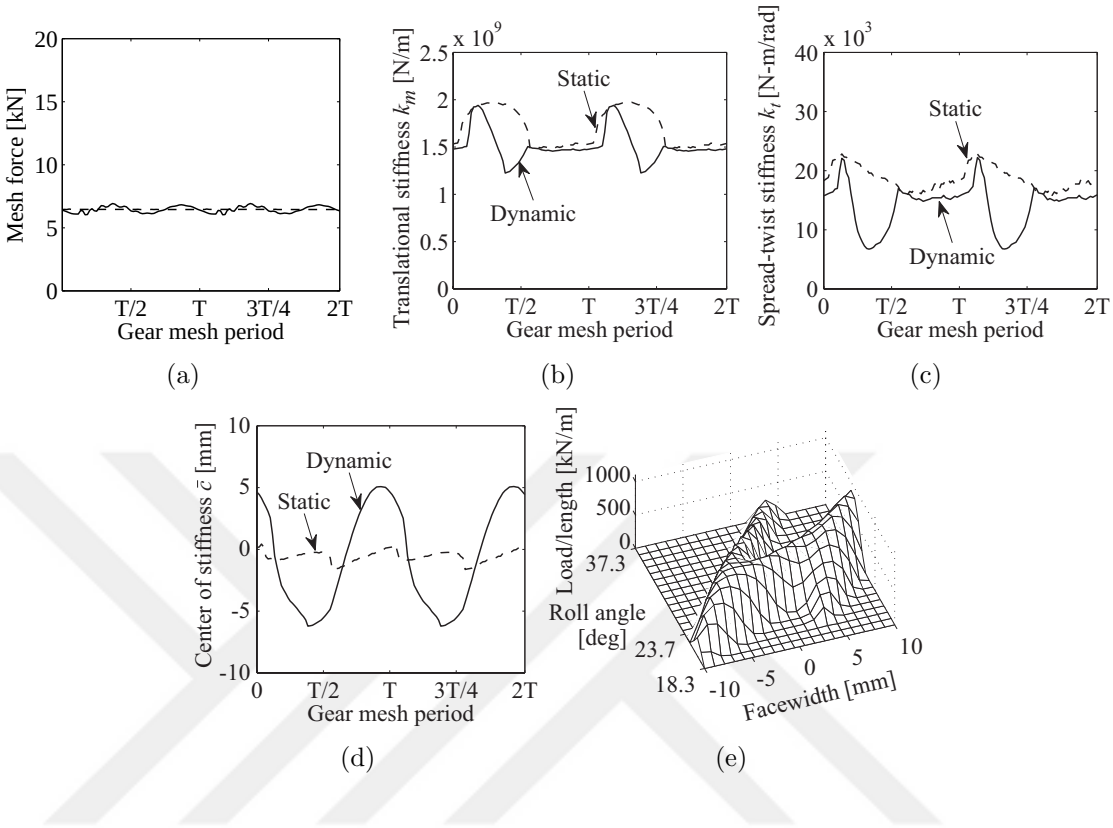

Figure 3.6: Dynamic response of the modified helical gear pair described in Tables 2.1 and 2.2 at 490 Hz. Time histories include static (dashed line) and dynamic (solid line) fluctuations. Contact pattern is for the dynamic case.

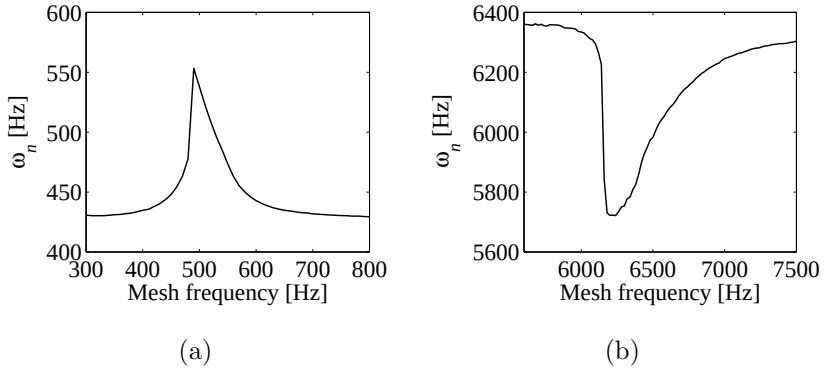

Figure 3.7: (a) Twist mode (7th) dynamic natural frequency around twisting resonance, (b) Mesh deflection mode (12th) natural frequency around mesh deflection resonance.

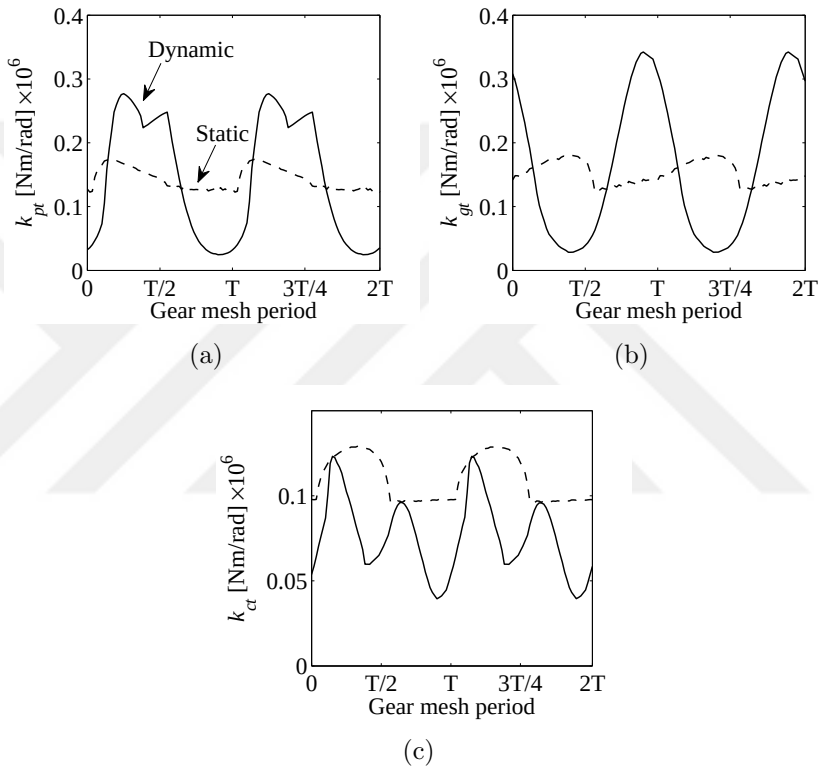

Figure 3.8: Dynamic twist stiffnesses from the gear mesh at 490 Hz. (a) Total pinion twist stiffness k_{pt}, (b) Total gear twist stiffness k_{gt}, (c) Coupling twist stiffness k_{ct}. Static (dashed line) and dynamic (solid line).

Subharmonic Peak at 1010 Hz

There is a peak in the response in Figure 3.9 when the mesh frequency is around 1010 Hz. The dynamic center of stiffness at 1010 Hz is plotted in Figure 3.10. The time history is periodic at twice the mesh period, which is also seen in the frequency components of the twist angle in Figure 3.11. High dynamic fluctuations indicate twist vibration consistent with mode 7.

This response is the subharmonic resonance of the twist mode (mode 7) where the mesh frequency is nearly twice ω_7. The indicators that this is a subharmonic resonance are: 1) The sharp peak at 1010 Hz in Figure 3.9 without a natural frequency near this value; 2) No linear response at 1010 Hz; and 3) The spectrum in Figure 3.11 at 1010 Hz with response at multiples of $n/2$ of the mesh frequency, $n = 1, 2$.

This resonance may be driven by parametric excitation from the time-varying twist stiffnesses. This is a previously unidentified kind of gear vibration because it stems from the twist mode. Had the twist mode been neglected, its subharmonic resonance would not appear.

Mesh Deflection Mode Peak at 6200 Hz

This is the primary resonance of the mesh deflection mode (mode 12). There is significant nonlinearity from partial contact loss, as evident by the difference between the linear and nonlinear response curves in Figure 3.12. The dynamic mesh force and both translational and twist stiffnesses at 6200 Hz reach zero in Figures 3.13(a), 3.13(b), and 3.13(c). Center of stiffness in Figure 3.13(d) is undefined at total contact loss instants. Partial and total contact loss is reflected in the contact pattern in Figure 3.13(e).

Figure 3.14 shows the static and dynamic mesh stiffnesses at selected operating speeds. There is a difference between the static and dynamic stiffnesses although the teeth remain in contact. The closer the operating speed to the resonant frequency, the greater the difference between static and dynamic stiffnesses. Similar behavior was observed in modified spur gears, and it is a result of partial contact loss.

When total contact loss occurs without prior partial contact loss, as in spur gears, a sharp kink would appear in Figure 3.12 where the nonlinear curve diverges from the linear curve [5, 44, 67, 72, 86]. Instead, the nonlinear response deviates slowly and smoothly from the linear response in Figure 3.12 because of partial contact loss.

Peak at 890 Hz

This is the resonance of mode 8. Despite the high pinion bearing displacement x_p at 890 Hz, the transmission error is low (Figure 3.15). Consequently, the dynamic fluctuations in mesh force and contact pattern are negligible (not plotted). The linear behavior of this resonance demonstrates that not all deflections cause nonlinearity. Dynamic displacements must be in the nonlinear mesh stiffnesses for a nonlinearity in the dynamic response to develop.

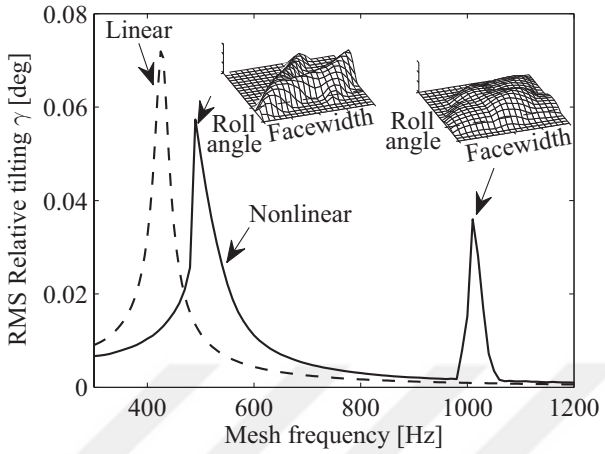

Figure 3.9: Dynamic twist angle γ from nonlinear (solid line) and linear (dashed line) solutions of the modified helical gear pair given in Tables 2.1 and 2.2.

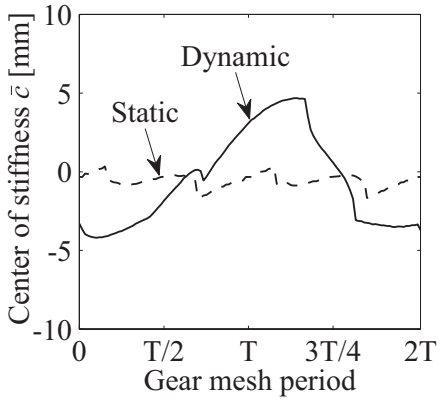

Figure 3.10: center of stiffness of the modified helical gear pair described in Tables 2.1 and 2.2 at 1010 Hz. Static fluctuations: dashed line), dynamic fluctuations: solid line.

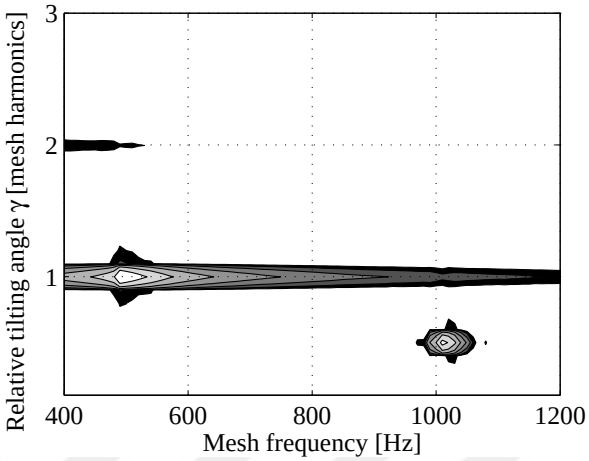

Figure 3.11: Twist angle spectrum of the modified helical gear pair from the nonlinear (speed-down) solution. Gear parameters are in Tables 2.1 and 2.2.

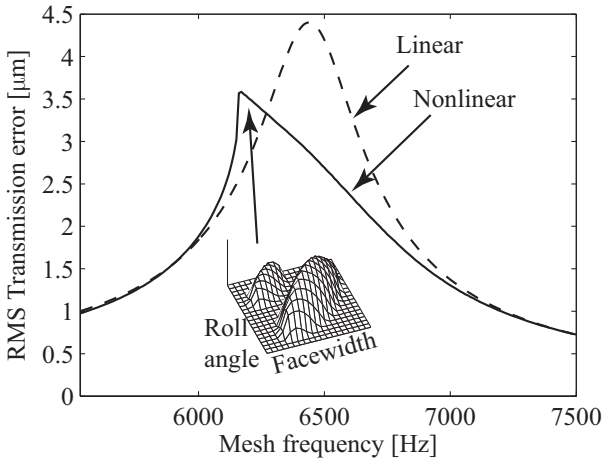

Figure 3.12: Dynamic transmission error from nonlinear (solid line) and linear (dashed line) solutions response of the modified helical gear pair given in Tables 2.1 and 2.2.

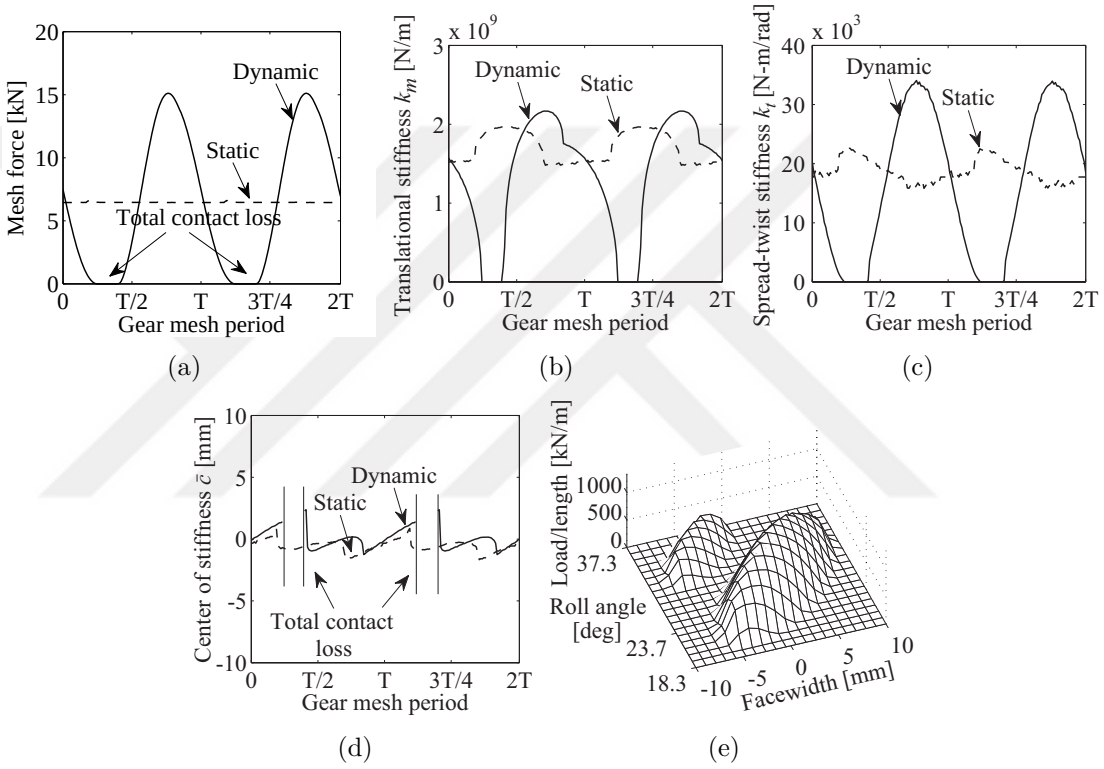

Figure 3.13: Dynamic response of the modified helical gear pair described in Tables 2.1 and 2.2 at 6200 Hz. Time histories include static (dashed line) and dynamic (solid line) fluctuations. Contact pattern is for the dynamic case.

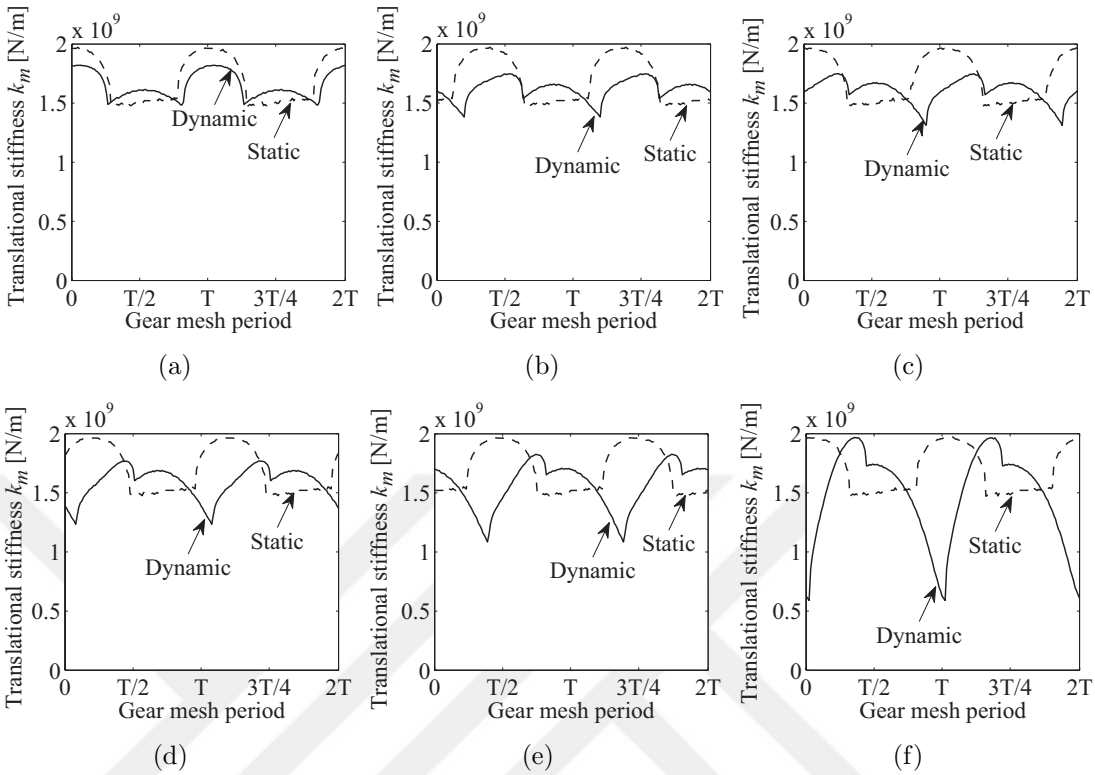

Figure 3.14: Static (dashed line) and dynamic (solid line) mesh stiffness at selected operating speeds of the helical gear pair described in Table 2.1 with tooth surface modifications given in Table 2.2. (a) 7500 Hz. (b) 7000 Hz. (c) 6900 Hz. (d) 6800 Hz. (d) 6700 Hz. (f) 6500 Hz.

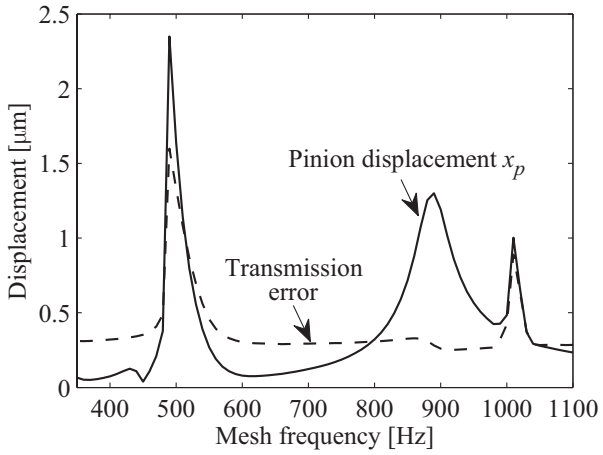

Figure 3.15: Dynamic transmission error (dashed line) and pinion bearing displacement x_p (solid line) from nonlinear solution of the modified helical gear pair.

3.3.5 Spur Gear Pair Without Modifications

In this subsection, an unmodified spur gear pair is analyzed. The gear parameters are given in Table 2.1 but the helix angle is zero. Figure 3.16 shows the linear and nonlinear dynamic transmission error. The linear solution is almost identical to the nonlinear solution until there is total contact loss. The nonlinear solution immediately deviates from the linear solution at the onset of total contact loss near 9000 Hz and the peak bends toward lower frequency. This nonlinear behavior of gears was reported in the literature [5, 44, 67, 72, 86]. It contrasts with the primary resonance of modified gear pairs discussed earlier. In the modified helical gear pair, softening nonlinearity always exists but in the form of partial contact loss, so the transition from partial to total contact loss is smooth. Thus, the nonlinear solution deviates gradually from the linear solution rather than with a marked change in the frequency response curve as in Figure 3.16 and [5, 44, 67, 72, 86].

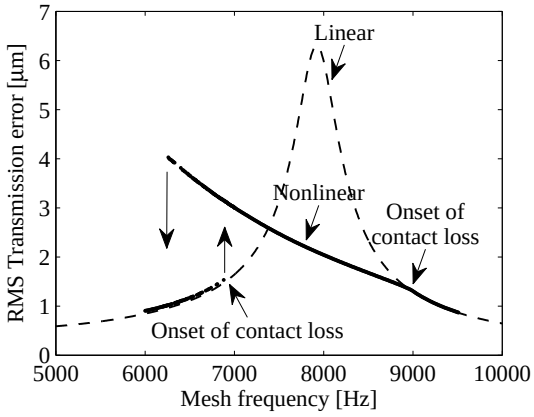

Figure 3.16: RMS transmission error from the linear (dashed line) and nonlinear (speed-up and speed-down, dots at data points) solutions of an unmodified spur gear pair. Note the high concentration of data points. Gear parameters are given in Table 2.1 except the helix angle is zero.

3.3.6 Discussion

From the computational observations we deduce that partial contact loss can appear when:

1. There are twisting vibrations. Gears may be helical or spur, but the twist mode needs to be excited either via the moments from the helical gear mesh, or via external periodic forcing. Twisting separates the edges of the gears hence partial contact loss. Modified and unmodified gears are both susceptible.

2. There are tooth surface modifications. At the mesh deflection mode resonance, the dynamic fluctuation of mesh force changes the contact, thus causing partial contact loss. The gears may be helical or spur, but unmodified gears show only total contact loss.

The observed dynamic response and the type of nonlinearity is summarized in Table 3.1 for spur and helical gears with and without modifications.

Table 3.1: Summary of dynamic response for spur and helical gears with and without modifications. PCL: Partial contact loss, TCL: Total contact loss

	Twist mode	**Mesh deflection mode**
Spur Gears (Unmodified)	Not excited	TCL
Spur Gears (Modified)	Not excited	PCL and TCL
Helical Gears (Unmodified)	PCL	TCL
Helical Gears (Modified)	PCL	PCL and TCL

3.4 Conclusions

This work uses a nonlinear three-dimensional gear mesh model, where portions of contact lines may disengage although the teeth may not totally lose contact. This is called partial contact loss. The resulting equations of motion intertwine the gear mesh nonlinearity with three-dimensional gear body displacements. Dynamic response is obtained by numerical integration of the nonlinear time-varying equations of motion and by frequency domain analysis of the linearized time-invariant equations of motion.

An equivalent lumped-parameter representation of the gear mesh (a translational mesh stiffness located at the center of stiffness and a spread-twist mesh stiffness) encapsulates the consequences of the intertwinement of the three-dimensional dynamic gear displacements with the nonlinear gear mesh. There are two important modes:

1. The mesh deflection mode involves compression of the translational mesh stiffness. The translational mesh stiffness and the spread-twist mesh stiffness both dynamically decrease as a result of partial contact loss. This decrease is observed when there are tooth surface modifications in both spur and helical gears. Eventually at higher amplitude vibrations contact is completely lost. Without modifications, however, there is only total contact loss. Dynamic partial contact loss in this mode is shown to exist in experiments, so it is not merely a theoretical find. Overall reduction of translational mesh stiffness decreases the peak resonance frequency.

2. The mesh twist mode involves relative twist between gears. The time dependence of the spread-twist stiffness and the center of stiffness excite this mode in helical gears. Twisting and the consequent partial contact loss severely distorts

the dynamic contact pattern and so the surface stresses. In the helical gears analyzed, partial contact loss near the twist mode resonance dynamically decreases the coupling twist stiffness. That increases the peak response frequency. This inverse relationship between the coupling-twist stiffness and response frequency is shown in a two degree-of-freedom, which is the simplest system that can reproduce the twist mode.

Chapter 4: Nonlinear Vibration of Gears with Tooth Surface Modifications and Sphere/Half-Space Contact

4.1 Introduction

Vibration of gear pairs can be considered under the general category of contact vibrations, which also includes vibration of bearings, splines, linkages, and other mechanical connections. In gear applications, the involute tooth surface shape is usually modified slightly to improve misalignment tolerance [17] and to avoid undesirable edge or corner contact [63]. With or without such tooth modifications gear vibrations exhibit softening nonlinearity [5, 24, 47, 86, 115, 121] near resonance as a result of total or partial contact loss. Partial contact loss is where portions of nominally contacting surfaces lose contact (and other nominally non-contacting portions potentially gain contact) as a result of dynamic motions, surface modification, or misalignment. Modifications are the major source of partial contact loss [23]. Although gear systems that exhibit total contact loss have been analyzed, only numerical solutions for the vibration of gears that exhibit partial contact loss are available in the literature, for example [3, 6, 9, 26, 56, 121]. To that end, this work applies approximate methods that yield analytical solutions for nonlinear gear contact vibrations.

Vibration of other contacting systems involve softening nonlinearity, in particular sphere/half-space contact vibration [73,91,94]. The approach and results in this work apply to such problems, and sphere/half-space contact is examined herein. Research on nonlinear sphere/half-space contact vibrations uses force-deflection relations from the Hertz formula, which can be treated by perturbation methods or harmonic balance [75, 106]. Hess and Soom [32] solve a single degree-of-freedom system with quadratic and cubic nonlinearities excited by harmonic forcing. Perret-Liaudet and Rigaud [89] analyze subharmonic resonances of sphere/half-space contact vibrations. Harmonic balance and perturbation analysis both compare well with experimental measurements [69, 91, 94].

The equations of motion for gear vibrations include time-dependent parameters such as periodic variation in mesh stiffness. In many cases, lumped-parameter gear models excited by static transmission error or time-varying mesh stiffness give satisfactory results [26,30,57,81,82,86,101,118]. A single spring is used to model the gear mesh interface in these works. Velex and Ajmi [118] examine the validity of approximating transmission error as the excitation source. Liu and Parker [65] explore the conditions under which the aforementioned approximations work.

Lumped-parameter gear models allow closed-form solutions using harmonic balance [11, 44, 49, 83] and perturbation methods [50, 72, 105]. The sole source of nonlinearity in the works listed above is total contact loss, a piecewise nonlinearity in which the gear mesh ceases to transmit any force. Gear tooth surface modifications are not included in the aforementioned works.

The modeling in [65,67] for the dynamic response of multi-mesh gears differs from the literature listed above because it considers tooth profile modifications and contact

loss at each of the individual meshing gear teeth rather than the gear mesh as a whole. In [65, 67], such contact loss is due to linear tooth profile modifications, which is the only type of modification they consider.

Detailed tooth contact models allow dynamic analysis for any type of tooth surface modification [24, 54, 71, 115, 121]. Such models predict partial contact loss arising from arbitrary tooth surface modification [3, 9, 24, 90, 121, 122]. Contact algorithms that allow for partial contact loss, however, are prohibitively complex for analytical methods and nonlinear dynamic response can only be obtained numerically. Numerical methods give only restricted generalizations about dynamic behavior because they are limited to selected parametric studies. There are no studies in the literature that provide analytical closed-form solutions for the nonlinear vibration of gears when partial contact loss is present.

This work gives analytical closed-form solutions for nonlinear rotational gear vibrations near primary resonance, that is, when the excitation frequency is close to the natural frequency. The solution includes the nonlinear behavior due to partial contact loss and admits arbitrary modifications of the gear tooth surface. The use of a general force-deflection function as an input means the dynamic equation of motion does not depend on the physical gear modeling assumptions and can apply to other contact problems. Sphere/half-space contact is the other physical system analyzed in this work. Considering gears, the force-deflection function effectively captures the phenomena of partial contact loss, parameter time-dependence, tooth surface modifications, changing number of teeth in contact, and so on. The sphere/half-space contact vibrations approximate Hertz contact behavior. With Taylor and Fourier

series expansions, the equation of motion takes a generalized polynomial form that enables use of the method of multiple scales.

4.2 Mathematical Model

4.2.1 Equation of Motion

This section presents a single degree-of-freedom equation of motion in a form suitable for perturbation analysis. The key assumption is that the force-deflection function and the applied load vary periodically with time. No further assumptions are made at this point to tailor the equation of motion to gears, sphere/half-space contact, or any other system.

The equation of motion is

$$m\ddot{x} + c\dot{x} + C(x,t)f(x,t) = F(t) \tag{4.1}$$

where $F(t)$ is the periodic applied load with period P_F, $f(x,t)$ is the nonlinear, time-dependent, periodic force-deflection function with period P_f, and $C(x,t)$ is the separation function given by

$$C(x,t) = \begin{cases} 0 & \text{if } x < g(t) \\ 1 & \text{if } x \geq g(t) \end{cases} \tag{4.2}$$

where $g(t)$ is the unloaded ($F(t) = 0$), quasi-static ($\dot{x} = \ddot{x} = 0$) deflection. It satisfies $f\left(g(t), t\right) = 0$.

This single degree-of-freedom mechanical oscillator can approximate the rotational vibration of gear pairs. In this case, the force-deflection function $f(x,t)$ considers the elastic tooth contact, tooth bending, shear, and so on. Because of the changing number of teeth in contact, the force-deflection function is periodic with tooth pass frequency. Equation (4.2) restricts contact loss to single-sided impacts. Elimination

of the rigid body motion [55, 81] lumps the rotational inertias of both the pinion (I_p) and gear (I_g) into $m = I_p I_g / \left(I_p r_g^2 + I_g r_p^2\right)$ in Eq. (4.1), where r_p and r_g are the pinion and gear base radii, and θ_p and θ_g are the rotational deflections of the pinion and gear. In this case, the load is constant and $F(t) = F = T_p/r_p$ represents the mesh force due to a constant applied torque T_p. Losses from all sources are lumped into the viscous damping coefficient c. With this formulation, $x(t) = \theta_p r_p + \theta_g r_g$ is the dynamic transmission error in Eq. (4.1), and $x_s = g(t)$ is the unloaded static transmission error.

Sphere/half-space contact is the other physical system examined in this work. The single degree-of-freedom nonlinear equation of motion from [89] models sphere/half-space contact vibration experiments. Although periodic irregularities on bearing races and railway tracks are physical examples of contact vibrations that result in time-dependence in $f(x,t)$ and $g(t)$, with sphere/half-space contact vibration experiments there are no surface irregularities, so $f(x,t) = f(x)$ and $g(t) = 0$. The periodic applied force $F(t)$ from a shaker excites the experimental system used as a benchmark for the current analysis.

The force-deflection function $f(x,t)$ is the crucial quantity in this work. For a variety of systems, it can be obtained from experiments, finite element analysis, and analytical contact models. In gears, it is routinely calculated from computational models and readily measured. The force-deflection function, independent of the physical system in question and the method used to obtain it, can be represented by a Taylor series around x_m up to the nth order by

$$f(x,t) = \sum_{i=0}^{n} \frac{1}{i!} \left. \frac{\partial^i f(x,t)}{\partial x^i} \right|_{x=x_m} (x - x_m)^i = \sum_{i=0}^{n} B_i(t) \, (x - x_m)^i \tag{4.3}$$

where x_m is the deflection induced by the mean applied load. Averaging the force-deflection function and the applied force over their shortest common period P, x_m is found from

$$\int_0^P F(t)\,\mathrm{d}t = \int_0^P f(x_m, t)\,\mathrm{d}t \tag{4.4}$$

The Fourier series expansion of $B_i(t)$ in Eq. (4.3) is

$$B_i(t) = \beta_{i,0} + \sum_{r=1}^{p} \beta_{i,r} \cos(r\xi t - \Phi_{i,r}), \quad i = 0, 1, \ldots, n \tag{4.5}$$

where $\xi = 2\pi/P_f$ is the frequency of $f(x,t)$. The Fourier expansion of $F(t)$ is

$$F(t) = F_0 + \sum_{r=1}^{p} F_r \cos(r\zeta t - R_r) \tag{4.6}$$

where $\zeta = 2\pi/P_F$ is the frequency of $F(t)$. Substitution of $y = x - x_m$, Eq. (4.5), and Eq. (4.6) into Eqs. (4.1) and (4.2) gives

$$m\ddot{y} + c\dot{y} + C(y,t) \sum_{i=0}^{n} \left[\beta_{i,0} + \sum_{r=1}^{p} \beta_{i,r} \cos(r\xi t - \Phi_{i,r}) \right] y^i = F_0 + \sum_{r=1}^{p} F_r \cos(r\zeta t - R_r) \tag{4.7}$$

$$C(y,t) = \begin{cases} 0 & \text{if } y < -x_m + g(t) \\ 1 & \text{if } y \geq -x_m + g(t) \end{cases} \tag{4.8}$$

Substitution of $\beta_{0,0} = F_0$, a result of Eqs. (4.4) and (4.5), and (4.6) into Eq. (4.7) eliminates the mean load F_0 under contact, giving

$$\begin{aligned} m\ddot{y} + c\dot{y} + C(y,t) \sum_{i=1}^{n} \left[\beta_{i,0} + \sum_{r=1}^{p} \beta_{i,r} \cos(r\xi t - \Phi_{i,r}) \right] y^i &= \sum_{r=1}^{p} F_r \cos(r\zeta t - R_r) \\ - C(y,t) \sum_{r=1}^{p} \beta_{0,r} \cos(r\xi t - \Phi_{0,r}) - F_0 \left[C(y,t) - 1 \right] & \end{aligned} \tag{4.9}$$

so the mean load F_0 acts only when contact is lost.

Fourier expansion of $g(t)$ gives

$$g(t) = g_0 + \sum_{r=1}^{p} g_r \cos(r\xi t - \Psi_r) \tag{4.10}$$

The definition $d = x_m - g_0$ and substitution of $T = \omega_n t$, $\omega_n = \sqrt{\beta_{1,0}/m}$, and $y = ud$ give the non-dimensional forms of Eqs. (4.8) and (4.9) as

$$u'' + 2\mu u' + C(u,T)\sum_{i=1}^{n}\left[\alpha_{i,0} + \sum_{r=1}^{p}\alpha_{i,r}\cos\left(r\Omega_f T - \phi_{i,r}\right)\right]u^i = \sum_{r=1}^{p} q_r \cos\left(r\Omega_F T - \rho_r\right)$$
$$- C(u,T)\left[\alpha_{0,1}\cos\Omega_f T + \sum_{r=2}^{p}\alpha_{0,r}\cos\left(r\Omega_f T - \phi_{0,r}\right)\right] - \alpha_{0,0}\left[C(u,t) - 1\right] \tag{4.11}$$

$$C(u,T) = \begin{cases} 0 & \text{if } u < -1 + \sum_{r=1}^{p} e_r \cos(r\Omega_f T - \psi_r) \\ 1 & \text{if } u \geq -1 + \sum_{r=1}^{p} e_r \cos(r\Omega_f T - \psi_r) \end{cases} \tag{4.12}$$

where $()' = \mathrm{d}/\,\mathrm{d}T$, the non-dimensional quantities are

$$\Omega_f = \frac{\xi}{\omega_n}, \Omega_F = \frac{\zeta}{\omega_n}, \quad \mu = \frac{c}{2m\omega_n}, \quad q_r = \frac{F_r}{d\beta_{1,0}}\,(r \neq 0), \quad \alpha_{i,r} = \frac{\beta_{i,r} d^{i-1}}{\beta_{1,0}}, \quad e_r = \frac{g_r}{d} \tag{4.13}$$

and the phase angles relative to $\Phi_{0,1}$ are ($i = 0, 1, \ldots, n$ and $r = 0, 1, \ldots, p$)

$$\phi_{i,r} = \Phi_{i,r} - \Phi_{0,1},\ \rho_r = R_r - \Phi_{0,1},\ \psi_r = \Psi_r - \Phi_{0,1} \tag{4.14}$$

Considering sphere/half-space contact vibrations, the equation of motion from Eq. (7) in [89] is

$$\begin{aligned} \ddot{z} + 2\mu\dot{z} + \left(1 + \frac{2}{3}z\right)^{3/2} &= 1 + k\cos\zeta t,\ \text{if } z \geq -3/2 \\ \ddot{z} + 2\mu\dot{z} &= 1 + k\cos\zeta t,\ \text{if } z < -3/2 \end{aligned} \tag{4.15}$$

This equation approximates the Hertz contact between a sphere and a half-space. A constant dimensionless load of 1 from the weight of the sphere and a sinusoidal excitation amplitude k from a shaker are applied to the sphere. The transformation $x = 1 + 2z/3$ converts Eq. (4.15) into the form of Eq. (4.1) as

$$\begin{aligned} \ddot{x} + 2\mu\dot{x} + \frac{2}{3}x^{3/2} &= \frac{2}{3} + \frac{2k}{3}\cos\zeta t,\ \text{if } x \geq 0 \\ \ddot{x} + 2\mu\dot{x} &= \frac{2}{3} + \frac{2k}{3}\cos\zeta t,\ \text{if } x < 0 \end{aligned} \tag{4.16}$$

where contact is lost when $x < 0$. Comparing this equation with Eqs. (4.1) and (4.2), $m = 1$, $c = 2\mu$, $f(x,t) = 2/3x^{3/2}$, and $F(t) = 2/3 + 2k/3\cos\zeta t$. The mean deflection is $x_m = 1$ using Eq. (4.4). $g(t) = g_0 = 0$, and so $d = 1$. The natural frequency is $\omega_n = 1$. Use of Eq. (4.13) gives $\alpha_{0,0} = 2/3$, $\alpha_{2,0} = 1/4$, $\alpha_{3,0} = -1/24$, $q_1 = 2k/3$. Damping μ and frequency ζ are unchanged by the transformation, and $\Phi_{0,1} = \rho_1 = 0$. Following [69], the Taylor coefficients $\alpha_{i,0}$ are modified slightly to match the boundary condition at contact loss such that $\alpha_{2,0} = 2/7$ and $\alpha_{3,0} = -1/21$.

4.2.2 Physical Interpretation

Meaning of Non-dimensional Parameters

The physical interpretation of the important non-dimensional parameters are listed below and summarized in Table 4.1.

1. The mean load $\alpha_{0,0}$, linear mean stiffness $\alpha_{1,0}$, and nonlinear stiffnesses $\alpha_{i,0}$ $(i > 1)$ come from Taylor expansion of the force-deflection function by Eq. (4.3). In gears, $\alpha_{0,0}$ represents the constant mesh force, $\alpha_{1,0}$ the linear mesh stiffness, and $\alpha_{i,0}$ $(i > 1)$ the stiffness nonlinearities that include partial contact loss, nonlinear Hertz contact and others. In sphere/half-space contact experiments, $\alpha_{0,0}$ represents the weight of the sphere and the assembly, $\alpha_{1,0}$ the linear stiffness due to Hertz contact, and $\alpha_{i,0}$ $(i > 1)$ the stiffness nonlinearity associated with Hertz contact mechanics.

2. The excitation harmonics from the force-deflection function, $\alpha_{0,r}$, the harmonics of linear stiffness, $\alpha_{1,r}$, the harmonics of stiffness nonlinearity $\alpha_{i,r}$ $(i > 1)$ $r > 0$ and associated phase angles $\phi_{i,r}$ come from Fourier expansion of the Taylor

coefficients $B_i(t)$ by Eq. (4.5). They exist in gears due to periodic engagement/disengagement of the gear teeth. They do not occur in sphere/half-space contact. The quantity $\alpha_{0,r}$ excites the dynamics. It is close to what is called the "static transmission error excitation" for unmodified gears. The $\alpha_{1,r}$ represent the periodic change in the linear mesh stiffness. The periodicity of the stiffness nonlinearity, that is, changes in the strength of nonlinearity as the gear teeth engage/disengage, is contained in $\alpha_{i,r}$, $(i > 1)$.

3. The harmonics of the external excitation q_r and associated phase angles ρ_r come from Fourier expansion of the applied force $F(t)$ by Eq. (4.6). For gears, the applied torque is constant, so $q_r = 0$. In sphere/half-space contact experiments q_1 excites the system.

4. The harmonics of the unloaded deflection e_r and associated phase angles ψ_r come from Fourier expansion of the unloaded deflection $g(t)$ by Eq. (4.10). They only exist in gears and represent the time-dependent unloaded transmission error.

Partial Contact Loss

Partial contact loss occurs when portions of nominal gear contact lines lose contact while the other parts are still in contact [23, 24]. This contrasts with total contact loss, where the gear mesh ceases to transmit any force. Gear vibrations and tooth surface modifications cause partial contact loss. Partial contact loss depends heavily on applied torque. The mesh stiffness of modified gears, which depends on the total length of the contacting lines, changes with applied torque. Figure 4.1 demonstrates

this dependence by comparing the dimensional mesh stiffness of unmodified and modified gears. The modified gears depend heavily on torque; the unmodified gears do not. This dependence of stiffness on torque is a source of nonlinearity, and it results from partial contact loss. As mentioned in the foregoing paragraph, the parameters $\alpha_{i,r}$ and $\phi_{i,r}$ for $i > 1$ incorporate partial contact loss, and any other nonlinearity present in the force-deflection function, into the equation of motion. Static finite element analysis at many points in a tooth mesh cycle is one effective way to compute the force-deflection function considering partial contact loss and Hertz contact nonlinearity. Commercial software can do this accurately.

Independence of Total Contact Loss from Applied Torque

The analysis to this point helps explain the observation in [8, 12, 65, 67, 86] that increasing the applied torque does not reduce the contact loss near primary resonance in unmodified gears, that is, if contact loss occurs at one torque it will occur at any other torque. Figure 4.2 shows dimensional, mean-removed excitations from an unmodified and a modified gear pair. The dimensional mean removed excitation $B_0(t) - F_0$ and the mean deflection x_m for unmodified gears are almost directly proportional to the applied torque. The modified gears show no such proportionality. The first harmonic of the non-dimensional excitation $\alpha_{0,1}$ is the dominant driver of vibrations near primary resonance. This quantity from the unmodified and modified gear pairs is shown in Figure 4.3. Changing the applied torque does not change the first harmonic of the excitation for the unmodified gear pair much, but it dramatically changes this quantity for the modified gear pair. In other words, the first harmonic of the excitation is sensitive to torque for modified gears, but insensitive to torque for unmodified gears. Because the first harmonic of the non-dimensional excitation $\alpha_{0,1}$

from unmodified gears is similar for any applied torque, the applied torque has no effect upon the non-dimensional response or the presence of contact loss. This mathematical explanation translates into a physical explanation as follows. In unmodified gears, a higher torque nearly linearly increases both: a) the excitation and so the vibration amplitude, and b) the threshold of vibration amplitude needed to trigger contact loss. As a result, the occurrence of contact loss remains independent of the applied torque.

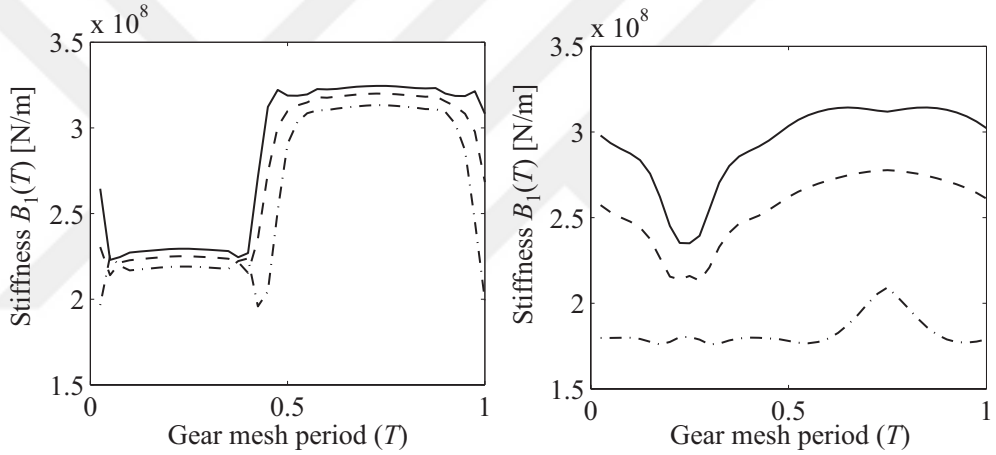

Figure 4.1: Dimensional gear mesh stiffness at 50 N-m (dash-dot line), 150 N-m (dashed line), and 250 N-m (solid line) using finite element analysis. a) Unmodified spur gear pair from [46] ($ICR = 1.37$). b) Modified spur gear pair from [47] (tip relief starts at 22.2 deg).

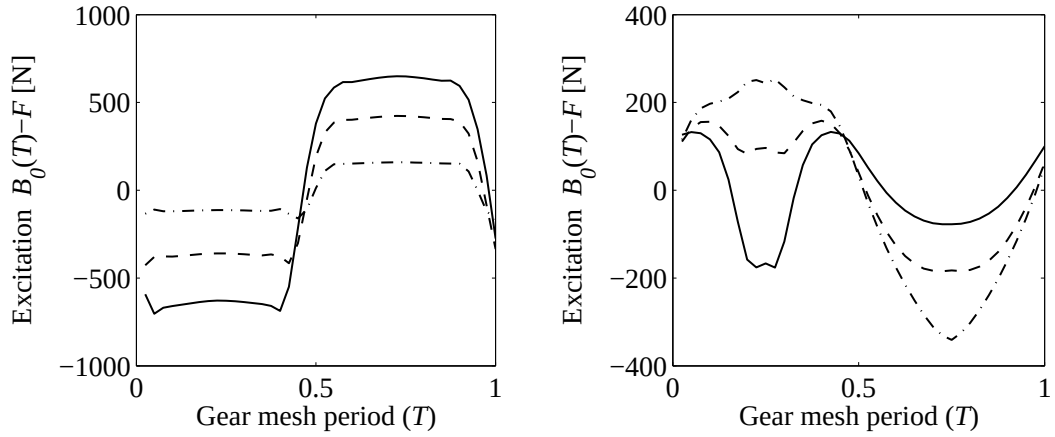

(a) (b)

Figure 4.2: Dimensional mean-removed excitation levels from the gears in Figure 4.1 at 50 N-m (dash-dot line), 150 N-m (dashed line), and 250 N-m (solid line) using finite element analysis. a) Unmodified spur gear pair. b) Modified spur gear pair.

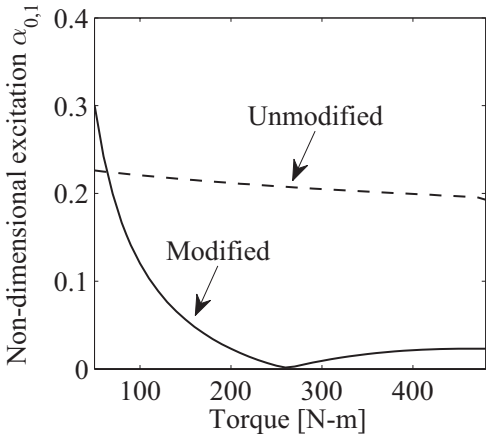

Figure 4.3: The first harmonic of non-dimensional excitation from the unmodified and modified gears with varying applied torque. The gears are the same as in Figure 4.1.

Table 4.1: Summary of non-dimensional parameters and their physical interpretation considering gear and sphere/half-space contact vibrations.

Parameter	**Definition**	**Source in gears**	**Source in sphere/half-space contact**
$\alpha_{0,0}$	Mean applied load Acts only when contact is lost	Constant mesh force	Sphere weight and constant load
$\alpha_{0,r}$ $r > 0$	Harmonics of parametric excitation from force-deflection function	Periodic change in the number of contacting teeth	Zero
$\alpha_{1,0}$	Linear mean stiffness	Linearized gear mesh stiffness at the operating torque	Linearized Hertz contact stiffness at the operating force
$\alpha_{1,r}$ $r > 0$	Harmonics of linear time dependent stiffness	Periodic change in the number of contacting teeth	Zero
$\alpha_{i,0}$	Nonlinear stiffness	Partial contact loss, nonlinear Hertz contact, etc.	Nonlinear Hertz contact
$\alpha_{i,r}$ $r > 0$	Harmonics of time dependent nonlinear stiffness	Periodic changes in partial contact loss, Hertz contact, etc.	Zero
e_r	Harmonics of unloaded deflection	Fluctuating unloaded transmission error	Zero
q_r	Harmonics of external excitation	Pulsations in applied torque (not analyzed in this work)	Shaker
d	Mean deflection	Mean loaded transmission error	Mean loaded contact deflection
Ω_f	Parametric excitation frequency of $f(x,t)$	Periodic change in the number of contacting teeth	Zero
Ω_F	External excitation frequency of $F(t)$	Pulsations in applied torque (not analyzed in this work)	Shaker

4.3 Analysis Method

4.3.1 Dynamic Response Near Primary Resonance

This section presents approximate analytical solutions of Eqs. (4.11) and (4.12) near the primary resonance region using the method of multiple scales. To unify the analysis, we consider that parametric and external excitations are both present and their frequencies are equal and close to the natural frequency, $\Omega = \Omega_f = \Omega_F \approx 1$. The reason for setting $\Omega_f = \Omega_F$ is to keep the length of the closed-form solution to a minimum because in gear vibrations periodic external torque excitation is not modeled here, and in sphere/half-space contact vibrations parametric excitation does not exist; thus there is no reason to consider $\Omega_f \neq \Omega_F$. Following [75] to expand u, T, and the forcing frequency Ω near the primary resonance gives

$$\begin{aligned} u(T,\epsilon) &= u_0(T_0,T_1,T_2) + \epsilon u_1(T_0,T_1,T_2) + \epsilon^2 u_2(T_0,T_1,T_2) \\ T_n &= \epsilon^n T, \quad \Omega = 1 + \sigma = 1 + \epsilon\hat{\sigma} \end{aligned} \tag{4.17}$$

The small parameter ϵ is a detuning parameter such that the excitation frequency is close to the natural frequency. The separation function in Eq. (4.12) is rewritten as $C = 1 + H$ where

$$H(u,t) = \frac{1}{2}\text{sgn}\left[u + 1 - \sum_{r=1}^{p} e_r \cos(rT - \psi_r)\right] - \frac{1}{2} \tag{4.18}$$

This allows p contact losses per period. Fourier expansion of $H(u,t)$ is admissible because, like $u(t)$, it has period 2π, giving

$$H = \Delta_0 + \sum_{r=1}^{N} \Delta_r \cos(rT_0 - \nu_r) \tag{4.19}$$

The quantities Δ_0 and Δ_r depend on $u(t)$ and are not yet known. Arbitrarily many harmonics can be used to represent the separation function H, but N must not be

less than the number of contact losses per period, $N \geq p$. These steps turn contact loss into a form manageable by the method of multiple scales [65, 67, 74, 134].

The $O(\epsilon)$ parameters are

$$\alpha_{0,1} = \epsilon\hat{\alpha}_{0,1},\ \alpha_{2,0} = \epsilon\hat{\alpha}_{2,0},\ \alpha_{3,0} = \epsilon\hat{\alpha}_{3,0},\ q_1 = \epsilon\hat{q_1},\ \mu = \epsilon\hat{\mu},\ \sigma = \epsilon\hat{\sigma},\ \Delta_0 = \epsilon\hat{\Delta}_0 \quad (4.20)$$

These orderings reflect the assumption that the nonlinearities, forcing, and damping are small. The mean value Δ_0 of the separation function H is ordered by assuming that the duration of contact loss is small compared to the period of vibration. Furthermore, all harmonics are assumed one order smaller than the corresponding mean values. This gives the $O(\epsilon^2)$ parameters as

$$\alpha_{2,1} = \epsilon^2\hat{\alpha}_{2,1}, \quad \Delta_1 = \epsilon^2\hat{\Delta}_1, \quad \Delta_2 = \epsilon^2\hat{\Delta}_2 \quad (4.21)$$

We consider up to the third order polynomial approximation of the nonlinear force-deflection function, that is, $\alpha_{i,r} \approx 0$ for $i \geq 4$, and the first harmonic of the periodically varying force-deflection function, that is, $\alpha_{i,r} \approx 0$ for $r \geq 2$. Parametric instability due to the first harmonic of the linear stiffness variation $\alpha_{1,1}$ is possible, but this needs to be treated separately. The third and higher harmonics of the separation function (Δ_r for $r \geq 3$) and excitations $\alpha_{0,r}$ and q_r for $r \geq 2$ do not contribute to the solution, so they are excluded from subsequent equations for brevity.

Substitution of Eq. (4.17) into Eq. (4.11) and combining like orders of ϵ gives the perturbation equations

$$D_0^2 u_0 + u_0 = 0 \quad (4.22)$$

$$\begin{aligned} D_0^2 u_1 + u_1 = &-2D_0 D_1 u_0 - \hat{\alpha}_{2,0} u_0^2 - \hat{\alpha}_{3,0} u_0^3 - 2\hat{\mu} D_0 u_0 - \hat{\Delta}_0 \left(u_0 + \alpha_{0,0}\right) \\ &- \frac{\hat{\alpha}_{0,1}}{2}\left(e^{iT_0} + e^{-iT_0}\right) + \frac{\hat{q}_1}{2}\left[e^{i(T_0-\rho_1)} + e^{-i(T_0-\rho_1)}\right] \end{aligned} \quad (4.23)$$

$$
\begin{aligned}
D_0^2 u_2 + u_2 = & -2\hat{\mu}(D_1 u_0 + D_0 u_1) - 2D_0 D_1 u_1 - 2D_0 D_2 u_0 - D_1^2 u_0 - 2\hat{\alpha}_{2,0} u_0 u_1 \\
& - (u_1 + \hat{\alpha}_{2,0} u_0^2 + \hat{\alpha}_{3,0} u_0^3)\hat{\Delta}_0 - 3\hat{\alpha}_{3,0} u_0^2 u_1 \\
& - \frac{\hat{\alpha}_{0,1}\hat{\Delta}_0}{2}\left(e^{iT_0} + e^{-iT_0}\right) - \frac{(\alpha_{0,0} + u_0)\hat{\Delta}_1}{2}\left[e^{i(T_0 - \nu_1)} + e^{-i(T_0 - \nu_1)}\right] \\
& - \frac{(\alpha_{0,0} + u_0)\hat{\Delta}_2}{2}\left[e^{i(2T_0 - \nu_2)} + e^{-i(2T_0 - \nu_2)}\right] - \frac{\hat{\alpha}_{2,1} u_0^2}{2}\left[e^{i(T_0 - \phi_{2,1})} + e^{-i(T_0 - \phi_{2,1})}\right]
\end{aligned}
\tag{4.24}
$$

where $D_i = \dfrac{\partial}{\partial T_i}$. The general solution of Eq. (4.22) is

$$
u_0 = A(T_1, T_2)e^{iT_0} + \bar{A}(T_1, T_2)e^{-iT_0} \tag{4.25}
$$

Substitution of Eq. (4.25) into the first order equation (4.23) yields secular terms that must be eliminated for u_0 to be periodic, giving the condition

$$
2iD_1 A + A\left[2i\hat{\mu} + \hat{\Delta}_0 + 3\hat{\alpha}_{3,0} A^2 \bar{A}\right] + \frac{\hat{\alpha}_{0,1}}{2} e^{i\hat{\sigma}T_1} - \frac{\hat{q}_1}{2} e^{i(\hat{\sigma}T_1 - \rho_1)} = 0 \tag{4.26}
$$

Transforming to polar coordinates by setting $A = \frac{1}{2} a e^{i\beta}$, $\beta = \hat{\sigma}T_1 - \gamma$, with $a, \gamma \in \mathbb{R}$ gives the real and imaginary parts of Eq. (4.26) as

$$
\begin{aligned}
a D_1 \gamma &= a\hat{\sigma} - \frac{1}{2} a\hat{\Delta}_0 - \frac{3}{8}\hat{\alpha}_{3,0} a^3 - \frac{1}{2}\hat{\alpha}_{0,1}\cos\gamma + \frac{1}{2}\hat{q}_1 \cos(\gamma - \rho_1) \\
D_1 a &= -\hat{\mu} a - \frac{\hat{\alpha}_{0,1}}{2}\sin\gamma + \frac{1}{2}\hat{q}_1 \sin(\gamma - \rho_1)
\end{aligned}
\tag{4.27}
$$

First Order Perturbation

If the process is terminated at the first order perturbation, only Eq. (4.27) is considered. The steady state solutions of Eq. (4.25) result from $D_1 a = 0$, $D_1 \gamma = 0$ in Eq. (4.27). This gives, after use of Eq. (4.20), the frequency-amplitude relation cast in terms of the original parameters independent of ϵ as

$$
\begin{aligned}
a\sigma - \frac{1}{2} a\Delta_0 - \frac{3}{8}\alpha_{3,0} a^3 - \frac{1}{2}\alpha_{0,1}\cos\gamma + \frac{1}{2} q_1 \cos(\gamma - \rho_1) &= 0 \\
-\mu a - \frac{1}{2}\alpha_{0,1}\sin\gamma + \frac{1}{2} q_1 \sin(\gamma - \rho_1) &= 0
\end{aligned}
\tag{4.28}
$$

These two equations can be combined by eliminating γ, giving

$$\mu^2 a^2 + \left(a\sigma - \frac{1}{2}\Delta_0 a - \frac{3}{8}\alpha_{3,0} a^3 \right)^2 - \frac{\alpha_{0,1}^2 + q_1^2}{4} + \frac{\alpha_{0,1} q_1}{2} \cos\rho_1 = 0 \tag{4.29}$$

Many parameters ($\alpha_{0,0}$, $\alpha_{2,0}$, $\alpha_{2,1}$, $\phi_{2,1}$, Δ_1, Δ_2, ν_1, and ν_2) do not appear in Eq. (4.28) and only contribute through the second order perturbation. After calculation of the general solution of Eq. (4.23), the approximate solution is constructed from $u = u_0 + \epsilon u_1 + O(\epsilon^2)$, giving

$$u = a\cos(T_0 - \gamma) + \frac{\alpha_{2,0} a^2}{2}\left[\frac{1}{3}\cos(2T_0 - 2\gamma) - 1\right] + \frac{\alpha_{3,0} a^3}{32}\cos(3T_0 - 3\gamma) - \alpha_{0,0}\Delta_0 + O(\epsilon^2) \tag{4.30}$$

Second Order Perturbation

Proceeding to the second order perturbation, substitution of Eq. (4.30) into Eq. (4.24) yields secular terms that need to be eliminated for u_1 to have a periodic solution, giving the condition

$$\begin{aligned} &D_1^2 A + 2iD_2 A + 2\mu D_1 A - \frac{10}{3}\hat{\alpha}_{2,0}^2 A\bar{A} + \frac{3}{8}\hat{\alpha}_{3,0}^2 A^3 \bar{A}^2 \\ &+ \hat{\Delta}_0 \left(\frac{\hat{\alpha}_{0,1}}{2} e^{i\hat{\sigma}T_1} - 2A\alpha_{0,0}\hat{\alpha}_{2,0} + 3A^2\bar{A}\hat{\alpha}_{3,0} \right) \\ &+ \frac{\alpha_{0,0}\hat{\Delta}_1}{2} e^{i(\sigma T_1 - \nu_1)} + \frac{A^2\hat{\alpha}_{2,1}}{2} e^{-i(\hat{\sigma}T_1 - \phi_{2,1})} + \frac{\bar{A}\hat{\Delta}_2}{2} e^{i(2\hat{\sigma}T_1 - \nu_2)} + A\bar{A}\hat{\alpha}_{2,1} e^{i(\hat{\sigma}T_1 - \phi_{2,1})} = 0 \end{aligned} \tag{4.31}$$

Substitution of $D_1 A$ from Eq. (4.26) into Eq. (4.31) and use of the polar coordinates $a(T_1, T_2)$ and $\gamma(T_1, T_2)$ give the real and imaginary parts of Eq. (4.31) as

$$
\begin{aligned}
aD_2\gamma = {} & [\hat{\alpha}_{0,1}\cos\gamma - \hat{q}_1\cos(\gamma-\rho_1)]\left(\frac{3}{32}\hat{\alpha}_{3,0}a^2 + \frac{1}{4}\hat{\sigma}\right) - \frac{3}{8}\hat{\Delta}_0\hat{\alpha}_{0,1}\cos\gamma + \frac{1}{4}\hat{\mu}\hat{\alpha}_{0,1}\sin\gamma \\
& - \frac{1}{4}\hat{\mu}\hat{q}_1\sin(\gamma-\rho_1) - \frac{1}{2}\alpha_{0,0}\hat{\Delta}_1\cos(\nu_1-\gamma) \\
& - \frac{1}{4}\hat{\Delta}_2 a\cos(\nu_2-2\gamma) - \frac{3}{8}\hat{\alpha}_{2,1}a^2\cos(\Phi_{2,1}-\gamma) \\
& + \frac{1}{8}\Delta_0^2 a - \frac{3}{16}\hat{\alpha}_{3,0}\hat{\Delta}_0 a^3 + \frac{1}{2}\hat{\mu}^2 a + \frac{15}{256}a^5\hat{\alpha}_{3,0}^2 + a\hat{\alpha}_{2,0}\alpha_{0,0}\hat{\Delta}_0 + \frac{5}{12}a^3\hat{\alpha}_{2,0}^2 \\
D_2 a = {} & [\hat{\alpha}_{0,1}\sin\gamma - \hat{q}_1\sin(\gamma-\rho_1)]\left(\frac{9}{32}\hat{\alpha}_{3,0}a^2 + \frac{1}{4}\hat{\sigma}\right) - \frac{3}{8}\hat{\Delta}_0\hat{\alpha}_{0,1}\sin\gamma - \frac{1}{4}\hat{\mu}\hat{\alpha}_{0,1}\cos\gamma \\
& + \frac{1}{4}\hat{\mu}\hat{q}_1\cos(\gamma-\rho_1) + \frac{3}{8}\hat{\mu}\hat{\alpha}_{3,0}a^3 + \frac{1}{2}\alpha_{0,0}\hat{\Delta}_1\sin(\nu_1-\gamma) \\
& + \frac{1}{4}\hat{\Delta}_2 a\sin(\nu_2-2\gamma) + \frac{1}{8}\hat{\alpha}_{2,1}a^2\sin(\Phi_{2,1}-\gamma)
\end{aligned}
\tag{4.32}
$$

Steady-state vibration requires $D_1 a = D_1\gamma = 0$ in Eq. (4.27) and $D_2 a = D_2\gamma = 0$ in Eq. (4.32). Combination of the real and imaginary parts of Eqs. (4.27) and (4.32) according to the reconstitution method [68, 134], substitution of $D_1 a = D_1\gamma = 0$ into Eq. (4.27) and $D_2 a = D_2\gamma = 0$ into Eq. (4.32), and use of Eqs. (4.20) and (4.21) in

that sequence give the frequency-amplitude relations

$$
\begin{aligned}
&a\sigma - \frac{\Delta_0}{2}a - \frac{3\alpha_{3,0}a^3}{8} - \frac{\alpha_{0,1}}{2}\cos\gamma + \frac{q_1}{2}\cos(\gamma-\rho_1) + \Bigg\{\frac{1}{4}\mu\alpha_{0,1}\sin\gamma - \frac{1}{4}\mu q_1\sin(\gamma-\rho_1) \\
&+ [\alpha_{0,1}\cos\gamma - q_1\cos(\gamma-\rho_1)]\left(\frac{3}{32}\alpha_{3,0}a^2 + \frac{1}{4}\sigma\right) - \frac{3}{8}\Delta_0\alpha_{0,1}\cos\gamma \\
&- \frac{1}{2}\alpha_{0,0}\Delta_1\cos(\nu_1-\gamma) - \frac{1}{4}\Delta_2 a\cos(\nu_2-2\gamma) - \frac{3}{8}\alpha_{2,1}a^2\cos(\Phi_{2,1}-\gamma) \\
&+ \frac{1}{8}\Delta_0^2 a - \frac{3}{16}\alpha_{3,0}\Delta_0 a^3 + \frac{1}{2}\mu^2 a + \frac{15}{256}a^5{\alpha_{3,0}}^2 + a\alpha_{2,0}\alpha_{0,0}\Delta_0 + \frac{5}{12}a^3{\alpha_{2,0}}^2\Bigg\} = 0 \\
&-\mu a - \frac{1}{2}\alpha_{0,1}\sin\gamma + \frac{1}{2}q_1\sin(\gamma-\rho_1) + \Bigg\{-\frac{1}{4}\mu\alpha_{0,1}\cos\gamma + \frac{1}{4}\mu q_1\cos(\gamma-\rho_1) \\
&+ [\alpha_{0,1}\sin\gamma - q_1\sin(\gamma-\rho_1)]\left(\frac{9}{32}\alpha_{3,0}a^2 + \frac{1}{4}\sigma\right) - \frac{3}{8}\Delta_0\alpha_{0,1}\sin\gamma \\
&+ \frac{3}{8}\mu\alpha_{3,0}a^3 + \frac{1}{2}\alpha_{0,0}\Delta_1\sin(\nu_1-\gamma) + \frac{1}{4}\Delta_2 a\sin(\nu_2-2\gamma) + \frac{1}{8}\alpha_{2,1}a^2\sin(\Phi_{2,1}-\gamma)\Bigg\} = 0
\end{aligned}
\tag{4.33}
$$

from which a and γ can be solved. The expressions outside of the brackets are the first order perturbation solution, and the expressions inside the brackets are the second order corrections.

Separation

The quantities Δ_r and ν_r in Eq. (4.19) are found using the separation instants T_i. These separation instants are solved by substitution of u from Eq. (4.30) into Eq. (4.18) for $H = -1$ (i.e., $C = 0$). For arbitrarily many contact losses per period p, the solutions T_i, $i = 1, \ldots, 2p+1$, mark the instants when contact is lost or re-established. Let H_i denote whether there is contact ($H_i = 0$) or not ($H_i = -1$) when $T_i \le T < T_{i+1}$. The Fourier coefficients and phase angles of the separation function H in Eq. (4.19) are then

$$\Delta_0 = \frac{1}{2\pi}\sum_{i=1}^{2p}(T_{i+1} - T_i)\,H_i \tag{4.34}$$

$$\Delta_r = \sqrt{\Delta_{r,a}^2 + \Delta_{r,b}^2}, \quad \nu_r = \tan^{-1}\left(\Delta_{r,b}, \Delta_{r,a}\right), \; r = 1, \ldots, N \tag{4.35}$$

$$\Delta_{r,a} = \frac{1}{r\pi} \sum_{i=1}^{2p} \left(\sin rT_{i+1} - \sin rT_i\right) H_i, \; r = 1, \ldots, N \tag{4.36}$$

$$\Delta_{r,b} = -\frac{1}{r\pi} \sum_{i=1}^{2p} \left(\cos rT_{i+1} - \cos rT_i\right) H_i, \; r = 1, \ldots, N \tag{4.37}$$

The perturbation solution considers a maximum of $N = 2$ because harmonics of H higher than the second, i.e., Δ_r for $r > 2$ in Eq. (4.19), do not yield secular terms. This limits contact loss to twice-per-period because $N \geq p$. Even when the contact loss is limited to twice-per-period, finding the separation instants T_i requires solving Eq. (4.18) for $p = 2$. Finding a closed-form solution is not feasible unless: a) contact loss occurs once per period ($p = 1$), and b) the mean change in solution u due to contact loss does not affect when contact loss starts and ends ($\alpha_{0,0}\Delta_0 = 0$). Adopting these assumptions gives the closed-form expressions

$$\begin{aligned} &\Delta_0 = -1 + \frac{\tau}{\pi}, \quad \Delta_r = \frac{2}{r\pi} \sin r\tau \\ &\nu_r = r \tan^{-1}\left(-a \sin\gamma + e_1 \sin\psi_1, a\cos\gamma - e_1 \cos\psi_1\right), \; r = 1, 2 \end{aligned} \tag{4.38}$$

$$\tau = \cos^{-1}\left(\frac{-1 + \alpha_{2,0} a/2}{\sqrt{\left(a\cos\gamma - e_1\cos\psi_1\right)^2 + \left(a\sin\gamma - e_1\sin\psi_1\right)^2}}\right) \tag{4.39}$$

The numerical solution for Δ_0, Δ_r, and ν_r using Eqs. (4.34) and (4.35) is computationally demanding. To save computation when analyzing a system with the second order perturbation solution Eq. (4.33), we use a coarse frequency resolution across the frequency range of interest to confirm that contact loss occurs once per period using numerical solutions of Eqs. (4.34) and (4.35). Once confirmed the analytical expressions in Eqs. (4.38) and (4.39) are used. The analytical expressions in Eqs. (4.38)

and (4.39) and numerical solution of Eqs. (4.34) and (4.35) give almost identical results for the cases analyzed in this work, so the presented results use the analytical expressions.

The vibration amplitude and frequency at the onset of total contact loss can be found from the foregoing analytical solution. Just before the onset of total contact loss, the mean value of the separation function and its harmonics are zero and $\Delta_0 = \Delta_r = 0$ in Eq. (4.38). This gives $\tau = \pi$. Substitution of $\tau = \pi$ into Eq. (4.39) gives the amplitude at the onset of total contact loss as

$$a = \frac{4e_1\cos(\gamma-\psi_1) - 2\alpha_{2,0} \pm 2\sqrt{e_1^2\alpha_{2,0}^2 + 4 - 4e_1^2\sin^2(\gamma-\psi_1) - 4e_1\alpha_{2,0}\cos(\gamma-\psi_1)}}{4-\alpha_{2,0}^2} \tag{4.40}$$

Substitution of a from Eq. (4.40) and $\Delta_0 = \Delta_r = 0$ into (4.33) gives the frequency σ and the phase γ at the onset of total contact loss. The closed-form solution is lengthy using the second order perturbation solution, but a compact expression can be obtained using the first order perturbation solution. The first order does not consider quadratic nonlinearity and unloaded fluctuations (they do not yield secular terms), so $\alpha_{2,0} = e_1 = 0$. Subsequently, Eq. (4.40) reveals that $a = 1$ initiates total contact loss. Substitution of $a = 1$ and $\Delta_0 = 0$ into Eq. (4.29) gives the two frequencies where total contact loss starts as

$$\sigma = \pm\sqrt{\frac{\alpha_{0,1}^2 + q_1^2}{4} - \mu^2 - \frac{\alpha_{0,1}q_1}{2}\cos\rho_1} + \frac{3}{8}\alpha_{3,0} \tag{4.41}$$

Key Points from the Analytical Solution

1. The first order perturbation gives the frequency amplitude relation by Eq. (4.29). It considers only the cubic nonlinearity $\alpha_{3,0}$ and the mean reduction of stiffness due to total contact loss Δ_0.

2. The second order perturbation solution gives the frequency amplitude relation by Eq. (4.33). It considers quadratic nonlinearities ($\alpha_{2,0}$, $\alpha_{2,1}$, $\phi_{2,1}$), and cubic nonlinearity ($\alpha_{3,0}$). The mean value of the separation (Δ_0) and its first two harmonics (Δ_1, Δ_2) with associated phase angles (ν_1, ν_2) contribute. In gears and sphere/half-space contact alike, these quantities account for total contact loss.

3. The mean value (Δ_0) and the first two harmonics (Δ_1, Δ_2) of the separation function and their phase angles (ν_1, ν_2) are found from the perturbation equations numerically from Eqs. (4.34) and (4.35) or analytically from Eqs. (4.38), (4.39) when contact loss is limited to once per period ($p = 1$). Both harmonics are crucial for an accurate response as the upcoming results will show.

4. When the expression inside $\cos^{-1}$ in Eq. (4.39) is not in the range $[-1, 1]$, total contact loss does not occur. The amplitude and frequency at onset of contact loss is analytically given by Eq. (4.41) from the first order perturbation. The second order approximation of the amplitude at onset of contact loss is found from Eq. (4.40) and the frequencies can be solved by substitution of that amplitude into Eq. (4.33).

4.3.2 Stability

The amplitude and phase evaluation Eqs. (4.27) and (4.32) linearized about a stationary point (a, γ) yields the matrix form

$$\frac{\mathrm{d}}{\mathrm{d}T}\begin{pmatrix} a \\ \gamma \end{pmatrix} = \mathbf{J}\begin{pmatrix} a \\ \gamma \end{pmatrix} \tag{4.42}$$

where the matrix **J** denotes the Jacobian. The solution is unstable if any eigenvalues of **J** have a positive real part. The algebraic expression for **J** is prohibitively long and provides no practical insight. For these reasons, the stability is found numerically from the Jacobian matrix **J** at the stationary points.

4.4 Results

In this section, dynamic response of the equation of motion Eq. (4.11) obtained using the perturbation solution in Eq. (4.30) is compared with sphere/half-space contact and gear vibration experiments from the literature, numerical integration, and the linearized solution. The first order perturbation solution is found from Eq. (4.29), and the second order perturbation solution is found from Eq. (4.33).

4.4.1 Key Regions in Dynamic Response and Comparison with Numerical Solution

Independent of the physical system analyzed, there are four possible distinct regions in the nonlinear response. These regions are common to both gear vibrations and sphere/half-space contact vibrations. To investigate the characteristics of these four regions, time domain numerical integration and the second order perturbation solution of an example system is shown in Figure 4.4. The linear time-invariant solution (only linear stiffness and external excitation exist, $\alpha_{1,0}, \alpha_{0,1} \neq 0$) is plotted to provide a comparison: **Region 1**: The linear and nonlinear solutions give almost identical responses. The response is relatively small. There is no contact loss, and nonlinear terms negligibly affect the response.

Region 2: The nonlinear solution deviates significantly from the linear solution as the vibration amplitude grows. This region does not exist, i.e., becomes identical

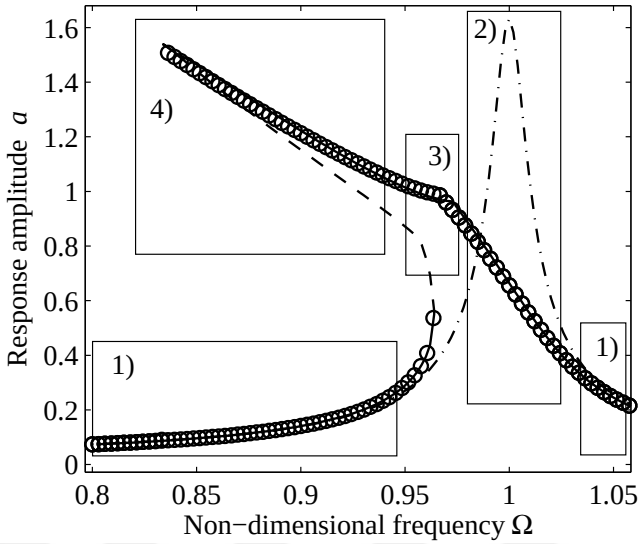

Figure 4.4: Dynamic response of equation of motion (4.11)-(4.12) using second order perturbation and numerical integration. Parameters are: $\alpha_{0,1} = 2/75$, $\alpha_{0,0} = 2/3$, $\alpha_{2,0} = 1/4$, $\alpha_{3,0} = -1/24$, $e_1 = 0.1$, $\psi_1 = 0$, $\alpha_{2,1} = 0$, $\mu = 0.0082$. Important regions of solutions are marked with 1) through 4). (Stable perturbation solution: solid line, unstable perturbation solution: dashed line, numerical integration: circles, linear solution: dash-dot line).

to region 1, if $\alpha_{2,0} = 0$ and $\alpha_{3,0} = 0$. Although the contact is maintained, this region represents partial contact loss in physical systems, where the nonlinearities are due to a reduction in instantaneous dynamic stiffness. The nonlinear terms $\alpha_{2,0}$, $\alpha_{3,0}$, and the time-dependence $\alpha_{2,1}$, $\phi_{2,1}$ dominate the response.

Region 3: Total contact loss, manifest from the kink in the response at $\Omega = 0.97$, starts in this region. Here $C = 0$. The vibration amplitude a and the frequency of excitation Ω at which total contact loss starts is given by Eq. (4.40). It depends on the quadratic nonlinearity, the fluctuation in the unloaded deflection e_1, and the relative phase angle $\gamma - \psi_1$.

Region 4: Total contact loss occurs. The solution is dominated by the mean reduction in stiffness Δ_0 due to separation, the first two harmonics of the separation function Δ_1, Δ_2, their phase angles ν_1, ν_2, and the mean load $\alpha_{0,0}$. The agreement between the numerical and perturbation solution is excellent, justifying the assumptions in the perturbation solution. The nonlinearities are stronger if the periods of separation become long, which would degrade the agreement somewhat as shown in [8] for a simpler tooth mesh contact model in planetary gears.

4.4.2 Sphere/Half-Space Contact Vibrations

The sphere/half-space contact vibration experiments, given in Figure 5(a) of [69], are compared with the first and second order perturbation solutions in Figure 4.5. The experimental measurements and the second order perturbation solution agree closely, even for strong nonlinearity.

The response around $\Omega \approx 1$ in Figure 4.5 corresponds to region 2 as described in Figure 4.4. The second order perturbation does well, but the first order perturbation is not accurate in this region. This is because the first order perturbation only includes the cubic nonlinear term ($\alpha_{3,0}$), but both the quadratic ($\alpha_{2,0}$) and cubic ($\alpha_{3,0}$) terms contribute to nonlinear response. When either of the $\alpha_{2,0}$ or $\alpha_{3,0}$ terms are set to zero, the second order perturbation solution becomes inaccurate.

The response when $0.73 < \Omega < 0.95$ in Figure 4.5 corresponds to region 4 as described in Figure 4.4. The second order perturbation solution agrees well with the experiment. The slight deviation toward the peak is attributed to the nonlinearity getting stronger. The first order perturbation solution does poorly in this region. It includes only Δ_0, whereas the second order perturbation solution includes several

parameters related to contact loss ($\alpha_{0,0}$, Δ_0, Δ_1, Δ_2, ν_1, and ν_2). When each one of these parameters is individually set to zero in the second order perturbation solution, the response becomes inaccurate. This confirms that $\alpha_{0,0}$, Δ_1, Δ_2, ν_1, and ν_2, which only the second order perturbation can consider, are necessary for obtaining accurate response in the contact loss region.

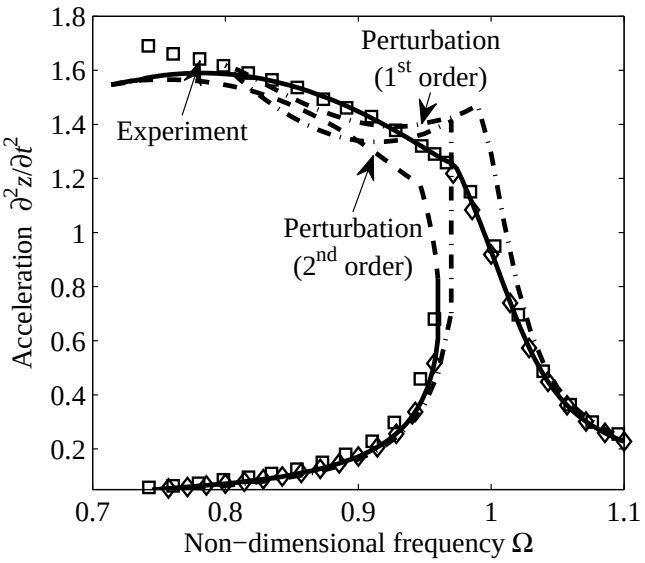

Figure 4.5: Peak-to-peak acceleration $\ddot{z}$ of sphere-plane contact using first and second order perturbation, experiment, and linearized model. Experimental measurements are from Figure 5(a) of [69]. Non-dimensional parameters are $q_1 = 0.08/3$, $\alpha_{0,0} = 2/3$, $\alpha_{2,0} = 2/7$, $\alpha_{3,0} = -1/21$, $\mu = 0.008$. (First order perturbation: dash-dot line, second order perturbation: solid line(stable), dashed line (unstable), experimental measurements: squares (speed-down), diamonds (speed-up)).

4.4.3 Gear Vibrations

Computational Results

Computational dynamic response of a helical gear pair is obtained using the contact algorithm in [23, 24]. That model has been successfully compared against experiments and a specialized finite element/contact mechanics model of gear dynamics. Some elastic behaviors, such as corner contact, radius of curvature effects, buttressing effects,and the coupling between the deflections of adjacent teeth, are neglected in this contact algorithm.

The gear parameters are given in Tables 2.1 and 2.2. The non-dimensional parameters are given in Table 4.2.

The dynamic response of the helical gear pair with profile and lead modifications and the force-deflection function shown in Figure 4.6 is plotted in Figure 4.7. The computational dynamic response and perturbation solution agree throughout most of the operating frequencies. There is a clear difference between the linear and the nonlinear response. Region 2 of Figure 4.4 identifies this type of response. Physically, this difference is attributed to partial contact loss, where some portions of the nominal contact lines separate while the gear mesh as a whole is still engaged. The perturbation solution predicts the nonlinear dynamics arising from partial contact loss.

The investigation of practical gear vibration raises the question of whether all the nonlinear terms ($\alpha_{2,0}$, $\alpha_{3,0}$, $\alpha_{2,1}$, $\phi_{2,1}$) are necessary to obtain an accurate response or not. The importance of these terms are assessed by investigating the perturbation solution when these are set to zero one at a time, as shown in Figure 4.8. The

response becomes inaccurate when any one of them is set to zero; all nonlinear terms are necessary to obtain an accurate response

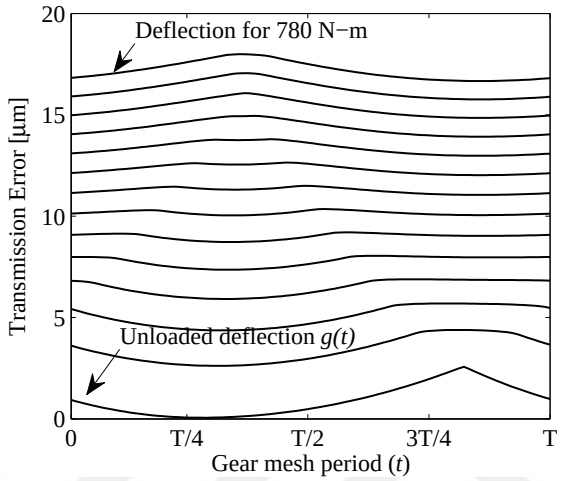

Figure 4.6: Force-deflection function $f(x,t)$ of a helical gear pair obtained by the method of Chapter 2. Tooth surface modifications are: quadratic profile tip and root crown of 10 μm and lead crown of 10 μm on the gear.

Experimental Results

In this section, experimental measurements of rotational vibration of unity ratio gear pairs with profile and lead modifications [47] are compared with the second order perturbation solution. The experimental measurements are available for various tip relief starting roll angles and for different applied torques. The gears in this test rig are sufficiently isolated from the vibrations of the supporting structure to justify use of a single degree-of-freedom oscillator to model the dynamics [11].

The force-deflection function would ideally come from the experimental setup by slowly rotating the gears through a mesh period and measuring transmission error

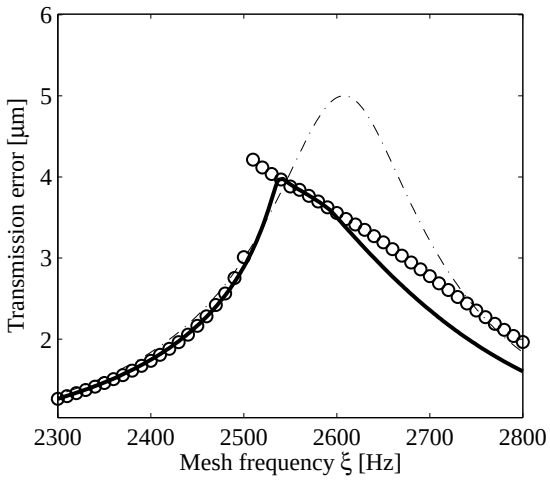

Figure 4.7: Primary resonance of a helical gear pair at 200 N-m using second order perturbation, numerical integration, and the linearized model. The numerical integration results are obtained using the method of Chapter 3. (Stable perturbation solution: solid line, computational data by numerical integration: circles, linear solution: dash-dot line).

at various applied torques. Because these data are not given, the force-deflection function is obtained from finite element analysis [124] of the gears. When the tip relief starts at roll angle 20.9 deg, the force-deflection function calculated by finite element analysis is shown in Figure 4.9 for various torques. Even if the finite element analysis could precisely replicate the elastic behavior of the experimental setup, the crucial gear tooth profile and lead modifications are specified within a manufacturing tolerance (3 μm). These errors can cause a mismatch between the experimental data and perturbation solution. To provide a visual sense of such errors that are *not* associated with the analysis methods of this work, the precision of the experiments (± 1 μm reported in a closely related study [46]) are added to the experimental results in the form of error bars in the upcoming figures.

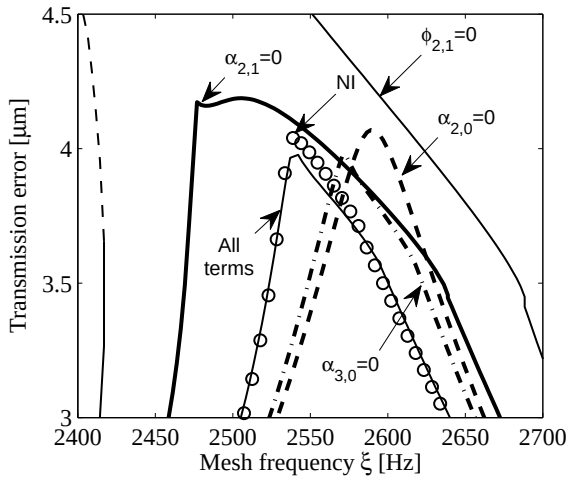

Figure 4.8: Perturbation solution when $\alpha_{2,0}$, $\alpha_{3,0}$, $\alpha_{2,1}$, and $\phi_{2,1}$ are set to zero one at a time are shown. The non-zero parameters are the same as in Figure 4.7. The circles denote numerical integration with no non-zero parameters.

The experimental measurements and the second order perturbation solution for three gear pairs are compared in Figure 4.10 (where the applied torque is 85 N-m and the 10 μm profile modification starts at 20.9 deg), Figure 4.11 (where the applied torque is 170 N-m and the 10 μm profile modification starts at 20.9 deg), and Figure 4.12 (where the applied torque is 170 N-m and the profile 10 μm modification starts at 23.6 deg). Table 4.2 lists the non-dimensional parameters used in these analysis. All gears have 5 μm lead crown modification.

The perturbation solutions agree accurately with the experimental results in all three cases. The onset of total contact loss is manifest by the kinks in the perturbation solution curves. Even in regions without total contact loss the linear response differs from the experimental measurements and perturbation solutions. Region 2 of Figure 4.4 characterizes this type of response. The difference is attributed to partial contact

loss, occurs due to the profile and lead modifications. The good agreement provides experimental evidence that the perturbation solution predicts the nonlinear dynamic response due to partial contact loss.

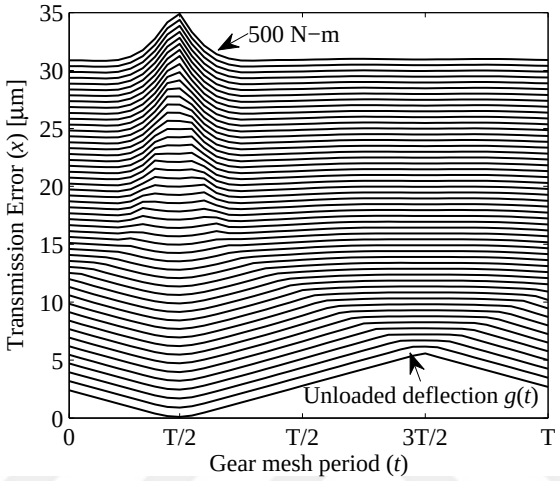

Figure 4.9: Force-deflection function $f(x,t)$ obtained by finite element analysis of a spur gear pair with increasing applied torque. Gear data from [47], linear tip relief of 10 μm starts at 20.9 deg.

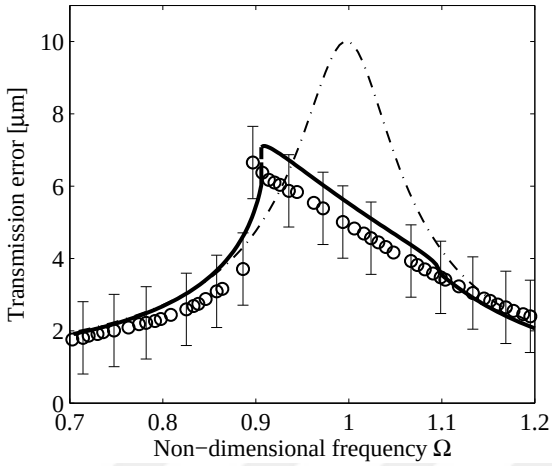

Figure 4.10: Primary resonance of a spur gear pair (tip relief start at 20.9 deg) at 85 N-m using second order perturbation and linearized model. Experimental data are from Figure 3(c) of [47]. (Stable second order perturbation: solid line, unstable second order perturbation solution: dashed line, experimental measurement: circles, linear solution: dash-dot line).

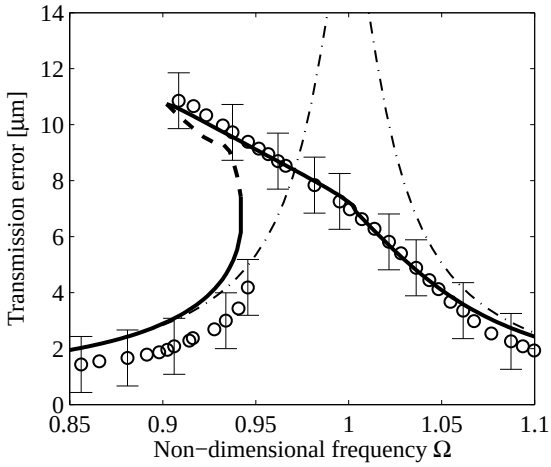

Figure 4.11: Primary resonance of a spur gear pair (tip relief start at 20.9 deg) at 170 N-m using second order perturbation and linearized model. Experimental data are from Figure 3(b) of [47]. (Stable second order perturbation: solid line, unstable second order perturbation solution: dashed line, experimental measurement: circles, linear solution: dash-dot line).

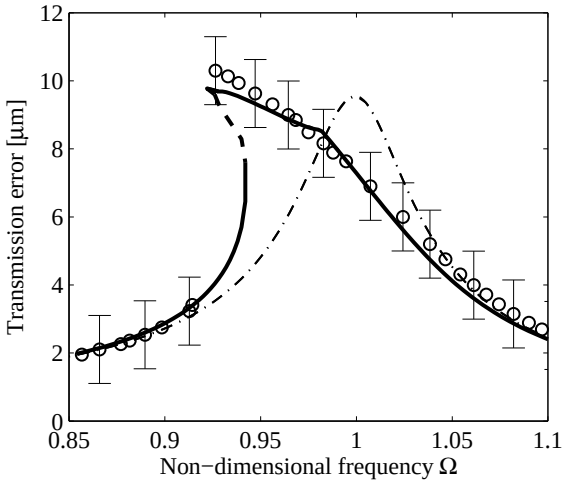

Figure 4.12: Primary resonance of a spur gear pair (tip relief start at 23.6 deg) at 170 N-m using second order perturbation and linearized model. Experimental data are from Figure 3(b) of [47]. (Stable perturbation solution: solid line, unstable perturbation solution: dashed line, experimental measurement: circles, linear solution: dash-dot line).

Table 4.2: Parameters of the analyzed gears in Figures 4.7 through 4.12.

	Figure 4.7	Figure 4.10	Figure 4.11	Figure 4.12
$\alpha_{0,0}$	0.727	0.727	0.716	0.714
$\alpha_{0,1}$	0.069	0.181	0.061	0.058
$\alpha_{2,0}$	0.209	0.213	0.197	0.202
$\alpha_{2,1}$	0.313	0.212	0.118	0.069
$\alpha_{3,0}$	-0.037	-0.034	-0.074	-0.074
$\phi_{2,1}$ [rad]	-2.891	-3.203	-3.228	-0.230
e_1	0.167	0.302	0.185	0.038
ψ_1 [rad]	-3.293	-3.124	-3.124	0.037
μ	0.030	0.050	0.016	0.028
d [μm]	4.350	5.516	9.005	9.201

4.5 Conclusions

This work derives approximate, closed-form analytical solutions for the nonlinear vibration of gear pairs with arbitrary tooth surface modifications. It applies equally to other contact problems described by a specified nonlinear, periodic force-deflection curve. To demonstrate this sphere/half-space contact vibrations are analyzed and compared to experiments. The method of multiple scales provides the analytical perturbation solutions in the primary resonance region.

I The dynamic excitation in gear pairs is mathematically shown to come from the periodicity of the force-deflection function. This periodicity is due to engagement/disengagement of the gear teeth resulting in linear and quadratic mesh stiffness fluctuations that drive the gear vibration.

II The presence of total contact loss in unmodified gears is shown to be independent of applied torque. The reason is this: as the vibration amplitude increases with larger torques, so does the threshold of vibrations needed to trigger total contact loss. This is not true for modified gears.

III The method of multiple scales gives the approximate, closed-form analytical solutions. Comparisons with gear vibration experiments, sphere/half-space contact vibration experiments, and numerical integration verify the analytical solution. The second order perturbation solution is significantly more accurate than the first order perturbation solution, indicating the nonlinearity is strong in the physical experiments.

IV Key regions in the nonlinear response common to both gear and sphere/half-space contact vibrations are:

1 Linear region: Vibration amplitude is relatively low, and the system behaves linearly.

2 Partial contact loss region: The mean stiffness drops due to dynamic displacements but contact is maintained. Partial contact loss in gears occurs when parts of nominal contact lines lose contact although the gear teeth remain engaged. It is most prominent in systems with tooth surface modifications. Quadratic and cubic nonlinearities capture the partial contact loss nonlinearity in modified gears and yield nonlinear dynamic response. In sphere/half-space contact, the dependence of the size of the contact area on dynamic contact load yields this type of nonlinearity.

3 Onset of total contact loss region: Vibrations reach the threshold to cause total contact loss.

4 Total contact loss region: The contact separates fully and the mean load brings the system back into contact. Total contact loss in gears occurs when the gear teeth disengage completely. It is captured by the mean reduction in mesh stiffness and its two harmonics. The amplitude and the frequency at the onset of total contact loss is analytically given and is consistent with experiments.

Chapter 5: Modal Properties of Three-Dimensional Helical Planetary Gears

5.1 Introduction

Knowledge of the modal properties of planetary gears is crucial for developing strategies to reduce vibration. Planetary gear dynamic models are developed in [7, 15, 19, 97]. Lin and Parker show that two-dimensional, spur planetary gears with equally spaced [58] and diametrically opposed [60] planets possess well-defined modal properties. They report all vibration modes belong to one of three categories: 1) Rotational modes where the central members (sun, carrier, and ring) rotate but do not translate. The planet motions are identical. 2) Translational modes with degenerate natural frequencies, where the central members translate but do not rotate. There are well-defined relations between the two independent vibration modes at each natural frequency. 3) Planet modes where only the planets move, and their motions are scalar multiples of the arbitrarily chosen first planet's motion. Kiracofe and Parker [52] prove that a similar categorization applies to compound planetary gears. Wu and Parker [133] prove the modal properties of spur planetary gears having elastically deformable ring gears.

These vibration mode characteristics are crucial in vibration suppression strategies using mesh phasing [62, 95, 97] and eigensensitivity analysis [29, 59] of planetary gears. Schlegel and Mard [95], Seager [97], and Hidaka et al. [33] assert that the vibration of planetary gears is reduced by proper gear mesh phasing. Hidaka et al. [33] experimentally and Kahraman [40] computationally investigate the effectiveness of vibration suppression by planet mesh phasing. Kahraman [40] uses a three-dimensional lumped-parameter model for computations. Blankenship and Kahraman [43] illustrate how some harmonics of the transmission error excitation vanish by adjusting the mesh phasing. Based on the well-defined modal properties of planetary gears, Parker [84] explains how proper mesh phasing suppresses many resonances of translational and rotational modes from certain harmonics of mesh frequency. Ambarisha and Parker [4] explain the vibration suppression of planet modes from mesh phasing.

Finite element analysis is incorporated with elaborate gear contact analysis in [1, 5,8,85,93] to capture the complex dynamic behavior of planetary gears. These studies enable computationally efficient analysis of complex planetary gears and survey the effects of design parameters on dynamic behavior.

Although the vibration modes of two-dimensional planetary gears have been studied, it remains to be seen what the vibration mode characteristics are for helical planetary gears with three-dimensional motion, a three-dimensional gear mesh interface, and the gear-shaft bodies supported by bearings at arbitrary locations along the shafts. A lumped parameter model is formulated to include the tilting and axial motions, thus including all six degrees of freedom for each gear-shaft body. A tilting mesh stiffness augments the gear mesh interface to produce the three-dimensional force and moment transmission.

This study proves that helical planetary gears with equally spaced planets have exactly three types of vibration modes. Unique properties of these vibration modes are given. Compared to two-dimensional spur gear models there are twice as many natural modes, and their properties are different. The modal properties hold for configurations that are asymmetric about the gear plane, such as when the bearings are not equidistant from the gears.

5.2 Planetary Gear Analytical Model

The planetary gear model consists of three central members (the sun, ring, and carrier) and p planets. The gears and the carrier are integrated with their supporting shafts, so that each gear-shaft is a single body. These combined gear-shaft bodies are each mounted on up to two bearings placed at arbitrary axial locations. The sun, ring, and carrier bearings are connected to ground while the planet bearings are connected to the carrier. The gear-shaft bodies and carrier are rigid; the compliant elements are the meshing gear teeth and bearings. Figures 5.1(a) and (b) depict the model with the parameters defining the system geometry. The vibration amplitudes are small, so geometric nonlinearities are neglected.

The indexing conventions $b = s, r, c, 1, \ldots, p$ for the sun, ring, carrier, and the planets, $h = s, r, c$ for the sun, ring, and carrier, and $i = 1, 2, \ldots, p$ for the planets are maintained throughout this work. There are $2p$ gear meshes. Odd numbers are assigned to the sun-planet meshes, and even numbers are assigned to the ring-planet meshes.

The origin is at the undeflected position of the center of the sun. A right handed, orthonormal basis $\{\mathbf{E}\} = \{\mathbf{E}_1, \mathbf{E}_2, \mathbf{E}_3\}$ rotates with the constant carrier angular speed

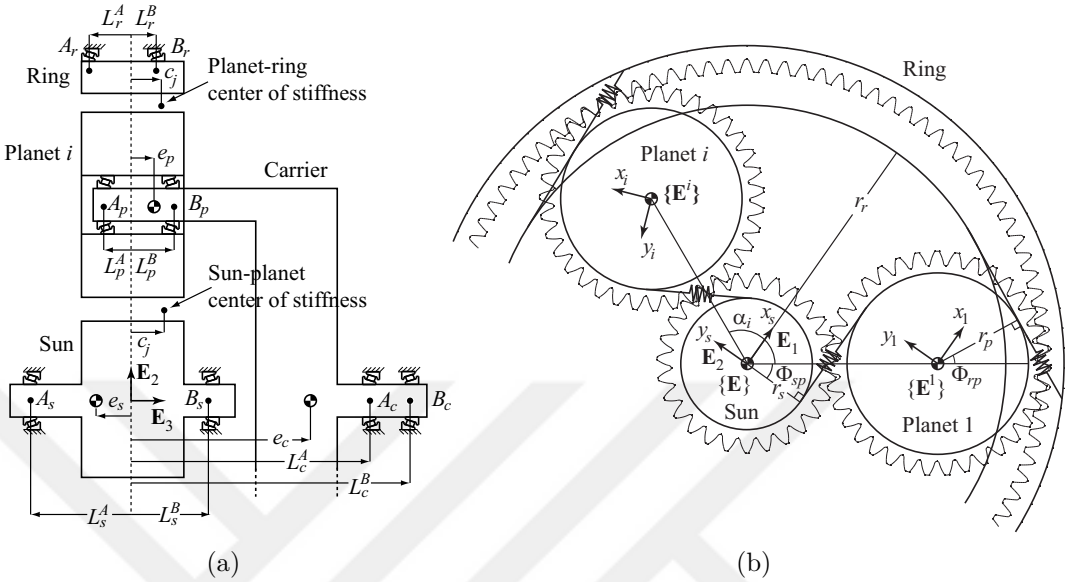

Figure 5.1: Coordinates and dimensions used in the planetary gear model.

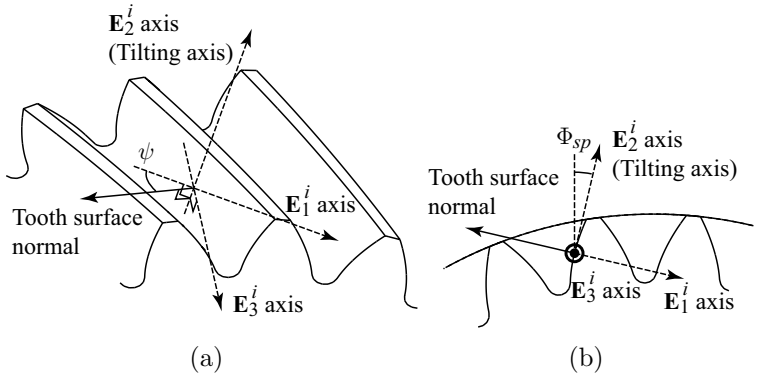

Figure 5.2: Tooth surface normal and the tilting axis for the ith sun-planet mesh. The ith planet gear is shown. ψ is the base helix angle, and Φ_{sp} is the transverse operating pressure angle.

Ω_c. For the central members, translational coordinates x_h, y_h, z_h are assigned to translations along $\mathbf{E}_1$, $\mathbf{E}_2$, and $\mathbf{E}_3$, respectively. Similarly, angular coordinates ϕ_h, θ_h, β_h are assigned to small rotations about $\mathbf{E}_1$, $\mathbf{E}_2$, and $\mathbf{E}_3$, respectively. Translational coordinates for the planets x_i, y_i, z_i are measured from the undeflected position of the centers of the planets in the bases $\{\mathbf{E}^i\} = \{\mathbf{E}^i_1, \mathbf{E}^i_2, \mathbf{E}^i_3\}$ that rotate with the carrier angular speed. The base vector $\mathbf{E}^i_1$ is parallel to the line of action of the ith sun-planet mesh because this selection algebraically simplifies the sun-planet mesh deflections. Angular coordinates ϕ_i, θ_i, β_i for the planets are assigned to rotations about $\mathbf{E}^i_1$, $\mathbf{E}^i_2$, and $\mathbf{E}^i_3$, respectively. Body fixed bases for all the bodies $\{\mathbf{e}^b\} = \{\mathbf{e}^b_1, \mathbf{e}^b_2, \mathbf{e}^b_3\}$ are adopted because the gear mesh deflection expressions are algebraically simpler in these bases.

Axial position quantities in Fig. 5.1(a) are measured from the datum position, which is at the center of the minimum active facewidth F and denoted by the dashed line. Any inactive facewidth is considered as part of the shaft. This setup allows arbitrary axial positioning of gears with different facewidths. Positive planet position angle α_i is measured counter-clockwise from the arbitrarily chosen first planet.

Two linear springs, one translational and one tilting, model the gear mesh interface. The translational stiffness (k_j) accounts for the transmitted force through the gear mesh. Its associated relative translational deflection (δ_j) is in the direction of the tooth surface normal. The tilting stiffness (κ_j) accounts for the moment transmitted through the gear mesh. Its associated angular deflection is about an axis that is in the gear plane and perpendicular to both the line of action $\mathbf{E}^i_1$ and the tooth surface normal. Figure 5.2 shows the line of action $\mathbf{E}^i_1$, the tooth surface normal, and the tilting axis $\mathbf{E}^i_2$ for the ith sun-planet mesh. These two deflections are calculated at a

specified point along the facewidth, called the center of stiffness. The axial position of the center of stiffness is c_j. The translational stiffness, tilting stiffness, and center of stiffness can be reduced from gear tooth contact models, such as [121], averaged over a mesh cycle.

The equations of motion come from Lagrange's equations for unconstrained generalized coordinates. The kinetic and potential energies are

$$\begin{aligned} T &= \frac{1}{2}\sum_{b=1}^{N}\left(\boldsymbol{\omega}_b^T\mathbf{J}_b\boldsymbol{\omega}_b + \dot{\mathbf{r}}_b^T m_b\dot{\mathbf{r}}_b\right), \\ V &= \frac{1}{2}\sum_{b=1}^{N}\left(\mathbf{d}_{A,b}^T\mathbf{K}_{A,b}\mathbf{d}_{A,b} + \mathbf{d}_{B,b}^T\mathbf{K}_{B,b}\mathbf{d}_{B,b}\right) \\ &\quad + \frac{1}{2}\sum_{b=1}^{N}\left(\boldsymbol{\zeta}_{A,b}^T\boldsymbol{\chi}_{A,b}\boldsymbol{\zeta}_{A,b} + \boldsymbol{\zeta}_{B,b}^T\boldsymbol{\chi}_{B,b}\boldsymbol{\zeta}_{B,b}\right) + \frac{1}{2}\sum_{j=1}^{2p}\left(k_j\delta_j^2 + \kappa_j\gamma_j^2\right), \end{aligned} \tag{5.1}$$

where $N = p + 3$ is the number of bodies, $\boldsymbol{\omega}_b$ is the angular velocity, m_b is the mass, $\mathbf{J}_b$ is the inertia tensor, $\dot{\mathbf{r}}_b$ is the velocity vector, $\mathbf{d}_{A,b}$ is the translational bearing deflection vector, $\boldsymbol{\zeta}_{A,b}$ is the angular bearing deflection vector, $\mathbf{K}_{A,b}$ is the bearing stiffness matrix for translation, and $\boldsymbol{\chi}_{A,b}$ is the bearing stiffness matrix for rotation. The translational gear mesh deflection is δ_j; the angular (tilting) gear mesh deflection is γ_j; the translational gear mesh stiffness is k_j; and, the tilting gear mesh stiffness is κ_j.

The angular velocity of the bth body in its corotational basis $\{\mathbf{e}^b\}$ is

$$\boldsymbol{\omega}_b = \left[\dot{\phi}_b - \theta_b\left(\dot{\beta}_b + \Omega_b\right)\right]\mathbf{e}_1^b + \left[\dot{\theta}_b + \phi_b\left(\dot{\beta}_b + \Omega_b\right)\right]\mathbf{e}_2^b + \left[\dot{\beta}_b + \Omega_b - \phi_b\dot{\theta}_b\right]\mathbf{e}_3^b, \tag{5.2}$$

where Ω_b is the constant kinematic rotation speed. The inertia tensor for each body in its principal axes is $\mathbf{J}_b = \mathrm{diag}\,[J_b^x, J_b^y, J_b^z]$ with constant components. All gears are axisymmetric, so $J_b^y = J_b^x$. The velocity vectors of the central members and planets

are

$$\dot{\mathbf{r}}_h = [\dot{x}_h - \Omega_c y_h]\,\mathbf{E}_1 + [\dot{y}_h + \Omega_c x_h]\,\mathbf{E}_2 + \dot{z}_h \mathbf{E}_3, \quad h = s, r, c, \tag{5.3}$$

$$\dot{\mathbf{r}}_i = [\dot{x}_h - \Omega_c\,(y_i - r_s - r_p)]\,\mathbf{E}_1^i + [\dot{y}_i + \Omega_c\,(x_i + \tan\Phi_{sp}(r_s + r_p))]\,\mathbf{E}_2^i + \dot{z}_i \mathbf{E}_3^i \tag{5.4}$$

$$i = 1, 2, \ldots, p,$$

where Φ_{sp} and Φ_{rp} are the sun-planet and ring-planet transverse operating pressure angles.

The bearings are attached to the points A_b and B_b on the left and right sides of the bth body, respectively. The bearing deflection vectors for central members at points A_h and B_h $(h = s, r, c)$ are

$$\mathbf{d}_{A,h} = \left[x_h - \left(e_h + L_h^A\right)\theta_h\right]\mathbf{E}_1 + \left[\left(e_h + L_h^A\right)\phi_h + y_h\right]\mathbf{E}_2 + z_h \mathbf{E}_3, \tag{5.5}$$

$$\mathbf{d}_{B,h} = \left[x_h - \left(e_h - L_h^B\right)\theta_h\right]\mathbf{E}_1 + \left[\left(e_h - L_h^B\right)\phi_h + y_h\right]\mathbf{E}_2 + z_h \mathbf{E}_3, \tag{5.6}$$

where e_h, L_h^A, and L_h^B are the axial positions of the mass centers, bearings A_h, and bearings B_h of the central members. Positive values of e_h and L_b^A are measured from the datum along $\mathbf{E}_3$, and positive values of L_b^B are measured from the datum along $-\mathbf{E}_3$. This sign convention is chosen so that for positive L_b^A and L_b^B the gears are in between the bearings. The bearing deflection vector for the planets is the relative position between the point that is on the carrier and the point that is on the planet shaft. The bearing deflection vectors for the planets at points A_i and B_i are

$$\begin{aligned}
\mathbf{d}_{A,i} = \Big\{ &- \left[y_c + \phi_c(e_s + L_p^A)\right]\sin\alpha_i + \left[\theta_c(e_s + L_p^A) - x_c\right]\cos\alpha_i \\
&- \beta_c(r_p + r_s) + x_i - \theta_i(e_p + L_p^A)\Big\}\mathbf{E}_1^i \\
&+ \Big\{ \left[x_c - \theta_c(e_s + L_p^A)\right]\sin\alpha_i - \left[y_c + \phi_c(e_s + L_p^A)\right]\cos\alpha_i \\
&- \beta_c(r_p + r_s)\tan\Phi_{sp} + y_i + \phi_i(e_p + L_p^A)\Big\}\mathbf{E}_2^i \\
&+ \Big\{ \left[-\phi_c(r_s + r_p)\tan\Phi_{sp} + \theta_c(r_s + r_p)\right]\sin\alpha_i \\
&+ \left[\theta_c(r_s + r_p)\tan\Phi_{sp} + \phi_c(r_s + r_p)\right]\cos\alpha_i + z_i - z_c\Big\}\mathbf{E}_3^i,
\end{aligned} \tag{5.7}$$

$$
\begin{aligned}
\mathbf{d}_{B,i} = \Big\{ & -\left[y_c + \phi_c(e_s - L_p^B)\right]\sin\alpha_i + \left[\theta_c(e_s - L_p^B) - x_c\right]\cos\alpha_i \\
& - \beta_c(r_p + r_s) + x_i - \theta_i(e_p - L_p^B)\Big\}\mathbf{E}_1^i \\
& + \Big\{ \left[x_c - \theta_c(e_s - L_p^B)\right]\sin\alpha_i - \left[y_c + \phi_c(e_s - L_p^B)\right]\cos\alpha_i \\
& - \beta_c(r_p + r_s)\tan\Phi_{sp} + y_i + \phi_i(e_p - L_p^B)\Big\}\mathbf{E}_2^i \\
& + \Big\{ \left[-\phi_c(r_s + r_p)\tan\Phi_{sp} + \theta_c(r_s + r_p)\right]\sin\alpha_i \\
& + \left[\theta_c(r_s + r_p)\tan\Phi_{sp} + \phi_c(r_s + r_p)\right]\cos\alpha_i + z_i - z_c\Big\}\mathbf{E}_3^i.
\end{aligned}
\tag{5.8}
$$

The angular bearing deflection vector is the relative angular displacements of the connected bodies. The angular bearing deflection vectors for the central members and planets at points A_h and A_i are

$$
\boldsymbol{\zeta}_{A,h} = \phi_h\mathbf{E}_1 + \theta_h\mathbf{E}_2 + \beta_h\mathbf{E}_3, \tag{5.9}
$$

$$
\begin{aligned}
\boldsymbol{\zeta}_{A,i} = & \left[\phi_i - \theta_c\sin\alpha_i - \phi_c\cos\alpha_i\right]\mathbf{E}_1^i + \left[\theta_i - \theta_c\cos\alpha_i + \phi_c\sin\alpha_i\right]\mathbf{E}_2^i \\
& + \left[\beta_i - \beta_c\right]\mathbf{E}_3^i.
\end{aligned}
\tag{5.10}
$$

The angular bearing deflection vectors at points B_h and B_i are identical to Eqs. (5.9) and (5.10) for rigid shafts.

The bearings are isotropic in the $\mathbf{E}_1 - \mathbf{E}_2$ plane. There is no coupling between different directions. For all bodies the bearing stiffness matrix for translation is $\mathbf{K}_{A,b} = \text{diag}\left[k_b^A, k_b^A, k_b^{Az}\right]$, and the bearing stiffness matrix for rotation is $\boldsymbol{\chi}_{A,b} = \text{diag}\left[\kappa_b^A, \kappa_b^A, \kappa_b^{Az}\right]$, where the equality of stiffness in the two in-plane translation directions is evident (and similarly for rotation). These stiffness components are in the $\{\mathbf{E}\}$ basis for the central members and in the $\{\mathbf{E}^i\}$ basis for each of the planets.

The translational gear mesh deflection δ_j is the relative compressive deflection at the center of stiffness in the direction normal to the tooth surface. The translational

gear mesh deflection for the sun-planet meshes ($j = 1, 3, 5, \ldots, 2p-1$) is

$$\begin{aligned}\delta_j = &\{[(e_s - c_j)\phi_s + y_s]\cos\psi + r_s\left[\theta_s - \phi_s\tan\Phi_{sp}\right]\sin\psi\}\sin\alpha_i \\ &+ \{[x_s - (e_s - c_j)\theta_s]\cos\psi + r_s\left[\phi_s + \theta_s\tan\Phi_{sp}\right]\sin\psi\}\cos\alpha_i \\ &+ [(e_p - c_j)\theta_i + r_s\beta_s + r_p\beta_i - x_i]\cos\psi \\ &+ [z_i - z_s + r_p(\phi_i + \theta_i\tan\Phi_{sp})]\sin\psi,\end{aligned} \tag{5.11}$$

where ψ is the base helix angle, and the center of stiffness for a gear mesh in the axial direction measured from the datum is c_j. For the ring-planet meshes ($j = 2, 4, \ldots, 2p$) the translational gear mesh deflection is

$$\begin{aligned}\delta_j = &\{r_r\left[(\phi_r - \theta_r\tan\Phi_{rp})\sin(\Phi_{sp}+\Phi_{rp}) - (\theta_r + \phi_r\tan\Phi_{rp})\cos(\Phi_{sp}+\Phi_{rp})\right]\sin\psi \\ &+ [((e_r - c_j)\,\theta_r - x_r)\sin(\Phi_{sp}+\Phi_{rp}) + ((e_r - c_j)\,\phi_r + y_r)\cos(\Phi_{sp}+\Phi_{rp})]\cos\psi\}\sin\alpha_i \\ &-\{r_r\left[(\theta_r + \phi_r\tan\Phi_{rp})\sin(\Phi_{sp}+\Phi_{rp}) + (\phi_r - \theta_r\tan\Phi_{rp})\cos(\Phi_{sp}+\Phi_{rp})\right]\sin\psi \\ &+ [((e_r - c_j)\,\phi_r + y_r)\sin(\Phi_{sp}+\Phi_{rp}) + ((c_j - e_r)\,\theta_r + x_r)\cos(\Phi_{sp}+\Phi_{rp})]\cos\psi\}\cos\alpha_i \\ &+ \{r_p\left[(\phi_i - \theta_i\tan\Phi_{rp})\cos(\Phi_{sp}+\Phi_{rp}) + (\phi_i\tan\Phi_{rp} + \theta_i)\sin(\Phi_{sp}+\Phi_{rp})\right] + z_r - z_i\}\sin\psi \\ &+ \{[(e_p - c_j)\,\theta_i - x_i]\cos(\Phi_{sp}+\Phi_{rp}) + [(c_j - e_p)\,\phi_i - y_i]\sin(\Phi_{sp}+\Phi_{rp}) - r_p\beta_i\}\cos\psi.\end{aligned} \tag{5.12}$$

The angular gear mesh deflection γ_j for the sun-planet and ring-planet meshes is

$$\gamma_j = \phi_s\sin\alpha_i - \theta_s\cos\alpha_i + \theta_i, \quad j = 1, 3, 5, \ldots, 2p-1, \tag{5.13}$$

$$\begin{aligned}\gamma_j = &-\left[\phi_r\cos(\Phi_{sp}+\Phi_{rp}) + \theta_r\sin(\Phi_{sp}+\Phi_{rp})\right]\sin\alpha_i \\ &-\left[\phi_r\sin(\Phi_{sp}+\Phi_{rp}) - \theta_r\cos(\Phi_{sp}+\Phi_{rp})\right]\cos\alpha_i \\ &+\phi_i\sin(\Phi_{sp}+\Phi_{rp}) - \theta_i\cos(\Phi_{sp}+\Phi_{rp}), \quad j = 2, 4, \ldots, 2p.\end{aligned} \tag{5.14}$$

Lagrange's equations of motion are obtained following substitution of Eqs. (5.2) through (5.14) into the energy expressions in Eq. (5.1). In matrix form they are

$$\mathbf{M}\ddot{\mathbf{q}} + \Omega_c\mathbf{G}\dot{\mathbf{q}} + \left(\mathbf{K} - \Omega_c^2\mathbf{C}\right)\mathbf{q} = \Omega_c^2\mathbf{c} + \mathbf{f}, \tag{5.15}$$

$$\begin{aligned} \mathbf{q} &= (\mathbf{q}_s, \mathbf{q}_r, \mathbf{q}_c, \mathbf{q}_1, \ldots, \mathbf{q}_p)\,, \\ \mathbf{q}_b &= (\phi_b, \theta_b, \beta_b, x_b, y_b, z_b)\,, \quad b = s, r, c, 1, \ldots, p. \end{aligned} \tag{5.16}$$

The diagonal inertia matrix $\mathbf{M}$ is

$$\mathbf{M} = \mathrm{diag}(\mathbf{M}_s, \mathbf{M}_r, \mathbf{M}_c, \mathbf{M}_1, \ldots, \mathbf{M}_i, \ldots, \mathbf{M}_p), \tag{5.17}$$

where an individual block is $\mathbf{M}_b = \mathrm{diag}(J_b^x, J_b^x, J_b^z, m_b, m_b, m_b)$. Only certain blocks of the stiffness matrix $\mathbf{K}$ are populated due to the geometric configuration of planetary gears. The $6N \times 6N$ matrix has the form

$$\mathbf{K} = \begin{bmatrix} \mathbf{K}_s & \mathbf{0} & \mathbf{0} & \mathbf{K}_{s,1} & \mathbf{K}_{s,2} & \ldots & \mathbf{K}_{s,p} \\ & \mathbf{K}_r & \mathbf{0} & \mathbf{K}_{r,1} & \mathbf{K}_{r,2} & \ldots & \mathbf{K}_{r,p} \\ & & \mathbf{K}_c & \mathbf{K}_{c,1} & \mathbf{K}_{c,2} & \ldots & \mathbf{K}_{c,p} \\ & & & \mathbf{K}_1 & \mathbf{0} & \ldots & \mathbf{0} \\ & & & & \mathbf{K}_2 & \ldots & \mathbf{0} \\ & \text{Symmetric} & & & & \ddots & \vdots \\ & & & & & & \mathbf{K}_p \end{bmatrix}_{n \times n}, \tag{5.18}$$

where the total number of degrees of freedom is $n = 6N$. The 6×6 sub-matrices $\mathbf{K}_h$, and $\mathbf{K}_{h,i}$, $h = s, r, c$, are expanded in the following section. The individual elements of these sub-matrices and of $\mathbf{K}_i$ are given in the appendix. Spinning of the system generates the block diagonal gyroscopic matrix

$$\mathbf{G} = \mathrm{diag}\left(\mathbf{G}_s, \mathbf{G}_r, \mathbf{G}_c, \mathbf{G}_1, \ldots, \mathbf{G}_i, \ldots, \mathbf{G}_p\right), \tag{5.19}$$

$$\mathbf{G}_b = \begin{bmatrix} 0 & -R_b\left(2J_b^x - J_b^z\right) & 0 & 0 & 0 & 0 \\ R_b\left(2J_b^x - J_b^z\right) & 0 & 0 & 0 & 0 & 0 \\ 0 & 0 & 0 & 0 & 0 & 0 \\ 0 & 0 & 0 & 0 & -2m_b & 0 \\ 0 & 0 & 0 & 2m_b & 0 & 0 \\ 0 & 0 & 0 & 0 & 0 & 0 \end{bmatrix}, \tag{5.20}$$

where the gear ratios R_b relate the rotation speeds by $\Omega_b = R_b\Omega_c$ (recall $b = s, r, c, 1, \ldots, p$). The centripetal stiffness matrix is

$$\mathbf{C} = \mathrm{diag}\left(\mathbf{C}_s, \mathbf{C}_r, \mathbf{C}_c, \mathbf{C}_1, \ldots, \mathbf{C}_i, \ldots, \mathbf{C}_p\right), \tag{5.21}$$

$$\mathbf{C}_b = \text{diag}\left[J_b^x R_b^2, J_b^x R_b^2, 0, m_b, m_b, 0\right], \quad b = s, r, c, 1, \ldots, p. \tag{5.22}$$

Carrier rotation induces constant planet centripetal accelerations evident in the $\Omega_c^2\mathbf{c}$ term of Eq. (5.15) where

$$\mathbf{c} = [\mathbf{0}, \mathbf{0}, \mathbf{0}, \mathbf{c}_1, \ldots, \mathbf{c}_i, \ldots, \mathbf{c}_p], \tag{5.23}$$

$$\mathbf{c}_i = m_p\,[0, 0, 0, -(r_s + r_p)\tan\Phi_{sp}, r_s + r_p, 0]. \tag{5.24}$$

If one considers motion $\mathbf{y} = \mathbf{q} - \mathbf{q}_e$ about the steady configuration $\mathbf{q}_e$ defined by $(\mathbf{K} - \Omega_c^2\mathbf{C})\,\mathbf{q}_e = \Omega_c^2\mathbf{c} + \mathbf{f}$, where $\mathbf{f}$ is the constant external loading vector, the governing equation is

$$\mathbf{M}\ddot{\mathbf{y}} + \Omega_c\mathbf{G}\dot{\mathbf{y}} + \left(\mathbf{K} - \Omega_c^2\mathbf{C}\right)\mathbf{y} = \mathbf{f}_d(t), \tag{5.25}$$

where $\mathbf{f}_d(t)$ is the zero-mean, dynamic external loading vector.

5.3 Modal Analysis

5.3.1 Eigenvalue Problem

The high-speed effects that arise from the constant kinematic rotation fall outside the scope of this study, so $\Omega_c = 0$ is specified. The eigenvalue problem is

$$(\mathbf{K} - \lambda\mathbf{M})\mathbf{q} = 0 \tag{5.26}$$

with natural frequencies $\sqrt{\lambda}$. The vibration modes are divided into 6×1 sub-vectors as

$$\mathbf{q} = (\mathbf{v}_s, \mathbf{v}_r, \mathbf{v}_c, \mathbf{v}_1, \ldots, \mathbf{v}_p). \tag{5.27}$$

The system is tuned, that is, all sun-planet and ring-planet mesh stiffnesses, and their centers of stiffnesses, are identical among all planets; the planet bearing stiffnesses, the axial locations of the planet bearings, and the planet inertias are the same

for all planets. Regardless of planet spacing, the stiffness and inertia sub-matrices satisfy

$$\begin{aligned}\mathbf{K}_h = \boldsymbol{\Upsilon}_h \sum_{i=1}^{p} \sin\alpha_i + \mathbf{R}\boldsymbol{\Upsilon}_h\mathbf{R}^T \sum_{i=1}^{p} \cos\alpha_i + \boldsymbol{\Theta}_h \sum_{i=1}^{p} \sin^2\alpha_i \\ + \mathbf{R}\boldsymbol{\Theta}_h\mathbf{R}^T \sum_{i=1}^{p} \cos^2\alpha_i + \boldsymbol{\Xi}_h \sum_{i=1}^{p} \sin\alpha_i\cos\alpha_i + \boldsymbol{\Psi}_h, \quad h = s, r, c,\end{aligned} \tag{5.28}$$

$$\mathbf{R} = \begin{bmatrix} 0 & 1 & 0 & 0 & 0 & 0 \\ -1 & 0 & 0 & 0 & 0 & 0 \\ 0 & 0 & 1 & 0 & 0 & 0 \\ 0 & 0 & 0 & 0 & 1 & 0 \\ 0 & 0 & 0 & -1 & 0 & 0 \\ 0 & 0 & 0 & 0 & 0 & 1 \end{bmatrix}, \tag{5.29}$$

$$\mathbf{K}_i = \mathbf{K}_j,\ \mathbf{M}_i = \mathbf{M}_j, \quad i, j = 1, 2, \ldots, p, \tag{5.30}$$

$$\mathbf{K}_{h,i} = \boldsymbol{\Lambda}_h \sin\alpha_i + \mathbf{R}\boldsymbol{\Lambda}_h \cos\alpha_i + \boldsymbol{\Gamma}_h. \tag{5.31}$$

System Matrices

Individual elements of $\boldsymbol{\Upsilon}_h$, $\boldsymbol{\Theta}_h$, $\boldsymbol{\Xi}_h$, $\boldsymbol{\Psi}_h$, $\boldsymbol{\Lambda}_h$, $\boldsymbol{\Gamma}_h$, and $\mathbf{K}_i$ are given below with all unspecified elements being zero. All sub-matrices in Eqs. (5.32) through (5.43) are associated with a particular mesh. Subscript s denotes the sun gear; for sub-matrices with the subscript s, $j = 1, 3, \ldots, 2p-1$ indicates the particular sun-planet mesh. Similarly, for sub-matrices with the subscript r, $j = 2, 4, \ldots, 2p$ indicates the particular ring-planet mesh.

$$\begin{aligned}&\boldsymbol{\Upsilon}_s^{(1,3)} = \boldsymbol{\Upsilon}_s^{(3,1)} = k_j r_s D_1(j)\cos\psi, \quad \boldsymbol{\Upsilon}_s^{(2,3)} = \boldsymbol{\Upsilon}_s^{(3,2)} = k_j r_s^2 \sin\psi\cos\psi, \\ &\boldsymbol{\Upsilon}_s^{(3,5)} = \boldsymbol{\Upsilon}_s^{(5,3)} = k_j r_s \cos^2\psi, \quad \boldsymbol{\Upsilon}_s^{(1,6)} = \boldsymbol{\Upsilon}_s^{(6,1)} = -k_j D_1(j)\sin\psi \\ &\boldsymbol{\Upsilon}_s^{(2,6)} = \boldsymbol{\Upsilon}_s^{(6,2)} = -k_j r_s \sin^2\psi.\end{aligned} \tag{5.32}$$

$$\begin{aligned}&\boldsymbol{\Theta}_s^{(1,1)} = \kappa_j + k_j D_1(j)^2, \quad \boldsymbol{\Theta}_s^{(1,2)} = \boldsymbol{\Theta}_s^{(2,1)} = k_j D_1(j) r_s \sin\psi, \\ &\boldsymbol{\Theta}_s^{(2,2)} = k_j r_s \sin^2\psi, \quad \boldsymbol{\Theta}_s^{(5,5)} = k_j\cos^2\psi, \\ &\boldsymbol{\Theta}_s^{(1,5)} = \boldsymbol{\Theta}_s^{(5,1)} = k_j D_1(j)\cos\psi, \quad \boldsymbol{\Theta}_s^{(2,5)} = \boldsymbol{\Theta}_s^{(5,2)} = k_j r_s \sin\psi\cos\psi.\end{aligned} \tag{5.33}$$

$$\begin{aligned}
&\Xi_s^{(1,1)} = 2k_j D_1(j) r_s \sin\psi, \quad \Xi_s^{(1,2)} = \Xi_s^{(2,1)} = k_j[r_s^2 \sin^2\psi - D_1(j)^2] - \kappa_j,\\
&\Xi_s^{(1,4)} = \Xi_s^{(4,1)} = k_j \cos\psi D_1(j), \quad \Xi_s^{(1,5)} = \Xi_s^{(5,1)} = k_j r_s \cos\psi \sin\psi,\\
&\Xi_s^{(2,2)} = -2k_j D_1(j) r_s \sin\psi, \quad \Xi_s^{(2,4)} = \Xi_s^{(4,2)} = k_j r_s \cos\psi \sin\psi,\\
&\Xi_s^{(2,5)} = \Xi_s^{(5,2)} = -k_j \cos\psi D_1(j), \quad \Xi_s^{(4,5)} = \Xi_s^{(5,4)} = k_j \cos^2\psi.
\end{aligned} \tag{5.34}$$

$$\begin{aligned}
&\Psi_s^{(1,1)} = k_s^A D_{17}^2 + k_s^B D_{18}^2 + \kappa_s^A + \kappa_s^B, \quad \Psi_s^{(1,5)} = \Psi_s^{(5,1)} = -k_s^A D_{17} - k_s^B D_{18},\\
&\Psi_s^{(2,2)} = k_s^A D_{17}^2 + k_s^B D_{18}^2 + \kappa_s^A + \kappa_s^B, \quad \Psi_s^{(2,4)} = \Psi_s^{(4,2)} = k_s^A D_{17} + k_s^B D_{18},\\
&\Psi_s^{(3,3)} = \kappa_s^{Az} + \kappa_s^{Bz} + k_j r_s^2 \cos^2\psi, \quad \Psi_s^{(3,6)} = -k_j r_s \cos\psi \sin\psi, \quad \Psi_s^{(4,4)} = k_s^A + k_s^B,\\
&\Psi_s^{(5,5)} = k_s^A + k_s^B, \quad \Psi_s^{(6,6)} = k_s^{Az} + k_s^{Bz} + k_j \sin^2\psi.
\end{aligned} \tag{5.35}$$

$$\begin{aligned}
&\Lambda_s^{(1,1)} = k_j D_1(j) r_p \sin\psi, \quad \Lambda_s^{(1,2)} = k_j D_1(j) D_2(j) + \kappa_j, \quad \Lambda_s^{(1,3)} = k_j D_1(j) r_p \cos\psi,\\
&\Lambda_s^{(1,4)} = -k_j D_1(j) \cos\psi, \quad \Lambda_s^{(1,6)} = k_j D_1(j) \sin\psi, \quad \Lambda_s^{(2,1)} = k_j r_s r_p \sin^2\psi,\\
&\Lambda_s^{(2,2)} = k_j r_s \sin\psi D_2(j), \quad \Lambda_s^{(2,3)} = k_j r_s r_p \sin\psi \cos\psi, \quad \Lambda_s^{(2,4)} = -k_j r_s \sin\psi \cos\psi,\\
&\Lambda_s^{(2,6)} = k_j r_s \sin^2\psi, \quad \Lambda_s^{(5,1)} = k_j r_p \cos\psi \sin\psi, \quad \Lambda_s^{(5,2)} = k_j \cos\psi D_2(j),\\
&\Lambda_s^{(5,3)} = k_j r_p \cos^2\psi, \quad \Lambda_s^{(5,4)} = -k_j \cos^2\psi, \quad \Lambda_s^{(5,6)} = k_j \sin\psi \cos\psi.
\end{aligned} \tag{5.36}$$

$$\begin{aligned}
&\Gamma_s^{(3,1)} = k_j r_s r_p \cos\psi \sin\psi, \quad \Gamma_s^{(3,2)} = k_j r_s \cos\psi D_2(j), \quad \Gamma_s^{(3,3)} = k_j r_p r_s \cos^2\psi,\\
&\Gamma_s^{(3,4)} = -k_j r_s \cos^2\psi, \quad \Gamma_s^{(3,6)} = k_j r_s \cos\psi \sin\psi, \quad \Gamma_s^{(6,1)} = -k_j r_p \sin^2\psi,\\
&\Gamma_s^{(6,2)} = -k_j \sin\psi D_2(j), \quad \Gamma_s^{(6,3)} = -k_j r_p \sin\psi \cos\psi, \quad \Gamma_s^{(6,4)} = k_j \sin\psi \cos\psi,\\
&\Gamma_s^{(6,6)} = -k_j \sin^2\psi,
\end{aligned} \tag{5.37}$$

where $j = 1, 3, \ldots, 2p-1$ for all matrices related to the sun.

$$\begin{aligned}
&\Upsilon_r^{(1,3)} = \Upsilon_r^{(3,1)} = k_j r_r D_3(j) \cos\psi, \quad \Upsilon_r^{(1,6)} = \Upsilon_r^{(6,1)} = k_j D_3(j) \sin\psi,\\
&\Upsilon_r^{(2,3)} = \Upsilon_r^{(3,1)} = k_j r_r D_4(j) \cos\psi, \quad \Upsilon_r^{(2,6)} = \Upsilon_r^{(6,2)} = k_j D_4(j) \sin\psi,\\
&\Upsilon_r^{(3,4)} = \Upsilon_r^{(4,3)} = k_j r_r D_5 \cos\psi, \quad \Upsilon_r^{(3,5)} = \Upsilon_r^{(5,3)} = k_j r_r D_6 \cos\psi,\\
&\Upsilon_r^{(4,6)} = \Upsilon_r^{(6,4)} = k_j D_5 \sin\psi, \quad \Upsilon_r^{(5,6)} = \Upsilon_r^{(6,5)} = k_j D_6 \sin\psi.
\end{aligned} \tag{5.38}$$

$$\boldsymbol{\Theta}_r^{(1,1)} = \kappa_j D_9^2 + k_j D_3(j)^2, \quad \boldsymbol{\Theta}_r^{(1,2)} = \boldsymbol{\Theta}_r^{(2,1)} = \kappa_j D_9 D_{10} + k_j D_3(j) D_4(j),$$

$$\boldsymbol{\Theta}_r^{(1,4)} = \boldsymbol{\Theta}_r^{(4,1)} = k_j D_3(j) D_5, \quad \boldsymbol{\Theta}_r^{(1,5)} = \boldsymbol{\Theta}_r^{(5,1)} = k_j D_3(j) D_6,$$

$$\boldsymbol{\Theta}_r^{(2,2)} = \kappa_j D_{10}^2 + k_j D_4(j)^2, \quad \boldsymbol{\Theta}_r^{(2,4)} = \boldsymbol{\Theta}_r^{(4,2)} = k_j D_4(j) D_5, \tag{5.39}$$

$$\boldsymbol{\Theta}_r^{(2,5)} = \boldsymbol{\Theta}_r^{(5,2)} = k_j D_4(j) D_6, \quad \boldsymbol{\Theta}_r^{(4,4)} = k_j D_5^2,$$

$$\boldsymbol{\Theta}_r^{(4,5)} = \boldsymbol{\Theta}_r^{(5,4)} = k_j D_5 D_6, \quad \boldsymbol{\Theta}_r^{(5,5)} = k_j D_6^2.$$

$$\begin{aligned}
\boldsymbol{\Xi}_r^{(1,1)} &= 2\kappa_j D_9 D_{10} + 2k_j D_3(j) D_4(j), \\
\boldsymbol{\Xi}_r^{(1,2)} &= \boldsymbol{\Xi}_r^{(2,1)} = k_j[D_4(j)^2 - D_3(j)^2] + \kappa_j(D_{10}^2 - D_9^2), \\
\boldsymbol{\Xi}_r^{(1,4)} &= \boldsymbol{\Xi}_r^{(4,1)} = k_j[D_3(j) D_6 + D_4(j) D_5], \\
\boldsymbol{\Xi}_r^{(1,5)} &= \boldsymbol{\Xi}_r^{(5,1)} = k_j[D_4(j) D_6 - D_3(j) D_5], \\
\boldsymbol{\Xi}_r^{(2,2)} &= -2\kappa_j D_9 D_{10} - 2k_j D_3(j) D_4(j), \\
\boldsymbol{\Xi}_r^{(2,4)} &= \boldsymbol{\Xi}_r^{(4,2)} = k_j[D_4(j) D_6 - D_3(j) D_5], \quad \boldsymbol{\Xi}_r^{(4,4)} = 2k_j D_5 D_6, \\
\boldsymbol{\Xi}_r^{(2,5)} &= \boldsymbol{\Xi}_r^{(5,2)} = -k_j[D_3(j) D_6 + D_4(j) D_5], \\
\boldsymbol{\Xi}_r^{(4,5)} &= \boldsymbol{\Xi}_r^{(5,4)} = k_j(D_6^2 - D_5^2), \quad \boldsymbol{\Xi}_r^{(5,5)} = -2k_j D_5 D_6.
\end{aligned} \tag{5.40}$$

$$\boldsymbol{\Psi}_r^{(1,1)} = k_r^A D_{19}^2 + k_r^B D_{20}^2 + \kappa_r^A + \kappa_r^B, \quad \boldsymbol{\Psi}_r^{(1,5)} = \boldsymbol{\Psi}_r^{(5,1)} = -k_r^A D_{19} - k_r^B D_{20},$$

$$\boldsymbol{\Psi}_r^{(2,2)} = k_r^A D_{19}^2 + k_r^B D_{20}^2 + \kappa_r^A + \kappa_r^B, \quad \boldsymbol{\Psi}_r^{(2,4)} = \boldsymbol{\Psi}_r^{(4,2)} = k_r^A D_{19} + k_r^B D_{20},$$

$$\boldsymbol{\Psi}_r^{(3,3)} = \kappa_r^{Az} + \kappa_r^{Bz} + k_j {r_r}^2 \cos^2\psi, \quad \boldsymbol{\Psi}_r^{(3,6)} = \boldsymbol{\Psi}_r^{(6,3)} = k_j r_r \cos\psi \sin\psi, \tag{5.41}$$

$$\boldsymbol{\Psi}_r^{(4,4)} = k_r^A + k_r^B, \quad \boldsymbol{\Psi}_r^{(5,5)} = k_r^A + k_r^B, \quad \boldsymbol{\Psi}_r^{(6,6)} = k_r^{Az} + k_r^{Bz} + k_j \sin^2\psi.$$

$$\mathbf{\Lambda}_r^{(1,1)} = k_j D_3(j) D_7(j) - \kappa_j D_9 D_{10}, \quad \mathbf{\Lambda}_r^{(1,2)} = k_j D_3(j) D_8(j) + \kappa_j D_9^2,$$

$$\mathbf{\Lambda}_r^{(1,4)} = -k_j D_3(j) D_6, \quad \mathbf{\Lambda}_r^{(1,5)} = k_j D_3(j) D_5, \quad \mathbf{\Lambda}_r^{(1,6)} = -k_j D_3(j) \sin\psi,$$

$$\mathbf{\Lambda}_r^{(1,3)} = -k_j r_p D_3(j) \cos\psi, \quad \mathbf{\Lambda}_r^{(2,3)} = -k_j r_p D_4(j) \cos\psi,$$

$$\mathbf{\Lambda}_r^{(2,1)} = k_j D_4(j) D_7(j) - \kappa_j D_{10}^2, \quad \mathbf{\Lambda}_r^{(2,2)} = k_j D_4(j) D_8(j) + \kappa_j D_9 D_{10},$$

$$\mathbf{\Lambda}_r^{(2,4)} = -k_j D_4(j) D_6, \quad \mathbf{\Lambda}_r^{(2,5)} = k_j D_4(j) D_5, \quad \mathbf{\Lambda}_r^{(2,6)} = -k_j \sin\psi D_4(j), \tag{5.42}$$

$$\mathbf{\Lambda}_r^{(4,1)} = k_j D_5 D_7(j), \quad \mathbf{\Lambda}_r^{(4,2)} = k_j D_5 D_8(j), \quad \mathbf{\Lambda}_r^{(4,3)} = -k_j D_5 r_p \cos\psi,$$

$$\mathbf{\Lambda}_r^{(4,4)} = -k_j D_5 D_6, \quad \mathbf{\Lambda}_r^{(4,5)} = k_j D_5^2, \quad \mathbf{\Lambda}_r^{(4,6)} = -k_j D_5 \sin\psi,$$

$$\mathbf{\Lambda}_r^{(5,1)} = k_j D_6 D_7(j), \quad \mathbf{\Lambda}_r^{(5,2)} = k_j D_6 D_8(j), \quad \mathbf{\Lambda}_r^{(5,3)} = -k_j r_p D_6 \cos\psi,$$

$$\mathbf{\Lambda}_r^{(5,4)} = -k_j D_6^2, \quad \mathbf{\Lambda}_r^{(5,5)} = k_j D_5 D_6, \quad \mathbf{\Lambda}_r^{(5,6)} = -k_j \sin\psi D_6.$$

$$\mathbf{\Gamma}_r^{(3,1)} = k_j r_r \cos\psi D_7(j), \quad \mathbf{\Gamma}_r^{(3,2)} = k_j r_r \cos\psi D_8(j), \quad \mathbf{\Gamma}_r^{(3,3)} = -k_j r_r r_p \cos^2\psi,$$

$$\mathbf{\Gamma}_r^{(3,4)} = -k_j r_r D_6 \cos\psi, \quad \mathbf{\Gamma}_r^{(3,5)} = k_j r_r D_5 \cos\psi, \quad \mathbf{\Gamma}_r^{(3,6)} = -k_j r_r \sin\psi \cos\psi,$$

$$\mathbf{\Gamma}_r^{(6,1)} = k_j \sin\psi D_7(j), \quad \mathbf{\Gamma}_r^{(6,2)} = k_j \sin\psi D_8(j), \quad \mathbf{\Gamma}_r^{(6,3)} = -k_j r_p \sin\psi \cos\psi, \tag{5.43}$$

$$\mathbf{\Gamma}_r^{(6,4)} = -k_j \sin\psi D_6, \quad \mathbf{\Gamma}_r^{(6,5)} = k_j \sin\psi D_5, \quad \mathbf{\Gamma}_r^{(6,6)} = -k_j \sin^2\psi,$$

where $j = 2, 4, \ldots, 2p$ for all matrices related to the ring.

$$\mathbf{\Upsilon}_c^{(1,3)} = \mathbf{\Upsilon}_c^{(3,1)} = -D_{13}(k_p^A D_{11} + k_p^B D_{15}), \quad \mathbf{\Upsilon}_c^{(1,6)} = \mathbf{\Upsilon}_c^{(6,1)} = -D_{12}(k_p^{Az} + k_p^{Bz}),$$

$$\mathbf{\Upsilon}_c^{(2,3)} = \mathbf{\Upsilon}_c^{(3,2)} = D_{12}(k_p^A D_{11} + k_p^B D_{15}), \quad \mathbf{\Upsilon}_c^{(2,6)} = \mathbf{\Upsilon}_c^{(6,2)} = -D_{13}(k_p^{Az} + k_p^{Bz}),$$

$$\mathbf{\Upsilon}_c^{(3,4)} = \mathbf{\Upsilon}_c^{(4,3)} = D_{12}(k_p^A + k_p^B), \quad \mathbf{\Upsilon}_c^{(3,5)} = \mathbf{\Upsilon}_c^{(5,3)} = D_{13}(k_p^A + k_p^B). \tag{5.44}$$

$$\mathbf{\Theta}_c^{(1,1)} = k_p^A D_{11}^2 + k_p^B D_{15}^2 + D_{12}^2(k_p^{Az} + k_p^{Bz}) + \kappa_p^A + \kappa_p^B,$$

$$\mathbf{\Theta}_c^{(1,2)} = \mathbf{\Theta}_c^{(2,1)} = D_{12} D_{13}(k_p^{Az} + k_p^{Bz}),$$

$$\mathbf{\Theta}_c^{(1,5)} = \mathbf{\Theta}_c^{(5,1)} = -k_p^A D_{11} - k_p^B D_{15},$$

$$\mathbf{\Theta}_c^{(2,2)} = k_p^A D_{11}^2 + k_p^B D_{15}^2 + D_{13}^2(k_p^{Az} + k_p^{Bz}) + \kappa_p^A + \kappa_p^B, \tag{5.45}$$

$$\mathbf{\Theta}_c^{(2,4)} = \mathbf{\Theta}_c^{(4,2)} = k_p^A D_{11} + k_p^B D_{15}, \quad \mathbf{\Theta}_c^{(4,4)} = k_p^A + k_p^B,$$

$$\mathbf{\Theta}_c^{(5,5)} = k_p^A + k_p^B.$$

$$\begin{aligned}
&\boldsymbol{\Xi}_c^{(1,1)} = 2D_{12}D_{13}(k_p^{Az} + k_p^{Bz}), \quad \boldsymbol{\Xi}_c^{(2,2)} = -2D_{12}D_{13}(k_p^{Az} + k_p^{Bz}),\\
&\boldsymbol{\Xi}_c^{(1,2)} = \boldsymbol{\Xi}_c^{(2,1)} = (D_{13}^2 - D_{12}^2)(k_p^{Az} + k_p^{Bz}).
\end{aligned} \tag{5.46}$$

$$\begin{aligned}
&\boldsymbol{\Psi}_c^{(1,1)} = k_c^A D_{21}^2 + k_c^B D_{22}^2 + \kappa_c^A + \kappa_c^B, \quad \boldsymbol{\Psi}_c^{(1,5)} = \boldsymbol{\Psi}_c^{(5,1)} = -k_c^A D_{21} - k_c^B D_{22},\\
&\boldsymbol{\Psi}_c^{(2,2)} = k_c^A D_{21}^2 + k_c^B D_{22}^2 + \kappa_c^A + \kappa_c^B, \quad \boldsymbol{\Psi}_c^{(2,4)} = \boldsymbol{\Psi}_c^{(4,2)} = k_c^A D_{21} + k_c^B D_{22},\\
&\boldsymbol{\Psi}_c^{(3,3)} = \kappa_c^{Az} + \kappa_c^{Bz} + \kappa_p^{Az} + \kappa_p^{Bz} + (D_{13}^2 + D_{12}^2)(k_p^A + k_p^B),\\
&\boldsymbol{\Psi}_c^{(4,4)} = k_c^A + k_c^B, \quad \boldsymbol{\Psi}_c^{(5,5)} = k_c^A + k_c^B, \quad \boldsymbol{\Psi}_c^{(6,6)} = k_c^{Az} + k_c^{Bz} + k_p^{Az} + k_p^{Bz}.
\end{aligned} \tag{5.47}$$

$$\begin{aligned}
&\boldsymbol{\Lambda}_c^{(1,2)} = k_p^A D_{11}D_{14} + k_p^B D_{15}D_{16} + \kappa_p^A + \kappa_p^B,\\
&\boldsymbol{\Lambda}_c^{(2,1)} = -k_p^A D_{11}D_{14} - k_p^B D_{15}D_{16} - \kappa_p^A - \kappa_p^B,\\
&\boldsymbol{\Lambda}_c^{(4,1)} = -k_p^A D_{14} - k_p^B D_{16}, \quad \boldsymbol{\Lambda}_c^{(4,5)} = k_p^A + k_p^B,\\
&\boldsymbol{\Lambda}_c^{(5,2)} = -k_p^A D_{14} - k_p^B D_{16}, \quad \boldsymbol{\Lambda}_c^{(5,4)} = -k_p^A - k_p^B,\\
&\boldsymbol{\Lambda}_c^{(1,4)} = k_p^A D_{11} + k_p^B D_{15}, \quad \boldsymbol{\Lambda}_c^{(2,5)} = k_p^A D_{11} + k_p^B D_{15},\\
&\boldsymbol{\Lambda}_c^{(1,6)} = D_{12}(k_p^{Az} + k_p^{Bz}), \quad \boldsymbol{\Lambda}_c^{(2,6)} = D_{13}(k_p^{Az} + k_p^{Bz}).
\end{aligned} \tag{5.48}$$

$$\begin{aligned}
&\boldsymbol{\Gamma}_c^{(3,1)} = -D_{12}(k_p^A D_{14} + k_p^B D_{16}), \quad \boldsymbol{\Gamma}_c^{(3,2)} = -D_{13}(k_p^A D_{14} + k_p^B D_{16}),\\
&\boldsymbol{\Gamma}_c^{(3,3)} = -\kappa_p^{Az} - \kappa_p^{Bz}, \quad \boldsymbol{\Gamma}_c^{(3,4)} = -D_{13}(k_p^A + k_p^B),\\
&\boldsymbol{\Gamma}_c^{(3,5)} = D_{12}(k_p^A + k_p^B), \quad \boldsymbol{\Gamma}_c^{(6,6)} = -k_p^{Az} - k_p^{Bz}.
\end{aligned} \tag{5.49}$$

Equation (5.50) relates to planet $i \in \{1, 2, \ldots, p\}$. The quantity $2i-1$ indicates the sun-planet mesh, and $2i$ indicates the planet-ring mesh.

$$
\begin{aligned}
&\mathbf{K}_i^{(1,1)} = k_{2i-1} r_p^2 \sin^2\psi + k_{2i} D_7(2i)^2 + \kappa_{2i} D_{10}^2 + k_p^A D_{14}^2 + k_p^B D_{16}^2 + \kappa_p^A + \kappa_p^B,\\
&\mathbf{K}_i^{(1,2)} = \mathbf{K}_i^{(2,1)} = k_{2i-1} D_2(2i-1) r_p \sin\psi + k_{2i} D_7(2i) D_8(2i) - \kappa_{2i} D_9 D_{10},\\
&\mathbf{K}_i^{(1,3)} = \mathbf{K}_i^{(3,1)} = [k_{2i-1} r_p \sin\psi - k_{2i} D_7(2i)] r_p \cos\psi,\\
&\mathbf{K}_i^{(1,5)} = \mathbf{K}_i^{(5,1)} = k_{2i} D_7(2i) D_5 - k_p^A D_{14} - k_p^B D_{16},\\
&\mathbf{K}_i^{(1,4)} = \mathbf{K}_i^{(4,1)} = -k_{2i-1} r_p \sin\psi\cos\psi - k_{2i} D_7(2i) D_6,\\
&\mathbf{K}_i^{(1,6)} = \mathbf{K}_i^{(6,1)} = k_{2i-1} r_p \sin^2\psi - k_{2i} D_7(2i)\sin\psi,\\
&\mathbf{K}_i^{(2,2)} = k_{2i-1} D_2(2i-1)^2 + k_{2i} D_8(2i)^2 + \kappa_{2i-1} + \kappa_{2i} D_9^2 + k_p^A D_{14}^2 + k_p^B D_{16}^2 + \kappa_p^A + \kappa_p^B,\\
&\mathbf{K}_i^{(2,3)} = \mathbf{K}_i^{(3,2)} = [k_{2i-1} D_2(2i-1) - k_{2i} D_8(2i)] r_p \cos\psi,\\
&\mathbf{K}_i^{(2,4)} = \mathbf{K}_i^{(4,2)} = -k_{2i-1} D_2(2i-1)\cos\psi - k_{2i} D_8(2i) D_6 + k_p^A D_{14} + k_p^B D_{16},\\
&\mathbf{K}_i^{(2,5)} = \mathbf{K}_i^{(5,2)} = k_{2i} D_5 D_8(2i),\\
&\mathbf{K}_i^{(2,6)} = \mathbf{K}_i^{(6,2)} = k_{2i-1} D_2(2i-1)\sin\psi - k_{2i} D_8(2i)\sin\psi,\\
&\mathbf{K}_i^{(3,3)} = (k_{2i-1} + k_{2i}) r_p^2 \cos^2\psi + \kappa_p^{Az} + \kappa_p^{Bz},\\
&\mathbf{K}_i^{(3,4)} = \mathbf{K}_i^{(4,3)} = (k_{2i} D_6 - k_{2i-1}\cos\psi) r_p \cos\psi,\\
&\mathbf{K}_i^{(3,5)} = \mathbf{K}_i^{(5,3)} = -k_{2i} D_5 r_p \cos\psi,\\
&\mathbf{K}_i^{(3,6)} = \mathbf{K}_i^{(6,3)} = (k_{2i-1} + k_{2i}) r_p \sin\psi\cos\psi,\\
&\mathbf{K}_i^{(4,4)} = k_{2i-1}\cos^2\psi + k_{2i} D_6^2 + k_p^A + k_p^B, \quad \mathbf{K}_i^{(4,5)} = \mathbf{K}_i^{(5,4)} = -k_{2i} D_5 D_6,\\
&\mathbf{K}_i^{(4,6)} = \mathbf{K}_i^{(6,4)} = -(k_{2i-1}\cos\psi - k_{2i} D_6)\sin\psi,\\
&\mathbf{K}_i^{(5,5)} = k_{2i} D_5^2 + k_p^A + k_p^B, \quad \mathbf{K}_i^{(5,6)} = \mathbf{K}_i^{(6,5)} = -k_{2i} D_5 \sin\psi,\\
&\mathbf{K}_i^{(6,6)} = (k_{2i-1} + k_{2i})\sin^2\psi + k_p^{Az} + k_p^{Bz}.
\end{aligned}
\tag{5.50}
$$

In the quantities below, $j \in \{1, 2, \ldots, 2p\}$ denotes one of the $2p$ tooth meshes.

$$D_1(j) = (e_s - c_j)\cos\psi - r_s \sin\psi \tan\Phi_{sp},$$

$$D_2(j) = (e_p - c_j)\cos\psi + r_p \sin\psi \tan\Phi_{sp},$$

$$D_3(j) = \cos(\Phi_{sp} + \Phi_{rp})\left[(e_r - c_j)\cos\psi - r_r \sin\psi \tan\Phi_{rp}\right] + r_r \sin\psi \sin(\Phi_{sp} + \Phi_{rp}),$$

$$D_4(j) = \sin(\Phi_{sp} + \Phi_{rp})\left[(e_r - c_j)\cos\psi - r_r \sin\psi \tan\Phi_{rp}\right] - r_r \sin\psi \cos(\Phi_{sp} + \Phi_{rp}),$$

$$D_5 = -\cos\psi \sin(\Phi_{sp} + \Phi_{rp}),\ D_6 = \cos\psi \cos(\Phi_{sp} + \Phi_{rp}),$$

$$D_7(j) = \sin(\Phi_{sp} + \Phi_{rp})\left[(c_j - e_p)\cos\psi + r_p \tan\Phi_{rp} \sin\psi\right] + r_p \sin\psi \cos(\Phi_{sp} + \Phi_{rp}),$$

$$D_8(j) = \cos(\Phi_{sp} + \Phi_{rp})\left[(e_p - c_j)\cos\psi - r_p \tan\Phi_{rp} \sin\psi\right] + r_p \sin\psi \sin(\Phi_{sp} + \Phi_{rp}),$$

$$D_9 = -\cos(\Phi_{sp} + \Phi_{rp}),\ D_{10} = -\sin(\Phi_{sp} + \Phi_{rp}),$$

$$D_{11} = -L_p^A - e_s, \quad D_{12} = -\tan\Phi_{sp}(r_s + r_p), \quad D_{13} = r_s + r_p, \quad D_{14} = -L_p^A - e_p,$$

$$D_{15} = L_p^B - e_s, \quad D_{16} = L_p^B - e_p, \quad D_{17} = -L_s^A - e_s, \quad D_{18} = L_s^B - e_s,$$

$$D_{19} = -L_r^A - e_r, \quad D_{20} = L_r^B - e_r, \quad D_{21} = -L_c^A - e_c, \quad D_{22} = L_c^B - e_c.$$

5.3.2 Computational Observation of Vibration Modes

Eigensolutions of a sample system (Table 5.1) with four and five equally spaced planets are evaluated numerically to expose the modal properties. Some natural frequencies and their corresponding mode types are given in Table 5.2. The vibration modes exhibit distinctive characteristics. There are three types of vibration modes. Figures 5.3, 5.4, 5.5, and 5.6 show two examples of each of the three types of vibration modes for the example system with four planets. Regardless of the system parameters the modal deflections of certain gears are zero, or there is a relation between certain degrees of freedom such that not all modal deflections are independent. Based on

these features, all vibration modes are categorized as rotational-axial, translational-tilting, and planet modes. These three types bear some similarities to those described by Lin and Parker [58], but they have important differences.

Table 5.1: Parameters of the planetary gear system.

Parameter	Sun	Mesh	Planet	Mesh	Ring	Carrier
Operating pressure angle, Φ [deg]		21.3		21.3		
Base helix angle, ψ [deg]		-28.5		28.5		
Translational mesh stiffness, k [N/m]		6.19×10^9		22.3×10^9		
Tilting mesh stiffness, κ [N m]		643×10^3		2.31×10^6		
Center of stiffness, c [mm]		0		0		
Base radius, r [mm]	24		16		56	
Center of mass, e [mm]	0		0		0	0
Bearing distance at point A, L^A [mm]	-20		-20		-20	-20
Bearing distance at point B, L^B [mm]	20		20		20	20
Radial bearing stiffnesses, k^A, k^B [N/m]	0.5×10^9		0.5×10^9		0.5×10^9	0.5×10^9
Axial bearing stiffnesses, k^{Az}, k^{Bz} [N/m]	0.5×10^9		0.5×10^9		0.5×10^9	0.5×10^9
Tilting bearing stiffnesses, κ^A, κ^B [N m]	50×10^6		5×10^6		50×10^6	50×10^6
Rotational brg. stiffnesses, κ^{Az}, κ^{Bz} [N m]	0		0		90×10^9	90×10^9
Mass, m [kg]	0.3		0.2		100×10^{-6}	0.5
Tilting inertia, J^x [kg m^2]	5×10^{-3}		50×10^{-6}		10×10^{-6}	4×10^{-3}
Rotational inertia, J^z [kg m^2]	10×10^{-3}		100×10^{-6}		20×10^{-6}	8×10^{-3}

Table 5.2: Lowest 10 natural frequencies [Hz] and mode types of the planetary gear system defined in Table 5.1 with four and five planets. R-A: Rotational-axial mode, T-T: Translational-tilting mode, P: Planet mode.

Four Planets		Five Planets	
Natural frequency [Hz]	Mode type	Natural frequency [Hz]	Mode type
953	R-A	1011	R-A
3120	T-T	3068	T-T
3120	T-T	3068	T-T
3251	R-A	3114	R-A
3743	R-A	3670	R-A
5426	T-T	5184	T-T
5426	T-T	5184	T-T
8177	P	8177	P
8537	T-T	8177	P
8537	T-T	8506	R-A

Observed Rotational-Axial Modes

There are 12 rotational-axial modes for systems with more than two planets. The natural frequency multiplicity is one. From the computed eigenvectors (in Fig. 5.3, for example) the central members rotate and translate axially, but they do not tilt or translate in-plane. The modal deflection of any central member is of the form

$$\mathbf{v}_h = (0, 0, \beta_h, 0, 0, z_h). \tag{5.51}$$

The planets move in all degrees of freedom, and their modal deflections are identical to one another as given by

$$\mathbf{v}_1 = \mathbf{v}_2 = \ldots = \mathbf{v}_p. \tag{5.52}$$

Observed Translational-Tilting Modes

There are 12 pairs of translational-tilting modes with natural frequency multiplicity of two for systems with three or more planets. In both modes of a translational-tilting mode pair the central members only translate in-plane and tilt but do not rotate or translate axially. Figures 5.4 and 5.5 show two examples of translational-tilting mode pairs. The modal deflections of any central member for a pair of vibration modes have the form

$$\mathbf{v}_h = (\phi_h, \theta_h, 0, x_h, y_h, 0),\ \mathbf{w}_h = (\theta_h, -\phi_h, 0, y_h, -x_h, 0) \ \rightarrow\ \mathbf{w}_h = \mathbf{R}\mathbf{v}_h, \quad h = s, r, c. \tag{5.53}$$

The planets move in all six degrees of freedom. Their motions are such that the modal deflections of any planet can be found from the modal deflections of the arbitrarily selected first planet using

$$\begin{pmatrix} \mathbf{v}_i \\ \mathbf{w}_i \end{pmatrix} = \begin{bmatrix} \cos\alpha_i\, \mathbf{I} & \sin\alpha_i\, \mathbf{I} \\ -\sin\alpha_i\, \mathbf{I} & \cos\alpha_i\, \mathbf{I} \end{bmatrix} \begin{pmatrix} \mathbf{v}_1 \\ \mathbf{w}_1 \end{pmatrix}, \quad i = 2, \ldots, p, \tag{5.54}$$

where $\mathbf{I}$ is the 6×6 identity matrix.

Observed Planet Modes

In two sample planet modes shown in Fig. 5.6 all central members are stationary. This is given by

$$\mathbf{v}_h = \mathbf{0}, \quad h = s, r, c. \tag{5.55}$$

The planets move in all six degrees of freedom, and their motions are related to that of the arbitrarily selected first planet, as given by

$$\mathbf{v}_i = w_i \mathbf{v}_1, \quad i = 2, \ldots, p, \tag{5.56}$$

where the w_i are constants. Planet modes are observed only when there are four or more planets ($p \geq 4$). The natural frequency multiplicity is $p - 3$.

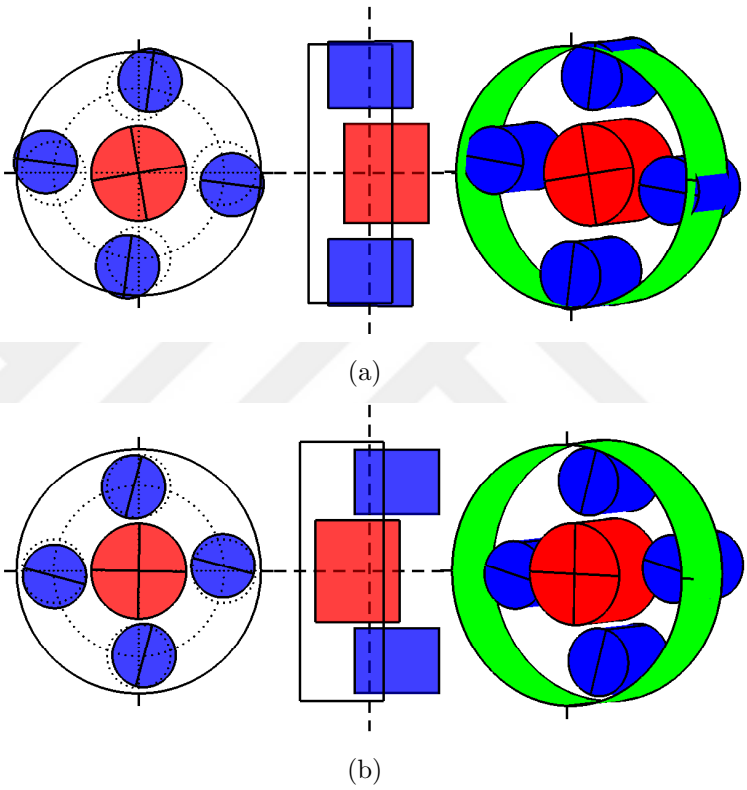

Figure 5.3: Two rotational-axial modes of the planetary gear system defined in Table 5.1 with four equally spaced planets. Angular and translational displacements are scaled independently to emphasize behavior. a) 953 Hz. b) 3251 Hz.

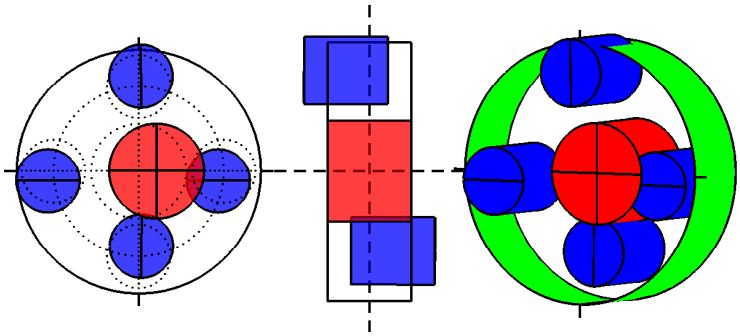

(a)

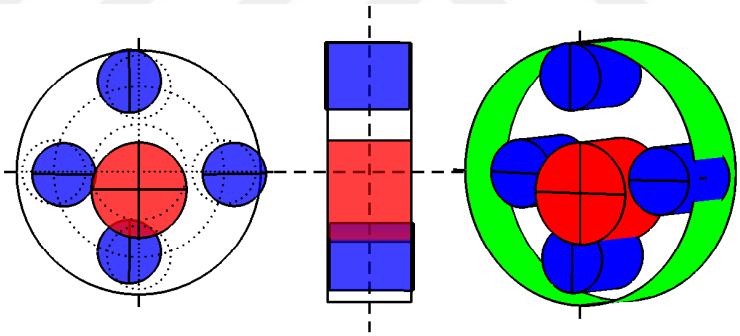

(b)

Figure 5.4: A pair of degenerate translational-tilting modes (10591 Hz) of the planetary gear system defined in Table 5.1 with four equally spaced planets. Angular and translational displacements are scaled independently to emphasize behavior.

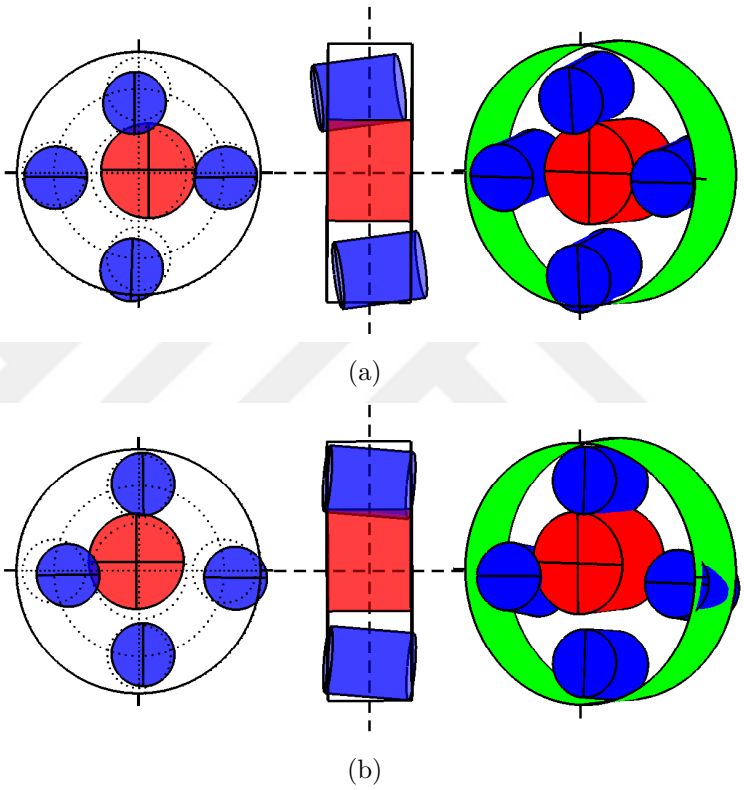

Figure 5.5: A pair of degenerate translational-tilting modes (25696 Hz) of the planetary gear system defined in Table 5.1 with four equally spaced planets. Angular and translational displacements are scaled independently to emphasize behavior.

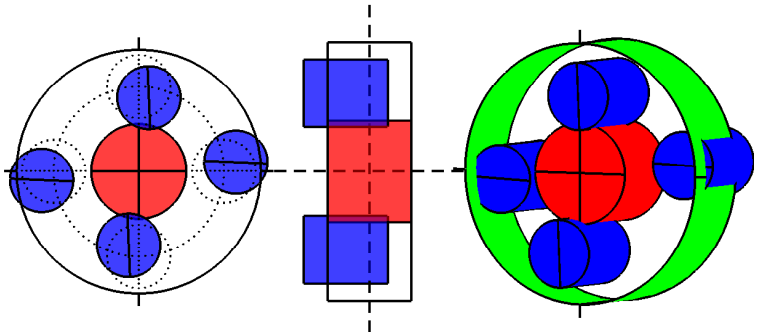

(a)

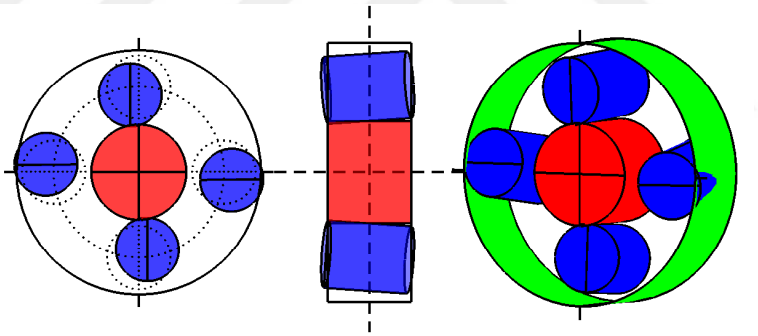

(b)

Figure 5.6: Two planet modes of the planetary gear system defined in Table 5.1 with four equally spaced planets. Angular and translational displacements are scaled independently to emphasize behavior. a) 8177 Hz. b) 80538 Hz.

5.3.3 Analytical Characterization of Vibration Modes

The observed properties of the different types of vibration modes will be proved for general systems with three or more planets. The proof consists of constructing a candidate vibration mode (for each mode type) based on the observed characteristics and substituting it into the eigenvalue problem Eq. (5.26). Showing that the eigenvalue problem is satisfied ensures that the proposed vibration mode is truly a system vibration mode.

The critical point for all three mode types is that some elements of the candidate vibration mode are linearly dependent on others. A candidate vibration mode is partitioned as

$$\mathbf{q} = (\mathbf{u}, \mathbf{q}^*), \quad \mathbf{q}^* = \mathbf{Y}\mathbf{u}, \tag{5.57}$$

where the vector $\mathbf{u}$ contains elements regarded as independent, and the vector $\mathbf{q}^*$ is the vector of dependent elements calculated from $\mathbf{u}$. How the modal deflections are partitioned between $\mathbf{u}$ and $\mathbf{q}^*$ as well as the matrix $\mathbf{Y}$ differ for each of the three mode types, but all three types can be expressed in this general form with known $\mathbf{Y}$. The three specific cases are discussed subsequently.

Substitution of the candidate vibration mode from Eq. (5.57) into the eigenvalue problem Eq. (5.26) results in

$$\begin{bmatrix} \mathbf{A} & \mathbf{B}^T \\ \mathbf{B} & \mathbf{E} \end{bmatrix} \begin{pmatrix} \mathbf{u} \\ \mathbf{q}^* \end{pmatrix} = \lambda \begin{bmatrix} \mathbf{M}_u & \mathbf{0} \\ \mathbf{0} & \mathbf{M}_l \end{bmatrix} \begin{pmatrix} \mathbf{u} \\ \mathbf{q}^* \end{pmatrix}, \tag{5.58}$$

where $\mathbf{A}$, $\mathbf{B}$, and $\mathbf{E}$ are partitioned matrices of $\mathbf{K}$; $\mathbf{M}_u$ and $\mathbf{M}_l$ are partitioned matrices of the diagonal $\mathbf{M}$. The upper row yields $\mathbf{A}\mathbf{u} + \mathbf{B}^T\mathbf{q}^* = \lambda\mathbf{M}_u\mathbf{u}$. Substitution of $\mathbf{q}^* = \mathbf{Y}\mathbf{u}$ expresses the upper row in the form of a reduced eigenvalue problem

$$(\mathbf{A} + \mathbf{B}^T\mathbf{Y})\mathbf{u} = \lambda\mathbf{M}_u\mathbf{u}. \tag{5.59}$$

This equation contains all the necessary information to find the natural frequencies and vibration modes of the type of vibration mode under consideration. The remaining elements $\mathbf{q}^*$ of $\mathbf{q}$ are found from Eq. (5.57). *For such a mode to indeed be a system mode, however, the lower row of Eq.* (5.58) *must hold, which is given by*

$$\mathbf{B}\mathbf{u} + \mathbf{E}\mathbf{q}^* = \lambda \mathbf{M}_l \mathbf{q}^*. \tag{5.60}$$

This equation is crucial for the rest of this chapter.

In what follows, we prove that Eq. (5.60) holds for appropriately selected candidate vibration modes of the form Eq. (5.57) constructed for each of the three mode types. In each case, $\mathbf{u}$ is calculated by the reduced eigenvalue problem in Eq. (5.59). In this process, the algebraic properties of the stiffness and inertia matrices are pivotal. Furthermore, we show that this process yields *all* of the system modes, that is, *every* mode is either a rotational-axial, translational-tilting, or planet mode.

Several elements of $\mathbf{q}^*$ are zero for each mode type. The non-zero elements are collected in $\mathbf{q}_N^*$. To simplify the subsequent algebra Eq. (5.60) is partitioned into two parts associated with the zero and non-zero elements of $\mathbf{q}^*$ as

$$\left[\begin{array}{c} \mathbf{B}_0 \\ \hline \mathbf{B}_N \end{array}\right] \mathbf{u} + \left[\begin{array}{c|c} \mathbf{D}_0 & \mathbf{E}_0 \\ \hline \mathbf{D}_N & \mathbf{E}_N \end{array}\right] \left(\begin{array}{c} \mathbf{0} \\ \hline \mathbf{q}_N^* \end{array}\right) = \left(\begin{array}{c} \mathbf{0} \\ \hline \lambda \mathbf{M}_N \mathbf{q}_N^* \end{array}\right), \tag{5.61}$$

where the subscripts 0 and N denote the partitioning, and Eq. (5.61) reflects $\mathbf{M}_l$ being diagonal. The upper and lower rows of Eq. (5.61) are

$$\mathbf{B}_0 \mathbf{u} + \mathbf{E}_0 \mathbf{q}_N^* = \mathbf{0}, \tag{5.62}$$

$$\mathbf{B}_N \mathbf{u} + \mathbf{E}_N \mathbf{q}_N^* = \lambda \mathbf{M}_N \mathbf{q}_N^*. \tag{5.63}$$

The construction of matrices $\mathbf{Y}$, $\mathbf{B}_0$, $\mathbf{B}_N$, $\mathbf{E}_0$, $\mathbf{E}_N$, $\mathbf{A}$, $\mathbf{M}_N$, and $\mathbf{M}_u$ are dictated by the partitioning of each candidate mode type by Eq. (5.57).

With the stipulations that the planets are equally spaced and the system is tuned, the following developments do not depend on, and are therefore valid for arbitrary values of, system parameters such as gear radii, pressure and helix angles, locations and stiffnesses of the bearings, mesh stiffnesses, and so on.

Rotational-Axial Modes

The decomposition of the candidate rotational-axial mode according to Eqs. (5.51), (5.52), and (5.57) is

$$\mathbf{u} = (\tilde{\mathbf{v}}_s, \tilde{\mathbf{v}}_r, \tilde{\mathbf{v}}_c, \mathbf{v}_1)\,, \quad \mathbf{q}^* = (\mathbf{0}, \mathbf{0}, \mathbf{0}, \underbrace{\mathbf{v}_1, \ldots, \mathbf{v}_1}_{p-1}), \tag{5.64}$$

where the zero vector has dimension 4×1. The tilde accent is used here and for the other two mode types to represent sub-vectors containing only the independent elements $\mathbf{u}$ of the candidate mode $\mathbf{q}$ in Eq. (5.57). The specific elements in the quantities with a tilde accent will differ based on the mode type in question. The tilting and translational motions of the central members in a candidate rotational-axial mode are zero as indicated in Eq. (5.51), so the sun, ring, and carrier modal deflection sub-vectors are

$$\tilde{\mathbf{v}}_s = (\beta_s, z_s), \quad \tilde{\mathbf{v}}_r = (\beta_r, z_r), \quad \tilde{\mathbf{v}}_c = (\beta_c, z_c). \tag{5.65}$$

The modal deflections of each planet are identical as given by Eq. (5.52). The modal deflection of the arbitrarily selected first planet $\mathbf{v}_1$ is chosen to be the independent one hence the appearance of $\mathbf{v}_1$ in Eq. (5.64). The dependent elements contained in $\mathbf{q}^*$ are all calculable from the vector of independent elements $\mathbf{u}$ using Eq. (5.57) and

$$\mathbf{Y} = \begin{bmatrix} \mathbf{0}_{12\times 6} & \mathbf{0}_{12\times 6} \\ \mathbf{0}_{6\times 6} & \mathbf{I}_{6\times 6} \\ \vdots & \vdots \\ \mathbf{0}_{6\times 6} & \mathbf{I}_{6\times 6} \end{bmatrix} \tag{5.66}$$

with dimension $12 + 6(p-1) \times 12$.

One can readily partition Eq. (5.26) to obtain Eq. (5.58), and the reduced eigenvectors $\mathbf{u}$ are found from Eq. (5.59). To confirm that Eq. (5.64) is indeed a mode, each of Eq. (5.62) and Eq. (5.63) must be satisfied for $\mathbf{u}$ and $\mathbf{q}^*$.

The matrices $\mathbf{B}_0$ and $\mathbf{E}_0$ in Eq. (5.62) are dictated by the partitioning given in Eq. (5.64) to be

$$\mathbf{B}_0 = \begin{bmatrix} \hat{\mathbf{K}}_s & \mathbf{0} & \mathbf{0} & \hat{\mathbf{K}}_{s,1} \\ \mathbf{0} & \hat{\mathbf{K}}_r & \mathbf{0} & \hat{\mathbf{K}}_{r,1} \\ \mathbf{0} & \mathbf{0} & \hat{\mathbf{K}}_c & \hat{\mathbf{K}}_{c,1} \end{bmatrix}, \quad \mathbf{E}_0 = \begin{bmatrix} \hat{\mathbf{K}}_{s,2} & \dots & \hat{\mathbf{K}}_{s,p} \\ \hat{\mathbf{K}}_{r,2} & \dots & \hat{\mathbf{K}}_{r,p} \\ \hat{\mathbf{K}}_{c,2} & \dots & \hat{\mathbf{K}}_{c,p} \end{bmatrix}. \tag{5.67}$$

The sub-matrices $\hat{\mathbf{K}}_h$, $h = s, r, c$, are constructed from the 1st, 2nd, 4th, and 5th rows and 3rd and 6th columns of the corresponding matrices $\mathbf{K}_h$ in Eq. (5.18). The sub-matrices $\hat{\mathbf{K}}_{h,i}$, $i = 1, \dots, p$, are constructed from the 1st, 2nd, 4th, and 5th rows and all columns of the corresponding matrices $\mathbf{K}_{h,i}$ in Eq. (5.18). $\mathbf{B}_0$ has dimension 12×12 and $\mathbf{E}_0$ has dimension $12 \times 6(p-1)$.

Substitution of matrices $\mathbf{B}_0$ and $\mathbf{E}_0$ from Eq. (5.67) into Eq. (5.62) yields

$$\hat{\mathbf{K}}_h \tilde{\mathbf{v}}_h + \sum_{i=1}^{p} \hat{\mathbf{K}}_{h,i} \mathbf{v}_1 = \mathbf{0}. \tag{5.68}$$

From Eq. (5.28), the sub-matrices $\hat{\mathbf{K}}_h$ satisfy

$$\hat{\mathbf{K}}_h = \hat{\boldsymbol{\Upsilon}}_h \sum_{i=1}^{p} \sin \alpha_i + \bar{\mathbf{R}} \hat{\boldsymbol{\Upsilon}}_h \hat{\mathbf{R}}^T \sum_{i=1}^{p} \cos \alpha_i, \tag{5.69}$$

because $\hat{\boldsymbol{\Theta}}_h = \hat{\boldsymbol{\Xi}}_h = \hat{\boldsymbol{\Psi}}_h = \mathbf{0}$ by Eqs. (5.33), (5.34), (5.35), (5.39), (5.40), (5.41), (5.45), (5.46), and (5.47). The hat accent on $\hat{\mathbf{R}}$ indicates the 3rd and 6th rows and 3rd and 6th columns of $\mathbf{R}$. The bar accent on $\bar{\mathbf{R}}$ indicates the 1st, 2nd, 4th, and 5th

rows and the 1st, 2nd, 4th, and 5th columns of $\mathbf{R}$. From [25]

$$\begin{aligned}\sum_{i=1}^{p}\sin i\alpha &= \sin\frac{p+1}{2}\alpha\sin\frac{p\alpha}{2}\mathrm{cosec}\frac{\alpha}{2}=0,\\ \sum_{i=0}^{p}\cos i\alpha &= \cos\frac{p+1}{2}\alpha\sin\frac{p\alpha}{2}\mathrm{cosec}\frac{\alpha}{2}+1=0,\end{aligned}\tag{5.70}$$

where the second equalities are from equal planet spacing $\alpha = 2\pi/p$. The sub-matrices $\hat{\mathbf{K}}_h$ in Eq. (5.68) vanish as a result of Eqs. (5.69) and (5.70). For vanishing $\hat{\mathbf{K}}_h$ Eq. (5.68) becomes, after use of Eq. (5.31) and $\hat{\mathbf{\Gamma}}_h = \mathbf{0}$ (by Eqs. (5.37), (5.43), and (5.49))

$$\sum_{i=1}^{p}\hat{\mathbf{K}}_{h,i}\mathbf{v}_1 = \hat{\mathbf{\Lambda}}_h\mathbf{v}_1\sum_{i=1}^{p}\sin\alpha_i + \bar{\mathbf{R}}\hat{\mathbf{\Lambda}}_h\mathbf{v}_1\sum_{i=1}^{p}\cos\alpha_i = \mathbf{0},\tag{5.71}$$

where the second equality results from Eq. (5.70). This confirms that Eq. (5.62) is satisfied for the candidate rotational-axial vibration mode defined in Eq. (5.64).

We now examine whether Eq. (5.63) is satisfied. The matrices $\mathbf{B}_N$, $\mathbf{E}_N$, and $\mathbf{M}_N$ are

$$\begin{aligned}\mathbf{B}_N &= \begin{bmatrix}\bar{\mathbf{K}}_{s,2}^T & \bar{\mathbf{K}}_{r,2}^T & \bar{\mathbf{K}}_{c,2}^T & \mathbf{0}\\ \vdots & \vdots & \vdots & \vdots\\ \bar{\mathbf{K}}_{s,p}^T & \bar{\mathbf{K}}_{r,p}^T & \bar{\mathbf{K}}_{c,p}^T & \mathbf{0}\end{bmatrix}, \quad \mathbf{E}_N = \mathrm{diag}\left(\mathbf{K}_2,\ldots,\mathbf{K}_p\right),\\ \mathbf{M}_N &= \mathrm{diag}\left(\mathbf{M}_2,\ldots,\mathbf{M}_p\right).\end{aligned}\tag{5.72}$$

The sub-matrices $\bar{\mathbf{K}}_{h,i}$ are constructed from all columns and the 3rd and 6th rows of $\mathbf{K}_{h,i}$ in Eq. (5.18), so using Eq. (5.31) and $\bar{\mathbf{\Lambda}}_h = \mathbf{0}$ (by Eqs. (5.36), (5.42), (5.48)) Eq. (5.31) becomes

$$\bar{\mathbf{K}}_{h,i} = \bar{\mathbf{\Gamma}}_h.\tag{5.73}$$

The zero matrices are 6×6. The matrices $\mathbf{B}_N$, $\mathbf{E}_N$, and $\mathbf{M}_N$ have dimensions $6(p-1)\times 12$, $6(p-1)\times 6(p-1)$, and $6(p-1)\times 6(p-1)$, respectively. Substitution of Eq. (5.72) into Eq. (5.63) yields $p-1$ matrix equations $\sum_{h=s,r,c}\bar{\mathbf{\Gamma}}_h^T\tilde{\mathbf{v}}_h + \mathbf{K}_i\mathbf{v}_1 = \lambda\mathbf{M}_i\mathbf{v}_1$,

$i = 2, \ldots, p$. Substitution of Eq. (5.30) gives

$$\sum_{h=s,r,c} \bar{\mathbf{\Gamma}}_h^T \tilde{\mathbf{v}}_h + \mathbf{K}_1 \mathbf{v}_1 = \lambda \mathbf{M}_1 \mathbf{v}_1. \tag{5.74}$$

We now show that this equality is satisfied for $\tilde{\mathbf{v}}_h$ and $\mathbf{v}_1$ calculated from the reduced eigenvalue problem Eq. (5.59). The matrices $\mathbf{A}$ and $\mathbf{M}_u$ in Eq. (5.59) are

$$\mathbf{A} = \begin{bmatrix} \acute{\mathbf{K}}_s & \mathbf{0} & \mathbf{0} & \bar{\mathbf{K}}_{s,1} \\ \mathbf{0} & \acute{\mathbf{K}}_r & \mathbf{0} & \bar{\mathbf{K}}_{r,1} \\ \mathbf{0} & \mathbf{0} & \acute{\mathbf{K}}_c & \bar{\mathbf{K}}_{c,1} \\ \bar{\mathbf{K}}_{s,1}^T & \bar{\mathbf{K}}_{r,1}^T & \bar{\mathbf{K}}_{c,1}^T & \mathbf{K}_1 \end{bmatrix}, \quad \mathbf{M}_u = \text{diag}\left(\acute{\mathbf{M}}_s, \acute{\mathbf{M}}_r, \acute{\mathbf{M}}_c, \mathbf{M}_1\right), \tag{5.75}$$

where $\acute{\mathbf{M}}_h$ and $\acute{\mathbf{K}}_h$ are constructed from the 3rd and 6th rows and the 3rd and 6th columns of the corresponding matrices in Eqs. (5.17) and (5.18). The matrices $\mathbf{A}$ and $\mathbf{M}_u$ have dimension 12×12. Upon substitution of $\mathbf{A}$, $\mathbf{M}_u$, $\mathbf{B}_0$, $\mathbf{B}_N$, and $\mathbf{Y}$ from Eqs. (5.75), (5.67), (5.72), (5.66), and (5.73) into Eq. (5.59), the reduced eigenvalue problem for rotational-axial modes is

$$\begin{bmatrix} \acute{\mathbf{K}}_s & 0 & 0 & p\bar{\mathbf{\Gamma}}_s \\ 0 & \acute{\mathbf{K}}_r & 0 & p\bar{\mathbf{\Gamma}}_r \\ 0 & 0 & \acute{\mathbf{K}}_c & p\bar{\mathbf{\Gamma}}_c \\ p\bar{\mathbf{\Gamma}}_s^T & p\bar{\mathbf{\Gamma}}_r^T & p\bar{\mathbf{\Gamma}}_c^T & p\mathbf{K}_1 \end{bmatrix} \begin{pmatrix} \tilde{\mathbf{v}}_s \\ \tilde{\mathbf{v}}_r \\ \tilde{\mathbf{v}}_c \\ \mathbf{v}_1 \end{pmatrix} = \lambda \begin{bmatrix} \acute{\mathbf{M}}_s & 0 & 0 & 0 \\ 0 & \acute{\mathbf{M}}_r & 0 & 0 \\ 0 & 0 & \acute{\mathbf{M}}_c & 0 \\ 0 & 0 & 0 & p\mathbf{M}_1 \end{bmatrix} \begin{pmatrix} \tilde{\mathbf{v}}_s \\ \tilde{\mathbf{v}}_r \\ \tilde{\mathbf{v}}_c \\ \mathbf{v}_1 \end{pmatrix}. \tag{5.76}$$

The last row of the reduced eigenvalue problem in Eq. (5.76) is the same equation as Eq. (5.74). Thus, $\mathbf{u}$ satisfying Eq. (5.59) ensures the satisfaction of Eq. (5.74), and so the satisfaction of Eq. (5.63).

We have shown that every rotational-axial mode $\mathbf{q}$ of the form Eqs. (5.57) and (5.64), defined by Eqs. (5.51) and (5.52) satisfies the full eigenvalue problem Eq. (5.26); each $\mathbf{u}$ is determined from the reduced eigenvalue problem Eq. (5.59). In the rotational-axial mode case, Eq. (5.59) is a 12×12 eigenvalue problem and the reduced eigenvector $\mathbf{u}$ has 12 elements. Therefore, there are 12 rotational-axial modes. Because each reduced eigenvector $\mathbf{u}$ produces only one rotational-axial mode, each rotational-axial mode has a distinct natural frequency.

Translational-Tilting Modes

The candidate pair of translational-tilting modes given by the relations Eqs. (5.53) and (5.54) satisfy the eigenvalue problem Eq. (5.26) with the same eigenvalue. This is expressed as

$$(\mathbf{K} - \lambda\mathbf{M})\mathbf{q}_1 = \mathbf{0}, \quad (\mathbf{K} - \lambda\mathbf{M})\mathbf{q}_2 = \mathbf{0}. \tag{5.77}$$

Any linear combination of $\mathbf{q}_1$ and $\mathbf{q}_2$ also satisfies the full eigenvalue problem with the same eigenvalue. To apply the formulation in Eqs. (5.59)-(5.63), we stack the two expressions in Eq. (5.77) into a single block-diagonal matrix eigenvalue problem of dimension $12(p+3)$ with eigenvector

$$\mathbf{q} = (\mathbf{q}_1, \mathbf{q}_2). \tag{5.78}$$

This eigenvalue problem is partitioned to give Eq. (5.58). To that end, decomposition of the candidate translational-tilting mode pair in Eq. (5.78) according to Eqs. (5.53), (5.54), and (5.57) gives

$$\begin{aligned} \mathbf{u} &= \left(\tilde{\mathbf{v}}_s, \tilde{\mathbf{v}}_r, \tilde{\mathbf{v}}_c, \mathbf{v}_1, \mathbf{w}_1\right), \\ \mathbf{q}^* &= \left(\mathbf{0}, \mathbf{0}, \mathbf{0}, \mathbf{w}_s, \mathbf{w}_r, \mathbf{w}_c, \mathbf{v}_2, \ldots, \mathbf{v}_p, \mathbf{w}_2, \ldots, \mathbf{w}_p\right), \end{aligned} \tag{5.79}$$

where the zero vectors are 2×1. The matrix $\mathbf{Y}$ combines Eqs. (5.53) and (5.54) to relate $\mathbf{q}^*$ to $\mathbf{u}$ in Eq. (5.57), and it is given by

$$\mathbf{Y} = \begin{bmatrix} \mathbf{0}_{6\times4} & \mathbf{0}_{6\times4} & \mathbf{0}_{6\times4} & \mathbf{0}_{6\times6} & \mathbf{0}_{6\times6} \\ \bar{\mathbf{R}} & \mathbf{0}_{4\times4} & \mathbf{0}_{4\times4} & \mathbf{0}_{4\times6} & \mathbf{0}_{4\times6} \\ \mathbf{0}_{4\times4} & \bar{\mathbf{R}} & \mathbf{0}_{4\times4} & \mathbf{0}_{4\times6} & \mathbf{0}_{4\times6} \\ \mathbf{0}_{4\times4} & \mathbf{0}_{4\times4} & \bar{\mathbf{R}} & \mathbf{0}_{4\times6} & \mathbf{0}_{4\times6} \\ \mathbf{0}_{6\times6} & \mathbf{0}_{6\times6} & \mathbf{0}_{6\times6} & \mathbf{I}\cos\alpha_2 & \mathbf{I}\sin\alpha_2 \\ \vdots & \vdots & \vdots & \vdots & \vdots \\ \mathbf{0}_{6\times6} & \mathbf{0}_{6\times6} & \mathbf{0}_{6\times6} & \mathbf{I}\cos\alpha_p & \mathbf{I}\sin\alpha_p \\ \mathbf{0}_{6\times6} & \mathbf{0}_{6\times6} & \mathbf{0}_{6\times6} & -\mathbf{I}\sin\alpha_2 & \mathbf{I}\cos\alpha_2 \\ \vdots & \vdots & \vdots & \vdots & \vdots \\ \mathbf{0}_{6\times6} & \mathbf{0}_{6\times6} & \mathbf{0}_{6\times6} & -\mathbf{I}\sin\alpha_p & \mathbf{I}\cos\alpha_p \end{bmatrix}, \tag{5.80}$$

where the bar accent on $\bar{\mathbf{R}}$ indicates the 1st, 2nd, 4th, and 5th rows and the 1st, 2nd, 4th, and 5th columns of $\mathbf{R}$.

The sub-matrices $\mathbf{B}_0$ and $\mathbf{E}_0$ in Eq. (5.62) are

$$\mathbf{B}_0 = \begin{bmatrix} \hat{\mathbf{K}}_s & \mathbf{0} & \mathbf{0} & \hat{\mathbf{K}}_{s,1} & \hat{\mathbf{K}}_{s,1} \\ \mathbf{0} & \hat{\mathbf{K}}_r & \mathbf{0} & \hat{\mathbf{K}}_{r,1} & \hat{\mathbf{K}}_{r,1} \\ \mathbf{0} & \mathbf{0} & \hat{\mathbf{K}}_c & \hat{\mathbf{K}}_{c,1} & \hat{\mathbf{K}}_{c,1} \end{bmatrix}, \tag{5.81}$$

$$\mathbf{E}_0 = \begin{bmatrix} \hat{\mathbf{K}}_s & \mathbf{0} & \mathbf{0} & \hat{\mathbf{K}}_{s,2} & \dots & \hat{\mathbf{K}}_{s,p} & \hat{\mathbf{K}}_{s,2} & \dots & \hat{\mathbf{K}}_{s,p} \\ \mathbf{0} & \hat{\mathbf{K}}_r & \mathbf{0} & \hat{\mathbf{K}}_{r,2} & \dots & \hat{\mathbf{K}}_{r,p} & \hat{\mathbf{K}}_{r,2} & \dots & \hat{\mathbf{K}}_{r,p} \\ \mathbf{0} & \mathbf{0} & \hat{\mathbf{K}}_c & \hat{\mathbf{K}}_{c,2} & \dots & \hat{\mathbf{K}}_{c,p} & \hat{\mathbf{K}}_{c,2} & \dots & \hat{\mathbf{K}}_{c,p} \end{bmatrix}. \tag{5.82}$$

The sub-matrices $\hat{\mathbf{K}}_h$ are constructed from the 1st, 2nd, 4th, and 5th columns and the 3rd and 6th rows of the corresponding matrices in Eq. (5.18). The sub-matrices $\hat{\mathbf{K}}_{h,i}$ are constructed from all columns and the 3rd and 6th rows of the corresponding matrices in Eq. (5.18). $\mathbf{B}_0$ has dimension 6×24 and $\mathbf{E}_0$ has dimension $6 \times 12p$.

Substitution of $\mathbf{B}_0$ and $\mathbf{E}_0$ from Eqs. (5.81) and (5.82) into Eq. (5.62) yields

$$\hat{\mathbf{K}}_h \tilde{\mathbf{v}}_h + \sum_{i=1}^{p} \hat{\mathbf{K}}_{h,i} \mathbf{v}_i = \mathbf{0}, \quad \hat{\mathbf{K}}_h \tilde{\mathbf{w}}_h + \sum_{i=1}^{p} \hat{\mathbf{K}}_{h,i} \mathbf{w}_i = \mathbf{0}, \quad h = s, r, c. \tag{5.83}$$

Considering the specified $\hat{\mathbf{K}}_h$ and Eq. (5.28), $\hat{\mathbf{\Theta}}_h = \hat{\mathbf{\Xi}}_h = \hat{\mathbf{\Psi}}_h = \mathbf{0}$ by Eqs. (5.33), (5.34), (5.35), (5.39), (5.40), (5.41), (5.45), (5.46), and (5.47). Thus, using Eq. (5.70), the sub-matrices $\hat{\mathbf{K}}_h$ vanish for equally spaced planets. Use of Eq. (5.31) and $\hat{\mathbf{\Lambda}}_h = \mathbf{0}$ (by Eqs. (5.36), (5.42), and (5.48)) simplifies the off-diagonal sub-matrices to $\hat{\mathbf{K}}_{h,i} = \hat{\mathbf{\Gamma}}_h$. For vanishing $\hat{\mathbf{K}}_h$, substitution of Eq. (5.54) into Eq. (5.83) yields

$$\hat{\mathbf{\Gamma}}_h \sum_{i=1}^{p} \mathbf{v}_1 \cos\alpha_i + \mathbf{w}_1 \sin\alpha_i = \mathbf{0}, \quad \hat{\mathbf{\Gamma}}_h \sum_{i=1}^{p} \mathbf{w}_1 \cos\alpha_i - \mathbf{v}_1 \sin\alpha_i = \mathbf{0}, \quad h = s, r, c. \tag{5.84}$$

These six matrix equations are satisfied in light of Eq. (5.70). This confirms that Eq. (5.62) is satisfied for the candidate mode given in Eq. (5.79), or equivalently, Eqs. (5.53) and (5.54).

The matrices $\mathbf{B}_N$, $\mathbf{E}_N$, and $\mathbf{M}_N$ in Eq. (5.63) are given by

$$\mathbf{B}_N = \begin{bmatrix} \mathbf{0}_{4\times4} & \mathbf{0}_{4\times4} & \mathbf{0}_{4\times4} & \mathbf{0}_{4\times6} & \bar{\mathbf{K}}_{s,1} \\ \mathbf{0}_{4\times4} & \mathbf{0}_{4\times4} & \mathbf{0}_{4\times4} & \mathbf{0}_{4\times6} & \bar{\mathbf{K}}_{r,1} \\ \mathbf{0}_{4\times4} & \mathbf{0}_{4\times4} & \mathbf{0}_{4\times4} & \mathbf{0}_{4\times6} & \bar{\mathbf{K}}_{c,1} \\ \bar{\mathbf{K}}_{s,2}^T & \bar{\mathbf{K}}_{r,2}^T & \bar{\mathbf{K}}_{c,2}^T & \mathbf{0}_{6\times6} & \mathbf{0}_{6\times6} \\ \vdots & \vdots & \vdots & \vdots & \vdots \\ \bar{\mathbf{K}}_{s,p}^T & \bar{\mathbf{K}}_{r,p}^T & \bar{\mathbf{K}}_{c,p}^T & \mathbf{0}_{6\times6} & \mathbf{0}_{6\times6} \\ \mathbf{0}_{6(p-1)\times4} & \mathbf{0}_{6(p-1)\times4} & \mathbf{0}_{6(p-1)\times4} & \mathbf{0}_{6(p-1)\times6} & \mathbf{0}_{6(p-1)\times6} \end{bmatrix}, \tag{5.85}$$

$$\mathbf{E}_N = \begin{bmatrix} \acute{\mathbf{K}}_s & \mathbf{0}_{4\times4} & \mathbf{0}_{4\times4} & \mathbf{0}_{4\times6} & \dots & \mathbf{0}_{4\times6} & \bar{\mathbf{K}}_{s,2} & \dots & \bar{\mathbf{K}}_{s,p} \\ \mathbf{0}_{4\times4} & \acute{\mathbf{K}}_r & \mathbf{0}_{4\times4} & \mathbf{0}_{4\times6} & \dots & \mathbf{0}_{4\times6} & \bar{\mathbf{K}}_{r,2} & \dots & \bar{\mathbf{K}}_{r,p} \\ \mathbf{0}_{4\times4} & \mathbf{0}_{4\times4} & \acute{\mathbf{K}}_c & \mathbf{0}_{4\times6} & \dots & \mathbf{0}_{4\times6} & \bar{\mathbf{K}}_{c,2} & \dots & \bar{\mathbf{K}}_{c,p} \\ \mathbf{0}_{6\times4} & \mathbf{0}_{6\times4} & \mathbf{0}_{6\times4} & \mathbf{K}_2 & \dots & \mathbf{0}_{6\times6} & \mathbf{0}_{6\times6} & \dots & \mathbf{0}_{6\times4} \\ \vdots & \vdots & \vdots & \vdots & \ddots & \vdots & \vdots & \ddots & \vdots \\ \mathbf{0}_{6\times4} & \mathbf{0}_{6\times4} & \mathbf{0}_{6\times4} & \mathbf{0}_{6\times6} & \dots & \mathbf{K}_p & \mathbf{0}_{6\times6} & \dots & \mathbf{0}_{6\times4} \\ \bar{\mathbf{K}}_{s,2}^T & \bar{\mathbf{K}}_{r,2}^T & \bar{\mathbf{K}}_{c,2}^T & \mathbf{0}_{6\times6} & \dots & \mathbf{0}_{6\times6} & \mathbf{K}_2 & \dots & \mathbf{0}_{6\times6} \\ \vdots & \vdots & \vdots & \vdots & \ddots & \vdots & \vdots & \ddots & \vdots \\ \bar{\mathbf{K}}_{s,p}^T & \bar{\mathbf{K}}_{r,p}^T & \bar{\mathbf{K}}_{c,p}^T & \mathbf{0}_{6\times6} & \dots & \mathbf{0}_{6\times6} & \mathbf{0}_{6\times6} & \dots & \mathbf{K}_p \end{bmatrix}, \tag{5.86}$$

$$\mathbf{M}_N = \operatorname{diag}\left(\acute{\mathbf{M}}_s, \acute{\mathbf{M}}_r, \acute{\mathbf{M}}_c, \mathbf{M}_2, \dots, \mathbf{M}_p, \mathbf{M}_2, \dots, \mathbf{M}_p\right). \tag{5.87}$$

The sub-matrices $\bar{\mathbf{K}}_{h,i}$ are constructed from all columns and the 1st, 2nd, 4th, and 5th rows of the corresponding matrices in Eq. (5.18). Use of Eq. (5.31) and $\bar{\mathbf{\Gamma}}_h = \mathbf{0}$ (by Eqs. (5.37), (5.43), and (5.49)) simplifies the off-diagonal sub-matrices to

$$\bar{\mathbf{K}}_{h,i} = \bar{\mathbf{\Lambda}}_h. \tag{5.88}$$

The sub-matrices $\acute{\mathbf{M}}_h$ and $\acute{\mathbf{K}}_h$ are constructed from the 1st, 2nd, 4th, and 5th rows and the 1st, 2nd, 4th, and 5th columns from the corresponding matrices in Eqs. (5.17) and (5.18). The planet stiffness and inertia sub-matrices $\mathbf{M}_i$ and $\mathbf{K}_i$ do not need partitioning; they are identical to the ones in Eqs. (5.17) and (5.18). $\mathbf{B}_N$ has dimension $12p \times 24$, and $\mathbf{E}_N$ and $\mathbf{M}_N$ have dimension $12p \times 12p$.

Substitution of Eqs. (5.85), (5.86), (5.87), and the candidate mode from Eq. (5.79) into Eq. (5.63) gives

$$\acute{\mathbf{K}}_h\tilde{\mathbf{w}}_h + \sum_{i=1}^{p}\bar{\mathbf{K}}_{h,i}\mathbf{w}_i = \lambda\acute{\mathbf{M}}_h\tilde{\mathbf{w}}_h, \quad h = s,r,c, \tag{5.89}$$

$$\sum_{h=s,r,c}\bar{\mathbf{K}}_{h,i}^T\mathbf{v}_h + \mathbf{K}_i\mathbf{v}_i = \lambda\mathbf{M}_i\mathbf{v}_i, \quad i = 2,\ldots,p, \tag{5.90}$$

$$\sum_{h=s,r,c}\bar{\mathbf{K}}_{h,i}^T\mathbf{w}_h + \mathbf{K}_i\mathbf{w}_i = \lambda\mathbf{M}_i\mathbf{w}_i, \quad i = 2,\ldots,p. \tag{5.91}$$

From [25]

$$\begin{aligned}
\sum_{i=1}^{p}\sin^2 i\alpha &= \frac{p}{2} - \frac{\cos(p+1)\alpha\sin p\alpha}{2\sin\alpha} = \frac{p}{2},\\
\sum_{i=1}^{p}\cos^2 i\alpha &= \frac{p}{2} + \frac{\cos(p+1)\alpha\sin p\alpha}{2\sin\alpha} = \frac{p}{2},\\
\sum_{i=1}^{p}\sin i\alpha\cos i\alpha &= \frac{1}{2}\sin[(p+1)\alpha]\sin(p\alpha)\mathrm{cosec}\alpha = 0,
\end{aligned} \tag{5.92}$$

where the second equalities result from equal planet spacing $\alpha = 2\pi/p$. Substitution of Eqs. (5.53), (5.54), and (5.92) into Eq. (5.89), premultiplication by $\bar{\mathbf{R}}^T$, and use of $\bar{\mathbf{R}}^T\acute{\mathbf{M}}_h\bar{\mathbf{R}} = \acute{\mathbf{M}}_h$, $\bar{\mathbf{R}}^T\acute{\mathbf{K}}_h\bar{\mathbf{R}} = \acute{\mathbf{K}}_h$ gives

$$\acute{\mathbf{K}}_h\tilde{\mathbf{v}}_h + \frac{p}{2}\bar{\mathbf{R}}\bar{\mathbf{\Lambda}}_h\mathbf{v}_1 + \frac{p}{2}\bar{\mathbf{\Lambda}}_h\mathbf{w}_1 = \lambda\acute{\mathbf{M}}_h\tilde{\mathbf{v}}_h, \quad h = s,r,c. \tag{5.93}$$

Substitution of Eqs. (5.30), (5.53), and (5.54) into Eqs. (5.90) and (5.91), and summing the $p-1$ equations, gives (for $\alpha_1 = 0$ and $\bar{\mathbf{R}}^T\bar{\mathbf{R}} = \mathbf{I}$)

$$\left(\sum_{h=s,r,c}\bar{\mathbf{\Lambda}}_h^T\bar{\mathbf{R}}^T\tilde{\mathbf{v}}_h + \mathbf{K}_1\mathbf{v}_1 - \lambda\mathbf{M}_1\mathbf{v}_1\right)\sum_{i=2}^{p}\cos\alpha_i = \mathbf{0}, \tag{5.94}$$

$$\left(\sum_{h=s,r,c}\bar{\mathbf{\Lambda}}_h^T\tilde{\mathbf{v}}_h + \mathbf{K}_1\mathbf{w}_1 - \lambda\mathbf{M}_1\mathbf{w}_1\right)\sum_{i=2}^{p}\cos\alpha_i = \mathbf{0}. \tag{5.95}$$

We now show that Eqs. (5.93), (5.94), and (5.95) are satisfied for $\tilde{\mathbf{v}}_h$, $\tilde{\mathbf{w}}_h$, $\mathbf{v}_i$, and $\mathbf{w}_i$ calculated from the reduced eigenvalue problem Eq. (5.59). $\mathbf{A}$ and $\mathbf{M}_u$ are given by

$$\mathbf{A} = \begin{bmatrix} \acute{\mathbf{K}}_s & \mathbf{0}_{4\times4} & \mathbf{0}_{4\times4} & \bar{\mathbf{K}}_{s,1} & \mathbf{0}_{4\times6} \\ \mathbf{0}_{4\times4} & \acute{\mathbf{K}}_r & \mathbf{0}_{4\times4} & \bar{\mathbf{K}}_{r,1} & \mathbf{0}_{4\times6} \\ \mathbf{0}_{4\times4} & \mathbf{0}_{4\times4} & \acute{\mathbf{K}}_c & \bar{\mathbf{K}}_{c,1} & \mathbf{0}_{4\times6} \\ \bar{\mathbf{K}}_{s,1}^T & \bar{\mathbf{K}}_{r,1}^T & \bar{\mathbf{K}}_{c,1}^T & \mathbf{K}_1 & \mathbf{0}_{6\times6} \\ \mathbf{0}_{6\times4} & \mathbf{0}_{6\times4} & \mathbf{0}_{6\times4} & \mathbf{0}_{6\times6} & \mathbf{K}_1 \end{bmatrix}, \quad \mathbf{M}_u = \operatorname{diag}\left(\acute{\mathbf{M}}_s, \acute{\mathbf{M}}_r, \acute{\mathbf{M}}_c, \mathbf{M}_1\right). \quad (5.96)$$

Substitution of $\mathbf{A}$, $\mathbf{M}_u$, $\mathbf{B}_0$, $\mathbf{B}_N$, and $\mathbf{Y}$ from Eqs. (5.96), (5.81), (5.85), (5.80), and (5.88) into Eq. (5.59), and using algebra similar to that in (5.93) to (5.95), gives the 24×24 reduced eigenvalue problem

$$\begin{aligned} &\begin{bmatrix} \acute{\mathbf{K}}_s & \mathbf{0}_{4\times4} & \mathbf{0}_{4\times4} & \frac{p}{2}\bar{\mathbf{R}}\bar{\mathbf{\Lambda}}_s & \frac{p}{2}\bar{\mathbf{\Lambda}}_s \\ \mathbf{0}_{4\times4} & \acute{\mathbf{K}}_r & \mathbf{0}_{4\times4} & \frac{p}{2}\bar{\mathbf{R}}\bar{\mathbf{\Lambda}}_r & \frac{p}{2}\bar{\mathbf{\Lambda}}_r \\ \mathbf{0}_{4\times4} & \mathbf{0}_{4\times4} & \acute{\mathbf{K}}_c & \frac{p}{2}\bar{\mathbf{R}}\bar{\mathbf{\Lambda}}_c & \frac{p}{2}\bar{\mathbf{\Lambda}}_c \\ \frac{p}{2}\bar{\mathbf{\Lambda}}_s^T\bar{\mathbf{R}}^T & \frac{p}{2}\bar{\mathbf{\Lambda}}_r^T\bar{\mathbf{R}}^T & \frac{p}{2}\bar{\mathbf{\Lambda}}_c^T\bar{\mathbf{R}}^T & \frac{p}{2}\mathbf{K}_1 & \mathbf{0}_{6\times6} \\ \frac{p}{2}\bar{\mathbf{\Lambda}}_s^T & \frac{p}{2}\bar{\mathbf{\Lambda}}_r^T & \frac{p}{2}\bar{\mathbf{\Lambda}}_c^T & \mathbf{0}_{6\times6} & \frac{p}{2}\mathbf{K}_1 \end{bmatrix} \begin{pmatrix} \tilde{\mathbf{v}}_s \\ \tilde{\mathbf{v}}_r \\ \tilde{\mathbf{v}}_c \\ \mathbf{v}_1 \\ \mathbf{w}_1 \end{pmatrix} \\ =&\lambda \begin{bmatrix} \acute{\mathbf{M}}_s & \mathbf{0} & \mathbf{0} & \mathbf{0} & \mathbf{0} \\ \mathbf{0} & \acute{\mathbf{M}}_r & \mathbf{0} & \mathbf{0} & \mathbf{0} \\ \mathbf{0} & \mathbf{0} & \acute{\mathbf{M}}_c & \mathbf{0} & \mathbf{0} \\ \mathbf{0} & \mathbf{0} & \mathbf{0} & \frac{p}{2}\mathbf{M}_1 & \mathbf{0} \\ \mathbf{0} & \mathbf{0} & \mathbf{0} & \mathbf{0} & \frac{p}{2}\mathbf{M}_1 \end{bmatrix} \begin{pmatrix} \tilde{\mathbf{v}}_s \\ \tilde{\mathbf{v}}_r \\ \tilde{\mathbf{v}}_c \\ \mathbf{v}_1 \\ \mathbf{w}_1 \end{pmatrix}. \end{aligned} \quad (5.97)$$

The first three rows of Eq. (5.97) are the same as Eq. (5.93). The fourth row of Eq. (5.97) is the same as Eq. (5.94) because $\sum_{i=2}^{p} \cos\alpha_i$ is non-zero. Similarly, the fifth row of Eq. (5.97) is the same as Eq. (5.95). Consequently, Eq. (5.63) is satisfied for $\mathbf{u}$ satisfying the reduced eigenvalue problem Eq. (5.97).

The foregoing analysis confirms that the degenerate mode pair $\mathbf{q}_1$ and $\mathbf{q}_2$ defined by Eqs. (5.53) and (5.54) each satisfy Eq. (5.26) with the same eigenvalue. The natural frequency multiplicity of two is also reflected in Eq. (5.97), which yields 12 degenerate eigenvalues with corresponding eigenvectors $\mathbf{u}_1 = (\tilde{\mathbf{v}}_s, \tilde{\mathbf{v}}_r, \tilde{\mathbf{v}}_c, \mathbf{v}_1, \mathbf{w}_1)$ and $\mathbf{u}_2 = (\tilde{\mathbf{w}}_s, \tilde{\mathbf{w}}_r, \tilde{\mathbf{w}}_c, \mathbf{w}_1, \mathbf{v}_1)$. This is true because one can exchange the letters $\mathbf{v}$ and

$\mathbf{w}$ in Eq. (5.79) with no change to any subsequent matrices or results. As a result, there are exactly 12 pairs of translational-tilting modes with twice repeated natural frequencies.

Planet Modes

The decomposition of the candidate planet mode according to Eqs. (5.55), (5.56), and (5.57) is

$$\mathbf{u} = w_1\mathbf{v}_1, \quad \mathbf{q}^* = (\mathbf{0}, \mathbf{0}, \mathbf{0}, w_2\mathbf{v}_1, \ldots, w_p\mathbf{v}_1)\,, \tag{5.98}$$

where the zero vectors are 6×1. We specify without loss of generality that $w_1\mathbf{v}_1 \neq 0$, that is, at least the arbitrarily selected first planet deflects. The modal deflections of other planets are a scalar multiple of the modal deflections of the first planet as given in Eq. (5.56), although the w_i $(i = 1, \ldots, p)$ are yet to be determined.

The matrices in Eq. (5.62) are

$$\mathbf{B}_0 = \begin{bmatrix} \mathbf{K}_{s,1} \\ \mathbf{K}_{r,1} \\ \mathbf{K}_{c,1} \end{bmatrix}, \quad \mathbf{E}_0 = \begin{bmatrix} \mathbf{K}_{s,2} & \ldots & \mathbf{K}_{s,p} \\ \mathbf{K}_{r,2} & \ldots & \mathbf{K}_{r,p} \\ \mathbf{K}_{c,2} & \ldots & \mathbf{K}_{c,p} \end{bmatrix}, \tag{5.99}$$

where $\mathbf{B}_0$ has dimension 18×6 and $\mathbf{E}_0$ has dimension $18 \times 6(p-1)$. Substitution of Eqs. (5.98) and (5.99) into Eq. (5.62) yields

$$\sum_{i=1}^{p} \mathbf{K}_{h,i} w_i \mathbf{v}_1 = \mathbf{0}, \quad h = s, r, c. \tag{5.100}$$

Substitution of Eq. (5.31) into Eq. (5.100) gives

$$\left(\mathbf{\Lambda}_h \sum_{i=1}^{p} w_i \sin\alpha_i + \mathbf{R}\mathbf{\Lambda}_h \sum_{i=1}^{p} w_i \cos\alpha_i + \mathbf{\Gamma}_h \sum_{i=1}^{p} w_i \right) \mathbf{v}_1 = \mathbf{0}, \tag{5.101}$$

which is satisfied if

$$\sum_{i=1}^{p} w_i \sin\alpha_i = 0, \quad \sum_{i=1}^{p} w_i \cos\alpha_i = 0, \quad \sum_{i=1}^{p} w_i = 0. \tag{5.102}$$

Equation (5.102) can be solved for $p-3$ solutions for $p \geq 4$ [4, 133]. Each solution gives a non-trivial set of w_i, $i = 1, \ldots, p$, and this set can be scaled by an arbitrary constant.

The matrices in Eq. (5.63) are

$$\mathbf{B}_N^T = \mathbf{0},\ \mathbf{E}_N = \mathrm{diag}\left(\mathbf{K}_2, \ldots, \mathbf{K}_p\right),\ \mathbf{M}_N = \mathrm{diag}\left(\mathbf{M}_2, \ldots, \mathbf{M}_p\right), \tag{5.103}$$

where $\mathbf{B}_N$ has dimension $6(p-1) \times 6$, and $\mathbf{E}_N$ and $\mathbf{M}_N$ have dimension $6(p-1)\times 6(p-1)$. Substitution of Eqs. (5.98) and (5.103) into Eq. (5.63) gives $\mathbf{K}_i w_i \mathbf{v}_1 = \lambda \mathbf{M}_i w_i \mathbf{v}_1$, $i = 2, \ldots, p$. With use of Eq. (5.30) and $w_i \neq 0$ for some i, these equations reduce to

$$\mathbf{K}_1 \mathbf{v}_1 = \lambda \mathbf{M}_1 \mathbf{v}_1. \tag{5.104}$$

We now show that this equation is satisfied by the reduced eigenvalue problem Eq. (5.59).

Considering Eq. (5.59), the matrices are given by $\mathbf{A} = \mathbf{K}_1$, $\mathbf{M}_u = \mathbf{M}_1$, and $\mathbf{B}^T\mathbf{Y} = \mathbf{0}$. With $\mathbf{u} = w_1 \mathbf{v}_1$ Eq. (5.59) becomes

$$\mathbf{K}_1 w_1 \mathbf{v}_1 = \lambda \mathbf{M}_1 w_1 \mathbf{v}_1. \tag{5.105}$$

Equation (5.104) is satisfied for $\mathbf{v}_1$ determined from Eq. (5.105) and $w_1 \neq 0$. Thus, both Eqs. (5.59) and (5.63) are satisfied. Equation (5.62) is satisfied by solution of Eq. (5.102) for the $p-3$ sets of w_i.

Thus, every mode of the form Eq. (5.98), defined by Eqs. (5.55) and (5.56) constructed from $\mathbf{v}_1$ and a set of w_i, satisfies the full eigenvalue problem Eq. (5.26). The reduced 6×6 eigenvalue problem in Eq. (5.105) yields six planet mode eigenvalues regardless of the number of planets. For each of the six eigensolution pairs $(\lambda, \mathbf{v}_1)$ one can construct $p-3$ ($p \geq 4$) eigenvectors of the full system using the solution sets

for the w_i from Eq. (5.102). Hence, each of the six planet mode natural frequencies has multiplicity $p-3$. There are no planet modes if there are less than four planets because no set of w_i satisfying Eq. (5.102) can be found.

5.3.4 Discussion

A helical planetary gear with p equally spaced planets and six degrees of freedom per component has $18+6p$ degrees of freedom. There are 12 rotational-axial modes with distinct natural frequencies; there are 24 translational-tilting modes (i.e., 12 degenerate mode pairs with natural frequency multiplicity two); there are six planet modes each with natural frequency multiplicity $p-3$ (i.e., $6(p-3)$ modes) provided $p \geq 4$. Thus, all $18+6p$ vibration modes have been accounted for. No other mode type is possible.

The only restrictions that the proof needs are the tuned system assumption and equal planet spacing. These restrictions are confined to the plane of the planetary gear. Parameter variations that do not disturb these stipulations have no effect on the properties of the vibration modes. There are no restrictions on the parameters that define the system in the axial direction. Therefore, contrary to intuition, the described mode types hold for configurations that are not symmetric about the plane of the gears, such as:

1. The bearings at opposite ends of a given gear-shaft body have different stiffness properties. An example is tapered roller bearings at one end and spherical roller bearings at the other end.

2. The bearings on a given gear-shaft body are at different distances from the gear plane; both bearings are on the same side of the gear plane; or, there is only one

bearing. An example of such a configuration would be overhung gears and/or carrier.

3. The mass centers of the various gear-shaft bodies are at different axial positions.

4. The contact pattern is off-centered at the gear meshes. This may be due to, for example, lead modifications and deflection of the system under load. Note, however, that the sun-planet contact patterns must be the same at each planet (and the same for the ring-planet meshes).

These four items destroy symmetry about the gear plane, but the modal properties hold for these configurations and any combination thereof.

5.4 Conclusions

We prove that there are exactly three types of vibration modes of any tuned single-stage helical planetary gear system with equally spaced planets. The helical planetary gear system is represented by a three-dimensional lumped parameter model that allows for six degrees of freedom per gear-shaft body supported by bearings at arbitrary axial positions. All vibration modes belong to one of these three types, described below:

1. Rotational-axial modes: The central members rotate and move axially but do not tilt or translate. The modal deflection of the planets are identical. There are 12 rotational-axial modes with distinct natural frequencies.

2. Translational-tilting modes: The central members tilt and translate in-plane but do not rotate or move axially. The modal deflections of all planets are

related to one another according to Eq. (5.54). There are 12 pairs of degenerate translational-tilting modes with natural frequency multiplicity two.

3. Planet modes: Only the planets have modal deflection. Each planet's modal deflection is a known scalar multiple of any other planet's modal deflection. The central members do not move. There are six planet mode sets, where each set consists of $p-3$ degenerate (for $p > 4$) modes having the same natural frequency. Planet modes exist only for systems with four or more planets ($p \geq 4$).

This classification of the vibration modes persists for systems that are not symmetric about the plane of the planetary gear because the proof is valid for arbitrary values of all parameters that lead to such asymmetry.

Chapter 6: Vibration Suppression Rules for 3-D Helical Planetary Gears Using Mesh Phasing

6.1 Introduction

Tooth counts and planet spacing in planetary gears alter the relative phase considering the periodic engagement-disengagement of the gear teeth. This is called planet mesh phasing in the literature. Cunliffe et al. [19] and Schlegel and Mard [95] point out the role of mesh phasing upon vibration reduction. The effectiveness of mesh phasing in vibration reduction has been demonstrated computationally [4, 84] and experimentally [16, 33, 107].

Dynamic analysis using a lumped parameter model, either 2-D [97, 98], or 3-D [40, 43] confirm that mesh phasing works, but they rely on modeling assumptions about the excitation, that is, the fluctuation in gear mesh force is assumed to be from static transmission error, thus limiting the applicability of the findings. Parker [84] explains how mesh phasing eliminates vibration in rotational and translational modes independent of modeling. That explanation, however, is limited to 2-D spur gears and applies to resonance at known mode types [58] of planetary gears.

There are distinct mode types in planetary gears due to their symmetry [19, 40, 42, 97]. Lin and Parker [58, 60] prove the identified properties of mode types in two-dimensional (2-D) spur planetary gears. That proof is extended to include elastic rings [87, 133] and to three-dimensional (3-D) helical planetary gears [22] with a 3-D gear mesh.

Most works cited above except [84] depend on static transmission error or mesh stiffness fluctuation as the excitation to show excitations cancel or add as a result of mesh phasing. With the cancellation of excitations, the dynamic model yields vanishing response. We claim that the symmetry of the system is sufficient to relate dynamic forces, thus the rules of vibration suppression may be stated independent of any dynamic model therefore of any assumptions that come with it.

6.2 Symmetry in Planetary Gears and Its Implications

We consider planetary gears in three-dimensions. The only distinguishable physical features are the tooth counts and planet spacing. Other than those, there are no features to distinguish the state of the system at a given angular position. The symmetry argument implies that forces and moments that develop at the gear meshes must be related with the only distinguishable quantity, their relative phase. Stated differently, the gear mesh forces and moments do not know any better about their state except the relative phase. That is the only quantity to distinguish the state of the system at a given time from another.

The required symmetry implies a tuned system. To name a few stipulations: all planet mass, inertia, bearing stiffnesses are identical, there are no splines on the sun or ring, gears and the carrier are perfectly circular and mounted without run-out

errors, the bearings have equal radial and tangential stiffnesses, and all gear teeth are identical to one another for a given gear. There are no symmetry restrictions on the features of the system except in the circumferential direction, consequently:

1. The system may be asymmetric in the axial direction, for example, shafts that support the gears, carrier, and ring/housing may be overhung, conical or have different stages of thickness. Gears may be helical or spur.

2. The forces and moments may include dynamic effects.

3. There is no restriction on deformations; gear bodies, shafts, housings may be elastic.

Some physical phenomena can destroy the circumferential symmetry even if the manufacturing had been perfectly symmetric. For example, severe vibrations may change the contact conditions at the gears and bearings (such as disengagement). Elastic deformations of a thin ring gear, contact conditions at ring-planet gear meshes may change. In these examples, the symmetry on which the above argument relies is destroyed. Furthermore, this work does not quantify the degree of symmetry destruction that may invalidate the results. In other words, to assess the effectiveness of vibration suppression for a system with an imperfect circumferential symmetry, one needs to perform dynamic analysis.

Figure 6.1 shows a planetary gear with the arbitrarily selected 1st planet, another ith planet, and the base vectors $\mathbf{B}^i$. The bases $\mathbf{B}^i$ are oriented such that the line-of-action of the sun-planet mesh is along $\mathbf{B}_1^i$. Planet spacing is denoted by α_i. The number of teeth on the sun gear is Z_s. The matrix $\mathbf{Q}_i$ that transforms vectors written

in $\mathbf{B}^i$ to $\mathbf{B}^1$ is given by

$$\mathbf{Q}_i = \begin{bmatrix} \cos\alpha_i & -\sin\alpha_i & 0 \\ \sin\alpha_i & \cos\alpha_i & 0 \\ 0 & 0 & 1 \end{bmatrix} \tag{6.1}$$

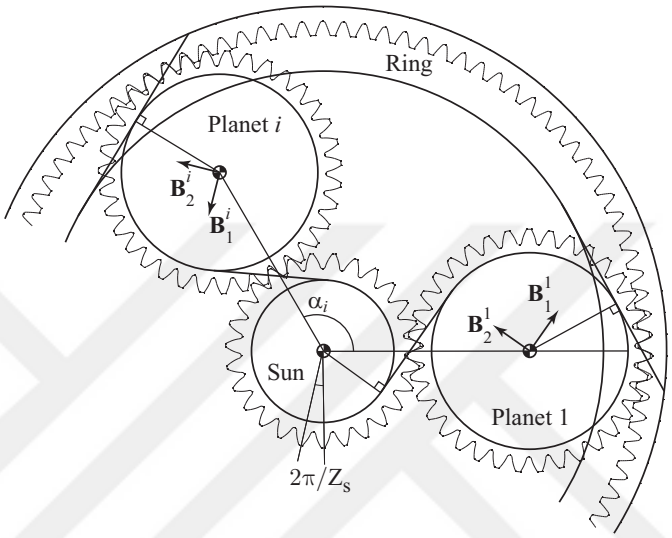

Figure 6.1: Bases and planet spacing definition of a single-stage planetary gear.

6.2.1 Gear Mesh Forces and Moments

The force and moment vectors at the ith gear mesh can be written as $\mathbf{F}_i^h(\theta)$ and $\mathbf{M}_i^h(\theta)$, where θ parametrizes angular position of the gear mesh. The superscript $h = s, r, c$ denotes the subject member: the sun, ring, and carrier, respectively. For example, $\mathbf{F}_3^s(\theta)$ denotes the mesh force on the sun from the 3rd sun-planet mesh. Because single-stage planetary gears have one mesh frequency, the angular position is a function of time, $\theta(t) = (\omega t + \phi_i)$ with known mesh frequency ω and phase angle ϕ_i of the ith mesh relative to the arbitrarily chosen first mesh. The crucial step is assuming the force and moment fluctuations are periodic with mesh period $T = 1/\omega$.

This assumption implies steady-state and linear time-invariant vibrations. It is not valid if there are transients with a natural period. Similarly, nonlinear response can have sub/super-harmonic components. Vibrations driven by parametric fluctuations may be locked at the natural period. In these cases, the assumption is not valid. Figure 6.2 describes the mesh force and moment fluctuation at two planet meshes, issutrates the mesh phase ϕ_i and the mesh period T.

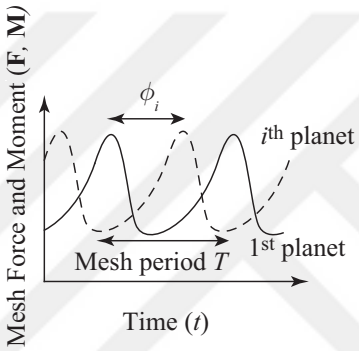

Figure 6.2: Force and moment fluctuation showing the mesh period and the relative phase at two arbitrarily chosen planet meshes.

Fourier expansion of the forces and moments using P harmonic components in the $\mathbf{B}^i$ basis gives

$$\mathbf{F}_i^h(t) = \sum_{p=1}^{P} \mathbf{F}_{i,p}^h(t), \quad \mathbf{M}_i^h(t) = \sum_{p=1}^{P} \mathbf{M}_{i,p}^h(t) \tag{6.2}$$

$$\mathbf{F}_{i,p}^h(t) = \Re\left[\begin{pmatrix} f_p^{h,1} \\ f_p^{h,2} \\ f_p^{h,3} \end{pmatrix} e^{j(p\omega t + p\phi_i)}\right], \quad \mathbf{M}_{i,p}^h(t) = \Re\left[\begin{pmatrix} m_p^{h,1} \\ m_p^{h,2} \\ m_p^{h,3} \end{pmatrix} e^{j(p\omega t + p\phi_i)}\right] \tag{6.3}$$

with complex $f_p^{h,i} = |f_p^{h,i}|e^{j\gamma_p}$, $i = 1, 2, 3$ where γ_p is the phase of the pth harmonic component. Defining $\mathbf{f}_p^h = \left(f_p^{h,1}, f_p^{h,2}, f_p^{h,3}\right)^T$ and $\mathbf{m}_p^h = \left(m_p^{h,1}, m_p^{h,2}, m_p^{h,3}\right)^T$, the forces

and moments on the ith planet mesh on the central members at the pth harmonic, in $\mathbf{B^i}$, are

$$\mathbf{F}^h_{i,p}(t) = \Re\left[\mathbf{f}^h_p e^{j(p\omega t + p\phi_i)}\right], \quad \mathbf{M}^h_{i,p}(t) = \Re\left[\mathbf{m}^h_p e^{j(p\omega t + p\phi_i)}\right] \tag{6.4}$$

Transforming the forces and moments to the 1st sun-planet basis $\mathbf{B}^1$ gives

$$\begin{aligned}
\mathbf{F}^h_{i,p}(t) =& \Re\left[\begin{pmatrix} f^{h,1}_p \cos\alpha_i - f^{h,2}_p \sin\alpha_i \\ f^{h,1}_p \sin\alpha_i + f^{h,2}_p \cos\alpha_i \\ f^{h,3}_p \end{pmatrix} e^{j(p\omega t + p\phi_i)}\right], \\
\mathbf{M}^h_{i,p}(t) =& \Re\left[\begin{pmatrix} m^{h,1}_p \cos\alpha_i - m^{h,2}_p \sin\alpha_i \\ m^{h,1}_p \sin\alpha_i + m^{h,2}_p \cos\alpha_i \\ m^{h,3}_p \end{pmatrix} e^{j(p\omega t + p\phi_i)}\right]
\end{aligned} \tag{6.5}$$

The sum of forces and moments from all sun-planet and ring-planet meshes (N: number of planets) at the pth harmonic in $\mathbf{B}^1$ is given by

$$\mathbf{F}^h_p(t) = \sum_{i=1}^{N} \mathbf{F}^h_{i,p}(t), \quad \mathbf{M}^h_p(t) = \sum_{i=1}^{N} \mathbf{M}^h_{i,p}(t) \tag{6.6}$$

6.2.2 Planet Gears

Each planet experiences a net, equal-and-opposite mesh force and moment from its sun-planet and the ring-planet mesh. The forces and moments on the ith planet from the sun and the ring meshes in the $\mathbf{B}^i$ basis are

$$\begin{aligned}
\mathbf{F}^{\mathrm{pl}}_{i,p}(t) =& -\mathbf{F}^s_{i,p}(t) - \mathbf{F}^r_{i,p}(t) = -\mathbf{F}^c_{i,p}(t) \\
\mathbf{M}^{\mathrm{pl}}_{i,p}(t) =& -\mathbf{M}^s_{i,p}(t) - \mathbf{M}^r_{i,p}(t) = -\mathbf{M}^c_{i,p}(t)
\end{aligned} \tag{6.7}$$

$$\mathbf{F}^{\mathrm{pl}}_{i,p}(t) = -\Re\left[\mathbf{f}^c_p e^{j(p\omega t + p\phi_i)}\right], \quad \mathbf{M}^{\mathrm{pl}}_{i,p}(t) = -\Re\left[\mathbf{m}^c_p e^{j(p\omega t + p\phi_i)}\right] \tag{6.8}$$

6.3 Phasing Rules

The mesh phase at a given harmonic is $p\phi_i = pZ_s\alpha_i$. When planets are equally-spaced

$$\alpha_i = \frac{2\pi i}{N} \tag{6.9}$$

the mesh phase becomes $p\phi_i = p\dfrac{2\pi Z_s i}{N}$. Defining

$$k = \text{mod}(pZ_s, N), \text{ stated differently } \frac{pZ_s}{N} = n + \frac{k}{N}\,,\ n \in \mathbb{Z} \tag{6.10}$$

the mesh phase becomes $p\phi_i = \dfrac{2\pi p Z_s i}{N} = 2\pi i n + \dfrac{2\pi i k}{N} = k\alpha_i$, where $2\pi i n$ is dropped because $n \in \mathbb{Z}$.

When the planets are diametrically-opposed $\alpha_{i+N/2} = \alpha_i + \pi$, so the mesh phase is $p\phi_{i+N/2} = pZ_s\alpha_{i+N/2} = pZ_s\alpha_i + pZ_s\pi$. Defining

$$k = pZ_s \tag{6.11}$$

the mesh phase becomes $p\phi_i = k\alpha_i$. For $i > N/2$ one gets $p\phi_{i+N/2} = k\alpha_{i+N/2} = k\alpha_i + k\pi$, giving

$$\sum_{i=1}^{N} e^{jk\alpha_i} = \begin{cases} 2\displaystyle\sum_{i=1}^{N/2} e^{jk\alpha_i} \neq 0 & k : \text{even} \\ 0 & k : \text{odd} \end{cases} \tag{6.12}$$

so the important property of k is that whether it is odd or even. With these definitions of k, for equally-spaced Eq. (6.10) and diametrically-opposed planets Eq. (6.11), the mesh phase has the same expression, that is

$$p\phi_i = k\alpha_i \tag{6.13}$$

Substitution of Eq. (6.13) into Eq. (6.4) gives the individual forces and moments on central members in $\mathbf{B}^i$ as

$$\begin{aligned} \mathbf{F}^h_{i,p}(t) &= \Re\left[\mathbf{f}^h_p e^{j(p\omega t + k\alpha_i)}\right] = \Re\left[\mathbf{f}^h_p e^{jk\alpha_i} e^{jp\omega t}\right] \\ \mathbf{M}^h_{i,p}(t) &= \Re\left[\mathbf{m}^h_p e^{jk\alpha_i} e^{jp\omega t}\right] \end{aligned} \tag{6.14}$$

The resultant forces and moments on central members are obtained by substitution of Eq. (6.10) into Eq. (6.6) in $\mathbf{B}^1$ as

$$\begin{aligned}
\mathbf{F}_p^h(t) =& \Re\left[\begin{pmatrix} \dfrac{f_p^{h,1}+jf_p^{h,2}}{2}\displaystyle\sum_{i=1}^{N} e^{j(k+1)\alpha_i} + \dfrac{f_p^{h,1}-jf_p^{h,2}}{2}\displaystyle\sum_{i=1}^{N} e^{j(k-1)\alpha_i} \\ \dfrac{f_p^{h,2}-jf_p^{h,1}}{2}\displaystyle\sum_{i=1}^{N} e^{j(k+1)\alpha_i} + \dfrac{f_p^{h,2}+jf_p^{h,1}}{2}\displaystyle\sum_{i=1}^{N} e^{j(k-1)\alpha_i} \\ f_p^{h,3}\displaystyle\sum_{i=1}^{N} e^{jk\alpha_i} \end{pmatrix} e^{jp\omega t}\right] \\
\mathbf{M}_p^h(t) =& \Re\left[\begin{pmatrix} \dfrac{m_p^{h,1}+jm_p^{h,2}}{2}\displaystyle\sum_{i=1}^{N} e^{j(k+1)\alpha_i} + \dfrac{m_p^{h,1}-jm_p^{h,2}}{2}\displaystyle\sum_{i=1}^{N} e^{j(k-1)\alpha_i} \\ \dfrac{m_p^{h,2}-jm_p^{h,1}}{2}\displaystyle\sum_{i=1}^{N} e^{j(k+1)\alpha_i} + \dfrac{m_p^{h,2}+jm_p^{h,1}}{2}\displaystyle\sum_{i=1}^{N} e^{j(k-1)\alpha_i} \\ m_p^{h,3}\displaystyle\sum_{i=1}^{N} e^{jk\alpha_i} \end{pmatrix} e^{jp\omega t}\right]
\end{aligned} \tag{6.15}$$

The resultant forces and moments on a planet is rewritten by substitution of Eq. (6.13) into Eq. (6.8) as

$$\begin{aligned}
\mathbf{F}_{i,p}^{\mathrm{pl}}(t) &= -\Re\left[\mathbf{f}_p^c e^{j(p\omega t+k\alpha_i)}\right] = -\Re\left[\mathbf{f}_p^c e^{jk\alpha_i} e^{jp\omega t}\right] \\
\mathbf{M}_{i,p}^{\mathrm{pl}}(t) &= -\Re\left[\mathbf{m}_p^c e^{j(p\omega t+k\alpha_i)}\right] = -\Re\left[\mathbf{m}_p^c e^{jk\alpha_i} e^{jp\omega t}\right]
\end{aligned} \tag{6.16}$$

Equations (6.14), (6.15), and (6.16) are crucial for the rest of the analysis as they combine the mesh phase with planet spacing. For equally-spaced planets, there are three possible phase relations in Eq. (6.10): In-phase ($k = 0$), sequential-phase ($k = 1, N-1$), and counter-phase ($k = 2, 3, \ldots, N-2$). For diametrically-opposed planet spacing, there are two possible phase relations: In-phase (k: even) and out-of-phase (k: odd).

In what follows substitution of the phasing relations into forces and moments given by Eqs. (6.14), (6.15), and (6.16) yields special mathematical relations.

6.3.1 Equal Planet Spacing

In-Phase

When $\dfrac{pZ_s}{N} \in \mathbb{Z}$, then $k = 0$. An in-phase design is independent of the harmonic p. Forces and moments on the sun and ring at a given planet mesh, from Eq. (6.14) for $k = 0$, in $\mathbf{B}^i$, are

$$\mathbf{F}^h_{1,p}(t) = \mathbf{F}^h_{2,p}(t) = \ldots = \mathbf{F}^h_{N,p}(t), \quad \mathbf{M}^h_{1,p}(t) = \mathbf{M}^h_{2,p}(t) = \ldots = \mathbf{M}^h_{N,p}(t) \tag{6.17}$$

so forces and moments at each planet mesh on the sun and ring are identical. The resultant forces and moments on the central members are given in Eq. (6.15) for $k = 0$, in $\mathbf{B}^1$, as

$$\mathbf{F}^h_p(t) = \begin{pmatrix} 0 \\ 0 \\ N\Re\left[f^{h,3}_p e^{jp\omega t}\right] \end{pmatrix}, \quad \mathbf{M}^h_p(t) = \begin{pmatrix} 0 \\ 0 \\ N\Re\left[m^{h,3}_p e^{jp\omega t}\right] \end{pmatrix} \tag{6.18}$$

so radial forces and tilting moments vanish, but axial thrust and torques exist. The net forces and moments on a planet, by Eq. (6.16), in $\mathbf{B}^i$, are equal

$$\mathbf{F}^{\mathrm{pl}}_{1,p}(t) = -\mathbf{F}^c_{2,p}(t) = \ldots = -\mathbf{F}^{\mathrm{c}}_{N,p}(t), \quad \mathbf{M}^{\mathrm{pl}}_{1,p}(t) = -\mathbf{M}^c_{2,p}(t) = \ldots = -\mathbf{M}^c_{N,p}(t) \tag{6.19}$$

Sequential-Phase (Out-of-Phase)

If a design is not in-phase $k \neq 0$, then it is out-of-phase. An out-of-phase design for equally-spaced planets fall into two subcategories: sequential-phase and counter-phase. Sequential-phase is defined by $\dfrac{pZ_s \pm 1}{N} \in \mathbb{Z}$, then $k = 1, N-1$ (or $k = \pm 1$). It exists for any number of planets $N \geq 2$. A three planet design, if out-of-phase, can only be sequentially-phased because only $k = 1$ or $k = 2$ are possible. Forces and moments on the sun and ring from each planet, given in from Eq. (6.14) in $\mathbf{B}^i$, are

related by

$$\begin{aligned}\mathbf{F}_{i,p}^{h}(t) =& \Re\left[\left(\mathbf{f}_{p}^{h}\cos\alpha_i \pm j\mathbf{f}_{p}^{h}\sin\alpha_i\right)e^{jp\omega t}\right]\\ \mathbf{M}_{i,p}^{h}(t) =& \Re\left[\left(\mathbf{m}_{p}^{h}\cos\alpha_i \pm j\mathbf{m}_{p}^{h}\sin\alpha_i\right)e^{jp\omega t}\right]\end{aligned} \tag{6.20}$$

The resultant forces and moments on central members, from Eq. (6.15) with $k = \pm 1$, are

$$\mathbf{F}_{p}^{h}(t) = \Re\left[\begin{pmatrix} \frac{N}{2}\left(f_{p}^{h,1} \mp j f_{p}^{h,2}\right) \\ \frac{N}{2}\left(f_{p}^{h,2} \pm j f_{p}^{h,1}\right) \\ 0 \end{pmatrix} e^{jp\omega t}\right], \quad \mathbf{M}_{p}^{h}(t) = \Re\left[\begin{pmatrix} \frac{N}{2}\left(m_{p}^{h,1} \mp j m_{p}^{h,2}\right) \\ \frac{N}{2}\left(m_{p}^{h,2} \pm j m_{p}^{h,1}\right) \\ 0 \end{pmatrix} e^{jp\omega t}\right] \tag{6.21}$$

so the pth harmonic of radial forces and tilting moments exist, but the axial thrust and torques vanish. The net forces and moments on each planet from Eq. (6.16) are related by

$$\begin{aligned}\mathbf{F}_{i,p}^{\mathrm{pl}}(t) =& -\Re\left[\left(\mathbf{f}_{p}^{c}\cos\alpha_i \pm j\mathbf{f}_{p}^{c}\sin\alpha_i\right)e^{jp\omega t}\right]\\ \mathbf{M}_{i,p}^{\mathrm{pl}}(t) =& -\Re\left[\left(\mathbf{m}_{p}^{c}\cos\alpha_i \pm j\mathbf{m}_{p}^{c}\sin\alpha_i\right)e^{jp\omega t}\right]\end{aligned} \tag{6.22}$$

Counter-Phase (Out-of-Phase)

In systems with four or more planets ($N > 3$), more out-of-phase designs are possible that are not sequentially-phased. Counter-phase is defined by $k = 2, 3, \ldots, N-2$. Forces on the sun and ring from each gear mesh, given by Eq. (6.14) for $k = 2, 3, \ldots, N-2$ at the pth harmonic, are

$$\begin{aligned}\mathbf{F}_{i,p}^{h}(t) =& \Re\left[\left(\mathbf{f}_{p}^{h}\cos k\alpha_i + j\mathbf{f}_{p}^{h}\sin k\alpha_i\right)e^{jp\omega t})\right]\\ \mathbf{M}_{i,p}^{h}(t) =& \Re\left[\left(\mathbf{m}_{p}^{h}\cos k\alpha_i + j\mathbf{m}_{p}^{h}\sin k\alpha_i\right)e^{jp\omega t})\right]\end{aligned} \tag{6.23}$$

The resultant forces and moments on central members, given by Eq. (6.15) for $k = 2, 3, \ldots, N-2$, vanish

$$\mathbf{F}_{p}^{h}(t) = (0,0,0)^{T}, \quad \mathbf{M}_{p}^{h}(t) = (0,0,0)^{T} \tag{6.24}$$

The forces and moments on a planet from Eq. (6.16) are

$$\begin{aligned}\mathbf{F}_{i,p}^{\mathrm{pl}}(t) &= -\,\Re\left[\left(\mathbf{f}_p^c\cos k\alpha_i + j\mathbf{f}_p^c\sin k\alpha_i\right)e^{jp\omega t})\right]\\ \mathbf{M}_{i,p}^{\mathrm{pl}}(t) &= -\,\Re\left[\left(\mathbf{m}_p^c\cos k\alpha_i + j\mathbf{m}_p^c\sin k\alpha_i\right)e^{jp\omega t})\right]\end{aligned} \tag{6.25}$$

Equation (6.25) reveals that force and moment fluctuations on any planet can be represented by a constant multiple w_i of the force and moment fluctuations on the first planet, given by

$$\begin{aligned}\mathbf{F}_{i,p}^{\mathrm{pl}}(t) =&\Re\left[w_i\left(\mathbf{f}_p^c\cos k\alpha_1 + j\mathbf{f}_p^c\sin k\alpha_1\right)e^{jp\omega t})\right]\\ \mathbf{M}_{i,p}^{\mathrm{pl}}(t) =&\Re\left[w_i\left(\mathbf{m}_p^c\cos k\alpha_1 + j\mathbf{m}_p^c\sin k\alpha_1\right)e^{jp\omega t})\right]\\ w_i =&e^{jk(\alpha_i-\alpha_1)}\end{aligned} \tag{6.26}$$

The same argument is valid for individual mesh force and moment fluctuations on the sun and ring gear by Eq. (6.23); the force and moment fluctuations from any planet mesh can be represented by a constant multiple w_i of the force and moment fluctuations from the first planet mesh. These findings for equally-spaced planets are summarized in Table 6.1.

6.3.2 Diametrically Opposed Planet Spacing

Using Eqs. (6.15) and (6.16), we get forces and moments for two cases: in-phase (k: even) and out-of-phase (k: odd).

In-phase

When the planet meshes are in-phase, k: even ($k \pm 1$: odd). Substitution of Eq. (6.12) into Eq. (6.15) and Eq. (6.16) gives the resultant forces and moments on

Table 6.1: Forces and moments for equal planet spacing on central members and planets at the pth harmonic, for given number of gear teeth on the sun Z_s, and number of planets N. In-phase relations are given by Eqs. (6.18) and (6.19), sequential-phase (Sq.) relations are given by Eqs. (6.21) and (6.22), and counter-phase (Ct.) relations are given by Eqs. (6.24) and (6.26).

		Central Members		**Planets**
Phase	$k = \mathrm{mod}(pZ_s, N)$	**Forces and moments**	**Thrust and torque**	**All forces and moments**
a) In	$k = 0$ (for any p)	0	$\neq 0$	Identical
b) Sq.	$k = 1, N-1$	$\neq 0$	0	Related
c) Ct.	$k = 2, \ldots, N-2$	0	0	Related

the central members and planets as

$$\mathbf{F}_p^h(t) = \begin{pmatrix} 0 \\ 0 \\ 2\Re\left[f_p^{h,3} \sum_{i=1}^{N/2} e^{jk\alpha_i} e^{jp\omega t} \right] \end{pmatrix}, \quad \mathbf{M}_p^h(t) = \begin{pmatrix} 0 \\ 0 \\ 2\Re\left[m_p^{h,3} \sum_{i=1}^{N/2} e^{jk\alpha_i} e^{jp\omega t} \right] \end{pmatrix} \tag{6.27}$$

$$\mathbf{F}_{i,p}^{\mathrm{pl}}(t) = -\Re\left[\mathbf{f}_p^c e^{jk\alpha_i} e^{jp\omega t} \right], \quad \mathbf{M}_{i,p}^{\mathrm{pl}}(t) = -\Re\left[\mathbf{m}_p^c e^{jk\alpha_i} e^{jp\omega t} \right] \tag{6.28}$$

so radial forces and tilting moments vanish but axial thrust and torques exist.

Out-of-phase

When the planet meshes are out-of-phase, k: odd ($k \pm 1$: even). Substitution of Eq. (6.12) into Eq. (6.15) and Eq. (6.16) gives the resultant forces and moments on

the central members and planets as

$$\begin{aligned}
\mathbf{F}_p^h(t) =& \Re\left[\begin{pmatrix} \left(f_p^{s,1} + jf_p^{s,2}\right)\sum_{i=1}^{N/2}\left(e^{j(k+1)\alpha_i} + e^{j(k-1)\alpha_i}\right) \\ \left(f_p^{s,2} - jf_p^{s,1}\right)\sum_{i=1}^{N/2}\left(e^{j(k+1)\alpha_i} + e^{j(k-1)\alpha_i}\right) \\ 0 \end{pmatrix} e^{jp\omega t}\right] \\
\mathbf{M}_p^h(t) =& \Re\left[\begin{pmatrix} \left(m_p^{s,1} + jm_p^{s,2}\right)\sum_{i=1}^{N/2}\left(e^{j(k+1)\alpha_i} + e^{j(k-1)\alpha_i}\right) \\ \left(m_p^{s,2} - jm_p^{s,1}\right)\sum_{i=1}^{N/2}\left(e^{j(k+1)\alpha_i} + e^{j(k-1)\alpha_i}\right) \\ 0 \end{pmatrix} e^{jp\omega t}\right]
\end{aligned} \tag{6.29}$$

$$\mathbf{F}_p^{\mathrm{pl}}(t) = -\Re\left[\mathbf{f}_p^c e^{jk\alpha_i} e^{jp\omega t}\right], \quad \mathbf{M}_p^{\mathrm{pl}}(t) = -\Re\left[\mathbf{m}_p^c e^{jk\alpha_i} e^{jp\omega t}\right] \tag{6.30}$$

so axial thrust and torques vanish but radial forces and tilting moments exist. These findings for diametrically-opposed planet spacing are summarized in Table 6.2.

Table 6.2: Forces and moments for diametrically-opposed planet spacing on central members and planets at the pth harmonic for given number of gear teeth on the sun Z_s. In-phase relations are given by Eqs. (6.27) and (6.28), and out-of-phase relations are given by Eqs. (6.29) and (6.30).

		Central Members	
Phase	$k = pZ_s$	**Radial forces**	**Axial thrust and torque**
a) In	k: even (for any p)	0	$\neq 0$
b) Out	k: odd	$\neq 0$	0

6.4 Conclusions

Net force and moment fluctuations in planetary gears with equally-spaced and diametrically-opposed planet spacing are formulated. There are two general fluctuations of forces and moments: in-phase and out-of-phase. The formulation depends solely on the circumferential symmetry of planetary gears and thus is independent of the physical model. The findings apply to static and dynamic cases and to systems with axial asymmetry, e.g., gears may be helical and shafts may be overhung from bearings. One can eliminate certain harmonic components of fluctuating forces and/or moments on central members using the rules given in Table 6.1 with equally-spaced planets and in Table 6.2 with diametrically-opposed planets.

For equally-spaced planets, if a design is in-phase, all mesh force and moment fluctuations are in-phase at any harmonic. An out-of-phase design can fall into either sequential-phase or counter-phase cases. Force and moment suppression rules are summarized below:

1. In-phase, $k = 0$. Net radial force and tilting moment fluctuations on central members vanish but axial thrust and torque fluctuations exist. All net force and moment fluctuations on each planet are identical.

2. Sequential-phase, $k = \pm 1$ (or $k = 1, N-1$). Net axial thrust and torque fluctuations on central members vanish but radial force and tilting moment fluctuations exist. All net force and moment fluctuations on each planet are related with a known transformation given in Eq. (6.22).

3. Counter-phase , $k = 2, 3, \ldots, N-2$. All net force and moment fluctuations on central members vanish. All net force and moment fluctuations on each planet are multiples of one another, as given by Eq. (6.26)

For diametrically-opposed planets, if a design is in-phase, all mesh force and moment fluctuations are in-phase at any harmonic. Otherwise, the fluctuations depend on the harmonic of interest as summarized below:

1. In-phase, k : even. Net radial force and tilting moment fluctuations on central members vanish but axial thrust and torque fluctuations exist.

2. Out-of-phase, k : odd. Net axial thrust and torque fluctuations on central members vanish but radial force and tilting moment fluctuations exist.

Chapter 7: Conclusions and Future Work

7.1 Conclusions

This body of work investigates the vibration of gears that arise from the interactions between 3-D motions of the gears and the 3-D nonlinear gear contact. The load distributions along the gear contact lines generate tilting and twisting moments and an axial thrust force as well as the useful power-transmitting mesh force. The load distribution depends on relative angular twist and translational displacements, so the gear mesh forces and moments respond to spatial gear motions. With large twisting and translation of gears, portions of contact lines lose contact (partial contact loss), thus introducing nonlinearity.

7.1.1 Nonlinearity in Gear Pairs Using a Lumped-Parameter Model

A 3-D lumped-parameter model is developed to consider the nonlinear force and moment transmission at the meshing gear teeth. The nonlinearity of the gear mesh is due to partial contact loss. It is shown that the lumped-parameter model needs only a translational stiffness acting at the calculated center of stiffness location and a twist stiffness to account for the net force and moment arising from an arbitrary load distribution including partial contact loss. The twist stiffness generates a moment,

named spread-twist moment, which is solely due to the spread of contact across the tooth face. The movement of the translational stiffness across the tooth face generates an additional moment, named off-mid-plane moment. The total twist stiffness is the sum of the spread-twist and the off-mid-plane twist stiffnesses.

The translational and twist stiffnesses and the center of stiffness location depend strongly on the relative translation and twist at the gear mesh. Tooth surface modifications smoothen the translational stiffness profile and decrease the twist stiffness. Spur gears have a symmetric nonlinear twist stiffness profile, while helical gears have an asymmetric twist stiffness profile. The twist stiffnesses fluctuate periodically with gear rotation except for aligned spur gears. The resulting fluctuating moments excite twisting vibrations.

7.1.2 Twisting Vibration and Partial Contact Loss in Gear Pairs

In a gear pair, there are two gear mesh modes: 1) a mesh twist mode where the twist stiffness is active, and 2) a mesh deflection mode where the translational stiffness is active. Resonances of both modes are nonlinear due to partial contact loss.

Near the mesh deflection mode resonance with modified gears, there is partial contact loss evident from the dynamic contact pattern and differences between the static and dynamic translational mesh stiffness. With increasing vibration amplitude, the dynamic translational stiffness decreases and so does the dynamic natural frequency. Consequently, the peak response frequency is lower than the natural frequency. Unmodified gears exhibit only total contact loss, if at all. Modifications combined with dynamic displacements, therefore, give rise to partial contact loss in the mesh deflection mode resonance.

Dynamic response near the mesh twist mode is nonlinear as a result of partial contact loss. This is seen from the increasing distortion in the dynamic contact pattern as the mesh frequency nears the mesh twist mode natural frequency. The nonlinearity is also evident in the dynamic spread-twist stiffness; it gradually deviates from the static stiffness as the operating mesh frequency approaches the natural frequency. The resonant peak occurs at a higher frequency than the natural frequency because of the nonlinear properties of total pinion and gear twist stiffnesses and the coupling-twist stiffnesses. In particular, the drop in the dynamic mean value of the coupling-twist stiffness increases the dynamic natural frequency and so the resonant frequency.

Partial contact loss, whether it is a consequence of mesh deflection combined with tooth surface modifications or mesh twist, makes the dynamic response nonlinear. At nonlinear peaks, the dynamic contact load distribution is distorted compared with the static contact load distribution.

7.1.3 Nonlinear Vibration of Gears with Tooth Surface Modifications and Sphere/Half-Space Contact

An analytical solution for the nonlinear vibration of gear pairs that exhibit partial and total contact loss is given. The gear teeth can have arbitrary tooth surface modifications. Unlike models in the literature that are excited by static transmission error or time-varying mesh stiffness, neither the excitation nor the nonlinearity are *a priori* specified. Instead, the excitation and the nonlinearity arise from Fourier and Taylor series expansions of the force-deflection function, which is provided by an independent source, such as a finite element model or Hertz contact formula. Quadratic and cubic nonlinear terms capture partial contact loss nonlinearity. Time-dependent fluctuations give dynamic excitation.

Although this work focuses on gear pairs with tooth surface modifications, the physical system from which the force-deflection function comes is not limited to gear pairs; sphere/half-space contact vibrations are also analyzed.

The method of multiple scales gives the dynamic response in terms of a frequency-amplitude relation. Comparisons with experiments from the literature on gear vibrations and sphere/half-space contact vibrations verify the method. The perturbation solution traces the nonlinear response due to partial contact loss and total contact loss. The nonlinear dynamic response deviates from linearized dynamic response although gear contact is maintained. This is the result of dynamic partial contact loss. Total contact loss appears in cases where the vibration amplitude exceeds an analytically found threshold value.

7.1.4 Modal Properties of Three-Dimensional Helical Planetary Gears

The structured modal properties of single-stage helical planetary gears with equally spaced planets are categorized and mathematically proved. The equivalent stiffness model of the gear mesh enables dynamic analysis of 3-D helical planetary gears. Three types of modes are observed following the modal analysis of a few example systems:

1. Rotational-axial modes: The central members rotate and move axially but do not tilt or translate. The modal deflection of the planets are identical. There are 12 rotational-axial modes with distinct natural frequencies.

2. Translational-tilting modes: The central members tilt and translate in-plane but do not rotate or move axially. The modal deflections of all planets are

related to one another according to Eq. (5.54). There are 12 pairs of degenerate translational-tilting modes with natural frequency multiplicity two.

3. Planet modes: Only the planets have modal deflection. Each planet's modal deflection is a known scalar multiple of any other planet's modal deflection. The central members do not move. There are six planet mode sets, where each set consists of $p-3$ degenerate (for $p > 4$) modes having the same natural frequency. Planet modes exist only for systems with four or more planets ($p \geq 4$).

These three types of modes are mathematically proven to be the only possible mode types. The proof consists of constructing a candidate mode from the observed properties listed above and substitution of these candidate modes into the full eigenvalue problem. This substitution yields three uncoupled reduced eigenvalue problems, the modes from which account for all the modes of the complete system, thus completing the proof. The properties of the vibration modes persists for systems that are not symmetric about the plane of the planetary gear, for example, different bearing stiffnesses at shaft ends, shaft stages with different thickness, and overhung shafts.

7.1.5 Vibration Suppression Rules for 3-D Helical Planetary Gears Using Mesh Phasing

A set of rules is found that eliminates certain harmonics of the net force and moment fluctuations on the central members (sun, ring carrier) of planetary gears. The analysis method relies solely on circumferential symmetry. The only distinguishable feature of one planet mesh from any other is its relative phase angle. The analysis

is independent from modeling assumptions provided that the system behaves linearly and is isotropic. The findings apply equally to static and steady-state dynamic response.

For equally-spaced planets, 3-D force/moment fluctuations from the gear mesh fall under three categories: 1) In-phase, 2) Sequential-phase, and 3) Counter-phase. Considering the forces and moments on central members, in-phase designs eliminate net radial force and tilting moment fluctuations, sequential-phase designs eliminate net axial thrust and torque fluctuations, and counter-phase designs eliminate all net force and moment fluctuations. These three phasing conditions yield distinctive relations in force and moment fluctuations on each planet and each mesh. In counter-phase designs, the net force and moment fluctuations on any planet are a known constant multiple of the net force and moment fluctuations on the arbitrarily chosen first planet. For diametrically-opposed planets, there are two phasing conditions: 1) In-phase, which eliminates net radial force and tilting moment fluctuations on the central members, and 2) Out-of-phase, which eliminates net axial thrust and torque fluctuations on central members.

7.2 Future Work

7.2.1 Equivalent Stiffnesses as Approximate Functions to Replace Contact Algorithms in Dynamic Analysis

The translational and twist stiffnesses and the center of stiffness depend on relative mesh deflection, relative mesh twist, and time. This dependence may be approximated using a polynomial curve-fit and Fourier series. Preliminary polynomial approximation for the translational stiffness, spread-twist stiffness, and the center of stiffness are shown in Figure 7.1. Comprehensive approximations must include mesh

deflection $\bar{\delta}$, twist γ, and time t such that

$$k_m = k_m\left(\bar{\delta}, \gamma, t\right), \quad k_t = k_t\left(\bar{\delta}, \gamma, t\right), \quad \bar{b} = \bar{b}\left(\bar{\delta}, \gamma, t\right), \quad \bar{c} = \bar{c}\left(\bar{\delta}, \gamma, t\right) \tag{7.1}$$

These approximate functions for the mesh stiffness, twist stiffness and center of stiffness can replace contact algorithms to enable fast nonlinear static and dynamic analysis.

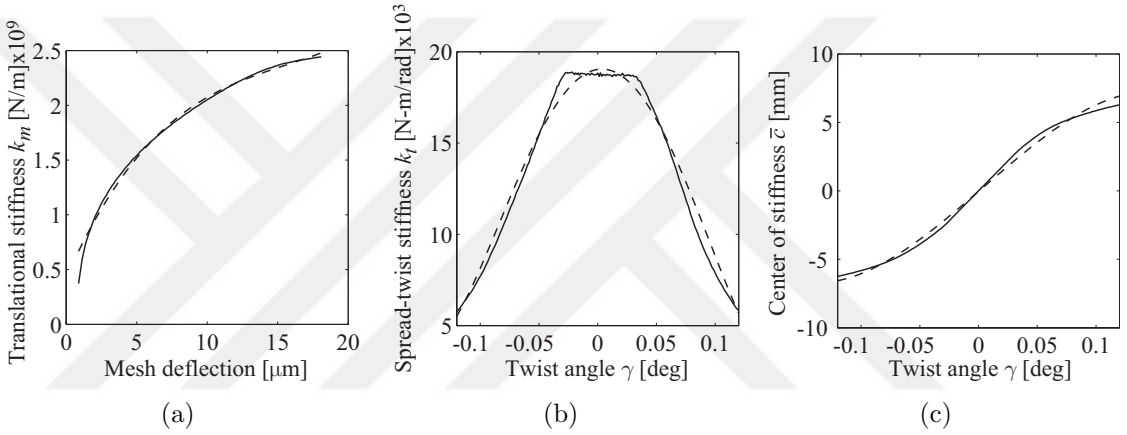

Figure 7.1: Numerical data (solid line) and cubic polynomial approximation $P = \sum_{i=1}^{n} a_i x^i$ (dashed line). (a) Mesh stiffness k_m versus mesh deflection with $a_3 = 0.03$, $a_2 = -0.11$, $a_1 = 0.31$, $a_0 = 2.12$. (b) Spread-twist stiffness k_t versus mesh twist with $a_4 = 1.47$, $a_3 = 0.29$, $a_2 = -9.71$, $a_1 = -1.4$, $a_0 = 19$. (c) Center of stiffness stiffness $\bar{c}$ versus mesh twist with $a_3 = -0.77$, $a_2 = -0.15$, $a_1 = 6.3$, $a_0 = 0.68$.

7.2.2 Analytical Solution for Twisting Vibrations of Gear Pairs

There is a twist vibration mode in gear pairs as explored in Chapter 3, and its resonance is nonlinear. In a twist vibration mode, only pinion and gear twist degrees-of-freedom θ_p and θ_g are active. As one degree-of-freedom system approximates mesh

deflection vibrations [11, 26, 30], it is likely that a two degree-of-freedom system can approximate the twist vibrations. Such approximation is given by

$$\begin{bmatrix} I_p & 0 \\ 0 & I_g \end{bmatrix} \begin{pmatrix} \ddot{\theta}_p \\ \ddot{\theta}_g \end{pmatrix} + \left(\begin{bmatrix} k_{pt} & k_{ct} \\ k_{ct} & k_{gt} \end{bmatrix} + \mathbf{B} \right) \begin{pmatrix} \theta_p \\ \theta_g \end{pmatrix} = \begin{pmatrix} m_p(t) \\ m_g(t) \end{pmatrix} \tag{7.2}$$

where I_p and I_g are pinion and gear inertias, k_{pt} and k_{gt} are the total pinion and gear twist stiffnesses, k_{ct} is the coupling twist stiffness, and $\mathbf{B}$ contains the appropriate boundary conditions, for example, bearing stiffnesses. Fluctuating twist moments $m_p(t)$ and $m_g(t)$ can approximate vibration excitation. Figure 7.2 compares the instantaneous dynamic twist stiffnesses at twist mode resonant frequency with the static mean value of twist stiffness at a twist angle for a helical gear pair with modifications. The dynamic and static values are not very different, so in a polynomial approximation

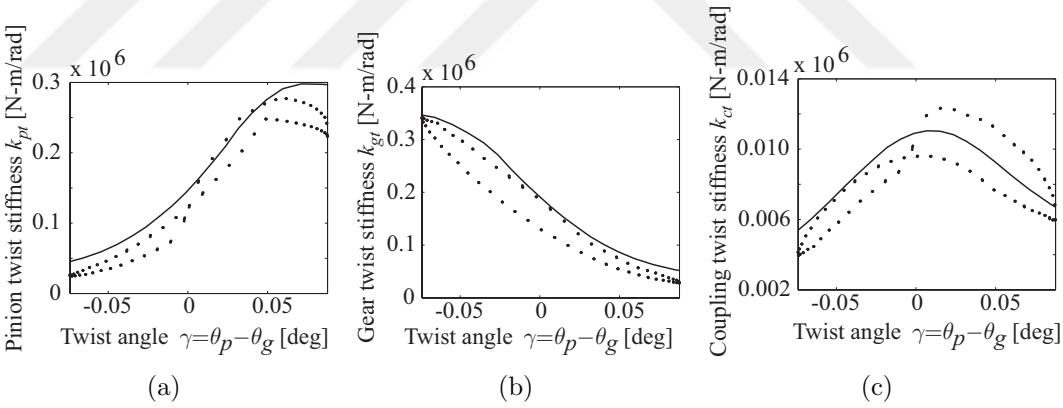

Figure 7.2: Instantaneous dynamic twist stiffnesses in a mesh period (dots), mean value of twist stiffness in a mesh period for a twist angle (solid line). (a) Pinion twist stiffness k_{pt}. (b) Gear twist stiffness k_{gt}. (c) Coupling twist stiffness k_{ct}.

(curve-fit) for twist stiffnesses time and mesh deflection dependence may be neglected. That makes twist stiffnesses functions of relative twist $k_{pt} = k_{pt}(\gamma)$, and so on, with perhaps only quadratic coefficients. If this approximation is verified, a perturbation

method or harmonic balance can be applied to give closed-form expressions for the nonlinear twist vibrations.

7.2.3 Nonlinear 3-D Vibration of Planetary Gears

This work focused on linear vibration of planetary gears using modal analysis with a rigid body model, so it has not explored the nonlinear dynamics or the dynamics when gear components vibrate as elastic bodies. There is preliminary experimental evidence of partial contact loss in planetary gears, plotted in Figure 7.3. The resonant frequencies depend on applied torque, which suggests partial contact loss. Dynamic response may become nonlinear in a fashion similar to the ones observed in Chapter 3. If the gears are helical, twist vibrations could be excited with ensuing nonlinear response.

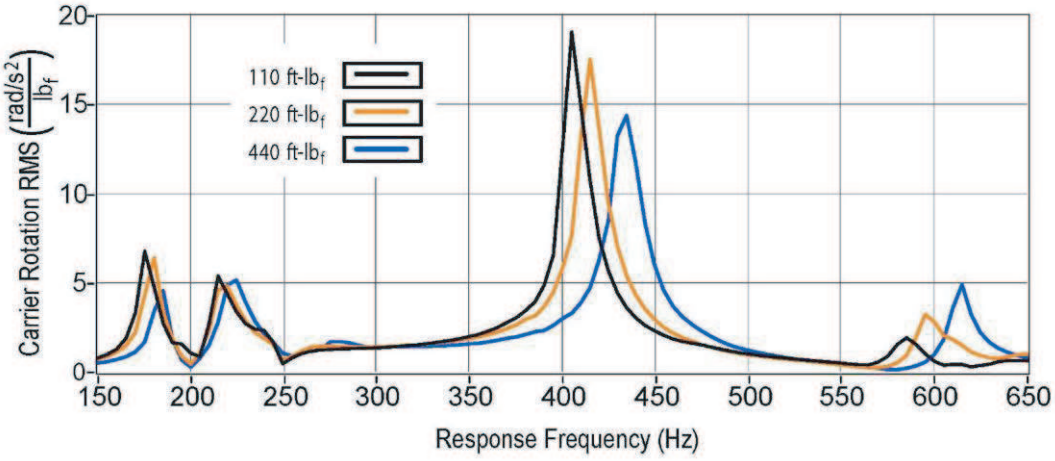

Figure 7.3: Dynamic response of spur planetary gears with tooth surface modifications on planets. Data is courtesy of Tristan M. Ericson using the test gears at the Dynamics and Vibrations Laboratory of The Ohio State University Mechanical and Aerospace Engineering Department.

The modal properties presented in Chapter 5 may not hold under dynamic resonant conditions. For example, if the resonance of a rotational-axial mode is nonlinear, then the symmetry of the system may be destroyed, which in turn destroys the classification of mode types. Whether this occurs, and if it does, to what extent remains to be seen. Similarly, vibration suppression rules may not hold if the dynamic response becomes nonlinear. Large elastic deformations of, for example, the ring gear may destroy the circumferential symmetry upon which the vibration suppression rules rely.

7.2.4 Verification and Extension of Vibration Suppression Rules

The set of rules that eliminate the net force and moment fluctuations needs to be computationally verified. The analysis must test that the force and moment fluctuations are eliminated with proper mesh phasing with: 1) Axially asymmetric system with uneven load distribution and staged shafts, 2) Static and dynamic operating conditions, 3) Elastic ring, sun, and carrier.

The vibration suppression rules come from circumferential symmetry, the periodicity in the gear meshing action, and planet spacing. The symmetry may still exist (or be destroyed) with other structural features such as splines on the ring gear, or bore holes on gears. The set of rules for vibration suppression, if it indeed exists, may be extended to include spacing of such modifications to the system. The use of splines and other such features in real-world applications make this extension practically important.

Bibliography

[1] V. Abousleiman and P. Velex. A hybrid 3d finite element/lumped parameter model for quasi-static and dynamic analyses of planetary/epicyclic gear sets. *Mechanism and Machine Theory*, 41(6):725–748, June 2006.

[2] V. Abousleiman, P. Velex, and S. Becquerelle. Modeling of spur and helical gear planetary drives with flexible ring gears and planet carriers. *Journal of Mechanical Design*, 129:95–106, January 2007.

[3] M. Ajmi and P. Velex. A model for simulating the quasi static and dynamic behaviour of solid wide faced spur and helical gears. *Mechanism and Machine Theory*, 40(2):173–190, February 2005.

[4] V. K. Ambarisha and R. G. Parker. Suppression of planet mode response in planetary gear dynamics through mesh phasing. *Journal of Vibration and Acoustics*, 128(2):133–142, April 2006.

[5] V. K. Ambarisha and R. G. Parker. Nonlinear dynamics of planetary gears using analytical and finite element models. *Journal of Sound and Vibration*, 302(3):577–595, May 2007.

[6] A. Andersson and L. Vedmar. A dynamic model to determine vibrations in involute helical gears. *Journal of Sound and Vibration*, 260(2):195–212, February 2003.

[7] R. August and R. Kasuba. Torsional vibrations and dynamic loads in a basic planetary gear system. *Journal of Vibration, Acoustics, Stress, and Reliability in Design*, 108(3):348–353, July 1986.

[8] C.-J. Bahk and R. G. Parker. Analytical solution for the nonlinear dynamics of planetary gears. *Journal of Computational and Nonlinear Dynamics*, 6(2):021007, Apr. 2011.

[9] S. Baud and P. Velex. Static and dynamic tooth loading in spur and helical geared systems-experiments and code validation. *Journal of Mechanical Design*, 124(2):334–346, June 2002.

[10] M. N. Bettaieb, P. Velex, and M. Ajmi. A static and dynamic model of geared transmissions: by combining substructure and elastic foundations - applications to thin rimmed gears. *Journal of Mechanical Design*, 129:184–194, February 2007.

[11] G. W. Blankenship and A. Kahraman. Steady state force response of a mechanical oscillator with combined parametric excitation and clearance type nonlinearity. *Journal of Sound and Vibration*, 185(5):743–765, 1995.

[12] G. W. Blankenship and A. Kahraman. Gear dynamics experiments part 1: Characterization of forced response. In *ASME Design Engineering Technical Conferences*, San Diego, CA, September 1996.

[13] G. W. Blankenship and R. Singh. Dynamic force transmissibility in helical gear pairs. *Mechanism and Machine Theory*, 30(3):323–339, April 1995.

[14] G. W. Blankenship and R. Singh. A new gear mesh interface dynamic model to predict multi-dimensional force coupling and excitation. *Mechanism and Machine Theory*, 30(1):43–57, January 1995.

[15] M. Botman. Epicyclic gear vibrations. *Journal of Engineering for Industry, Series B*, (98):811–815, August 1976.

[16] M. Botman. Vibration measurement on planetary gears of aircraft turbine engines. *J. Aircraft*, (5), May 1980.

[17] S. Chang, D. R. Houser, and J. Harianto. Tooth flank corrections of wide face width helical gears that account for shaft deflections. *International Design Engineering Technical Conferences and Computers and Information in Engineering*, 2003. Proceedings of ASME, Chicago, IL, DETC2003/PTG-48072.

[18] T. F. Conry and A. Seireg. Mathematical programming technique for evaluation of load distribution and optimal modification for gear systems. *Journal of Engineering for Industry*, 95(4):1115–1122, 1973.

[19] F. Cunliffe, J. D. Smith, and D. B. Welbourn. Dynamic tooth loads in epicyclic gears. *Journal of Engineering for Industry*, 5(95):578–584, May 1974.

[20] F. Cunliffe and D. B. Welbourn. Epicyclic gear vibration. In *Conference on Vibration in Rotating Systems*, page 5, London,England, February 1972. Institute of Mechanical Engineers.

[21] T. Eritenel and R. G. Parker. A static and dynamic model for three-dimensional multi-mesh gear systems. *International Design Engineering Technical Conferences and Computers and Information in Engineering*, 2005. , Proceedings of the ASME, DETC2005-85673.

[22] T. Eritenel and R. G. Parker. Modal properties of three-dimensional helical planetary gears. *Journal of Sound and Vibration*, 325:397–420, August 2009. DOI:10.1016/j.jsv.2009.03.002.

[23] T. Eritenel and R. G. Parker. An investigation of nonlinearity in gear pairs using a lumped-parameter model. *Journal of Applied Mechanics (Submitted)*, 2011.

[24] T. Eritenel and R. G. Parker. Three-dimensional nonlinear vibration of gear pairs. *Journal of Sound and Vibration (Submitted)*, 2011.

[25] I. S. Gradshteyn and I. M. Ryzhik. *Table of integrals, series, and products.* Academic Press, New York, 1980.

[26] R. W. Gregory, S. L. Harris, and R. G. Munro. Dynamic behavior of spur gears. *Proceedings of the Institution of Mechanical Engineers*, 178(8):261–266, 1963.

[27] R. Guilbault, C. Gosselin, and L. Cloutier. Helical gears, effects of tooth deviations and tooth modifications on load sharing and fillet stresses. *Journal of Mechanical Design*, 128:444–456, March 2006.

[28] Yichao Guo and R. G. Parker. Sensitivity of general compound planetary gear natural frequencies and vibration modes to model parameters. *International Design Engineering Technical Conferences and Computers and Information in Engineering Conference*, Sep 4-7 2006. DETC2007-35802.

[29] Yichao Guo and R. G. Parker. Sensitivity of general compound planetary gear natural frequencies and vibration modes to model parameters. *Journal of Vibration and Acoustics*, 132(011006-1), February 2010.

[30] S. L. Harris. Dynamic loads on the teeth of spur gears. *IMechE Applied Mechanics*, 172:87–100, 1958.

[31] Song He, R. Gunda, and R. Singh. Inclusion of sliding friction in contact dynamics model for helical gears. *Journal of Mechanical Design*, 129:48–57, January 2007.

[32] D. P. Hess and A. Soom. Normal vibrations and friction under harmonic loads: Part 1 - hertzian contacts. *Journal of Tribology*, 113:80–86, January 1991.

[33] T. Hidaka, Y. Terauchi, and K. Nagamura. Dynamic behavior of planetary gear (6th report, influence of meshing-phase). *Bulletin of JSME*, 22(169):1026–1033, July 1979.

[34] F. Hiroki and A. Toshio. Fundamental research on gear noise and vibration (7th report, generation mechanism of radial and axial vibration of spur gears). *Bulletin of JSME*, 17(113):1502–1512, 1974.

[35] F. Hiroki, F. Toyoaki, and A. Toshio. Fundamental research on gear noise and vibration (6th report, generation mechanism of radial and axial vibration of spur gears). *Bulletin of JSME*, 16(97):1094–1107, 1973.

[36] D. R. Houser, V. M. Bolze, and J. M. Graber. Static and dynamic transmission error measurements and predictions for spur and helical gear. In *Proceedings of the 7th ASME International Power Transmission and Gearing Conference*, volume 88, pages 365–372, 1996.

[37] D. R. Houser and J. Borner. Friction and bending moments as gear noise excitations. *SAE Transactions*, 105(6):1669–1676, May 1996. Paper Number: 961816.

[38] K. L. Johnson. *Contact Mechanics*. Cambridge University Press, 1985.

[39] A. Kahraman. Effect of axial vibrations on the dynamics of a helical gear pair. *Journal of Vibration and Acoustics*, 115(1):33–39, January 1993.

[40] A. Kahraman. Planetary gear train dynamics. *Journal of Mechanical Design*, 116(3):713–720, September 1993.

[41] A. Kahraman. Dynamic analysis of a multi mesh helical gear train. *Journal of Mechanical Design*, 116(3):706–712, September 1994.

[42] A. Kahraman. Natural modes of planetary gear trains (letters to the editor). *Journal of Sound and Vibration*, 173(1):125–130, 1994.

[43] A. Kahraman and G. W. Blankenship. Planet mesh phasing in epicyclic gear sets. In *International Gearing Conference*, pages 99–104, Newcastle, UK, 1994.

[44] A. Kahraman and G. W. Blankenship. Interactions between commensurate parametric and forcing excitations in a system with clearance. *Journal of Sound and Vibration*, 194(3):317–336, 1996.

[45] A. Kahraman and G. W. Blankenship. Experiments on nonlinear dynamic behavior of an oscillator with clearance and periodically time-varying parameters. *Journal of Applied Mechanics*, 64(1):217–226, March 1997.

[46] A. Kahraman and G. W. Blankenship. Effect of involute contact ratio on spur gear dynamics. *Journal of Mechanical Design*, 121(1):112–118, March 1999.

[47] A. Kahraman and G. W. Blankenship. Effect of involute tip relief on dynamic response of spur gear pairs. *Journal of Mechanical Design*, 121(5):313–315, June 1999.

[48] A. Kahraman, H. N. Özgüven, D. R. Houser, and J. J. Zakrajsek. Dynamic analysis of geared rotors by finite elements. *Journal of Mechanical Design*, 114(3):507–514, September 1992.

[49] A. Kahraman and R. Singh. Non-linear dynamics of a spur gear pair. *Journal of Sound and Vibration*, 142(1):49–75, October 1990.

[50] A. Kahraman and R. Singh. Interactions between time-varying mesh stiffness and clearance non-linearities in a geared system. *Journal of Sound and Vibration*, 146(1):135–156, April 1991.

[51] R. Kasuba and J. W. Evans. An extended model for determining dynamic loads in spur gearing. *ASME*, 103:398–409, 1981.

[52] D. R. Kiracofe and R. G. Parker. Structured vibration modes of general compound planetary gear systems. *Journal of Vibration and Acoustics*, 129(1):1–16, February 2007.

[53] S. Kiyono, T. Aida, and Y. Fujii. Vibration of helical gears: Part 2 experimental investigation. *Bulletin of JSME*, 21(155):923–930, May 1978.

[54] A. Kubo. Stress condition, vibration exciting force and contact pattern of helical gears with manufacturing and alignment error. *Journal of Mechanical Design*, 100:77–84, January 1978.

[55] A. Kubo, S. Kiyono, and F. Makoto. On analysis and prediction of machine vibration caused by gear meshing : 1st report, nature of gear vibration and the total vibrational excitation. *Bulletin of JSME*, 29(258):4424–4429, 1986.

[56] M. Kubur, A. Kahraman, D. M. Zini, and K. Kienzle. Dynamic analysis of a multi-shaft helical gear transmission by finite elements: Model and experiment. *Journal of Vibration and Acoustics*, 126(3):398–406, July 2004.

[57] C. Lee, H-H. Lin, F. B. Oswald, and D. P. Townsend. Influence of linear profile modification and loading conditions on the dynamic tooth load and stress of high-contact- ratio spur gears. *Journal of Mechanical Desing*, 113(4):473–480, December 1991.

[58] J. Lin and R. G. Parker. Analytical characterization of the unique properties of planetary gear free vibration. *Journal of Vibration and Acoustics*, 121(3):316–321, July 1999.

[59] J. Lin and R. G. Parker. Sensitivity of planetary gear natural frequencies and vibration modes to model parameters. *Journal of Sound and Vibration*, 228(1):109–128, November 1999.

[60] J. Lin and R. G. Parker. Structured vibration characteristics of planetary gears with unequally spaced planets. *Journal of Sound and Vibration*, 233(5):921–928, June 2000.

[61] J. Lin and R. G. Parker. Natural frequency veering in planetary gears. *Mechanics of Structures and Machines*, 29(4):411–429, 2001.

[62] J. Lin and R. G. Parker. Mesh phasing relationships in planetary and epicyclic gears. *Journal of Mechanical Design*, 126:365–370, March 2004.

[63] F. L. Litvin, A. Fuentes, I. Gonzalez-Perez, L. Carnevali, and K. Kawasaki. Modified involute helical gears: Computerized design, simulation of meshing, and stress analysis. Technical Report ARL-CR-514, NASA, 2003.

[64] F. L. Litvin, D. Vecchiato, K. Yukishima, A. Fuentes, I. Gonzalez-Perez, and K. Hayasaka. Reduction of noise of loaded and unloaded misaligned gear drives. *Computer Methods in Applied Mechanics and Engineering*, 195(41–43):5523 – 5536, 2006. John H. Argyris Memorial Issue. Part II.

[65] Gang Liu and R. G. Parker. Dynamic modeling and analysis of tooth profile modification for multimesh gear vibration. *Journal of Mechanical Design*, 130(2), December 2008. 121402.

[66] Gang Liu and R. G. Parker. Impact of tooth friction and its bending effect on gear dynamics. *Journal of Sound and Vibration*, 320(4-5):1039–1063, March 2008.

[67] Gang Liu and R. G. Parker. Nonlinear dynamics of idler gear systems. *Nonlinear Dynamics*, 53(4):345–367, September 2008.

[68] A. Luongo and A. Paolone. On the reconstitution problem in the multiple time-scale method. *Nonlinear Dynamics*, 19(2):133–156, June 1999.

[69] Qinglong Ma, A. Kahraman, J. Perret-Liaudet, and E. Rigaud. An investigation of steady-state dynamic response of a sphere-plane contact interface with contact loss. *Journal of Applied Mechanics*, 74(2):249–255, March 2007.

[70] M. Maatar and P. Velex. Quasi-static and dynamic analysis of narrow-faced helical gears with profile and lead modifications. *Journal of Mechanical Design*, 119(4):474–480, December 1997.

[71] S. Matsumura, K. Umezawa, and H. Houjoh. Rotational vibration of a helical gear pair having tooth surface deviation during transmission of light load. *JSME international journal. Ser. C, Dynamics, control, robotics, design and manufacturing*, 39(3):614–620, 1996.

[72] S. Natsiavas, S. Theodossiades, and I. Goudas. Dynamic analysis of piecewise linear oscillators with time periodic coefficients. *International Journal of Non-Linear Mechanics*, 35(1):53–68, January 2000.

[73] P. R. Nayak. Contact vibrations. *Journal of Sound and Vibration*, 22(3):297–322, 1972.

[74] A. H. Nayfeh. *Problems in Perturbation*. John Wiley & Sons, Inc., 1993.

[75] A. H. Nayfeh and D. T. Mook. *Nonlinear Oscillations*. Wiley, 1979.

[76] T. Nishino. Integrated excitation models of the helical gear system. In *ASME Design Engineering Technical Conferences*, number DETC2007-34134, Las Vegas, NV, September 2007.

[77] T. Nishino. Vibration analysis of the helical gear system using the integrated excitation model. *JSME Journal of Advanced Mechanical Design, Systems, and Manufacturing*, 1(4):541–552, 2007.

[78] S. Oda, T. Koide, and K. Miyachika. Dynamic behavior of thin-rimmed helical gears with various web arrangements. *Bulletin of JSME*, 28(244):2434–2441, October 1985.

[79] Y. Ogawa, S. Matsumura, H. Houjoh, T. Sato, and K. Umezawa. Rotational vibration of a spur gear pair considering tooth helix deviation: Development of simulator and verification. *JSME International Journal, Series C*, 43(2):423–431, 2000.

[80] F. B. Oswald, D. P. Townsend, M. J. Valco, R. H. Spencer, R. J. Drago, and J. W. Lenski. Influence of gear design parameters on gearbox radiated noise. Technical Report ARL TR-381, NASA, 1994.

[81] H. N. Özgüven and D. R. Houser. Dynamic analysis of high speed gears by using loaded static transmission error. *Journal of Sound and Vibration*, 125(1):71–83, August 1988.

[82] H. N. Özgüven and D. R. Houser. Mathematical-models used in gear dynamics - a review. *Journal of Sound and Vibration*, 121(3):383–411, 1988.

[83] C. Padmanabhan and R. Singh. Analysis of periodically forced nonlinear hill's oscillator with application to a geared system. *The Journal of the Acoustical Society of America*, 99(1):324–334, January 1996.

[84] R. G. Parker. A physical explanation for the effectiveness of planet phasing to suppress planetary gear vibration. *Journal of Sound and Vibration*, 236:561–573, September 2000.

[85] R. G. Parker, V. Agashe, and S. M. Vijayakar. Dynamic response of a planetary gear system using a finite element/contact mechanics model. *Journal of Mechanical Design*, 122(3):304–310, September 2000.

[86] R. G. Parker, S. M. Vijayakar, and T. Imajo. Non-linear dynamic response of a spur gear pair: Modelling and experimental comparisons. *Journal of Sound and Vibration*, 237(3):435–455, October 2000.

[87] R. G. Parker and X. Wu. Vibration modes of planetary gears with unequally spaced planets and an elastic ring gear. *Journal of Sound and Vibration*, 329(11):2265–2275, May 2010.

[88] J. L. M. Peeters, D Vandepitte, and P. Sas. Analysis of internal drive train dynamics in a wind turbine. *Wind Energy*, 9:141–161, 2006.

[89] J. Perret-Liaudet and E. Rigaud. Response of an impacting hertzian contact to an order-2 subharmonic excitation : Theory and experiments. *Journal of Sound and Vibration*, 296(1-2):319–333, September 2006.

[90] J. P. Raclot and P. Velex. Simulation of the dynamic behaviour of single and multi-stage geared systems with shape deviations and mounting errors by using a spectral method. *Journal of Sound and Vibration*, 220(5):861–903, March 1999.

[91] E. Rigaud and J. Perret-Liaudet. Experiments and numerical results on non-linear vibrations of an impacting hertzian contact. part 1: harmonic excitation. *Journal of Sound and Vibration*, 265(2):289–307, August 2003.

[92] E. Rigaud, J. Perret-Liaudet, and M. S. Mecibah. Effect of an original gear mesh modeling on the gearbox dynamic behavior. *International Design Engineering Technical Conferences and Computers and Information in Engineering*, Sep. 4-7 2007. , Proceedings of the ASME, Las Vegas, NV, DETC2007-34070.

[93] A. Saada and P. Velex. An extended model for the analysis of the dynamic behavior of planetary trains. *Journal of Mechanical Design*, 117(2):241–247, June 1995.

[94] J. Sabot, P. Krempf, and C. Janolin. Non-linear vibrations of a sphere-plane contact excited by a normal load. *Journal of Sound and Vibration*, 214(2):359–375, 1998.

[95] R. G. Schlegel and K. C. Mard. Transmission noise control approaches in helicopter design. In *ASME Design Engineering Conference*, number 67-DE-58, New York, NY, 1967.

[96] D. L. Seager. Dynamic behavior of helical gears. *American Society of Mechanical Engineers*, 100(69-VIBR-16), May 1969.

[97] D. L. Seager. Conditions for the neutralization of excitation by the teeth in epicyclic gearing. *Journal of Mechanical Engineering Science*, 17(5):293–298, 1975.

[98] D. L. Seager. Excitation in epicyclic gear teeth. *IMechE*, 17(5):293–298, 1975.

[99] Avinash Singh. Application of a system level model to study the planetary load sharing behavior. *Journal of Mechanical Design*, 127(3):469–476, May 2005.

[100] Avinash Singh. Influence of planetary needle bearings on the performance of single and double pinion planetary systems. *Journal of Mechanical Design*, 129(1):85–94, January 2007.

[101] R. Singh, D. R. Houser, and A. Kahraman. Non-linear dynamic analysis of geared systems. Technical report, NASA, February 1990. Final Report, Part II.

[102] J. D. Smith. *Gear noise and vibration*. Marcel Dekker, New York, 2 edition, 2003.

[103] V. K. Tamminana, A. Kahraman, and S. M. Vijayakar. A study of the relationship between the dynamic factors and the dynamic transmission error of spur gear pairs. *Journal of Mechanical Design*, 129(1):75–84, January 2007.

[104] M. S. Tavakoli and D. R. Houser. Optimum profile modifications for the minimization of static transmission error of spur gears. *Journal of Mechanisms Transmission and Automation in Design*, 108(1):86–95, March 1986.

[105] S. Theodossiades and S. Natsiavas. Non-linear dynamics of gear-pair systems with periodic stiffness and backlash. *Journal of Sound and Vibration*, 229(2):287–310, January 2000.

[106] J. J. Thomsen. *Vibrations and Stability*. Springer, 2 edition, 2003.

[107] A. Toda and M. Botman. Planet indexing in planetary gears for minimum vibration. *ASME*, (79-DET-73), 1980.

[108] M. Umeyama, M. Kato, and K. Inoue. Effects of gear dimensions and tooth surface modifications on the loaded transmission error of a helical gear pair. *Journal of Mechanical Design*, 120(1), March 1998.

[109] K. Umezawa. The meshing test on helical gears under load transmission : 1st report, the approximate formula for deflections of gear tooth. *Bulletin of JSME*, 15(90):1632–1639, 1972.

[110] K. Umezawa. The meshing test on helical gears under load transmission : 2nd report, the approximate formula for bending-moment distribution of gear tooth. 16(92):407–413, Feb. 1973.

[111] K. Umezawa. The meshing test on helical gears under load transmission : 3rd report, the static behaviours of driven gear. *Bulletin of JSME*, 17(112):1348–1355, Oct. 1974.

[112] K. Umezawa, Takumi Ajima, and H. Houjoh. Vibration of three axis gear system. *Bulletin of JSME*, 29(249):950–957, March 1986.

[113] K. Umezawa, H. Houjoh, and S. Matsumura. Experimental precise identification of dynamic behavior of a helical gear system. In *Proceedings of International Conferences on Gear*, pages pp779–792, Dresden, Germany, 1996.

[114] K. Umezawa, H. Houjoh, S. Matsumura, S. Wang, and S. Ohshima. Experimental investigation on modal behavior of helical gear units with various contact ratio. In *Proceedings of the 7th ASME International Power Transmission and Gearing Conference*, volume 88, pages 509–517, 1996.

[115] K. Umezawa, T. Sato, and J. Ishikawa. Simulation of rotational vibration of spur gears. *Bulletin of JSME*, 27(223):102–109, Jan. 1984.

[116] K. Umezawa, T. Suzuki, and H. Houjoh. Estimation of vibration of power transmission helical gears by means of performance diagrams on vibration. *JSME international journal. Ser. 3, Vibration, control engineering, engineering for industry*, 31(3):598–605, 1988.

[117] M. Vaishya and D. R. Houser. Vibration analysis of helical gear system including a gearbox. study on analysis method. In *ASME Design Engineering Technical Conferences*, number DETC2000/PTG-14431 in Power Transmission and Gearing Conference, Baltimore, Maryland, Sep. 2009.

[118] P. Velex and M. Ajmi. On the modelling of excitations in geared systems by transmission errors. *Journal of Sound and Vibration*, 290(3-5):882–909, March 2006.

[119] P. Velex and M. Ajmi. Dynamic tooth loads and quasi-static transmission errors in helical gears - approximate dynamic factor formulae. *Mechanism and Machine Theory*, 41(11):1512–1526, November 2007.

[120] P. Velex and V. Cahouet. Experimental and numerical investigations on the influence of tooth friction in spur and helical gear dynamics. *Journal of Mechanical Design*, 122(4):515–522, December 2000.

[121] P. Velex and M. Maatar. A mathematical model for analyzing the influence of shape deviations and mounting errors on gear dynamic behavior. *Journal of Sound and Vibration*, 191(5):629–660, April 1996.

[122] P. Velex, M. Maatar, and J. P. Raclot. Some numerical methods for the simulation of geared transmission dynamic behavior formulation and assessment. *Journal of Mechanical Design*, 119(2):292–298, June 1997.

[123] P. Velex and P. Sainsot. An analytical study of tooth friction excitations in errorless spur and helical gears. *Mechanism and Machine Theory*, 37(7):641–658, May 2002.

[124] S. M. Vijayakar. A combined surface integral and finite-element solution for a three-dimensional contact problem. *International Journal for Numerical Methods in Engineering*, 31(3):525–545, March 1991.

[125] S. M. Vijayakar. *Helical3D User's Manual*. Advanced Numerical Solutions LLC, Hilliard, Ohio, 43026 USA, February 2005. http://www.ansol.us/Manuals/Helical3DManual.pdf.

[126] S. M. Vijayakar, H. R. Busby, and D. R. Houser. Linearization of multibody frictional contact problems. *Computers and Structures*, 29(4):569–576, 1988.

[127] S. M. Vijayakar, H. R. Busby, and Lowell Wilcox. Finite element analysis of three-dimensional conformal contact with friction. *Computers and Structures*, 33(1):49–61, 1989.

[128] H. Vinayak, R. Singh, and C. Padmanabhan. Linear dynamic analysis of multi mesh transmissions containing external, rigid gears. *Journal of Sound and Vibration*, 185(1):1–32, August 1995.

[129] S. Wang, K. Umezawa, H. Houjoh, and S. Matsumura. An analytical investigation of the dynamic behavior of a helical gear system. In *ASME 7th International Power Transmission and Gearing Conference*, pages 169–176, San Diego, CA, 1996.

[130] D. B. Welbourn. Fundamental knowledge of gear noise - a survey. In *Proceedings of Conference on Noise and Vibrations of Engines and Transmissions, Institute of Mechanical Engineers*, pages 9–14, 1979. C117.

[131] C. H. Wink and A. L. Serpa. Investigation of tooth contact deviations from the plane of action and their effects on gear transmission error. *Proceedings of the Institution of Mechanical Engineers, Part C: Journal of Mechanical Engineering Science*, 219(5):501–509, 2005.

[132] C. H. Wink and A. L. Serpa. Performance assessment of solution methods for load distribution problem of gear teeth. *Mechanism and Machine Theory*, 43(1), January 2008.

[133] X. Wu and R. G. Parker. Modal properties of planetary gears with an elastic continuum ring gear. *Journal of Applied Mechanics*, 75(3):1–10, May 2008.

[134] Farong Zhu and R. G. Parker. Perturbation analysis of a clearance-type nonlinear system. *Journal of Sound and Vibration*, 292(3-5):969–979, 2006.